A Theoretical and Experimental Study of Cell Specification in the Female Gametophyte

Dissertation

zur Erlangung

der naturwissenschaftlichen Doktorwürde

(Dr. sc. nat.)

vorgelegt

der Mathematisch-naturwissenschaftlichen Fakultät

der Universität Zürich

von

Dmytro Sergiiovyč Lituiev

aus der Ukraine

Promotionskomitee

Prof. Dr. Ueli Grossniklaus (Leitung der Dissertation)

Prof. Dr. Enrico Martinoia

Prof. Dr. Barbara Hellriegel

Dr. Bruno Müller

Zürich 2013

Typeset with LaTeX

Contents

Curriculum Vitæ

Personal Data

Surname	Lituiev
Given name	Dmytro
Patronymic	Segiiovyč
Date of birth	September 9, 1986
Place of Birth	Donetsk, Ukraine

Education

2001 — 2003	High school	Lyceum of the Donetsk National University, Ukraine
2003 — 2007	Undergraduate studies	Taras Shevchenko National University of Kyiv, Ukraine
2007 — 2009	Master studies	National University of 'Kyiv-Mohyla Academy', Ukraine
2009	Master thesis (Hons)	Development and characterization of monoclonal antibodies against human sodium-phosphate cotransporter NaPi2b. (wth Prof. Dr. Valery Filonenko and Dr. Ramziya Kiyamova)
2009 — 2013	Doctoral studies	University of Zürich, Switzerland (wth Prof. Dr. Ueli Grossniklaus)

Zusammenfassung

In Blütenpflanzen ist der weibliche Gametophyt ein Teil der Samenanlage. Nach der Bestäubung und Befruchtung der weiblichen Gameten im Gametophyten entwickelt sich ein Same. In den meisten Pflanzen entwickelt sich der siebenkernige weibliche Gametophyt aus einer einkernigen Zelle. Obwohl viele Einzelheiten über die Entwicklung des weiblichen Gametophyten bekannt sind, kann man sie kaum so zusammenfassen, daßsie ein klares Bild ergeben. Versuche an der Modellpflanze Ackerschmalwand (*Arabidopsis thaliana*) führten vor Kurzem zu einer Behauptung, die das Problem umfassend erklären sollte. Angeblich soll das Pflanzenhormon Auxin das Schicksal der Zellen des weiblichen Gametophyten bestimmen. Im vorliegenden Werk gehe ich dieser Hypothese nach. Zuerst ging ich an diese Hypothese durch Zusammenstellung eines mathematischen Modells heran, welches die früher vorgeschlagenen Faktoren zur Unterhaltung des Auxingradienten aufnimmt. Dieses Model samt Hilfsexperimenten machte deutlich, daß früher unberücksichtigte Faktoren, wie die Hemmung der Diffusion durch die grosse Vakuole des weiblichen Gametophyten und der Transport von Auxin durch Membranen zur Entstehung des Gradienten beitragen und ihn steiler machen können. Dahingegen führen die effektiven Raten des Auxin-Abbaus und der Auxin-Diffusion zu einem Gradienten mit einer Konzentrationsdifferenz von nur 3.21 % zwischen den Polen. Weiterhin zeigte ich, daß bei einer Schwankung der Auxinzufuhr von mehr als 3.31% die Differenzierung der Zelltypen, die durch einen solchen Gradienten felstgelegt werden kann, nicht mehr stattfinden würde. Im Vergleich zu *Drosophila* als analogem Modell, bei dem es sich um Schwankung von 10% handelt, wäre das eine relativ geringfügige Veränderung. Daraus schloss ich, daß bis dato entweder nicht alle Faktoren zur Entstehung des Auxingradienten bekannt sind oder bestehende Angaben über den Gradienten falsch sind.

Um zwischen diesen möglichen Erklärungen zu unterscheiden, wiederholte ich Experimente um die Auxin-Aktivität in den Samenanlagen von Arabidopsis sichtbar zu machen. Überraschenderweise fand ich in allen Versuchen keine Auxin-Aktivität. Dennoch beobachtete ich im Laufe der Entwicklung der Samenanlage eine Verschiebung des Auxin-Maximums von der Kuppe (Mikropyle) zu den inwendigen, den Gametophyten umgebenden Geweben an der Basis (Chalaza).

Deshalb schlage ich einige Hypothesen vor, die die Auswirkungen von Auxin auf die Zelltypspezifizierung des weiblichen Gametophyten erklären. Eine von einem mathematischen Modell untermauerte Hypothese postuliert, daß die umliegenden Gewebe einen nicht-zellautonomen Faktor absondern der die Zelltypspezifizierung im weiblichen Gametophyten beeinflusst. Eine erhöhte Auxin-Konzentration kann ihrerseits die Identität der umliegenden Zellen beeinflussen und somit die Abgabe des nicht-zellautonomen Faktors, was wiederum die Entwicklung des weiblichen Gametophyten beeinträchtigen kann. An-

dererseits könnte ein flacher Gradient unterhalb der Nachweisgrenze aller venwendeten Sensorenkonstrukte bestehen und den Bruch der Symmetrie bzw. die Polarisierung auslösen. Zwar findet man für beide Hypothesen indirekte Bestätigungen in der Literatur, aber ein experimenteller Nachweis steht noch aus.

Zusätzlich zum Hauptthema dieser Dissertation stelle ich zwei neue Instrumentarien für die biologische Datenverarbeitung vor: (1) ein Algorithmus für Mutationskartierungen durch Hochdurchsatzsequenzierungen und (2) ein Werkzeug zur Expert- bzw. Expertin-unterstützten Verfolgung wachsender Pollenschläuche.

Abstract

The female gametophyte of flowering plants is the organ located within the plant ovule which upon pollination and fertilization gives rise to the seed. In most flowering plants, female gametophytes contain seven cells which develop from a single one-nuclear cell. Numerous details on how these cells acquire distinct cellular fate have been proposed. However, these facts still cannot be assembled into a coherent picture. One idea promising to provide a holistic explanation of female gametophytic patterning appeared recently based on observations in *Arabidopsis thaliana* plants, stating that a gradient of plant hormone auxin provides positional information to all cell types. Here I examined this idea by theoretical and experimental approaches.

First, I investigated this hypothesis by constructing a mathematical model incorporating several factors proposed to sustain the auxin gradient. The model combined with experiments identified that factors previously unaccounted for, such as inhibition of diffusion by a large vacuole and trans-membrane fluxes, theoretically can make auxin gradient within the female gametophyte steeper. However, under the rates of auxin degradation, diffusion, and transport known from literature, the gradient which can be actually achieved results in concentration difference between the opposite poles of only 3.21%. Further I showed that cell fate differentiation controlled by such a low gradient will be fail under any change in the auxin supply rate higher than 3.31%, which is low compared to perturbations of 10% usually considered in an analogous system of *Drosophila* egg. Therefore, I conclude that whether not all mechanisms of auxin gradient formation are known, or current data about auxin gradient are wrong.

To distinguish between these two possibilities, I repeated experiments visualizing auxin activity within the *Arabidopsis* ovules using various auxin-sensitive constructs. Surprisingly, in all experiments I detected no auxin activity within the female gametophyte. However, I found that during ovule development, the auxin maximum relocates from the tip (micropyle) of the ovule to its inner tissues adjacent to the female gametophyte from the basal (chalazal) side.

Hence, I put forth several hypothesis explaining the effects of auxin on the fate of female gametophytic nuclei. One hypothesis substantiated by a mathematical model, states that the surrounding tissues influence patterning within female gametophyte by secreting a non-cell-autonomous factor; overproduction of auxin performed in earlier experiments in turn can change the identity of the surrounding tissues and thus secretion pattern of a non-cell-autonomous factor, affecting thus the patterning within the female gametophyte. Alternatively, a very shallow auxin gradient at the levels lower than detection limit of all auxin-sensitive constructs might exist and trigger symmetry breakage (i. e. generation of polarity) within the female gametophyte through additional molecular mechanisms.

Though indirect substantiating evidence for both hypotheses can be found in literature, they still remain to be investigated experimentally.

Additionally to the main theme of the dissertation, I present two tools for analysis of biological data: (1) an inference algorithm for mutation mapping with high-throughput sequencing and (2) a tool for expert-assisted pollen tube tracking.

Preface

General notes. In this thesis I present my work accomplished during my doctoral studies between December 2009 — October 2013. During this period I worked on my main project, whose subject gave the title to this work. Additionally I applied my knowledge in other collaborative projects aimed to assist processing of various biological data in the laboratory of Developmental Genetics. The iPhD project was funded by the SystemsX.ch, the Swiss initiative for Systems Biology.

The aim of this study is to examine the mechanisms of formation of auxin gradient in the *Arabidopsis* female gametophyte through juxtaposing current experimental knowledge in a mathematical model and applying complementary experimental techniques intended to clarify the conditions of the model.

Structure. The thesis is organized in following way. First, I provide an introduction to the biological problem and briefly preview the results of this work. Further, in the Chapter 1 I present results of a modelling study to the question of auxin gradient in the female gametophyte juxtaposed to experimental data. This piece of have been accepted as a paper to the *Development* journal in August 2013. In the Chapter 2 I elaborate on the model of auxin reaction-transport-diffusion in the female gametophyte in further detail. This chapter also can be read as a separate article. Further I provide general Conclusions and Outlook as to the work presented in these two chapters.

In Appendix 1, I present technical background which might help to understand analytical derivations and numerical simulations presented in the chapter 2 in more detail. In the Appendix 2, I provide a supplementary material to the chapter 2 with derivation of parameters of the model.

In next appendices I describe results of additional projects initiated during my doctoral studies. In the Appendix 3, I present a statistical tool for mutation mapping with high-throughput sequencing. In the Appendix 4, I describe a new tool for expert-assisted tracking and intensity measurement for growing pollen tubes. In the Appendix 5, I present a work in co-authorship with Aurélien Boisson-Dernier and co-authors where I performed data analysis for data on protein diffusivity (fluorescence recovery after photo-bleaching) and processing of ratiometric Ca^{+2} signals. Finally, in the Appendix 6 I present a paper in co-authorship with Evelyne Zürcher, Deborah Tavor-Deslex, Bruno Müller and others, where I performed initial screening of the cytokinin-sensitive reporter lines.

Acknowledgements. First of all, I would like to thank Ueli Grossniklaus, Bruno Müller and Barbara Hellriegel for giving me opportunity to work on this interdsciplinary project and supporting me during these four years.

I would like to thank Christoph Eichenberger, Célia Jäger-Baroux, and Quy Ai Ngo for sharing their valuable expertise in microscopy. I would like to say many thanks to Bruno Müller specifically for proof-reading of my abstracts. Also I would like to acknowledge technical support from Katalin Enkerli, Peter Kopf, Daniela Kleen-Guthörl, Arturo Bolaños, and Valeria Gagliardini.

I say big thanks to Anna Nesterova, Quy Ai Ngo, Hannes Vogler, Afif Hedhly, Deborah Tavor-Deslex, Wenjing She, Aurélien Boisson-Dernier and Stephan Wyder for helpful discussions of both scientific and everyday matter and help with laboratory work and plant growing. Special thanks goes to Anja Schmidt who discussed and corrected the German version of the abstract of this thesis.

I express special aknowledgement to the whole community of the SystemsX.ch, Swiss initiative for Systems Biology, for creating nurturing and collaborative atmosphere fostering scientific and general communication. Specifically, I am grateful to Daniel Vonder Mühll, Katy Pegg and former scientific coordinators Pierra Cicchetti and Jens Selige for the extraordinary retreats they organised in 2010—2013.

I would like to thank people from other departments and institutions who gave their valueble advice on the main topic of this work, namely Enrico Martinoia (University of Zurich), Marcus Geisler (University of Fribourg), and Pierre Barbier de Reuille (University of Berne). I would like to thank Niko Beerenwinkel and Armin Topfer (BSSE ETHZ, Basel) for discussion of the project on mutation mapping. Also I would like to thank Ricard Delgado Gonzalo (EPF Lausanne) for his feedback on the tool for expert-assisted tracking for growing pollen.

Last but not least I say thank-you to my parents and my grilfriend Mariia Burdyniuk and other friends for supporting me emotionally.

Introduction

0.1 Morphology of the female gametophyte in flowering plants

The life cycle of terrestrial plants alternates between two phases: diploid *sporophyte* phase and a haploid *gametophyte* phase. In all terestrial plants but mosses, the sporophyte is the main vegetative form, while the other, gametophyte, is short-living and accumulating less biomass. While male gamtophyte embodied in the form of pollen grain after maturation can travel by airflows, carried by a pollinator or any other means, the female gametophyte, called also *embryo sac* remains encapsulated into sporophytic tissues. A typical morphology of the female gametophyte within the context of flower is presented in Figure 0.1.

Development of the haploid female gametophyte starts with the megaspore, which is a product of a meiotic cell division (one which leads to a reduction of the chromosome number by factor of two) within the reproductive tissue of the sporophyte. In lower terrestrial plants, such as ferns and mosses, the megaspore is further detached from the sporogenic tissue and travels with the wind or water drops to initiate a free-living gametophyte. In higher plants, spermatophytes, including Gymnospermæ, like conifers and ginkgos, and Angiospermæ, i.e. flowering plants, the female gametophyte develops enclosed in the sporophytic tissues and consist of a pre-defined set of cells.

In *Arabidopsis*, as in most flowering plants, including cereal crops, the female gametophyte develops from a single megaspore cell, which through three consecutive endo-mitotic divisions produces eight nuclear syncytium[1]. Next, the embryo sac builds the membranes between the nuclei to form two synergids, the egg cell, the bi-nuclear central cell and three antipodals. Two of the nuclei further fuse to form the bi-haploid nucleus of central cell.

After the fertilization by a male gamete contained in pollen nuclei of the egg cell and the male gamete fuse to form a zygote, which further gives rise to a plant embryo. In angiosperms, the second nucleus of the pollen fertilizes the central cell to give rise to a triploid nutritive tissue, the endosperm.

[1] a cell with multiple nuclei

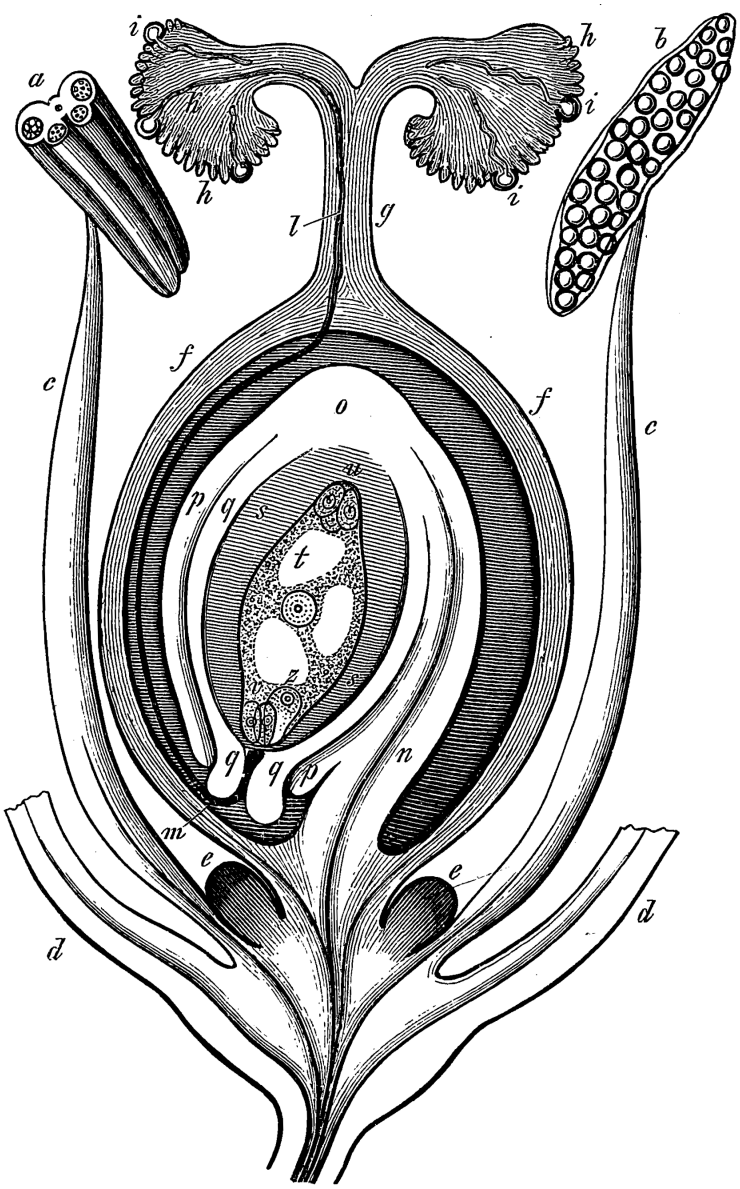

Fig. 442. Schema einer sehr einfach gebauten Blüthe im Längsdurchschnitt gesehen; *a* Querdurchschnitt einer Anthere vor ihrem Aufspringen; *b* eine der Länge nach aufgesprungene Anthere mit Pollen; *c* Filament; *d* Basis der Blüthenhülle; *e* Nektarien; *f* Wand des Fruchtknotens; *g* Griffel desselben; *h* Narbe; *i* keimende Pollenkörner; *k*, *l*, *m* ein Pollenschlauch bis in die Mikropyle vorgedrungen; *n* Stiel der Samenknospe; *o* Basis derselben; *p* äußeres, *q* inneres Integument; *s* der Kern der Samenknospe; *t* der Raum des Embryosackes; *u* Basaltheil desselben mit den Antipoden; *v* die Synergiden; *z* Eizelle.

Figure 0.1: **Schematic depiction of a longitudinal section of a flower with an ovule and female gametophyte inside** (taken from von Sachs (1882, p.931)). *a* section of an anther before opening; *b* an opened anther with pollen; *c* filament; *d* basis of the perianth (sepals and petals); *e* nectaries; *f* wall of the pistil; *g* the neck of the pistil ; *h* stigma; *i* germinating pollen grains; *k, l, m* a pollen tube before penetrating the micropyle; *n* stalk of the ovule; *o* basis of the ovule (chalaza); *p* outer integument; *q* inner integument; *s* nucellus of the ovule; *t* the central cell of the embryo sac (female gametophyte) ; *u* chalazal part of the female gametophyte with antipodal cells; *v* the synergids; *z* the egg cell.

0.2 Patterning in the female gametophyte of flowering plants through the prisms of theoretical paradigms *(mini-review)*

Dmytro S. Lituiev, Ueli Grossniklaus

Institute of Plant Biology, University of Zürich and Zürich-Basel Plant Science Centre, Switzerland

Key words: patterning, female gametophyte, morphogen, positional information

Abbreviations: FG — female gametophyte; FM — functional megaspore; MMC — megaspore mother cell.

Abstract

Specification of nuclei in the female gametophytes of higher plants has been in focus of study last decade. A failure to find a global positional clue in the female gametophyte stimulates reconsidering of the available data on developmental mutants and fate markers in a in light of theoretical frameworks of biological patterning. While some results have been earlier interpreted in terms of static positional information, a large number of evidence show that local interactions are important. We argue that further dissection of the mechanisms may be complicated by combinatorial and dynamical nature of developmental cues and accounting for these properties is necessary to disentangle the diversity of phenotypic manifestations of molecular interactions.

0.2.1 Introduction

The life cycle of terrestrial plants alternates between two phases: diploid *sporophyte* phase and a haploid *gametophyte* phase. Development of the haploid female gametophyte (FG), also referred to as megagametogenesis, starts with the functional megaspore (FM), which is a product of a meiotic division of the diploid sporophytic megaspore mother cell (MMC). In lower terrestrial plants, such as ferns and mosses, the megaspore is further detached from the sporogenic tissue and travels with the wind or water drops to initiate a free-living gametophyte. In higher plants, the FG develops enclosed in the sporophytic tissues and consist of a pre-defined set of cells.

Most flowering plants, 80% including model species *Arabidopsis* as well as cereal crops, develop FG with seven cells of *Polygonum*-type. Such FG develops from a single functional

megaspore cell, which through three consecutive endo-mitotic divisions produces eight nuclei (see Fig. 0.2). Next, the embryo sac builds the membranes between the nuclei to form two synergids, the egg cell, the bi-nuclear central cell and three antipodals. Two of the nuclei further fuse to form the bi-haploid nucleus of central cell (Huang and Sheridan, 1994; Schneitz et al., 1995; Christensen et al., 1997). This architecture is characteristic to most crop plants and *Arabidopsis* and is most common, though there are variations in other flowering plants. In the most primitive flowering plant, *Amborella trichopoda* Baill., an extra synergid is present (Friedman and Ryerson, 2009), while in Plumbaginaceae family the FG develops from all four spores of meiosis and bears no synergids, with the egg cell taking over their functions (Cass and Karas, 1974).

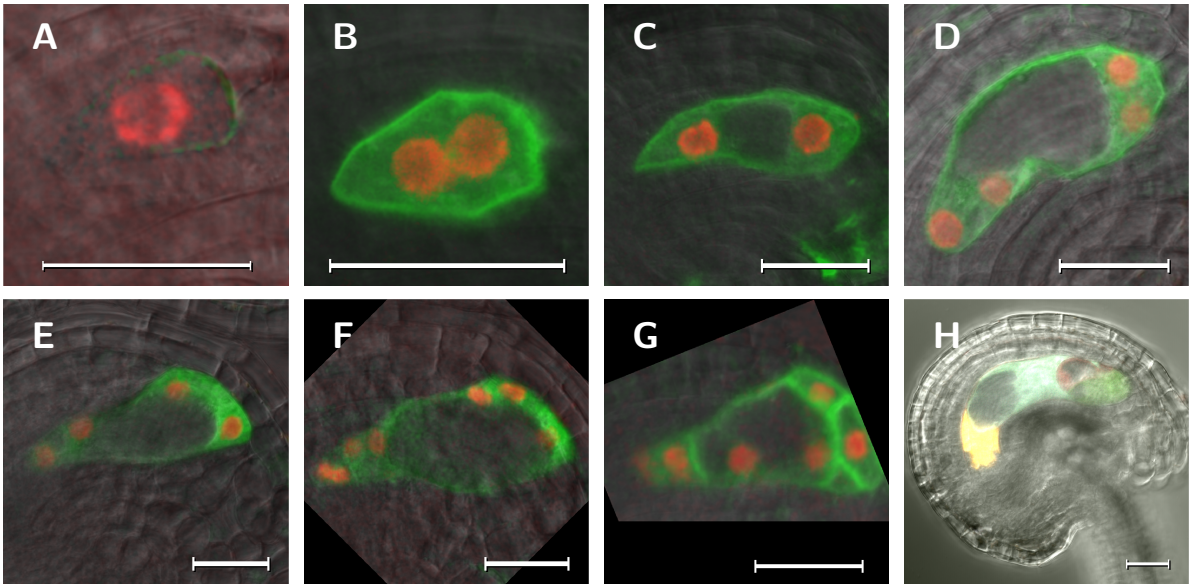

Figure 0.2: **Female gametophyte of *Arabidopsis* at different stages of development.** (A) functional megaspore (FG1). (B) Early bi-nucleate stage FG2. (C) Late bi-nucleate stage FG3. (D) Early four-nucleate stage FG4, note that the micropylar nuclei locate in a plane almost perpendicular to the micropylar-chalazal axis. (E) Late four-nucleate stage FG4, one micropylar nucleus migrates closer to the centre of the cell. (F) Early eight-nucleate FG5 stage. (G) Late eight-nucleate stage FG5; the cell plasma membranes separating the cells are visible in the micropylar part; the polar nuclei are unfused. (H) Fully differentiated seven-nucleate stage FG6. The scanning fluorescent micrographs of ovules from transgenic plants are given in developmental sequence. The images (A–G) are taken from plants carrying YFP (red) localized to nuclei and GFP (green) localized to membranes under a gametophyte-specific promoter (Rotman et al., 2005; Escobar-Restrepo et al., 2007); the image (H) is taken from plants with quadruple fluorescent protein-labelled cell fate marker (Lawit et al., 2013). In (H), the synergids are coloured in green, the egg cell is coloured in red, the central cell is coloured in blue, and the antipodals in orange. Scale bar: 20 μm.

A large progress have been made in study of mutants with aberrant FG development and cell fate markers last decade. Still the interpretation of these results rely only on old

paradigm of positional information. Thus here we review this information and put it within the context of both modern and classical theoretical frameworks on patterning. To this end, we systematize current data within the classical and modern theoretical frameworks of patterning and then discuss the facts falling beyond the current frameworks.

0.2.2 Classical paradigms of patterning

Two paradigms of biological pattern formation exist in modern literature. One of them puts the accent on the spontaneous *de novo* pattern formation after the works of Alan Turing (Turing, 1952) as a consequence of self-organization. The other paradigm developed by Lewis Wolpert (Wolpert, 1969) treats pattern formation as interpretation of 'positional information' imposed from the beginning or from outside of the developing structure. The physical basis of positional information is commonly a gradient of a morphogenic substance having a local pre-existing or external source. The cellular fate in this view is defined by the morphogen concentration in a threshold-wise manner, leading to formation of the morphogenic zones (as explained by the French flag model, which exemplifies three zones). As the Wolpertian paradigm leaves aside interactions and dynamical properties of signalling and transcriptional networks, it is easier to apply and therefore it is usually the first framework drawn upon to explain data, both in animals and plants.

0.2.3 Sorting out

Recently, an old alternative explanation of patterning has been revived that is based on completely different premises than two theories mentioned before. Not necesserily cells receive information according to their position, but by arranging in space (sorting out) according to some guiding signal and their (potentially randomly) acquired fate do they make a pattern. The most striking example of such mechainsm is found in the *Dictyostelium* slime mold (Kay and Thompson, 2009, and references therein), whose single dispersed amœbæ acquire different fates before crawling together to form a fruiting body. Surprisingly, analogous mechanisms were found in zebrafish during neural tube development (Xiong et al., 2013).

0.2.4 In pursuit of factors deterimining positional information in developing female gametophyte

Polarity of the FG The most conceptually simple instance of spatial patterning in the living cells is the symmetry loss, happening when a symmetric cell becomes polarized. This is a well studied process for unicellular organisms and single cells (Iber et al., 2006; Mori et al., 2008). In the megagametogenesis, the determination of the polarity of female

germ line cell is probably the first instance of patterning. The polarity is morphologically traceable as early as the MMC stage (Bajon et al., 1999). However, it is not clear whether the polarization during the earlier stages is irreversible, in other words it is stably memorized by the system and hence does not require any further input, or it is reversible and needs further supply of asymmetrical clues from the sporophytic tissues is not clear. The cytoplasm of the FG becomes more homogenous at the FM stage (Bajon et al., 1999). Plasmodesmata are present throughout MMC, tetrade, and FM stages, which point to the interaction between the gametophyte and sporophyte (Bajon et al., 1999). However, at the FM stage, the plasmodesmata are absent from the micropylar side of the cell, where it neighbours to the degenerating products of meiosis (Bajon et al., 1999). Whatever is the developmental stage when the asymmetry is memorized by the female germ line, the coherence of the polarity of the FG and the sporophytic tissue is a fact straightforwardly pointing to the existence of hierarchical instructive positional information coming from outside to the FG. The question whether its downstream interpretation allows for some liberties nevertheless, is discussed in next sections.

Putative global positional clues in the FG Several examples from genetic studies in model plants suggest that the global positional information must determine nuclear fate within the female gametophyte. The studies on the *rbr1* mutant in *Arabidopsis* (Ebel et al., 2004; Johnston et al., 2008), in which the number of nuclei is higher than normal, showed that the extra nuclei acquire their fate according to their position. In the maize *indeterminate gametophyte 1* (*ig1*) mutant, where the proliferation-differentiation switch is impaired (Evans, 2007), the cell number and identity is strongly disturbed (Lin, 1978). The identity of the cells of the egg cell apparatus, synergids and the egg cell, is hardly distinguishable in *ig1*; however, some dependence of the cell fate on their location is still traceable (Lin, 1978). Moreover, in female gametophytic mutants with abnormal nuclear fate, *eostre*, *lachesis*, *clotho*, and *atropos* in *Arabidopsis* (reviewed in Sprunck and Gross-Hardt, 2011), the nuclei are mislocated, though their number is normal. One of the easiest interpretation of these facts is that a global positional clue dictates the cells their identity, therefore mislocalization of nuclei leads to the mis-specification.

A recent work (Pagnussat et al., 2009) suggested auxin as the factor linking the polarity of the sporophyte to the polarity within the female gametophyte, and as a morphogen dictating fate to all cell types within the FG in *Arabidopsis*. They suggest that asymmetric auxin supply causes polarization at the FG stage. This supply is due to the activity of PIN1 auxin efflux carrier localized in the micropylar subepidermal cell layer. Later, after the first nuclear division, this external supply ceases to exist, and its role is overtaken by the polarly distributed YUC1 enzyme catalysing auxin synthesis(Pagnussat et al., 2009). However,

further examinations reproducibly could not find any auxin activity within the female gametophytes of *Arabidopsis* (Ceccato et al., 2013; Lituiev et al., 2013), maize (Lituiev et al., 2013), and *Hieracium* (Tucker et al., 2012). Moreover, the diffusion and degradation rates of auxin do not permit formation of a significant gradient within the FG (Lituiev et al., 2013). On the other hand it has been shown that stage-specific down-regulation of PIN1 and PIN3 with the onset of the megagametogenesis results in early arrest (at FG1 or FG2 stage) of the female gametophyte development (Ceccato et al., 2013). This can argue for the fact, that auxin is generally required for the early female gametophyte development, though its level is under the detection limit. Alternatively, auxin may induce secretion of a cell-non-autonomous clue in the sporophyte (Lituiev et al., 2013), such as an auxin-inducible ScRALF3 peptide found to be crucial for FG development in Solanaceae (Chevalier et al., 2013). However, there is no sufficient evidence for it to be a global morphogen.

0.2.5 Combinatorial and dynamic nature of positional information

Both Turing's and Wolpertian models have found their application in animal development. The experimental evidence substantiates the Turing model in the pigmentation of fish (Kondo and Miura, 2010), establishment of polarity in sea urchin and ordering of tentacles in hydra (**Meinhardt2012**). However, actual involvement of the Turing mechanisms in formation of the Turing-like patterns in other biological systems, such as limb digit formation, still remains polemic (Maini et al., 1997; Badugu et al., 2012; Zeng et al., 2004). From the late 1970s, the Wolpert's model has been used to explain the formation of anterior-posterior axis in insects (Sander, 1976) as well as in *Xenopus* frog (reviewed in Green, 2002). However, further investigations suggested that the assumption that formation and interpretation of the morphogen gradients are strictly separated in time underlying the concept of 'positional information' (Wolpert, 1969), is often violated in *Drosophila*. The reason is that dynamic interactions of several morphogenic substances, often with hierarchical relations between the tiers of substances acting on different spatial scales often come into play (Dessaud et al., 2008; Nüsslein-Volhard and Wieschaus, 1980; Jaeger and Reinitz, 2006). A paradigm attempting to reconcile the Wolpert's simplification with the dynamic and coordinative nature of positional information in its modified definition gained the name of 'drunken French flag' (Jaeger and Reinitz, 2006).

By analogy to many animal systems, one can assume that in the megagametogenesis the cellular fate is determined by a combination of morphogenic factors. An alternative way to interpret the presence of common factors and thus common cellular fate in a group of nuclei is to assume their common origin from one ancestral nucleus. The interpretation within this paradigm gives inconsistent results when different data sets and different metrics are

applied (Wuest et al., 2010), though. If, however, different morphogens act in combinations simultaneously and cause cell specification in polytomous manner, i.e. if more than two the cell fates (dichotomous scenario) develop at once, lineage tracing from the expression profiles might have no biological meaning. From the pattern of expression of common markers (see Fig. 0.3) it is hard to infer any dichotomy either, and more precise models allowing to distingush between these two possibilities remain to be developed.

Within the paradigm of hierarchical morphogens, theoretically two or three hierarchical morphogen levels can be sufficient, as the number of nuclei is 8 and the number of cell types is 4, suggesting that the maximal number of the fate choice events in the FG is between 2 (=$\log_2 4$) and 3 (=$\log_2 8$). First attempts to explore the combinatorial complexity of the FG developmental program have been made (Hosseinpour et al., 2012); however, they lack temporal and spatial component as the experimental data in these dimensions are still missing.

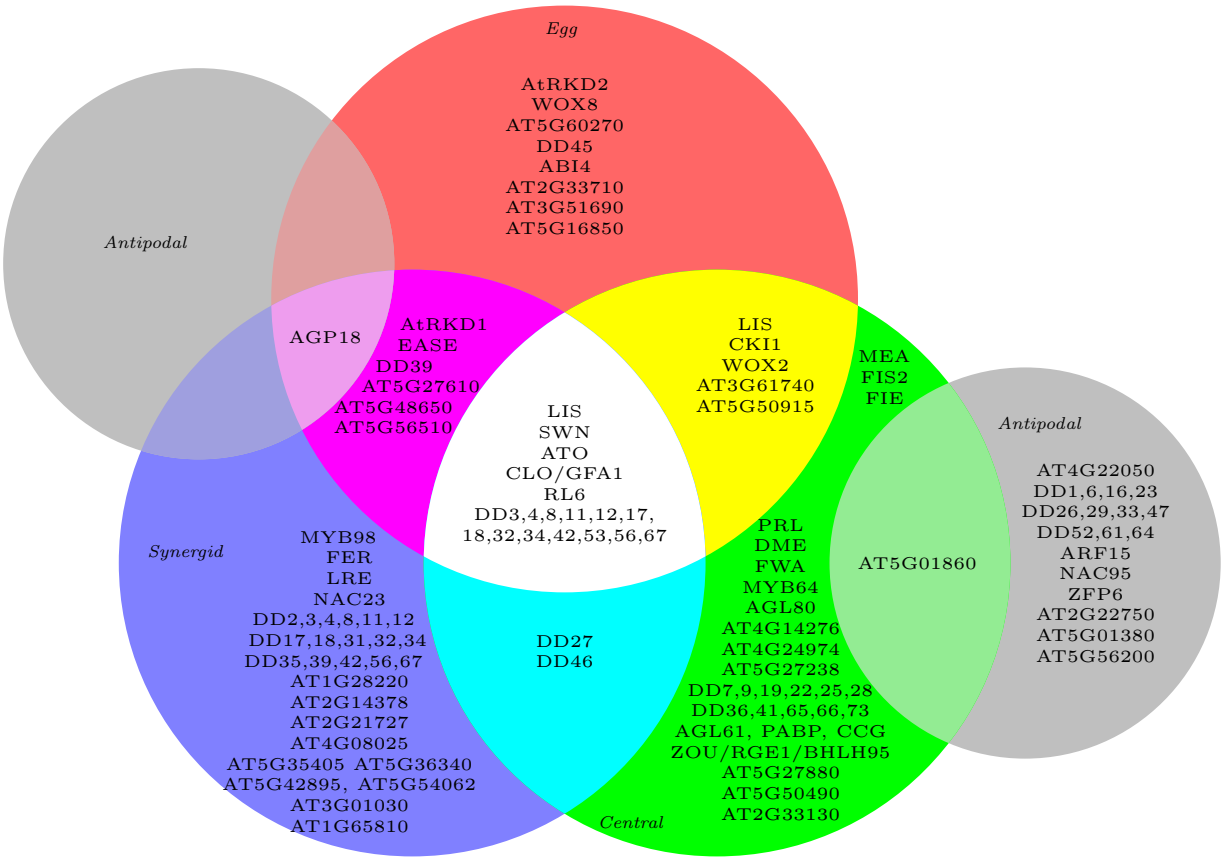

Figure 0.3: **Overlapping domains of expression of cell-specific markers in the FG.** Compiled from (Yu et al., 2005; Steffen et al., 2007; Wang et al., 2010; Wuest et al., 2010; Drews et al., 2011).

Local non-cell autonomous signalling in the FG Several instances of local morphogenic interactions are known in flowering plants, which are seemingly only mere pieces of puzzle

of a larger interaction network. In the *lachesis* mutant, the egg, synergid and central cell fate is often spread to other FG cells (Groß-Hardt et al., 2007). The facts that the central cell marker is often expressed in the antipodal-like cells, while the product of the mutated gene, a splicing factor LACHESIS, upon maturation concentrates to the gametic cells (i.e. egg and central cells), suggests that the in the gametic cells LACHESIS is necessary for expression of a hypothetical non-cell autonomous signal inhibiting gametic fate in surrounding cells (Groß-Hardt et al., 2007). Though other components of splicing machinery, CLOTHO and ATROPOS, acting synergistically with LACHESIS to restrict the gametic fate (Moll et al., 2008) are known, downstream non-cell autonomous signal of the spliceosome affecting the nuclear fate remains elusive. Additional support for the model of non-cell autonomous regulation of the death of antipodal cells comes from the results of study of the *FIONA /SYCO ARATH* gene function (Kägi et al., 2010). The SYCO ARATH protein localizes to mitochondria of the central cell and its expression there is necessary for degeneration of antipodals. Similarly in maizem a secreted peptide ZmEAL1 synthesised in the micropylar pole regulates expression of IG1 protein in the chalazal end of the FG (Krohn et al., 2012)

Cell-type specific signals AtRKD1 and AtRKD2 are two transcription factors specific to egg apparatus and egg cell correspondingly. The ectopic expression of both factors under a ubiquitous promoter leads to cell fate switch towards egg-cell-like phenotype (Köszegi et al., 2011). Thus AtRKD1 and AtRKD2 are the only two proven morphogenic regulators, though cell-type specific, with knock-in phenotype known today.

0.2.6 Robustness as a measure of (theoretical) success

Biological systems are subject to different kinds of noise and perturbations. Accounting for their ability to tolerate noise, *robustness*, has been providing a measure to judge which explanation of a morphogenic mechanism better suits the real world in a wide literature on *Drosophila* (Lander et al., 2009). Further we discuss the patterning mechanisms in the female gametophyte in the light of how well they can sustain uncertainties introduced by environmental factors and genetic failures.

Wide-sense robustness Together with the narrow-sense tactical robustness of cell specification used in *Drosophila* literature, here we need to account for the strategic robustness of the mission of the development. Namely, in the oligocellular female gametophyte, some cells are unique and cannot be redundant, thus they have higher significance (gametic cells), while other are redundant (synergids and antipodals). In this light, one can consider the fate switch from accessory cell types to neighbouring gametic cell types as a

mechanism of such strategic robustness. Based on this framework, the scenarios which conform this kind of robustness must be considered more plausible.

Robustness of the mission of the FG development The functional significance of the cells in the mature female gametophyte is unequal. Whilst one egg cell, one central cell and at least one synergid are indispensible for fertilization and seed development, the second synergid functions as a backup (Pagnussat et al., 2007; Maruyama et al., 2013; Völz et al., 2013). The antipodals, even less essential, die before fertilization, and thus are not required further at all. Therefore, to accomplish its mission, the female gametophyte needs to have one cell of each of three types (egg, central, synergid), with an option of having two of the latter one. In accordance to this postulated minimal set, ablation of the egg cell leads to the fate switch in one synergid (Lawit et al., 2013). Additionally, in *wyrd* (Kirioukhova et al., 2011) and *eostre* (Pagnussat et al., 2007) mutants, two egg-like cells and one synergid are formed. Therefore, the synergid fate is very labile, i.e. the synergids can change their identity to the egg cell, which can be a mechanism of robustness to errors in the program of egg cell development.

0.2.7 What first: Positioning or Specification

Oligocellularity: a unique feature of the female gametophyte. As the discourse on the patterning in the FG is largely influenced by the *Dropsophila* egg model, a temptation remains to implicitly transfer the assumptions made for *Dropsophila*, even when such analogy is obviously wrong. The main difference between two is that the *Drosophila* embryo the number of nuclei is 256 to around 6000, while in the FG of Angiosperms during its patterning it is only up to eight. Moreover, these few nuclei are spaced even more non-uniformly than in *Drosophila* egg. Whether the final pattern of nuclear placement arises independently of the patterning have not been brought into discussion yet.

When the nuclei are positioned? Though the nuclear mis-specification in the female gametophyte development is often associated with the mis-location of nuclei, the interpretation of the casual links between these two phenomena has been interpreted differently dependent on concomitant phenotypes. It is commonly assumed that when the final mitosis is accomplished, the nuclei acquire their final fate after they have been positioned. Still the availability of markers specific to micropylar and chalazal subsets of nuclei already at FG2 (Yu et al., 2005) and FG4 (Marc Schmid, unpublished) stages argue for the fact that at least these subsets are distinct far before their final positioning. Thus an alternative mechanism based on nuclear sorting (reviewed in Kay and Thompson, 2009) can be hypothesised.

Nuclear migration is known to require microtubular apparatus (Huang and Sheridan, 1994) including γ-tubulin (Pastuglia et al., 2006), kinesin motor (Tanaka et al., 2004) and other related components as ZmDSUL (Srilunchang et al., 2010). In cytoskeletal mutants having too few nuclei in the FG due to inhibition of mitosis as in the *tubg1-1 tubg2-1* γ-tubulin double mutant (Pastuglia et al., 2006) or degeneration of nuclei as in *atnack1 atnack2* kinesin mutant (Tanaka et al., 2004), two or three nuclei locate in the centre of the cell and by their size resemble central nucleus, though their molecular fate signatures has not been studied. As in other FG patterning mutants the affected genes are involved in transcriptional or post-transcriptional gene regulation, one can suspect that they have pleiotropic effects and therefore it is usually impossible to distinguish whether the patterning disfunction causes nuclear mis-positioning or vice versa. Similarly in a maize *ZmDSUL* mutant the nuclear migration and cell specification are affected (Srilunchang et al., 2010).

The microtubular forces bring the nuclei in strictly specified positions. The two synergid nuclei migrate even closer to the micropylar pole, while egg and one polar nuclei arrange in a row along the longest axis of the FG. No explanation has been proposed why the nuclei locate in such a distinct non-uniform way. Here, it is not unrealistic to assume that before being positioned the nuclei are labelled by some molecules that further guide cytoskeletal motions, though such labelling may be reversible. Still, the casual link between the patterning and positioning remains to be elucidated. A related question is how the patterning temporally and casually relates to the phragmoplast formation, whose defects are exemplified by *gemini pollen 2* (Park et al., 2004) and *two-in-one-1* (Oh et al., 2005) mutants, also remains to be addressed.

0.2.8 Conclusion and Outlook

No realisations of conceptually simple and attractive conception of a global morphogen have been found in the female gametophyte yet. Though several locally acting factors have been discovered, the results of their interplay remains still unexplored. Therefore we think that further understanding of the exact mechanisms of the patterning will require change of the ideology of the patterning research to explore dynamic interactions between new and already known morphogenic factors in the FG. Such studies were technically challenging till recent times, particularly in the FG that is hidden under several layers of integument cells. However, availability of a plethora of genetic markers (Yu et al., 2005; Wuest et al., 2010; Drews et al., 2011) and increased affordability of life-cell imaging techniques must stimulate the change of accents in research and progress in understanding of the female gametophytic patterning.

Acknowledgements

We would like to thank Célia Jäger-Baroux (University of Zurich) for providing a homozygous seeds of the line carrying GFP and YFP under the AKV gametophyte-specific promoter and Shai Joshua Lawit (Ag Biotech Pioneer Hi-Bred, A DuPont Business, Johnston, IA, USA) for providing the seeds of the quadruple cell fate marker.

0.3 Auxin and its role in plant morphogenesis

0.3.1 Morphogensis in plants and phytohormones: A historical overview

In contrast to animals, in most plants growth and cell differentiation continue throughout their life. Consequently, the time scale of mechanical physiological reactions in most plants is very close to the time scale of the growth and differentiation to such an extent that it is hard to treat them separately. This particularly relates to such reactions as gravitropism and phototropism.

First conjectures about mobile signals coordinating plant growth and physiological reactions were made in the 18^{th} century by Julius von Sachs (1865) and Darwin (1880), reviewed in (Michniewicz et al., 2007). Further studies shown that plant hormone auxin are involved in these developmental reactions by changing the cell proliferation rate (Cholodny, 1927; Went, 1926). Several years later, a first known form of auxin was purified (Kögl and Haagen-Smith, 1931). Other hormones such as gibberellins (Kurosawa, 1926; Yabuta, 1938)), ethylene (Neljubov, 1901) were discovered about the same time. Cytokinins were discovered in 1960s (Skoog et al., 1965). A number of novel plant hormones (reviewed in Vanstraelen and Benková, 2012; Wang and Irving, 2011) such as brassinosteroids , salicylic acid, jasmonates (Reinbothe et al., 1994), and strygolactones (Ruyter-Spira et al., 2013) have been discovered in 1990s due to success of molecular genetics and biochemistry. As other mobile signals, such as gasotransmitters (García-Mata and Lamattina, 2013) and numerous mobile peptide substances such as CLAVATA3 and FLOWERING LOCUS T / florigen to name a few, were still discovered during the last decade , one can expect that our knowledge of the plant hormone world will keep growing further.

The growing number of hormones together with vast redundancy of the proteins involved in their sensing and signalling (Vanstraelen and Benková, 2012) poses both experimental and theoretical challenges in the study of plant physiology. The redundancy, i.e. the high number of protein isoforms (up to 30) with overlapping function, on several levels of the signal transduction pathway adds combinatorial complexity to the problem. One possible interim solution to this problem might be use of lower model plants such as *Marchantia polymorpha*, which often have only one player for each function in the signalling network.

0.3.2 Role of auxin and its polar transport in plant morphogensis

In contrast to both morphogens in animal systems, which are mostly transported by diffusion (Lander et al., 2002), and animal hormones, which are delivered by convection of blood and lymph, the transport of auxin and probably some other plant hormones as cytokinin (B. Müller and E. Zürcher, personal communication) is mediated mostly by active transmembrane transport.

Auxin is required for establishment of polarity in all plant organs. Such broad involvement of auxin as a morphogenic substance in higher plants is (1) due to its ability to promote cell proliferation and expansion and (2) due to the physiological mechanisms directing its flow to form auxin maxima and minima; a crucial property of these mechanisms is that they create and adjust the positions of maxima correspondingly to the growth program and adequately to the environmental conditions.

Further I review the mechanisms of auxin transport, sensing and metabolism.

0.3.2.1 Forms of auxin

Auxin is a general name for a family of compounds with similar growth-promoting activity. There are natural forms of auxin and synthetic auxin compounds broadly used in research.

Natural auxins. The indole-acetic acid (IAA) is major natural form of auxin. A chlorinated form of IAA, 4-chloroindole-3-acetic acid, and phenylacetic acid are other putative auxin forms found in some species and in certain developmental contexts, reviewed in (Ljung, 2013). Further in the text, if not otherwise specified, by the word 'auxin' I refer to IAA.

Synthetic auxins. Driven by commercial applications of auxins (primarily as herbicide in agricultural and also as rooting agents and in *ex vivo* plant culture), synthetic chemists have produced many auxin-like compounds, reviewed in (Ljung, 2013). Of them, most common in research practice are 2,4-dichlorophenoxyacetic acid (2,4-D), which is more stable than IAA, and α-naphthaleneacetic acid (α-NAA), which is taken up faster than IAA by plant cells.

0.3.2.2 Auxin transport

Passive transport. Early experimental and theoretical studies concluded that due to the difference of the pH within the cell and in the apoplast, auxin can easily enter the cells in its protonized form but within the cell it dissociates and stays trapped (Rubery and Sheldrake, 1974; Raven, 1975).

Active auxin efflux. Three families of auxin efflux carriers are known to participate in auxin efflux, PIN-FORMED (PIN), ATP-BINDING CASSETTE B (ABCB)/P-GLYCOPROTEIN (PGP) / MULTIDRUG RESISTANCE (MDR) and PIN-LIKES (PILS).

PIN family. The first member of PIN family, PIN1 is expressed in both shoot and root meristems and is indispensable for initiation of lateral organs and phyllotaxis. The name of the protein comes from the pin-like shape of the *pin1* mutatants, which often lack lateral shoots, shoot leafs and inflorescences (Okada et al., 1991).

All eight transporters of the PIN family function as auxin transporters, whether as efflux carriers localized on the plasma membrane — PIN1,2,3,4,7, or as carriers localized to the endoplasmic reticulum (ER) — PIN5,6,8. Particularly, PIN5 pumps auxin in the ER (Mravec et al., 2009). PIN6 and PIN8 act antagonistically to PIN5 during leaf vein patterning, suggesting that they probably pump auxin out of the ER lumen (Sawchuk et al., 2013).

PIN1 has been shown to localize to epidermal cells adjacent to the female gametophyte pointing in chalazal direction (Pagnussat et al., 2009) and to be necessary for its early development (Ceccato et al., 2013). PIN3 is also expressed in the *Arabidopsis* ovules and polarized in a similar manner as PIN1; however, its expression is not crucial for ovule development (Ceccato et al., 2013). PIN8 is specifically expressed in pollen and *pin8-1* mutant has been shown to have no fertility problems, suggesting that it is not required for female gametophyte development (Dal Bosco et al., 2012).

ABCB/PGP/MDR family. Two members of the ABCB family, ABCB1 (PGP1) and ABCB19 (PGP19), function as auxin efflux carriers (Geisler et al., 2005). The members of this family have been shown to have a lower transport rate compared to PIN1,2,7 (Petrášek et al., 2006). However, transport rates and Michaëlis-Menten constants have not been measured for ABCB1 and ABCB19.

Traditionally, ABCB1 and ABCB19 auxin efflux carriers are considered to be ubiquitously expressed (Kramer and Bennett, 2006). However, here we show that they are expressed differently in the female gametophyte, namely it is only ABCB19 which is detectable there.

PILS family. PILS family of auxin carriers has been discovered quite recently. All members of the family, PILS1–7, localize to the ER membrane and are believed to participate in intracellular auxin homoeostasis (Barbez et al., 2012).

Active auxin influx: AUX1/LAX family. It has been long known that auxin is imported not only by passive transport, but also by some proteins (Rubery and Sheldrake, 1974).

Further characterization of *aux1* mutant (Maher and Martindale, 1980) and AUX1 protein (Bennett et al., 1996) showed that AUX1 facilitates auxin influx and is necessary for root gravitropic reaction. Additional paralogues of *AUX1* gene, *LAX1*, *LAX2*, and *LAX3* share 74% or more of similarity within the family. These proteins have eleven transmembrane domains and are localized to the plasma membrane. The are expression of the AUX1/LAX family members is mostly does not overlap (Swarup and Péret, 2012).

It is known that 75% of 2,4-D auxin is imported into the cells by active mechanism (Delbarre et al., 1996). The Michaëlis-Menten constants of AUX1 and LAX3 have been determined as 843 nM (Yang et al., 2006) and 858 nM (Swarup et al., 2008) correspondingly.

0.3.2.3 Auxin perception

Two sub-networks are known to date in *Arabidopsis* as in other higher plants. One network depends on sensing of auxin by AUXIN BINDING PROTEIN 1 (ABP1), which is localized to endoplasmatic reticulum and plasma membrane. This sub-network to current knowledge is fast and transcription-independent. The second, most studied network relies on auxin sensing by a SCF ubiquitin ligase complex carrying as its component one of the enzymes of the TIR1/AFB family (TIR1, AFB1, AFB2, or AFB3).

Transcription-independent sensing via ABP 1. The transcription-independent auxin signalling pathway mediated by the ABP1 protein has been better studied in maize. It is a soluble 22 kDa glycoprotein found predominantly within the endoplasmic reticulum (ER), and in smaller quantities at the cell surface associated with the plasma membrane (Diekmann et al., 1995). It binds auxins with submicromolar affinity (57 nM for NAA) (Löbler and Klämbt, 1985). ABP1 mediates auxin-induced plasma membrane hyperpolarizations and ion fluxes. Recently, the ABP1 was found to be involved in the Rho GTPase-based auxin-signaling mechanisms (Xu et al., 2010) and clathrin-mediated endocytosis (Robert et al., 2010), reviewed in (Sauer and Kleine-Vehn, 2011).

Transcriptional regulation via TIR1/AFB ubiquitin-ligase pathway. Most of the auxin-dependent transcriptional regulation is mediated by the TIR1/AFB family of F-box protein receptors. TIR1/AFB receptors participate in ARF – Aux/IAA - TIR1/AFB network of auxin-dependent transcriptional regulation. The down-most components of this network are the ARF transcription factors which bind to auxin responsive elements (AuxRE, TGTC, (Ulmasov et al., 1999)). Members of different ARF subfamilies act both as transcriptional activators or repressors. Aux/IAA transcriptional repressors can bind ARFs, both free or bound to promoters and repress transcription of downstream targets (Guilfoyle et al., 1998). Most of the Aux/IAA transcriptional repressors are in turn are sus-

ceptible to auxin-dependent degradation acting through TIR1/AFB receptors (Tan et al., 2007). Auxin binds to these receptors in nanomolar concentrations (TIR1 binds IAA with $K_d = 84$ nM, while the K_d for synthetic auxins is in micromolar range) (Dharmasiri et al., 2005). The association to auxin renders them a significant affinity to Aux/IAA transcriptional repressors (IAATRs), which is not observed in the absence of auxins (Dharmasiri et al., 2005). Auxin-dependent binding of the IAATRs to the F-box protein receptors leads to ubiquitination and subsequent proteasome-mediated degradation of the former.

0.3.2.4 Metabolism of auxin

Auxin synthesis. Auxin is mainly synthesised from L-tryptophane (L-Trp), which is in turn produced by shikamate pathway. Additional L-Trp-independent pathway using the indole-3-glycerol phosphate (IGP) as a precursor has also been found, though it remains poorly studied. There are at least four known chemical pathways producing IAA from L-Trp: (1) the indole-3-pyruvic acid (IPyA) pathway, (2) the indole-3-acetamide (IAM) pathway, (3) the tryptamine (TRA) pathway, and (4) indole-3-acetaldoxime (IAOx) pathway. The TAA1/TAR and YUCCA enzymes, which are mentioned further participate in the IPyA pathway.

Auxin degradation and conjugation. The auxin levels can be lowered by its degradation and conjugation to other organic compounds such as amino acids and sugars. Degradation of auxin operates mostly through oxidation (Woodward and Bartel, 2005). Conjugation of auxin is accomplished mostly by GH3 family of amido synthases. The GH3 genes are induced upon auxin application (Woodward and Bartel, 2005).

0.3.2.5 Properties of the auxin-dependent regulatory network

Negative feed-back loops. Aux/IAA transcriptional regulators (TRs) were first identified not as transcriptional regulators, but as targets of auxin-dependent transcriptional upreguation. Thus transcription of Aux/IAA TRs is negatively regulated by themselves, i.e. they repress their own transcription. Some ARFs , namely ARF4, 5, 16, and 19, were shown to be slightly upregulated by auxin (reviewed by Guilfoyle and Hagen (2007)). GH3 family of auxin conjugating enzymes are induced upon auxin application (Woodward and Bartel, 2005), functioning as a negative feedback regulators.

Auxin-like transcriptional response. Not all transcriptional response regulated through the transcriptional auxin-response element is a reaction to auxin. ARF3 and ARF17 isoforms do not have domains for dimerization with IAA TRs and are not regulated by auxin, but contribute to auxin-related response.

Abundance and specificity of the network components. All the components of the auxin perception network are highly abundant (4 isoforms of TIR1/AFB family, 34 isoforms of Aux/IAATRs, 23 isoforms of ARFs). Moreover, biochemical properties, including those underlying their susceptibility to feedback and feed-forward regulation, vary among the isoforms.

0.3.2.6 Modelling of auxin fluxes

A number of models have been developed to explain and predict the role of hormones and their transport in plant development. Among the questions addressed recently by the studies modelling auxin transport are the following:

- the mechanisms and paths of auxin flux in roots (Grieneisen et al., 2012);
- role of auxin in the gravitropic response (Band et al., 2012);
- dynamic properties of the auxin-dependent signalling and its interaction with other hormonal signals (Middleton et al., 2010; Liu et al., 2010; Sankar et al., 2011);
- mechanisms of spontaneous pattern formation and phyllotaxis due to auxin transport in shoots (Jönsson et al., 2006; Smith et al., 2006; Stoma et al., 2008);
- interaction of polar auxin transport with mechanical stimuli in shoot development (Heisler and Jönsson, 2007)
- root branching (Lucas et al., 2008)

The process treated in this thesis, namely the patterning of the female gametophyte, stands apart from most other developmental processes in plants, as it is expected to be least sensitive to environmental inputs, as the shape and the cell set of the female gametophyte does not normally vary as much as the those of the sporophytic stage. On the other hand, the assignment of the nuclear fate within the female gametophyte syncytium has an analogue in the development in *Drosophila* embryo, where only a limited number of cells acquire strictly determined set of fates. Therefore, in our consideration of the female gametophyte development we shall rely more on analogy to *Drosophila* models, while using parameters from other models describing auxin transport and metabolism.

Chapter 1. Theoretical and experimental evidence indicates that there is no detectable auxin gradient in the angiosperm female gametophyte (*Development paper*)

Dmytro S. Lituiev[1] , Nádia G. Krohn[2] , Bruno Müller[1] , David Jackson[3] , Barbara Hellriegel[4], Thomas Dresselhaus[2] and Ueli Grossniklaus[1],*

ABSTRACT

The plant life cycle alternates between a diploid sporophytic and a haploid gametophytic generation. The female gametophyte (FG) of flowering plants is typically formed through three syncytial mitoses, followed by cellularisation that forms seven cells belonging to four cell types. The specification of cell fates in the FG has been suggested to depend on positional information provided by an intrinsic auxin concentration gradient. The goal of this study was to develop mathematical models that explain the formation of this gradient in a syncytium. Two factors were proposed to contribute to the maintenance of the auxin gradient in *Arabidopsis* FGs: polar influx at early stages and localised auxin synthesis at later stages. However, no gradient could be generated using classical, one-dimensional theoretical models under these assumptions. Thus, we tested other hypotheses, including spatial confinement by the large central vacuole, background efflux and localised degradation, and investigated the robustness of cell specification under different parameters and assumptions. None of the models led to the generation of an auxin gradient that was steep enough to allow sufficiently robust patterning. This led us to re-examine the response to an auxin gradient in developing FGs using various auxin reporters, including a novel degron-based reporter system. In agreement with the predictions of our models, auxin responses were not detectable within the FG of *Arabidopsis* or maize, suggesting that the effects of manipulating auxin production and response on cell fate determination might be indirect.

KEY WORDS: *Arabidopsis*, Auxin, Female gametophyte, Gradient, Maize, Modelling

---

[1] Institute of Plant Biology and Zürich-Basel Plant Science Center, University of Zürich, Zollikerstrasse 107, CH-8008 Zürich, Switzerland.

[2] Cell Biology and Plant Biochemistry, Biochemie-Zentrum Regensburg, University of Regensburg, Universitätsstrasse 31, D-93053 Regensburg, Germany.

[3] Cold Spring Harbor Laboratory, 1 Bungtown Road, Cold Spring Harbor, NY 11724, USA.

[4] Anthropological Institute and Museum, University of Zürich, Winterthurerstrasse 190, CH-8057 Zürich, Switzerland.

*Author for correspondence (grossnik@botinst.uzh.ch)

Published in *Development* 2013(140), doi:10.1242/dev.098301

Submitted 28 April 2013; Accepted 22 August 2013

1.1 Introduction

The life cycle of plants alternates between a diploid sporophytic and a haploid gametophytic generation. In flowering plants, the sporophytic generation is the dominant form of the plant life cycle, whereas the gametophytic generation is highly reduced and short lived, and develops within the sexual organs of the flower. In most flowering plants (70%), including *Arabidopsis thaliana* and *Zea mays* (maize), a postmeiotic female reproductive cell termed the functional megaspore (FM) undergoes three mitoses to form a female gametophyte (FG) comprising seven cells of four distinct cell types (Fig. 1).

In FG mutants with abnormally positioned or extra nuclei in maize (Evans, 2007; Srilunchang et al., 2010) and *Arabidopsis* (Gross-Hardt et al., 2007; Johnston et al., 2010; Moll et al., 2008; Pagnussat et al., 2007), the nuclei acquire their fate according to their spatial positioning along the micropylar-chalazal axis, suggesting that cell specification in the FG is driven by positional information. This hypothesis was strengthened by a microscopy study showing a graded activity of the auxin-sensitive reporter *DR5* (Ottenschläger et al., 2003) along the micropylar-chalazal axis of the FG (Pagnussat et al., 2009). Furthermore, overexpression of the auxin biosynthesis enzyme YUC1 and the artificial microRNA (amiRNA)-based knockdown of a group of auxin-dependent transcription factors (auxin response factors, ARFs) leads to the mis-specification of gametophytic cells (Pagnussat et al., 2009). Therefore, it was proposed that the phytohormone auxin is distributed in a gradient and serves as the morphogen driving cell specification in the *Arabidopsis* FG (Fig. 1) (Pagnussat et al., 2009; Sundaresan and Alandete-Saez, 2010).

Here, we attempted to reproduce the mechanisms of auxin gradient formation *in silico* for maize and *Arabidopsis* in order to verify whether the processes proposed previously, i.e. polar auxin influx at early stages and localised auxin synthesis at later stages (Pagnussat et al., 2009), are sufficient for the auxin gradient to be sustained, or whether additional factors should be considered. Using auxin degradation rates and diffusion coefficients from the literature, we found that only a very shallow auxin gradient can be maintained in *Arabidopsis* and a moderate one in maize, even if additional factors, such as background efflux or localised degradation, are incorporated into the model. Moreover, we showed that the steepness of the gradient obtained in our models does not allow a sufficiently robust cell fate acquisition, especially in the small *Arabidopsis* FG. Thus, we reanalysed the auxin response within ovules to refine our model. Surprisingly, we could not detect auxin-dependent *DR5* activity inside the FGs of either maize or *Arabidopsis* at any developmental stage. However, in both species we observed an auxin maximum in sporophytic nucellar cells at the micropylar pole of young ovules. As development progressed, *DR5* activity migrated towards the chalazal pole in the sporophytic tissues surrounding the FG. We propose a model involving non-cell-autonomous effects of auxin in the sporo-

phytic tissues of the ovule, in which auxin overproduction in the FG can explain the cell fate changes observed by Pagnussat and colleagues (Pagnussat et al., 2009). Thus, auxin may affect cell specification indirectly through a function in sporophytic tissues rather than via a gradient in the FG.

1.2 Results

1.2.1 Mathematical modelling shows that only shallow auxin gradients can be maintained in FGs

In order to elucidate potential mechanisms underlying the formation of an auxin gradient in angiosperm FGs, we developed a series of reaction-diffusion models based on the following assumptions: (1) auxin is produced or imported in the micropylar region of the FG; (2) auxin is degraded with first-order kinetics; and (3) diffusion of auxin is isotropic and homogenous throughout the cytoplasm. We tested the contribution of different factor combinations (hereafter referred to as 'regimes') as described in Table 1. We included processes such as localised influx, both uniform and localised synthesis and degradation, as well as background efflux at the chalazal pole. As preliminary inspection showed that most parameter values produced only a very shallow gradient, we used parameter values that resulted in the steepest gradient, whenever alternative values were available from the literature (supplementary material Table S1).

1.2.2 PGP19 and AUX1 auxin carriers are expressed in the *Arabidopsis* FG.

The distribution of auxin within plant tissues largely depends on polar auxin transport across membranes (reviewed by Garnett et al., 2010; Petrašek and Friml, 2009). Pagnussat and colleagues (Pagnussat et al., 2009) examined the expression of members of the PIN-FORMED (PIN) family of auxin transporters encoded by the PIN1-4 and PIN7 genes in the ovules and detected only PIN1 in the micropylar nucellar cells prior to the FG2 stage [all stages of FG development are given according to Christensen et al. (Christensen et al., 1997)]. Here, we further examined the expression of all other known auxin transporters in the FG. According to our RNA-Seq data, neither PIN5 nor PIN6 transcripts are detected in developing ovules (M. Schmid and U.G., unpublished). The PIN8 protein is not detected in ovules either (supplementary material Fig. S1), which is consistent with the fact that the *pin8-1* mutant is completely fertile (Dal Bosco et al., 2012).

In maize, we found ZmPIN1a-mRFP expression in sporophytic nucellar cells but not in the FG before the eight-nucleate stage (FG5), similar to previous findings in *Arabidopsis* (supplementary material Fig. S2; see also Fig. 7). In contrast to *Arabidopsis*, however, ZmPIN1a is expressed in the antipodal cells during FG maturation (stages FG6 and FG7). Because ZmPIN1a is expressed only at stages when the fate of the FG cells has already been determined, we

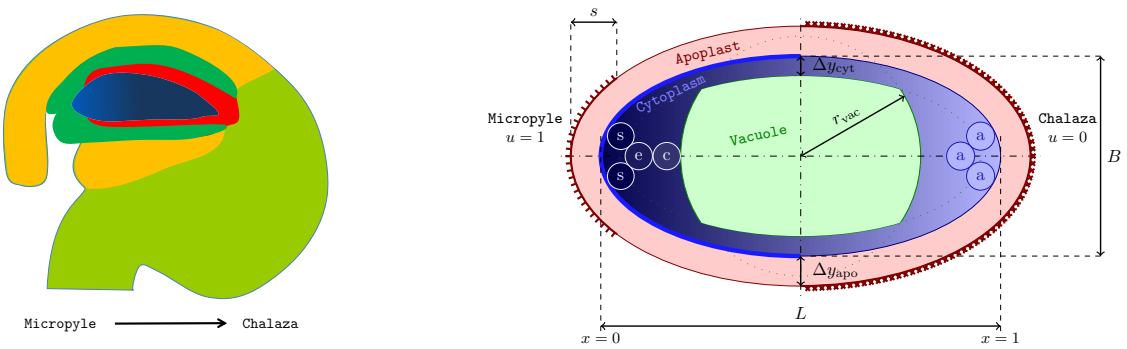

Fig. 1: **Schematic representation of an FG**. (Left) FG embedded in the context of the ovule. The endothelial tissue is shown in red, the inner integuments in green and the outer integuments in brown. (Right) Schematic of the FG showing features and geometrical parameters used in the simulations. An auxin gradient, which has been proposed to determine the cell fate of the synergids (s), egg cell (e), central cell (c) and antipodals (a), with decreasing concentration along the micropylar-chalazal axis is indicated in blue. The long axis of the FG from the micropylar (x=0) to the chalazal (x=1) pole is aligned with the x-axis in all models. The zone of auxin efflux is shown in dark-red pin lining. The zone where the concentration was set to zero is shown by dark-red x lining. The micropylar half of the plasma membrane where AUX1 was assumed to be expressed $\geq$5-fold higher than in the rest, is shown by a thick dark blue line. Not all proportions are preserved

Table 1: **Description of the regimes used for the reaction-diffusion models**

Regime 1	Regime 2	Regime 3	Regime 4
No synthesis	*Localized synthesis*	No synthesis	No synthesis
Uniform degradation	Uniform degradation	*Localized degradation*	Uniform degradation
Influx in ant. pole	*No influx*	Influx in ant. pole	Influx in ant. pole
No efflux	No efflux	No efflux	*Efflux in post. pole*

did not consider this in our model. The PGP1 (ABCB1) and PGP19 (ABCB19) efflux transporters are also known to participate in polar auxin transport (Geisler et al., 2005). Only PGP19 was found to be expressed in the *Arabidopsis* FG (supplementary material Figs S3, S4). The rates of PGP19-dependent and background auxin efflux used in our models were thus estimated based on earlier work by Geisler and colleagues (Geisler et al., 2005).

The AUXIN1/LIKE-AUX1 (AUX/LAX) family of transporters are known to facilitate auxin influx in *Arabidopsis* (Swarup and Péret, 2012). We found AUX1 to be expressed in the *Arabidopsis* FG starting at the four-nucleate stage (FG4). Moreover, the protein accumulated in the micropylar part (supplementary material Fig. S5). Active auxin influx has been estimated to contribute up to 75% (Delbarre et al., 1996) of total auxin influx, with AUX1 contributing 50% (Marchant et al., 1999), which was considered in our models. Close paralogs of AUX1 with similar characteristics are either not detectable in the FG (LAX3) or are expressed at negligibly low levels (LAX1 and LAX2 at 2.2% and 1.0% of AUX1 level, respectively; M. Schmid and U.G., unpublished).

1.2.3 Measures of gradient steepness

As in most models of morphogen diffusion, our models were rescaled for analyses by combining the length of the FG, the diffusion coefficient, and the auxin degradation rate into a single parameter termed the characteristic length scale λ (Lander et al., 2009). However, as the models developed here account for boundary conditions relying on additional parameters, we could not use λ as a measure of the gradient steepness to compare different solutions. Therefore, we compared the different solutions based on a new measure termed the gradient steepness (GS), defined as the percentage by which the concentration drops towards the chalazal pole ($u_{\min}$) from its maximum value ($u_{\max}$) at the micropylar pole:

$$\mathrm{GS} = \frac{u_{\max} - u_{\min}}{u_{\max}}$$

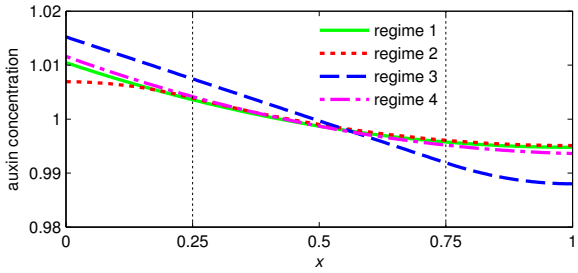

Fig. 2: Auxin concentration profiles in different regimes (one dimension) for *Arabidopsis*. The origin of the x-coordinate lies in the micropylar pole ($x = 0$) and the axis runs towards the chalazal pole ($x = 1$). Shaded areas represent the domains of localized synthesis (left) and degradation (right). Auxin concentration (y-coordinate) is presented in arbitrary units, assuming the mean concentration equals one.

1.2.4 Simulation of the model in one dimension

Based on previous data indicating that the greatest variation in auxin concentration is observed along the micropylar-chalazal axis

(Pagnussat et al., 2009), we studied a simplified one-dimensional model featuring spatial inhomogeneity of the processes along this axis. The spatial coordinate representing position along the micropylar-chalazal axis has its origin in the micropylar-most point (denoted as $x = 0$) and spans the cytoplasm until the chalazal-most point ($x = 1$) (Fig. 1). A numerical study of regime 1 (Table 1) in one dimension showed that the rate of auxin reaction-diffusion was much faster than the rate of FG growth, which allowed us to apply the quasi-steady state assumption with regard to reaction-diffusion (for details, see supplementary material Appendix S1). The absolute value of the error due to this simplification did not exceed 0.002% after 45 minutes of initial equilibration (supplementary material Fig. S6). Therefore, we focused on the eight-nucleate stage of FG development (FG5), when cell specification is believed to occur. At this stage, the FG of *Arabidopsis* reaches a length of up to 70 µm, whereas the maize FG is between 100 and 130 µm in the inbred line A188 (supplementary material Fig. S7).

The GS achieved under different regimes with parameter values obtained from the literature is shown in Fig. 2 and Table 2. Using regime 1 (localised influx and uniform degradation), a rather low GS of 0.78% was obtained for *Arabidopsis*; in maize, the GS reaches 2.66%. If we included local production of auxin at the micropylar pole instead of localised influx, as was suggested for late stages of FG development (Pagnussat et al., 2009), the simulation resulted in gradients that were even flatter than in the case of localised influx (Fig. 2, Table 2). By contrast, if we considered either localised degradation or background efflux of auxin, the steepness of the gradient increased (Figs 2, 4). Taken together, the simulations based on this one-dimensional model identified two factors capable of increasing GS compared with a result obtained with the simplest model (regime 1): background efflux producing a GS of 0.91% and 2.89% (regime 4) and localised degradation increasing the GS up to 1.36% and 4.55% (regime 3) in *Arabidopsis* and maize, respectively. The large central vacuole can impede auxin diffusion in the FG, thereby increasing gradient steepness

At the two-nucleate stage (FG2), a large vacuole begins to form in the centre of the FG (Christensen et al., 1997; Schneitz et al., 1995; Huang and Sheridan, 1994). We investigated whether this vacuole can contribute to the maintenance of an auxin gradient in the FG by impeding the diffusion of auxin. To test this hypothesis, we set up a two-dimensional reaction-diffusion model with regimes 1 and 4, and solved it with the finite element method.

The results of this simulation showed that the large central vacuole will indeed impede diffusion, making the gradient steeper (Fig. 3, Table 2). This effect depends on the width of the cytoplasmic isthmus between the vacuolar and plasma membranes. Without the vacuole, two-dimensional models result in a GS that deviates less than 1% from that obtained with a one-dimensional model. However, with a width of the cytoplasmic isthmus of 1 µm, which is character-

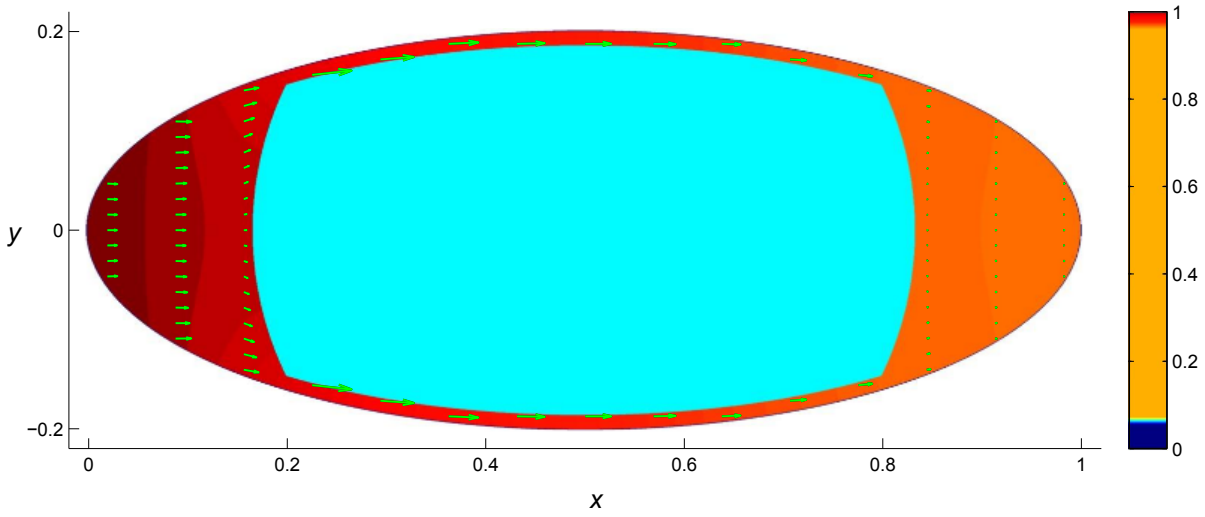

Fig. 3: **Simulation result of the two-dimensional model in regime4.** Total auxin concentration is shown by colour code and auxin flux is indicated by green arrows (the length indicates flux intensity in logarithmic scale, arbitrary units). Note the maximal flux inside the cytoplasm is observed in the cytoplasmic isthmuses around the central vacuole. The colour code (right) is specially adjusted to emphasize the gradient.

istic for *Arabidopsis* (supplementary material Fig. S8), the GS increases approximately two- to threefold in the two-dimensional model as compared with the model without a vacuole: from 1.33% to 3.21% in *Arabidopsis* and from 3.65% to 6.95% in maize (Fig. 4). In addition, taking localised AUX1-dependent influx into account, the GS decreases slightly by some thousandth of a percentage point (Fig. 4). Thus, our simulations identify the effect of a vacuole together with carrier-dependent fluxes of auxin (by PGP19 and AUX1) as the most effective mechanisms that increase the steepness of a potential auxin gradient in the FG, leading to a GS of 3.21% and 6.95% in *Arabidopsis* and maize, respectively.

Table 2: **Gradient steepness in % under different regimes**

species	*Arabidopsis*	maize
Reg.1, 1D	0.783	2.658
Reg.2, 1D	0.588	2.004
Reg.3, 1D	1.361	4.55
Reg.4, 1D	0.909	2.885
Reg. 4, 2D, evenly distributed AUX1, no vacuole	1.328	3.647
Reg. 4, 2D, evenly distributed AUX1, with vacuole	3.213	6.947
Reg. 4, 2D, polar AUX1, with vacuole	3.207	6.945

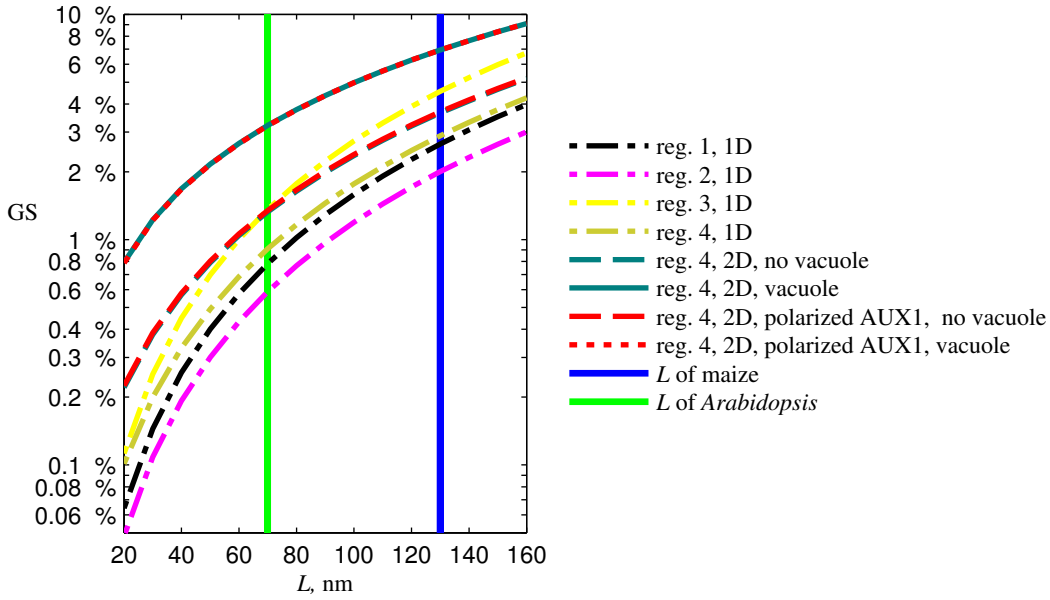

Fig. 4: Dependence of the gradient steepness on the FG lengthof the FG *L* for different model modifications. Localised synthesis (regime 2) is assumed to occur in the 1/4 micropylar-most part, whereas localised degradation (regime 3) is assumed to occur in the 1/4 chalazal-most part of the FG. The FG sizes (L) for *Arabidopsis* and maize at stage FG5 are indicated by vertical lines. Regime 4 in two dimensions results in maximal gradient steepness, especially when a vacuole is included. Addition of AUX1 to the model in regime 4 (2 dimensions) results in only a very minor increase in the gradient steepness. In maize, due to the larger size of the FG, steeper gradients can be achieved.

1.2.5 The theoretically achievable gradient of auxin cannot provide a sufficiently robust readout of positional information for cell specification

The morphogenetic signal providing positional information for cell specification can be corrupted by noise at different levels, both in its generation and perception (Lander et al., 2009). Perturbations of morphogen gradients can thus cause severe developmental aberrations and result in embryo lethality. Therefore, robustness is regarded as a major evolutionary constraint and is often used as an argument for or against the feasibility of theoretical models for morphogenetic gradients (e.g. Lander et al., 2009). In order to theoretically assess the robustness of cell specification, we analysed the sensitivity of the theoretically achievable auxin gradient to perturbations in auxin concentration (for details see supplementary material Fig. S9 and Appendix S1). The auxin gradient obtained with physiological parameters is very shallow and makes the threshold position demarcating any two cell fate zones highly sensitive to perturbations in auxin concentration. A moderate perturbation of the auxin source by 3.5% leads to a positional shift of a given local auxin threshold throughout the entire length of the FG. Even a very small change of 0.5% in the auxin source leads to a shift of the threshold of at least 20%, which, for instance, is sufficient to disrupt cell specification in the micropylar part of the FG (Fig. **5**; supplementary material Table S2). By contrast, a perturbation of the *Drosophila* Bicoid (Bcd) gradient by 5% results in changes in the perceived position of less than 5% in the region where the positional information is read out under all parameters tested (de Lachapelle and Bergmann, 2010). Therefore, the theoretical auxin gradient in the FG is extremely sensitive to perturbations compared with the well-studied *Drosophila* Bcd gradient and is thus highly unlikely to provide the stable positional information required for cell specification. In summary, the auxin gradient obtained with known, realistic parameters is very sensitive to variation in the auxin source and thus would make cell specification highly unreliable. This result can be interpreted as follows: (1) the rate of auxin diffusion or background efflux in the FG is drastically different from that in all other known cases, which is very unlikely; (2) additional factors, for instance efflux mediated by as yet unknown transporters, contribute to the maintenance of the gradient; or (3) the auxin gradient achieved under these realistic conditions is not sufficient, or provides only part of the positional information needed, for cell fate determination; for instance, auxin might be a trigger of polarisation but not provide the positional information required for cell specification.

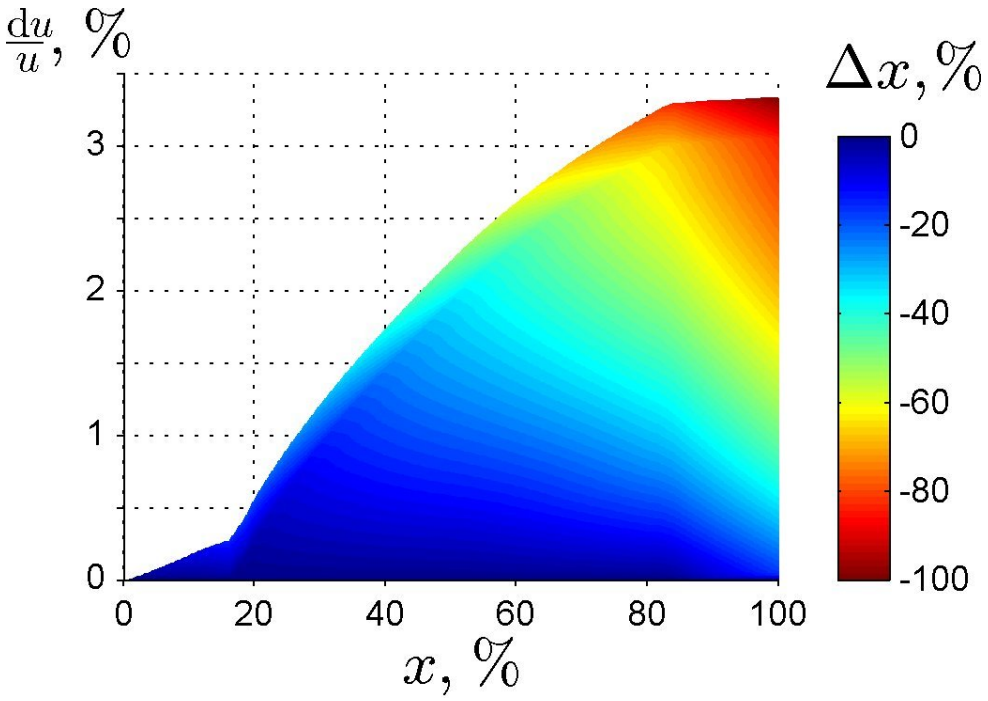

Fig. 5: **The theoretically achievable auxin gradient is highly sensitive to noise in the auxin concentration.** The value of the predicted positional variability of the threshold position as a response to a perturbation in the auxin concentration (equivalent to a shift in source intensity) in percentage of the length of the FG is indicated in colour code. The blank space represents the positions where the perturbation shifts the perceived threshold position out of the domain boundaries (i.e. no cells in the FG can achieve the cell fate determined left of the corresponding threshold position anymore). Note that a perturbation of ~0.51% disrupts cell specification in the micropylar part of the FG ($x < 0.2$) and any perturbation higher than 3.5% disrupts it in the entire FG.

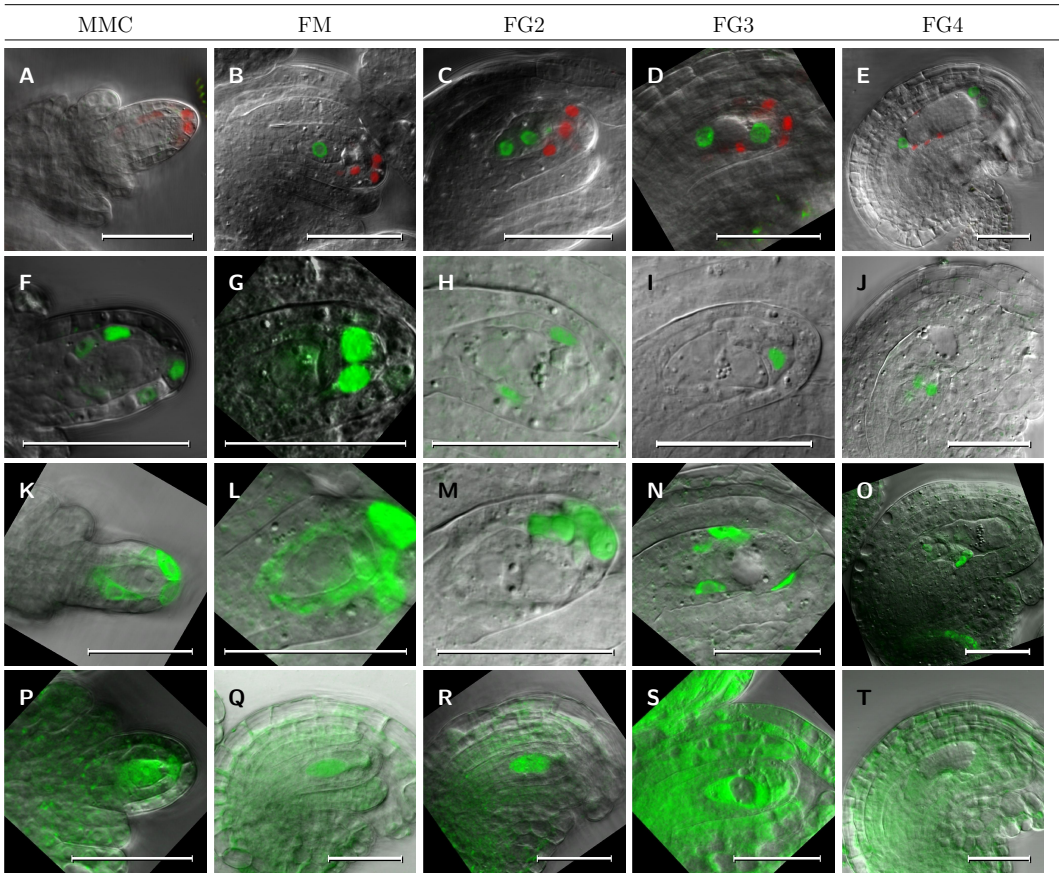

Fig. 6: **Auxin response in *Arabidopsis* ovules during female gametophyte development.** Stages of ovule development using four independent auxin reporter lines (see text for details). The following stages are shown: megaspore mother cell (MMC), functional megaspore (FM, also referred to as FG1), two-nucleate FG (FG2), two-nucleate FG with large central vacuole (FG3) and four-nucleate FG (FG4). (A-E) DR5::Dof1a:tdTomato (red) line with the AKV::H2B:YFP gametophytic fate marker (green); (F-J) DR5::SV40:3×GFP; (K-O) DR5::GFP-ER; (P-T) pUBQ10::degron-GFP. The images are oriented such that the micropylar pole of the ovules points to the right. At the MMC (A,F,K,P), FM (B,G,L,Q) and FG2 (C,H,M,R) stages auxin activity is observed only in cells surrounding the MMC or FG. At early stages, the maximum auxin activity is in the epidermal cells at the very micropylar tip of the ovule; later, also sporophytic cells in lateral regions of the nucellus show high auxin activity. At the FG2 stage (D,I,N,S) the nucellar tissue surrounding the FG begins to degenerate, starting at the micropylar pole. Some lateral sporophytic cells show auxin activity. At the FG4 stage (E,J,O,T) the surrounding nucellar tissue continues to degenerate; cells with a maximum in auxin activity are found more towards the chalazal pole. Throughout its development, no auxin activity can be observed within the FG (note that there is no overlap of the green gametophytic cell fate marker with the red DR5-driven fluorescent protein in the top row). Scale bars: 30 μm.

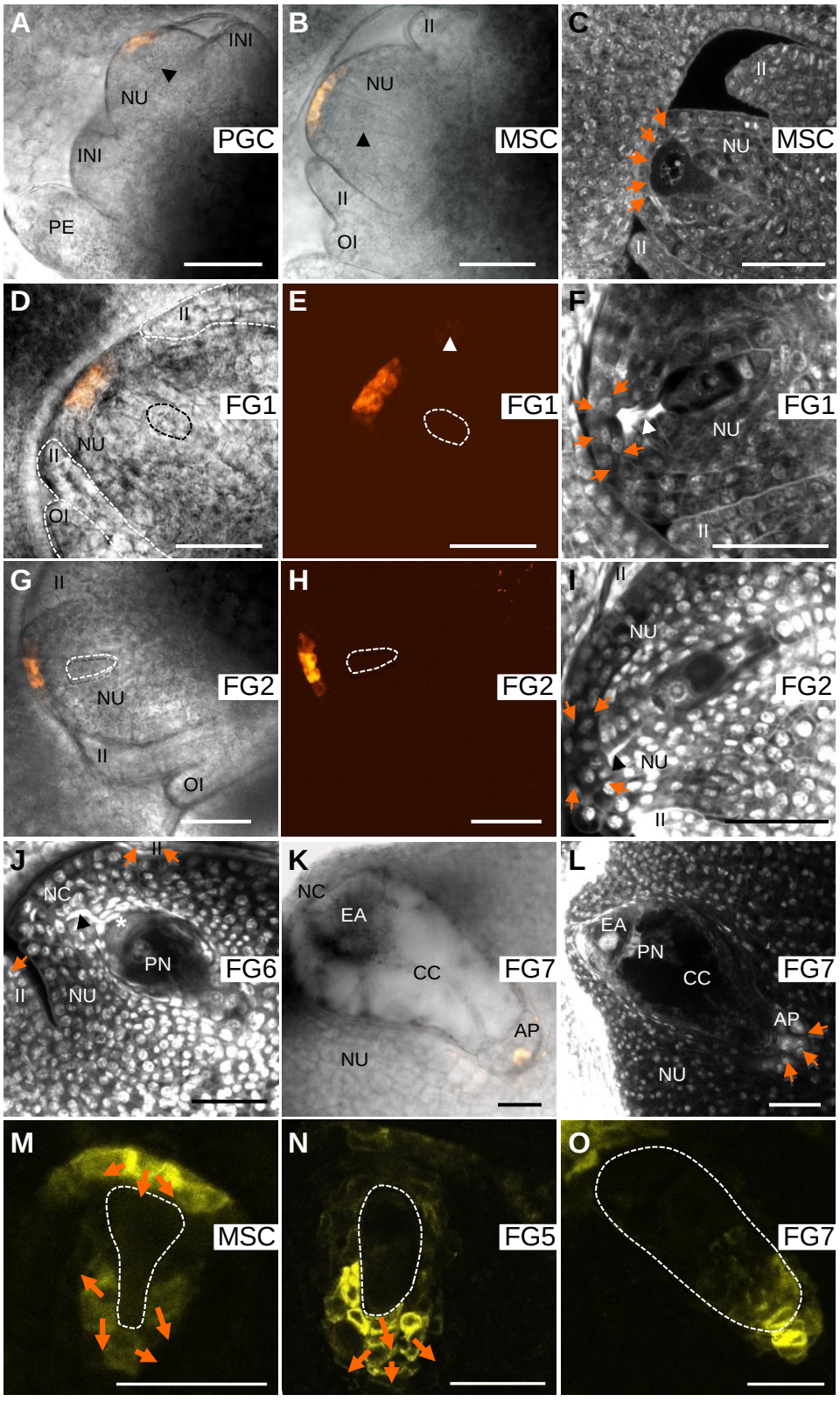
A
INI
NU
PGC
INI
PE
B
II
NU
MSC
II
OI
C
II
NU
MSC
II
D
II
FG1
NU
II
OI
E
FG1
F
FG1
NU
II
G
II
FG2
NU
II
OI
H
FG2
I
II
NU
FG2
NU
II
J
II
NC
*
PN
FG6
II
NU
K
NC
EA
CC
FG7
AP
NU
L
EA
PN
CC
FG7
AP
NU
M
MSC
N
FG5
O
FG7

Fig. 7 *(preceding page)*: **Auxin response and flux in the maize ovule during female germline development.** (**A-L**) DR5::mRFP:ER and (**M-O**) ZmPIN1a::PIN1a:YFP. Developmental stages are indicated in each panel. (**A**) A subepidermal L2 nucellus cell in immediate proximity to strongest *DR5* reporter expression in L1 is differentiating into the primordial germ cell (PGC; arrowhead). (**B**) The PMC has differentiated into a highly polar megaspore mother cell (MMC; arrowhead). (**C**) Section through the ovule at MMC stage. MMC is in pachytene stage of meiosis I. Arrows point towards single L1 nucellus cell layer displaying a strong auxin response in (B). (**D**) *DR5* expression after meiosis at stage FG1. Three megaspores degrade and the functional megaspore is encircled. *DR5* activity is expanded to L2 micropylar nucellus. (**E**) Enhanced fluorescence image of (D). (**F**) Section through the ovule at stage FG1. Remnants of degenerated megaspores are indicated by an arrowhead. Arrows point towards L1 and L2 nucellus cell layers showing a strong auxin response in fluorescent images. (**G**) Stage FG2. The female gametophyte is indicated by the white dashed line. (**H**) Fluorescence image of (G). (**I**) Section through the ovule at stage FG2. Remnants of degenerated megaspores are indicated by an arrowhead and nucellus cells showing an auxin response in fluorescent images are indicated by arrows. (**J**) Section through an ovule at stage FG6. Cellularization is completed. The egg cell nucleus is located below the asterisk. Arrowhead indicates remnants of degenerated megaspores and arrows indicate an auxin response in integument tips of fluorescent images. (**K**) Mature embryo sac containing more than 20 antipodal cells. Integuments were removed. (**L**) Section through the ovule at mature stage FG7. Antipodal cells showing an auxin response are indicated by arrows. (**M**) Auxin flux at L1 micropylar nucellus cells points towards the highly polar MMC (outlined by dashed line), but is depleted at its chalazal pole. (**N**) At stage FG5, ZmPIN1a is visible at high levels in nucellus cells surrounding the chalazal pole of the embryo sac. (**O**) At stage FG6 ZmPIN1a occurs inside antipodal cells. (A, B, D and K) merged bright field und epifluorescent images. (E, H) Fluorescence images of (D) and (G), respectively. (C, F, I, J and L) stack of CLSM sections of fixed ovules. (M-O) Fluorescent images of ZmPIN1a expressing ovules. Orange arrows indicate the cells showing a strong auxin response, as shown by DR5 expression. Abbreviations: AP: antipodal cells, CC: central cell, EA: egg apparatus, II: inner integument, INI: integument initials, NC: nucellar cap, NU: nucellus, OI: outer integument, PE: pericarp, PN: polar nuclei. Scale bars: 50µm.

1.2.6 Microscopy analyses of auxin activity in *Arabidopsis* and maize ovules reveal no auxin activity inside the FG

Our modelling results predicted only very shallow auxin gradients using known, realistic parameters in *Arabidopsis* and, to a lesser extent, in maize. To test this prediction, we aimed to characterise auxin activity in the ovule and FG experimentally in both *Arabidopsis* and maize using the classical *DR5* auxin-sensitive promoter (Ulmasov et al., 1997) and novel reporters based on auxin-dependent protein degradation.

Auxin response in ovules of *Arabidopsis thaliana*. Three different *DR5* lines were studied, each harbouring a different fluorescent protein: an endoplasmic reticulum (ER)-targeted GFP (Ottenschläger et al., 2003), a nuclear-targeted triple GFP (Weijers et al., 2006), and a nuclear localised tandem Tomato (tdTomato) fluorescent protein; the latter line additionally carried a nuclear YFP expressed under the gametophyte-specific AKV promoter (Rotman et al., 2005), marking all gametophytic nuclei. All three lines displayed the same pattern of *DR5* activity. At the megaspore mother cell (MMC) stage (Fig. 6A,F,K), *DR5* activity was observed in cells of the L1 and sometimes L2 layer of the nucellus surrounding the MMC, mostly at the future micropylar pole. Later, at the FM stage (FG1, Fig. 6B,G,L), the highest *DR5* activity was observed in the micropylar region of the nucellus in cells of the L1 and L2 layer, with some activity in the L2 cells surrounding the FM laterally. At the early two-nucleate stage of FG development (FG2, Fig. 6C,H,M), the pattern remained largely the same; however, the FG begins to displace the nucellar tissue (Schneitz et al., 1995) and, in the late two-nucleate stage (FG3, Fig. 6D,I,N), at its micropylar pole the FG comes into contact with the inner integuments, which lack *DR5* expression. At the four-nucleate stage (FG4, Fig. 6E,J,O), most of the nucellar tissue in the micropylar and medial part has degenerated and *DR5* activity is concentrated in the nucellar tissue adjacent to the chalazal pole of the FG. Later, at the final developmental stages (FG5 and FG6), some sporophytic cells adjacent to the chalazal pole of the FG were found to express *DR5* (supplementary material Fig. S10). From the four-nucleate until the final stages, a single *DR5*-expressing cell can be seen at the micropylar tip of the inner integument in fewer than a quarter of the ovules.

To obtain an alternative auxin signalling readout, we developed transgenic plants carrying a novel degron-GFP sensor, which exploits the auxin-dependent degradation of AUX/IAA proteins. Auxin binding to the ubiquitin ligase TRANSPORT INHIBITOR RESPONSE 1 (TIR1) causes the degradation of AUX/IAA proteins via their domain II (Ramos et al., 2001). We used the six amino acid domain II core VGWPPV peptide, which is common to more than 70% of AUX/IAA isoforms (Ramos et

al., 2001), as a C-terminal fusion to GFP6. An analogous reporter, DII-Venus, was developed in parallel (Vernoux et al., 2011) but is driven by the 35S promoter, which is thought to be inactive in the FG (Desfeux et al., 2000) (U.G., unpublished) and was not detected in the FG (supplementary material Fig. S11). By contrast, a bright signal of degron-GFP driven by the ubiquitin 10 (*UBQ10*) promoter (*pUBQ10*) is visible throughout FG development (Fig. **6**P-T), indicating that there is not a sufficiently high auxin concentration to cause degradation of the reporter. Although degron-GFP levels during the initial stages of ovule development are lower in sporophytic tissues than in the developing FG, an even lower level was detected in nucellar cells that express *DR5* (Fig. **6**P,Q). Thus, the pattern of auxin activity inferred from degron-GFP is complementary to the pattern displayed by the *DR5* promoter. Thus, even though the dynamic range of degron-GFP activity apparently lies in a lower range of concentrations than that of *DR5*-driven fluorescent proteins, the qualitative patterns displayed by both are consistent. We observed lower levels of degron-GFP in many sporophytic cells than in the FG, even though neither displayed *DR5* activity. This prompted us to test whether *pUBQ*10 showed differential activity in these cells and to use a control *pUBQ*10::GFP line to estimate relative auxin levels. A comparison of fluorescence intensities between *pUBQ*10::degron-GFP and control *pUBQ*10::*GFP* lines allowed us to correct for inhomogeneities in the protein levels due to differences in promoter activity. Accounting for these corrections, degradation of degron-GFP is significantly higher in the nucellar cells surrounding the FG than in the FG at both the FM (FG1) and late two-nucleate (FG3) stages (supplementary material Fig. S12, Table S3), which is in agreement with the pattern displayed by the *DR5* promoter. In conclusion, we could not detect any auxin activity inside the *Arabidopsis* FG experimentally. On the contrary, we found that until the late two-nucleate stage (FG3) the ovule's minimum auxin activity is localised in the FG. Moreover, the pattern of auxin activity in the sporophytic nucellus tissue is highly dynamic and exhibits the following features: (1) an auxin maximum usually in the two epidermal cells (L1 layer) at the tip of the ovule as the MMC differentiates in the L2 layer; (2) migration of the *DR5* activity maximum from the micropylar towards the chalazal pole; and (3) degeneration of *DR5*-expressing cells in the micropylar region of the nucellus.

Auxin response in ovules of *Zea mays*. In maize, we studied the expression pattern of *DR5* driving an ER-targeted red fluorescent protein (mRFP:ER) (Gallavotti et al., 2008). As shown in Fig. 7A, a strong *DR5* signal was visible at the tip of an ovule primordium in a few epidermal cells of the L1 layer in immediate proximity to a subepidermal cell of the L2 layer that differentiates into the MMC. The auxin response expanded around this cell, which enlarges at its micropylar pole and elongates longitudinally, and which appears smaller towards its

chalazal pole (Fig. 7B,C). The nucleus of the emerging, highly polarised MMC moved towards the micropylar pole close to the auxin maximum, and initiated meiosis. After completion of meiosis, the three micropylar-most megaspores degenerated and the FM (FG1) became more deeply embedded into the L3 layer of the developing ovule (Fig. 7D-F).

Although the cells showing *DR5* activity at the tip of the ovule expanded to the L2 layer, these sporophytic auxin-responsive cells were no longer neighbouring the FG after the FG1 stage. During FG development, *DR5* activity decreased, beginning at stage FG2 (Fig. 7G-I), and was no longer detectable in micropylar nucellar cells from stage FG5 onwards (Fig. 7J). In mature ovules, *DR5* activity was entirely absent from this region at stage FG7 (Fig. 7K,L; supplementary material Fig. S13). By contrast, a strong *DR5* signal became visible in the tips of the inner and outer integuments (Fig. 7J; supplementary material Fig. S13A,B), as well in the gametophytic antipodal cells, with the strongest signals in the antipodal cells located furthest from the central cell (Fig. 7K,L; supplementary material Fig. S13C,D). In conclusion, *DR5* activity, and thus a nuclear auxin response gradient, was not observed inside the developing FG of maize before the completion of cellularisation at stage FG6, by which time cell specification has presumably already taken place. The only gametophytic *DR5* signal was observed in the antipodal cells, after cellularisation and during their proliferation.

1.2.7 Sporophytic non-cell-autonomous effects may explain cell fate changes in the FG

Our theoretical results suggested that, with known parameters, an auxin gradient cannot be maintained in the FG, and our experimental data showed that indeed no auxin activity can be detected inside the FGs of *Arabidopsis* and maize. However, earlier experiments had shown that auxin overproduction in the *Arabidopsis* FG can lead to changes in the fate of gametophytic nuclei (Pagnussat et al., 2009). Based on the results presented here, this change in cell fate does not come about by altering the auxin gradient inside the FG as previously interpreted. Here, we suggest an alternative hypothesis that can explain such changes through effects of auxin overproduction in the FG on the surrounding sporophytic tissues. Given that there is no detectable auxin gradient in the FG but that (1) there is polarised auxin activity in the sporophyte and (2) there are effects of auxin overproduction on gametophytic cell specification, it is likely that auxin has some effect in sporophytic tissues that indirectly affects cell fate decisions in the FG, namely via a non-cell-autonomous signal (NCAS). To examine whether such a scenario could explain the experimental observations made by Pagnussat and colleagues (Pagnussat et al., 2009), we used as a basis the two-dimensional steady state model with a vacuole described above. We developed a math-

ematical model that is based on the assumption that the promoter of NCAS is responsive to auxin in sporophytic cells. Auxin leads to its activation in an all-or-none manner, i.e. the promoter becomes active if the concentration of auxin exceeds a certain threshold concentration c_{thr}. This serves as a good approximation for a more realistic scenario using a Hill activation function (e.g. Alon, 2007). The NCAS diffuses throughout the domain and is degraded inside the cells with the rate a_{NCAS}. For simplicity, we assumed that its diffusion coefficient in the membrane has the same value as in the cytoplasm (D_{NCAS}) (see supplementary material Table S4 for the values of parameters used). Using this model, we studied the impact of auxin overproduction inside the FG on the spatial distribution of the NCAS. The concentration of auxin, the activity of the NCAS promoter, and the concentration of NCAS itself are visualised in Fig. 8 under different levels of auxin synthesis. It is obvious that, depending on the level of auxin production in the FG (and the promoter activation threshold; data not shown), different spatial distributions of the NCAS can be achieved. In fact, high levels of auxin production lead to a complete loss of polarity in the spatial distribution of NCAS (Fig. 8), which is expected to result in cell fate changes. In summary, the changes in nuclear fate observed upon auxin overproduction inside the FG can be explained by auxin flux into the surrounding sporophytic tissues. This will lead to an expansion of the auxin response beyond the area seen in wild-type ovules at the chalazal pole and may have indirect effects on cell specification inside the FG.

1.3 Discussion

Our modelling results show that even under the most beneficial parameters and assumptions, the concentration of auxin drops from one end of the FG to the other only by 3.2% and 6.9% in *Arabidopsis* and maize, respectively. This is much lower than, for instance, the steepness of the Bcd gradient in *Drosophila*, which is more than 90% (Gregor et al., 2005; He et al., 2010). We found that such a shallow gradient is highly sensitive to perturbations in the auxin source, and perturbations of 3.5% or more in the auxin source completely disrupted patterning in the FG, whereas for the Bcd gradient such perturbations would lead to a shift of the threshold position of merely 4%. Therefore, such a shallow gradient would compromise the robustness of cell specification with regard to the various fluctuations that are inherent to biological systems, especially in the intensity of the auxin source. We conclude that the factors studied do not allow the production of a sufficiently steep auxin gradient to provide enough positional information for cell specification in the FG. This led us to an attempt to quantify *DR5* activity in the FG in order to refine the model. Unexpectedly, our microscopy studies showed that, in contrast to a previous report (Pagnussat et al., 2009), auxin-dependent activity cannot be detected inside developing FGs in *Arabidopsis* or maize. Additionally, we found that the pattern of

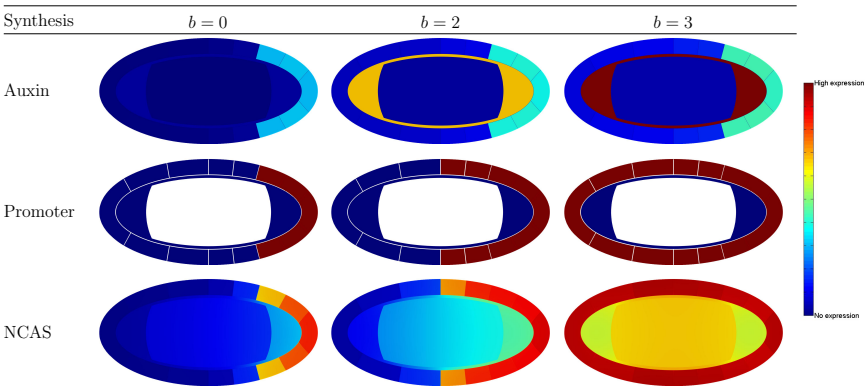

Fig. 8: **Over-production of auxin in the embryo sac can lead to expansion of a auxin-induced non-cell-autonomous signal in the sporophyte and loss of polarity.** Expression of auxin is shown in a heat map colour code. The FG is oriented such that the micropylar pole is on the left. Different levels of auxin expression ($b = 0, 2, 3$) are represented in the three columns: the first column represents a situation when no auxin is synthesized in the FG, whereas the following two columns show increasing levels of auxin expression inside the FG, which ultimately leads to a loss of polarity in the sporophytic tissues surrounding the FG. See text for details.

auxin activity in sporophytic cells adjacent to the FG is highly dynamic. The most notable developmental change in the pattern of auxin activity in the *Arabidopsis* ovule is the progressive movement of auxin maxima in cells adjacent to the developing FG from the micropylar towards the chalazal pole. It is tempting to speculate that this polarised activity could trigger indirect, non-cell-autonomous effects that influence cell specification inside the FG. Similarly, in maize, auxin activity was not observed inside the FG until cellularisation was complete. Instead, auxin activity was detected in adjacent sporophytic nucellar cells of the micropylar pole at early stages and in proliferating antipodal cells during FG maturation. A similar pattern has recently been described in *Hieracium pilosella*, in which no evidence for *DR5* activity inside the FG was found (Tucker et al., 2012). Taken together, our theoretical and experimental studies are inconsistent with the earlier report of a graded auxin-dependent activity in the FG of *Arabidopsis* (Pagnussat et al., 2009). This gives us reason to believe that these earlier results were misinterpreted and that the area with *DR5* activity assigned to the FG in fact encompassed a larger area including sporophytic cells in the nucellus, which indeed express DR5::GFP-ER. The exact boundary of the FG might not be easily identifiable by epifluorescence microscopy, as used in the previous study (Pagnussat et al., 2009), but is very clear under a confocal laser-scanning microscope and, especially, with nuclear localised reporters (Fig. **6**A-J). However, the experimental manipulations of auxin synthesis (by YUC1 overexpression) and signalling (amiRNA-mediated knockdown of ARFs) in the FG that perturbed gametophytic cell fate seemed consistent with the hypothesis of an auxin gradient (Pagnussat et al., 2009) and warrant an explanation. Here, we propose hypotheses that are consistent with the effects on cell specification observed in these studies. First, changes in the fate of gametophytic nuclei can be explained by sporophytic effects of auxin overproduction in the FG. Using a modelling approach, we showed that auxin overproduction can indeed lead to a breakdown of polarity and loss of positional information inside the FG that results from auxin leakage into sporophytic tissues. In fact, our theoretical results agree with previous observations that showed an expansion of *DR5* activity into the surrounding sporophytic tissues upon YUC1 overexpression [figure S5 in Pagnussat et al. (Pagnussat et al., 2009)]. Such an effect would be mediated by a hypothetical auxin-dependent NCAS, which is produced in sporophytic cells and controls cell specification in the FG. For instance, the peptide ZmEAL1 secreted from the egg cell has recently been shown to regulate cell fate within the maize FG in a non-cell-autonomous manner (Krohn et al., 2012). Similarly, peptides controlling cell fate in the FG could be secreted by surrounding nucellar cells. Second, the effects observed by Pagnussat and colleagues (Pagnussat et al., 2009) could be mediated by some auxin-independent components of auxin signalling in the FG. For example, the transcription

factors ARF3 and ARF17 possess auxin-like activity but are uncoupled from auxin signalling (Guilfoyle and Hagen, 2007). Both are transcribed in the central cell (Schmid et al., 2012) and show polarised mRNA expression in FGs at the four-nucleate stage (M. Schmid and U.G., unpublished). Downregulation of one of these factors, such as ARF3 in the experiment described by Pagnussat and colleagues (Pagnussat et al., 2009), would reduce such an auxin-independent auxin-like signal, whereas auxin overproduction would mask effects of ARF3 and/or ARF17 expression. Nevertheless, the activity of ARF3 or ARF17 should theoretically be detectable by the *DR5* sensor; the fact that *DR5* activity is not observed in the FG could mean that this activity is below the threshold of detection. Finally, there could be minimal auxin-dependent activity in the FG that is below the detection level of any of our reporter systems with a very shallow gradient. Even though our modelling has shown that this gradient cannot provide positional information that is sufficiently robust for cell specification, it could determine the polarity of another morphogen through so-called wave-pinning (Mori et al., 2008). Such a model depends on two interconverting molecular species, whereby a progressing but eventually decelerating activation wave of one species would be initiated at one pole of the FG, leading to the depletion of the second species in this process. Thus, wave pinning could convert a spatially more or less homogeneous concentration profile into an asymmetric stationary front profile. However, wave pinning crucially depends on very different rates of diffusion of the two species, with the active form having the low diffusion rate. For instance, the interconversion of membrane-bound and a soluble forms of Rho GTPases can polarize cells by wave-pinning (Mori et al., 2008). Auxin is known to activate the ROP2 and ROP6 Rho GTPases in *Arabidopsis* epidermal cells through a yet poorly understood transcription-independent auxin signalling pathway (Xu et al., 2010). However, it is unknown whether Rho GTPases play a role in FG development or whether any other signaling molecules in the FG fulfil the requirements for wave pinning, i.e. rapid interconversion and highly different diffusion rates. Although alternative explanations for the outcome of the experiments perturbing auxin production and signalling can be provided, there are currently not enough data to suggest a more precise mechanism. In particular, the most frequent cell fate change observed in both auxin overproduction and ARF amiRNA knockdown experiments was a loss of cell fate marker expression, whereas misexpression of egg and synergid cell markers was rather rare (Pagnussat et al., 2009). Thus, additional experiments that allow a more precise manipulation of auxin and/or other factors within and outside the FG will be required to develop accurate models of cell specification in the FG. In conclusion, neither our theoretical nor experimental evidence supports the hypothesis that a gradient in auxin activity provides the positional information for cell specification in the FG of flowering plants.

1.4 Materials and Methods

Mathematical simulations One-dimensional solutions were found analytically and were simulated in MATLAB 2011b software (MathWorks, Natick, MA, USA) using the *pdepe* function. Two-dimensional simulations were carried out with COMSOL Multiphysics 4.3a software (COMSOL Group, Stockholm, Sweden), exploiting the finite element method. To study the robustness of patterning, one-dimensional data or one-dimensional averages of two-dimensional simulations were used. Details are provided in supplementary material Appendix S1 and Tables S1, S4 and S5.

Generation of transgenic constructs The DR5::NLS:tdTomato plasmid was constructed using a 35Smin:TMVΩ:Dof1a:tdTomato vector (B.M., unpublished), which is derived from a pCB302 binary vector (Xiang et al., 1999), carrying the *TMVΩ* translational enhancer (Gallie, 2002) and the Dof1a nuclear localisation signal (NLS) (Yanagisawa and Sheen, 1998) translationally fused to the *tdTomato* fluorescent protein gene (Shaner et al., 2004). The PCR-amplified *DR5* synthetic promoter from the DR5::GFP-ER plasmid (Ottenschläger et al., 2003) was inserted into the *Ω:Dof1a:tdTomato* vector. The pUBQ10::degron:GFP plasmid was obtained by inserting a sequence encoding the degron consensus core of AUX/IAA proteins (VGWPPV) into the pMDC111 vector (Curtis and Grossniklaus, 2003) with subsequent Gateway insertion of the 2.5 kb *Arabidopsis* ubiquitin *UBQ10* promoter as explained in supplementary material Fig. S14. The control pUBQ10::GFP construct was obtained similarly. The constructs were verified by sequencing.

Plant material and growth conditions The *Arabidopsis* DR5::GFP:ER line (Ottenschläger et al., 2003) was obtained from Jiří Friml (Flanders Institute of Biotechnology, Belgium), DR5::SV40:3×GFP (Weijers et al., 2006) from Dolf Weijers (Wageningen University, The Netherlands), and the DR5::NLS:tdTomato line is described here for the first time (see above). The PGP1::PGP1:GFP line in a *pgp1* homozygous background, the PGP19::PGP19:GFP line in a *pgp19* homozygous background (Geisler et al., 2005), and the AUX1::AUX1:YFP line in a *aux1-22* homozygous background (Swarup et al.,. 2004) were provided by Markus Geisler (Université de Fribourg, Switzerland); the PIN8::PIN8:GFP line (Dal Bosco et al., 2012) was provided by Cristina Dal Bosco (Albert-Ludwigs-Universität Freiburg, Germany). Unless indicated otherwise, all plants used were *Arabidopsis thaliana* (L.) Heynh. var. Columbia-0 (Col-0). DR5::NLS:tdTomato transformants were obtained by *Agrobacterium*-mediated floral dip transformation (Bent, 2006). Seven independent transformants were recovered from BASTA selection and microscopically screened for tdTomato expression in ovules in the T1 (heterozygous plants) and T3 (homozygous plants) gen-

erations; a qualitative variation in expression patterns among the seven independent lines was not observed. A representative DR5::NLS:tdTomato line was crossed with the AKV::H2B:YFP gametophytic fate marker line (Rotman et al., 2005), provided by Wei-Cai Yang (Chinese Academy of Science, Beijing, China), which is in the Landsberg (*erecta* mutant, L*er*) background, and F3 plants homozygous for both constructs were analysed. *Arabidopsis* plants were grown as described (Schmid et al., 2012). For DR5::SV40:3×GFP seeds, the plates were supplemented with kanamycin (AppliChem, Darmstadt, Germany) to a final concentration of 50 µg/ml. Glufosinate (Plüss-Staufer, Oftringen, Switzerland) was sprayed onto plants carrying the *DR5*::NLS:tdTomato transgene on the third and sixth day after transfer to soil at a final concentration of 0.2 g/l. Maize inbred lines A188 and H99 and transgenic lines (Gallavotti et al., 2008) were grown under standard greenhouse conditions at 26°C with 16 hours of light and a relative air humidity of 60%.

Microscopy and image acquisition Ovules of *Arabidopsis* plants at various stages were dissected and studied either cleared for 5-15 minutes with 1 M glycine (pH 9.6) solution (as in Fig. 6H-J,M,O) or untreated in water (all other images). The pictures were taken with a Leica SP2 laser-scanning confocal microscope (Leica Microsystems AG, Heerbrugg, Switzerland). The GFP fluorescence was collected at wavelengths of 501-532 nm. For simultaneous YFP and tdTomato imaging, scanning was performed sequentially. Emission light of 503-575 nm and 575-632 nm was collected for the yellow and red channels, respectively. An excitation beam splitter DD 488/543 was used in both cases. Image capture was performed using Leica Confocal Software 2.61 and channel overlay was performed using a custom MATLAB script. Maize cobs were harvested from greenhouse-grown plants. Whole cobs were treated as described (Srilunchang et al., 2010). For microscopy analyses, ovaries were dissected after clearing, mounted in methyl salicylate, and analysed with an LSM 510-META confocal laser-scanning microscope (Carl Zeiss Microscopy GmbH, Oberkochen, Germany) with 488 nm excitation and a LP 505 filter. For selective ZmPIN1a::PIN1a:YFP visualisation, 514 nm excitation and a BP 530-600 filter were applied, whereas DR5::mRFP:ER fluorescence was observed with 543 nm excitation in combination with a BP 560-615 filter. Image capture and processing were performed using the Zeiss LSM 510 META software and Zeiss LSM Image Browser version 3.5.0.359.

Acknowledgements

We thank Dolf Weijers (Wageningen University), Jiří Friml (Flanders Institute of Biotechnology), Wei-Cai Yang (Chinese Academy of Science), Markus Geisler (Université de Fribourg) and Cristina Dal Bosco (Albert-Ludwigs-Universität Freiburg) for seeds; Célia Baroux and Christof Eichen-

berger (University of Zürich) for advice on confocal microscopy; Marc Schmid (University of Zürich) for allowing us to cite unpublished data; Pierre Barbier de Reuille (University of Berne), Enrico Martinoia (University of Zürich), Leah Edelstein-Keshet (University of British Columbia) and Markus Geisler for discussion; and Lucia Colombo (Universita degli Studi di Milano) for critical comments on the manuscript.

Author contributions

D.S.L. developed and simulated the mathematical models; D.S.L. and N.G.K. conducted experimental studies in *Arabidopsis* and maize, respectively; B.M. and D.J. provided materials; B.H. provided expertise for modeling; T.D. initiated and supervised the maize experiments; U.G. conceived and supervised the project; D.S.L. and U.G. wrote the manuscript, with input from all authors.

Funding

This work was supported by the Universities of Zürich and Regensburg, a postgraduate scholarship (Coordenação de Aperfeiçoamento de Pessoal de Nível Superior-CAPES-Brasília/Brazil) to N.G.K, and an iPhD Project of SystemsX.ch, the Swiss Initiative in Systems Biology to U.G., B.H. and B.M.

Note added in proof

While our manuscript was under revision, Ceccatto and colleages (Ceccatto et al., 2013) also reported the absence of *DR5* activity in the *Arabidopsis* FG.

References

Alon, U. (2007). *An Introduction to Systems Biology: Design Principles of Biological Circuits*. P.15. Chapman & Hall / CRC

Bent, A. (2006). *Arabidopsis thaliana* floral dip transformation method. *Methods Mol Biol* **343**, 87–103.

Brukhin, V., Curtis, M.D. and Grossniklaus, U. (2005). The angiosperm female gametophyte : No longer the forgotten generation. *Current Science* **89**, 1844–1852.

Christensen, C.A., King, E.J., Jordan, J.R., and Drews, G.N.(1997). Megagametogenesis in *Arabidopsis* wild type and the *Gf* mutant. *Sex. Plant Reprod.***10,**49–64.

Dal Bosco, C., Dovzhenko, A., Liu, X., Woerner, N., Rensch, T., Eismann, M., Eimer, S., Hegermann, J., Paponov, I.A., Ruperti, B., Heberle-Bors, E., Touraev, A., Cohen, J.D. and Palme, K. (2012). The endoplasmic reticulum localized PIN8 is a pollen specific auxin carrier involved in intracellular auxin homeostasis. *Plant J.* doi: 10.1111/j.1365-313X.2012.05037.x.

Delbarre, A., Muller, P., Imhoff, V., and Guern, J. (1996). Comparison of mechanisms controlling uptake and accumulation of 2,4-dichlorophenoxy acetic acid, naphthalene-1-acetic acid, and indole-3-acetic acid in suspension-cultured tobacco cells. *Planta.* **198**,

532–541

Evans, M. M.S. (2007). The *indeterminate gametophyte1* gene of maize encodes a LOB domain protein required for embryo sac and leaf development. *Plant Cell* **19**, 46–62.

Gallavotti, A., Yang, Y., Schmidt, R.J. and Jackson, D. (2008). The relationship between auxin transport and maize branching. *Plant Physiol.* **147**, 1913–1923.

Gallie, D.R. (2002). The 5'-leader of tobacco mosaic virus promotes translation through enhanced recruitment of eIF4F. *Nucleic Acids Res* **30**, 3401–3411.

Garnett, P., Steinacher, A., Stepney, S., Clayton, R. and Leyser, O. (2010). Computer simulation: the imaginary friend of auxin transport biology. *Bioessays* **32**, 828–835.

Geisler, M., Blakeslee, J. J., Bouchard, R., Lee, O. R., Vincenzetti, V., Bandyopadhyay, A., Titapiwatanakun, B., Peer, W. A., Bailly, A., Richards, E. L. et al. (2005) Cellular efflux of auxin catalyzed by the *Arabidopsis* MDR/PGP transporter AtPGP1. *Plant J.* **44**, 179-194.

Gregor, T., Bialek, W., van Steveninck, R. R. de R., Tank, D.W. and Wieschaus, E.F. (2005).Diffusion and scaling during early embryonic pattern formation. *Proc Natl Acad Sci USA* **102**, 18403-18407.

Groß-Hardt, R., Kägi, C., Baumann, N., Moore, J.M., Baskar, R., Gagliano, W.B., Jürgens, G. and Grossniklaus, U. (2007). *LACHESIS* restricts gametic cell fate in the female gametophyte of *Arabidopsis*. *PLoS Biol* **5**, e47.

Guilfoyle, T.J. and Hagen, G. (2007). Auxin response factors. *Curr. Opin. Plant Biol.* **10**, 453–460.

Huang, B. Q. and Sheridan, W.F. (1994). Female gametophyte development in maize: Microtubular organization and embryo sac polarity. *Plant Cell* **6**, 845–861.

Johnston, A.J., Kirioukhova, O., Barrell, P.J., Rutten, T., Moore, J.M., Baskar, R., Grossniklaus, U. and Gruissem, W. (2010). Dosage-sensitive function of retinoblastoma related and convergent epigenetic control are required during the *Arabidopsis* life cycle. *PLoS Genet* **6**, e1000988.

Kepinski S., and Leyser O. (2005).The *Arabidopsis* F-box protein TIR1 is an auxin receptor. *Nature* **435***:446-451.*

Křeček, P., Skůpa, P., Libus, J., Naramoto, S., Tejos, R., Friml, J. and Zažímalová, E. (2009). The PIN-FORMED (PIN) protein family of auxin transporters.*Genome Biol* **10,** 249.

Krohn, N.G., Lausser, A., Juranić, M. and Dresselhaus, T. (2012). Egg cell signaling by the secreted peptide ZmEAL1 controls antipodal cell fate. *Dev Cell* **22**, July issue.

Lander, A.D., Lo, W.-C.C., Nie, Q. and Wan, F.Y. (2009). The measure of success: constraints, objectives, and tradeoffs in morphogen-mediated patterning. *Cold Spring Harb. Perspect. Biol.* **1**.

Ma, H. and Sundaresan, V. (2010). Development of flowering plant gametophytes. *Curr Top Dev Biol* **91**, 379–412.

Marchant, A., Kargul, J., May, S. T., Muller, P., Delbarre, A., Perrot-Rechenmann, C., and Bennett, M. J. (1999). *AUX1* regulates root gravitropism in *Arabidopsis* by facilitating auxin uptake within root apical tissues. *EMBO J.* **18,** 2066–2073

Moll, C., von Lyncker, L., Zimmermann, S., Kägi, C., Baumann, N., Twell, D., Grossniklaus, U. and Gross-Hardt, R. (2008). CLO/GFA1 and ATO are novel regulators of gametic cell fate in plants. *Plant J* **56**, 913–921.

Mori, Y., Jilkine, A., and Edelstein-Keshet, L. (2008) Wave-pinning and cell polarity from a bistable reaction-diffusion system. *Biophys J* **94**, 3684–3697.

Mravec, J., Kubes, M., Bielach, A., Gaykova, V., Petrášek, J., Skůpa, P., Chand, S., Benková, E., Zažímalová, E. and Friml, J. (2008). Interaction of PIN and PGP transport mechanisms in auxin distribution-dependent development. *Development* **135**, 3345–3354.

Ottenschläger, I., Wolff, P., Wolverton, C., Bhalerao, R.P., Sandberg, G., Ishikawa, H., Evans, M. and Palme, K. (2003). Gravity-regulated differential auxin transport from columella to lateral root cap cells. *Proc Natl Acad Sci USA* **100**, 2987–2991.

Pagnussat, G.C., Alandete-Saez, M., Bowman, J.L. and Sundaresan, V. (2009). Auxin-dependent patterning and gamete specification in the *Arabidopsis* female gametophyte. *Science* **324**, 1684–1689.

Pagnussat, G.C., Yu, H.-J. and Sundaresan, V. (2007). Cell-fate switch of synergid to egg cell in *Arabidopsis eostre* mutant embryo sacs arises from misexpression of the BEL1-like homeodomain gene *BLH1*. *Plant Cell* **19**, 3578–3592.

Petrášek, J. and Friml, J. (2009). Auxin transport routes in plant development. *Development* **136**, 2675–2688.

Petrášek, J., Mravec, J., Bouchard, R., Blakeslee, J.J., Abas, M., Seifertová, D., Wiśniewska, J., Tadele, Z., Kubeš, M., Čovanová, M., Dhonukshe, P., Skůpa, P., Benková, E., Perry, L., Křeček, P., Lee, O.R., Fink, G.R., Geisler, M., Murphy, A.S., Luschnig, C., Zažímalová, E. and Friml, J. (2006). PIN proteins perform a rate-limiting function in cellular auxin efflux. *Science* **312**, 914–918.

Rotman, N., Durbarry, A., Wardle, A., Yang, W.C., Chaboud, A., Faure, J.E., Berger, F. and Twell, D. (2005). A novel class of MYB factors controls sperm-cell formation in plants. *Curr. Biol.* **15**, 244–248.

Schmid, M.W., Schmidt, A., Klostermeier, U.C., Barann, M., Rosenstiel, P. and Grossniklaus, U. (2012). A powerful method for transcriptional profiling of specific cell types in eukaryotes: laser-assisted microdissection and RNA sequencing. *PLoS ONE* **7**, e29685.

Schneitz, K., Hülskamp, M. and Pruitt, R.E. (1995). Wild-type ovule development in *Arabidopsis thaliana*: a light microscope study of cleared whole-mount tissue. *Plant J* **7**, 731–749.

Shaner, N.C., Campbell, R.E., Steinbach, P.A., Giepmans, B. N.G., Palmer, A.E. and Tsien, R.Y. (2004). Improved monomeric red, orange and yellow fluorescent proteins derived from *Discosoma* sp. red fluorescent protein. *Nat Biotechnol* **22**, 1567–1572.

Skinner, D. J. and Gasser, C. S. (2009). Expression-based discovery of candidate ovule development regulators through transcriptional profiling of ovule mutants. *BMC Plant Biol* **9**, 29.

Sprunck, S. and Gross-Hardt, R. (2011).

Nuclear behavior, cell polarity, and cell specification in the female gametophyte. *Sex Plant Reprod* **24**, 123–136.

Srilunchang, K.-o., Krohn, N.G. and Dresselhaus, T. (2010). DiSUMO-like DSUL is required for nuclei positioning, cell specification and viability during female gametophyte maturation in maize. *Development* **137**, 333–345.

Sundaresan, V. and Alandete-Saez, M. (2010). Pattern formation in miniature: the female gametophyte of flowering plants. *Development* **137**, 179–189.

Swarup, R., Kargul, J., Marchant, A., Zadik, D., Rahman, A., Mills, R., Yemm, A., May, S., Williams, L., Millner, P., Tsurumi, S., Moore, I., Napier, R., Kerr, I.D., and Bennett, M.J. (2004). Structure-function analysis of the presumptive *Arabidopsis* auxin permease AUX1. *Plant Cell* **16**, 3069–83.

Swarup, K. and Benková, E., Swarup, R., Casimiro, I., Péret, B., Yang, Y., Parry, G., Nielsen, E., DeSmet,I., Vanneste, S. et al. (2008) The auxin influx carrier LAX3 promotes lateral root emergence. *Nat Cell Biol* **10**, 946–954.

Swarup, R. and Péret, B. (2012). AUX/LAX family of auxin influx carriers – an overview. *Frontiers in Plant Sci.* **3**, 225.

Tucker, M.R., Okada, T., Johnson, S.D., Takaiwa, F. and Koltunow, A. M.G. (2012). Sporophytic ovule tissues modulate the initiation and progression of apomixis in *Hieracium*. *J. Exp. Bot.* **63**, 3229-3241.

Ulmasov, T., Murfett, J., Hagen, G. and Guilfoyle, T.J. (1997). Aux/IAA proteins repress expression of reporter genes containing natural and highly active synthetic auxin response elements. *Plant Cell* **9**, 1963–1971.

Weijers, D., Schlereth, A., Ehrismann, J.S., Schwank, G., Kientz, M. and Jürgens, G. (2006). Auxin triggers transient local signaling for cell specification in *Arabidopsis* embryogenesis. *Dev Cell* **10**, 265 – 270.

Xiang, C., Han, P., Lutziger, I., Wang, K. and Oliver, D.J. (1999). A mini binary vector series for plant transformation. *Plant Mol Biol* **40**, 711–717.

Xu, T., Wen, M.. Nagawa, S., Fu, Y., Chen, J.-G., Wu, M.-J., Perrot-Rechenmann, C., Friml, J., Jones, A. M. and Yang, Z. (2010). Cell surface- and Rho GTPase-based auxin signaling controls cellular interdigitation in Arabidopsis. *Cell* **143**, 99 – 110.

Yadegari, R. and Drews, G.N. (2004). Female gametophyte development. *Plant Cell* **16** Suppl, S133–S141.

Yanagisawa, S. and Sheen, J. (1998). Involvement of maize Dof zinc finger proteins in tissue-specific and light-regulated gene expression. *Plant Cell* **10**, 75–89.

Yang, Y., Hammes, U.Z., Taylor, C.G., Schachtman, D. P. and Nielsen, E. (2006). High-affinity auxin transport by the AUX1 influx carrier protein.*Curr Biol* **16**, 1123–1127.

Vernoux, T., Brunoud, G., Farcot, E., Morin, V., Van den Daele, H., Legrand, J., Oliva, M., Das, P., Larrieu, A., Wells, D et al. (2011). The auxin signalling network translates dynamic input into robust patterning at the shoot apex. *Mol. Syst. Biol.* **7**, 508

APPENDIX 1

(Lituiev et al. 2013, Development 140)

SUPPLEMENTARY TEXT

Simulation conditions and parameter values

The reaction-diffusion model described in the main text was studied in the form of a partial differential equation with boundary conditions:

$$\frac{\partial u}{\partial t} = D \cdot \nabla^2 u - \hat{a} \cdot u + \hat{b}$$

$$\nabla u|_{\Gamma_1} = -\hat{p}$$

$$\nabla u|_{\Gamma_2} = -\hat{q} \cdot u$$

Where u is the auxin concentration, D is the diffusion coefficient, $\hat{a}$ is the degradation rate, $\hat{b}$ is the synthesis rate, $\hat{p}$ is the influx rate, and $\hat{q}$ is efflux rate, Γ_1 is the boundary domain of influx (micropyle, $x = 0$ in one dimension) and Γ_2 is the boundary domain of efflux (chalaza, $x = 1$ in one dimension). The ∇ sign represents the gradient operation (first spatial derivative), and ∇^2 is the Laplacian operator (second spatial derivative). The equation thus describes the local instanteneous change of the auxin concentration, which is influenced by the diffusion ($D \nabla^2 u$ term), degradation ($-\hat{a}\, u$), and synthesis ($\hat{b}$).

Further, we rescale the degradation rate and the efflux rate by the length (L) of the female gametophyte (FG) and diffusion rate (D); the rescaled degradation rate becomes $a = \hat{a} \cdot \frac{L^2}{D} = \left(\frac{\lambda}{L}\right)^{-2}$ and the rescaled efflux rate $q = \hat{q} \cdot \frac{L}{D}$. As the differential equation is linear, the influx rate and synthesis rate can be selected arbitrary. We chose these parameters such to equal the mean concentration of auxin with the value of one.

One-dimensional solutions were found analytically and were simulated using MATLAB software. We set the *pdepe* function for non-negative solutions, and used otherwise standard numeric settings (relative error tolerance 10^{-3}, absolute error tolerance 10^{-6}), unless otherwise specified. The values used are shown in Table S4.

Two-dimensional simulations using the COMSOL software package were carried out with a relative error tolerance of 10^{-7}. For both one- and two-dimensional models, we assumed homogeneous and isotropic auxin diffusion throughout the cytoplasm and apoplastic space. This is an approximation, as the presence of cellular compartments can slow down diffusion by about 4-fold (Sbalzarini et al., 2005), and the presence of cytoplasmic streaming can increase the effective transport rate. Degradation of auxin was assumed to be homogeneous throughout the cytoplasm (or part of it in regime 3). The key parameter grouping of the model under these assumptions is the rescaled characteristic length scale of degradation λ/L, whose estimated values are presented in the Table S1.

Arabodpisis and maize FG lengths were measured from pictures using ImageJ software. The distribution of FG lengths is shown in Fig. S7.

In order to assess the width of the cytoplasmic isthmus, we analyzed *Arabidopsis* wild-type (L*er*) plants expressing a membrane-localized GFP under the control of an FG-specific promoter (*pAtD123::EGFP-AtROP6C*, Escobar-Restrepo et al., 2007). As shown in Fig. S8, the width of the isthmus is in the order of 1 μm.

Estimation of the membrane permeability parametes.

We estimated auxin flux parameters from the data of Geisler et al. (2005). We assumed the following:

1. Linear dependence of the auxin trans-membrane flux on auxin concentration. This assumption can be justified by the fact that the auxin concentration applied in the experiment (500 nM) is lower than the known Km for the auxin transporters (more than 840 nM; Yang et al., 2006; Swarup et al., 2008).
2. Fast diffusion rate compared to transport. The data suggests that the assumption holds because the characteristic diffusion time (the ratio of the diffusion coefficient to the protoplast radius) is around $6 \cdot 10^{-5}$ m/s, with diffusion coefficient of $6 \cdot 10^{-10}$ m^2/s (Grieneisen et al, 2007), while the estimated transmembrane flux values are slower than 10^{-8} m/s.
3. Background auxin in- and efflux are mediated by the protonated form only.
4. The effect of vacuolar trapping is insignificant.
5. Auxin flux in wild-type protoplasts kept in the dark does not involve any auxin transporter proteins.

6. PGP1 activity in mesophyll protoplasts is the same as in the FG.
7. As no auxin efflux carriers except for PGP1 are expressed in the FG, similarly to the *pgp19* mutant, we used the estimate of the transport rate in *pgp19* mutant protoplasts for further simulations of the wild-type FG.

Based on these assumptions we made the following estimations: the auxin efflux rate in the *pgp19* mutant is $1.1 \cdot 10^{-8}$ m/s; net passive auxin efflux (wild-type protoplasts in darkness) $5.6 \cdot 10^{-9}$ m/s; net passive auxin influx $4.3 \cdot 10^{-8}$ m/s; and the permeability of the membrane to the protonated form of auxin $1.3 \cdot 10^{-6}$ m/s.

Note that the parameter values for passive auxin flux, estimated based on the data by Geisler et al. (2005), indicate a lower membrane permeability in *Arabidopsis* protoplasts compared to the one estimated earlier by Gutknecht and Walter (1980) for lecitine bilayer membranes. However, we used the former, as they are obtained in a biological, and thus more relevant system for our studies.

Geometrical features of the two-dimensional model

For this model, we assumed that key properties of the FG can be described by the following geometry:

1. The shape of the FG is approximated by an ellipsoid.
2. The large central vacuole is represented by an intersection of an ellipsoid whose both semiradii are less than the semiradii of the FG by the value of Δy and a shpere of radius 1/3.
3. The apoplast is modeled as a space between the plasma membrane of the FG and another membrane located at distance of Δw from it, representing the plasma membranes of surrounding sporophytic cells.
4. The influx of auxin occurs in the micropylar pole of the plasma membrane of a surrounding cell.
5. The concentration of protonated auxin at the plasma membrane of cells located at the chalazal half of the FG is set to zero.

The geometry is thus axi-symmetrical two-dimensional. The values of the geometric parameters are presented in the Table S5.

Antagonistic auxin fluxes occur during polarization of germ lineage cells

The auxin efflux carrier ZmPIN1a of maize was expressed as YFP fusion protein under control of the endogenous promoter (Gallavotti et al., 2008) to study the auxin flux occurring during ovule and germline development. As shown in Fig. 7M of the main text and in Fig. S2A,B, auxin flux as indicated by the polar localization of ZmPIN1a is directed at the tip of the ovule primordium towards the micropylar pole of the primordial germ cell (PGC) and megaspore cell (MSC), but is removed from the chalazal pole towards the ovule axis. After meiosis, ZmPIN1a localization at the micropylar pole starts to disappear, becoming very weak already at stage FG2/3 (Fig. S2C,D). In contrast, expression increased at the chalazal pole, presumably directing auxin towards the axis of the developing ovule and removing it from the chalazal pole of the developing FG. Strong ZmPIN1a-YFP signals were observed in nucellus cells surrounding the chalazal pole of the FG at stage FG5 (Fig. 7N of main text and Fig. S2E,F), when cellularization and separation of gametic and accessory cells occurs. During proliferation of antipodal cells, ZmPIN1a-YFP signals were also detectable inside these cells (Fig. 7O of main text and Fig. S2G,H) and appeared to accumulate in endosomes of antipodal cells within fully mature FGs (Fig. S2I,J). Whether auxin was removed from the chalazal pole of the maturing central cell could not be definitely determined, but as shown by DR5 promoter activity, the highest auxin response was observed in the antipodal cell most distant from the central cell (Fig. 7K of main text and Fig. S13D), indicating that auxin flux is likely kept low in the immediate surrounding of the central cell.

Sensitivity analysis

Independent parameter groups taken into analysis. The mathematical model under regime 4 contains 12 linearly independent non-dimensional groupings.

1. Cytoplasmic isthmus width Δy_{cyt} (Table S5)
2. Apoplast isthmus width Δy_{apo} (Table S5)
3. Vacuole length r_{vac} (Table S5)

4. Width *B* of the FG (Table S5)

5. Characteristic degradation rate (regarded as a ratio between the degradation velocity $\hat{q}_a := \hat{a} \cdot L$ and the diffusion velocity $\hat{q}_D := \frac{D}{L}$, and equivalent to the inverse of squared rescaled characteristic degradation length scale)

$$a = \frac{\hat{q}_a}{\hat{q}_D} = \hat{a} \cdot \frac{L^2}{D} = \left(\frac{\lambda}{L}\right)^{-2}$$

6. Rescaled active efflux rate of auxin from the cytoplasm to apoplast: $q_{c-a} = \frac{\hat{q}_{c-a}}{\hat{q}_D}$

7. Characteristic dissociation velocity of auxin: $\beta := \frac{\hat{\beta}}{\hat{a}}$

8. Rescaled passive flux rate for protonized auxin: $q_{IAAH} = \frac{\hat{q}_{IAAH}}{\hat{q}_D}$

9. pKd of auxin

10. pH of the vacuole

11. pH of the cytoplasm

12. pH of the apoplast

The rate parameters here are normalized with respect to the characteristic diffusion velocity ($\hat{q}_D = \frac{D}{L}$), while the geometrical parameters are normalized with respect to the FG length *L*. *D* represents diffusion rate, the FG length *L*, and $\hat{a}$ is degradation rate in natural dimensions.

Alternatively, given fast auxin dissociation, six parameters influencing auxin flux (7—12) can be collected into three following parameters:

7.a. Rescaled influx from the apoplast to the cytoplasm $q_{a—c}$;

8.a. Rescaled efflux from the vacuole to the cytoplasm $q_{v—c}$;

9.a. Rescaled influx from the cytoplasm to the vacuole $q_{c—v}$.

Calculation of the sensitivity. The robustness and sensitivity of the morphogen gradient can be addressed by studying how the perceived threshold concentration (x_{thr}) is shifted upon the perturbation in the parameter values (α). Namely, we are interested in the fixed (threshold) level of the morphogen concentration at the physiological parameter value (α_0) (de Lachapelle and Bergmann 2010). The sensitivity of the solution to deviation in the parameter values (α) can be estimated from the full derivative formula:

$$\frac{du}{dx} = \frac{\partial u}{\partial x}\cdot\frac{dx}{dx} + \frac{\partial u}{\partial \alpha}\cdot\frac{d\alpha}{dx} + \sigma\left(\frac{1}{2}\cdot\frac{\partial^2 u}{\partial x^2} + \frac{1}{2}\cdot\frac{\partial^2 u}{\partial \alpha^2}\cdot\left(\frac{d\alpha}{dx}\right)^2\right) \qquad (*)$$

We are interested in the effects of finitesimally small shifts in the values of du, dx, and dα which according to (*) are approximately related as follows:

$$du \approx \frac{\partial u}{\partial x}\cdot dx + \frac{\partial u}{\partial \alpha}\cdot d\alpha$$

At this stage we can address the *sensitivity of the concentration to the changes in the parameter values*, i.e. how the concentration in some point x_0 (dx = 0) will be shifted upon perturbation dα (Fig. S9). Dividing both sides by u_0 we obtain:

$$\frac{du}{u_0} \approx \left.\frac{\partial \ln u}{\partial \ln \alpha}\right|_{\alpha_0,u_0}\cdot\frac{d\alpha}{\alpha_0} \equiv \varepsilon_{u\alpha}\cdot\frac{d\alpha}{\alpha_0}$$

Where $\varepsilon_{u\alpha}$ is the coefficient of sensitivity of concentration to the parameter values.

Then, we can question the *sensitivity of the threshold position to the concentration*, i.e. how the position of the threshold concentration will move if the concetration is changed under the fixed parameter values:

$$\mathrm{d}x \approx \left(\frac{\partial \ln u}{\partial x}\Big|_{u_0, x_0} \right)^{-1} \cdot \frac{\mathrm{d}u}{u_0} \equiv \varepsilon_{ux} \cdot \frac{\mathrm{d}u}{u_0}$$

Where ε_{ux} is the coefficient of sensitivtiy of the threshold position to the concentration. One can notice that it is given by the concentration value divided by the gradient at a given point:

$$\varepsilon_{ux} = u_0 \,/\, \frac{\partial u}{\partial x}\Big|_{x_0}$$

Further, we can study the *sensitivity of the threshold position to the perturbation in the parameter value*, i.e. how some position at which concentration is equal to some threshold concentration u_0 (du = 0) will shift upon perturbation in the parameter vale dα:

$$\mathrm{d}x \approx \left(\frac{\partial \ln u}{\partial x}\Big|_{u_0, x_0} \right)^{-1} \cdot \frac{\partial \ln u}{\partial \ln \alpha}\Big|_{\alpha_0, u_0} \cdot \frac{\mathrm{d}\alpha}{\alpha_0} \equiv \varepsilon \cdot \frac{\mathrm{d}\alpha}{\alpha_0}$$

Where $\varepsilon = \varepsilon_{ux} \cdot \varepsilon_{u\alpha}$. Particularly, as the partial differential equation under consideration is linear, the sensitivity of the concentration to the source intensity (the concentration of auxin at the micropylar pole) is equal to one ($\varepsilon_{u\alpha} = 1$), i.e. the sensitivity of the threshold position to the perturbation in the source is equivalent to the sensitivity to the perturbation in concentration.

The sensitivity of the concentration to changes in the parameter values. The concentration is highly sensitive to the changes in the pH of the apoplast and the source (i.e. auxin concentration in the neighbouring cells at the micropylar pole). Perturbations in these

former parameters will be amplified by about 10 times. The perturbation in the rest of the parameters will be dampened, however (Table S2).

The sensitivity of the threshold position to the concentration change. The threshold position could not be correctly distinguished in the micropylar part (i.e. it is shifted out of the FG) if the perturbation in the auxin concentration exceeds around 1%. With perturbations higher than 3.5%, the threshold determination becomes impossible also in the chalazal part (see Fig. 5 in the main text).

The sensitivity of the threshold position to the perturbation in the parameter value can be found as the product of the two previously mentioned sensitivity coefficient.

REFERENCES

Abbruzzetti, S., Grandi, E., Viappiani, C., Bologna, S., Campanini, B., Raboni, S., Bettati, S. and Mozzarelli, A. (2005). Kinetics of acid-induced spectral changes in the GFPmut2 chromophore. *J. Am. Chem. Soc.* **127**, 626–635.

Chavarría-Krauser, A. and Ptashnyk, M. (2010). Homogenization of long-range auxin transport in plant tissues. *Nonlinear Anal. Real World Appl.* **11**, 4524–4532.

Escobar-Restrepo, J.-M., Huck, N., Kessler, S., Gagliardini, V., Gheyselinck, J., Yang, W.-C. and Grossniklaus, U. (2007). The FERONIA receptor-like kinase mediates male-female interactions during pollen tube reception. *Science*. **317**, 656–660.

Gallavotti, A., Yang, Y., Schmidt, R. J. and Jackson, D. (2008). The relationship between auxin transport and maize branching. *Plant Physiol.* **147**, 1913–1923.

Grieneisen, V. A., Xu, J., Maree, A. F. M., Hogeweg, P. and Scheres, B. (2007). Auxin transport is sufficient to generate a maximum and gradient guiding root growth. *Nature* **449**, 1008–1013.

Gutknecht, J. and Walter, A. (1980). Transport of auxin (indoleacetic acid) through lipid bilayer membranes. *J. Membr. Biol.* **56**, 65–72.

Liu, J., Mehdi, S., Topping, J., Tarkowski, P. and Lindsey, K. (2010). Modelling and experimental analysis of hormonal crosstalk in *Arabidopsis*. *Mol. Syst. Biol.* **6**.

Ljung, K., Ostin, A., Lioussanne, L. and Sandberg, G. (2001). Developmental regulation of indole-3-acetic acid turnover in Scots pine seedlings. *Plant Physiol.* **125**, 464–475.

Mravec, J., Kubes, M., Bielach, A., Gaykova, V., Petrásek, J., Skůpa, P., Chand, S., Benková, E., Zazímalová, E. and Friml, J. (2008). Interaction of PIN and PGP transport mechanisms in auxin distribution-dependent development. *Development* **135**, 3345–3354.

Rapparini, F., Tam, Y. Y. Y., Cohen, J. D. and Slovin, J. P. (2002). Indole-3-acetic acid metabolism in *Lemna gibba* undergoes dynamic changes in response to growth temperature. *Plant Physiology* **128**, 1410–1416.

Sequeira, L. and Mineo, L. (1966). Partial purification and kinetics of indoleacetic acid oxidase from tobacco roots. *Plant physiology* **41**, 1200–1208.

Slifkin, M. (1984). Protonation rate constants of proline. *J. Mol. Liq.* **29**, 75–80.**Slifkin, M. A. and Ali, S. M.** (1991). Thermodynamic and rate parameters for alanine protonation reactions. *J. Chem. Soc., Faraday Trans.* **87**, 3241–3243.

SUPPLEMENTARY TABLES

Table S1. Values of degradation rate and corresponding gradient steepness at regime 1

Ref.	Object	Degradation rate, $\hat{a}$	Half-life	a	λ	GS
(Sequeira and Mineo,1966)	Tobacco leaf protoplasts	$5 \cdot 10^{-4}$	23 min	$4.08 \cdot 10^{-3}$	15.6	0.204%
(Ljung et al., 2001)	Scots pine seedlings	$2.67 \cdot 10^{-5}$	7.2 h	$2.18 \cdot 10^{-4}$	67.7	0.0109%
(Rapparini et al., 2002)	*Lemna gibba* (aquatic monocot)	$<1.93 \cdot 10^{-3}$	<6 min	$1.58 \cdot 10^{-2}$	7.97	0.783%
(Grieneisen et al.,2007)	Model fitting	$5 \cdot 10^{-6}$	3.85 h	$4.08 \cdot 10^{-5}$	156	0.00204 %
(Liu et al., 2010)	Model fitting	2	0.35 s	$1.63 \cdot 10^{1}$	0.247	96.49%

Table S2. Sensitivity of the model to perturbation in parameters (regime 4 in two dimensions). For description of parameters see Table 2 and 3.

Parameter	median of |ε|	maximum of |ε|
Δy	$2.66 \cdot 10^{-2}$	$3.98 \cdot 10^{-2}$
w	$1.15 \cdot 10^{-2}$	$1.91 \cdot 10^{-2}$
B	$4.85 \cdot 10^{-5}$	$6.56 \cdot 10^{-5}$
r_{vac}	$8.79 \cdot 10^{-4}$	$4.91 \cdot 10^{-3}$
s	$1.67 \cdot 10^{-2}$	$2.94 \cdot 10^{-2}$
D	$6.57 \cdot 10^{-3}$	$9.78 \cdot 10^{-3}$
k_{AUX1}^{micr}	$2.00 \cdot 10^{-2}$	$2.98 \cdot 10^{-2}$
$q_{c\text{-}a}$	$6.08 \cdot 10^{-5}$	$7.24 \cdot 10^{-5}$
$q_{a\text{-}c}$	$1.50 \cdot 10^{-2}$	$2.26 \cdot 10^{-2}$
$q_{c\text{-}v}$	$2.62 \cdot 10^{-4}$	$2.85 \cdot 10^{-4}$
$q_{v\text{-}c}$	$7.50 \cdot 10^{-4}$	$1.94 \cdot 10^{-3}$
p_{IAA}	$1.50 \cdot 10^{-2}$	$2.26 \cdot 10^{-2}$
K	$1.40 \cdot 10^{-3}$	$2.34 \cdot 10^{-3}$
pH_{apo}	$1.36 \cdot 10^{-3}$	$2.31 \cdot 10^{-3}$
pH_{cyt}	$2.41 \cdot 10^{-3}$	$2.65 \cdot 10^{-3}$
pH_{vac}	$1.21 \cdot 10^{-2}$	$3.11 \cdot 10^{-2}$

Table S3. The *p*-value of the one-sided Wilcoxon signed rank test with the alternative hypothesis that the $\log_2$ fluorescence ratios in the ovules of the degron plants (pUBQ10:degron-GFP) are higher than in ovules of the control plants (pUBQ10:degron-GFP).

Stage	$\log_2$[ES / integument]	$\log_2$[ES / nucellus]	$\log_2$[integument / nucellus]
FM	0.1397	0.0005 *	0.0026 *
FG3	0.7665	0.1409	0.0033 *

* significant within 0.05 confidence interval

Table S4. Reaction, diffusion and transport parameters

Abbreviation	Parameter	Value	Notes
a	dimensionless degradation rate	0.0158	
λ/L	rescaled characteristic length scale	$a^{-1/2} = 7.97$	
β	dimensionless protonation rate	$8.33 \cdot 10^4$	
pH_{apo}	apoplastic pH	5.00	
pH_{cyt}	cytoplasmatic pH	7.60	(Chavarría-Krauser and Ptashnyk, 2010)
pK_d	IAA dissociation constant	4.75	(Chavarría-Krauser and Ptashnyk, 2010)
k_d	dissociation rate (estimation for auxin)	$1.4 \cdot 10^6 s^{-1}$	(Chavarría-Krauser and Ptashnyk, 2010)
$P_{[HA]}$	permeability to non-ionized auxin	$3.3 \cdot 10^{-5}$ m/s	(Gutknecht and Walter, 1980)
$P_{[A-]}$	permeability to ionized auxin	$<10^{-11}$ m/s	(Gutknecht and Walter, 1980)
q_1	dimensionless membrane permeability to IAAH	5.50	
q_2	dimensionless membrane permeability to IAA^-	$1.67 \cdot 10^{-6}$	
v_1	dimensionless IAAH diffusion coefficient in the membrane	$q_1 \times \Delta x = P_1 \Delta \hat{x}/D$	
v_2	dimensionless IAA^- diffusion coefficient in the membrane	$q_2 \times \Delta x$	

b^{ES}_{IAA}	auxin production rate in the ES (NCAS model)	{0,2,3}	
$b^{adj.c.}_{IAA}$	auxin production rate in the adjacent cells (NCAS model)	0.189	
c_{thr}	threshold of [IAA] for NCAS promoter activation	0.189	
$b^{adj.c.}_{NCAS}$	NCAS production rate in the adjacent cells	5	
a_{NCAS}	NCAS degratation rate in the cytoplasm	30	
D_{NCAS}	NCAS diffusion coefficient	0.05	

Table S5: Geometric parameter values

Abbrev.	Value	Description
L	70 µm	*A. thaliana* FG length at FG5 stage
$\Delta\hat{x}$	5 nm	membrane width
Δx	$\Delta\hat{x}/L$	dimensionless membrane width
$\Delta\hat{y}$	1 µm	width of cytoplasmic path around the vacuole
Δy	$\Delta\hat{y}/L$	dimensionless width of cytoplasmic path around the vacuole
$\hat{w}$	50 nm	the width of the apoplast
w	$\hat{w}/L$	rescaled width of the apoplast
s	$L/10$	the localization of the sporophytic cells providing the source of auxin
B	2/5 L	FG width-to-length ratio
r_{vac}	2/3 L	vacuole length

FIGURES

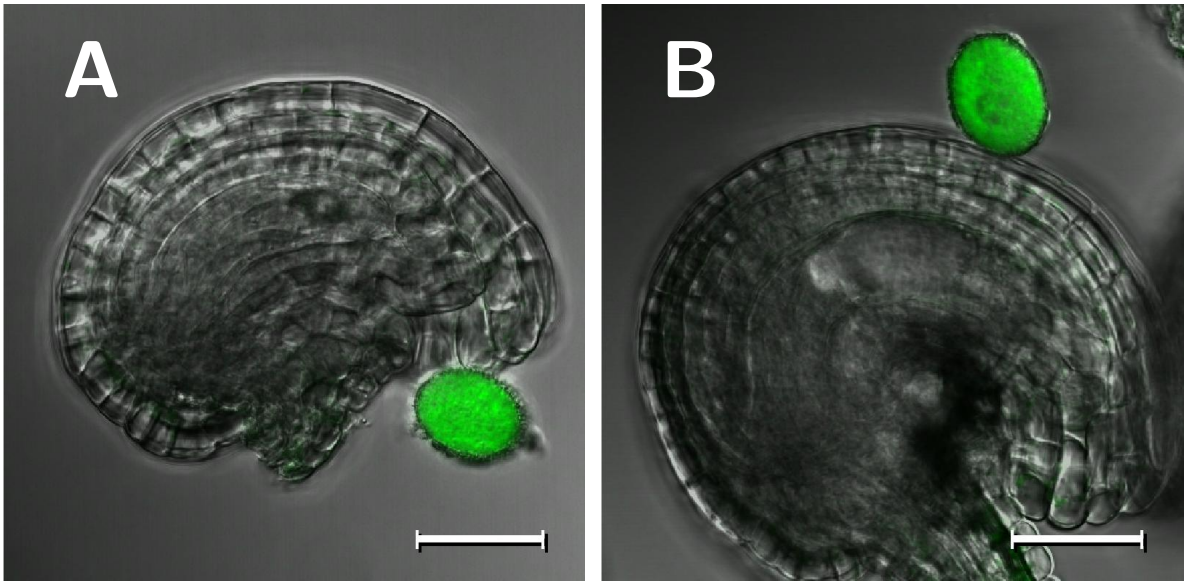

Fig. S1. PIN8 protein is not detected in the *Arabidopsis* ovules. Ovules and pollen from plants carrying PIN8::PIN8:GFP promoter-fusion construct were analysed. While a PIN8:GFP signal is clearly observed in the pollen grains as expected, no signal can be detected in ovules during FG4 (**A**) and FG6 (**B**) stages. Scale bars: 30 μm.

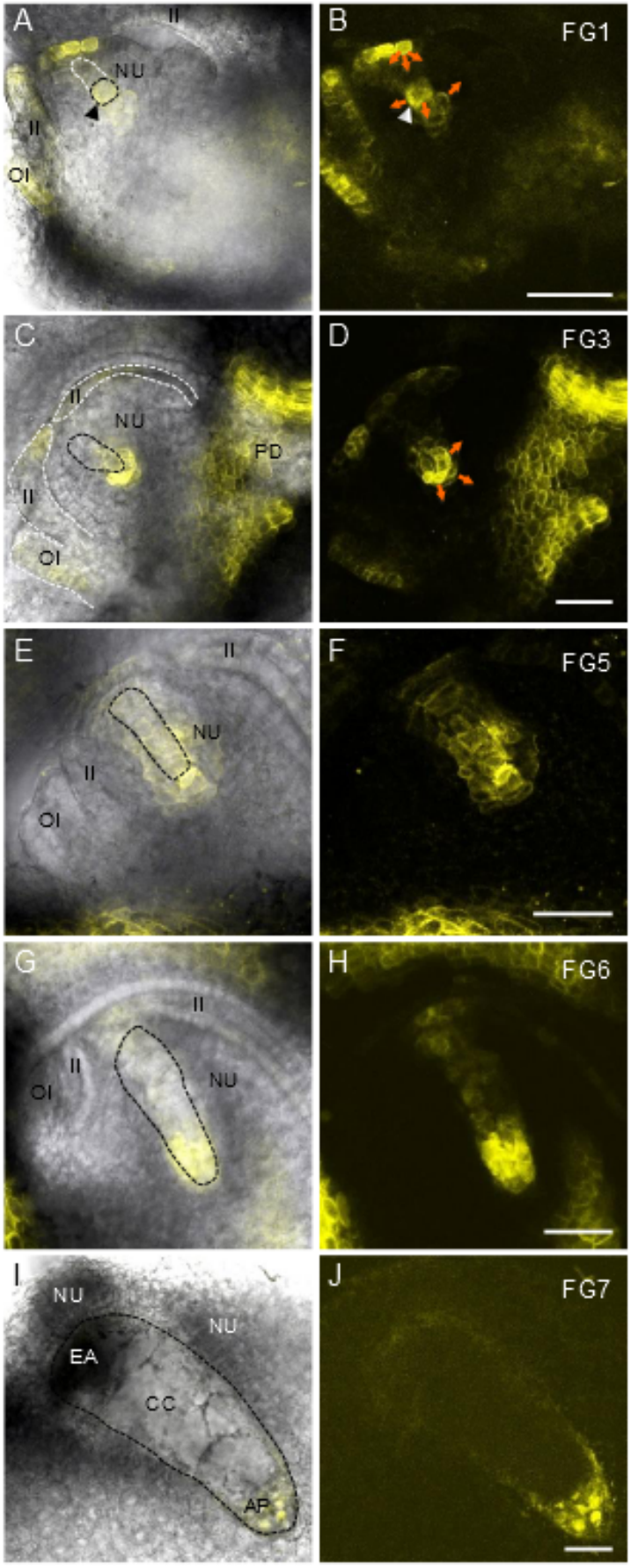
A
II
NU
II
OI
B
FG1
C
II
NU
FD
II
OI
D
FG3
E
II
NU
II
OI
F
FG5
G
II
II
OI
NU
H
FG6
I
NU
NU
EA
CC
AP
J
FG7

Fig. S2 *(preceding page)*. Localization of the auxin efflux carrier ZmPIN1a during ovule development in maize. ZmPIN1a was expressed as a YFP fusion protein under control of its endogenous promoter. Orange arrows indicate the predicted auxin flux according to polarized ZmPIN1a localization. (**A**) A female gametophyte at stage FG1 (shortly after meiosis): ZmPIN1a-YFP is localized at the plasma membrane of micropylar nucellus cells pointing towards the degenerating megaspores (encircled by a white dashed line) as well as around the functional megaspore (indicated by a black dashed line and arrowhead). Additionally, ZmPIN1a-YFP is visible in the developing integuments. (**B**) Fluorescence image of (A). The arrowhead points towards the position of the functional megaspore. (**C**) Stage FG3: ZmPIN1a-YFP is no longer detectable at micropylar nucellus cells. YFP signals in nucellus cells, surrounding the chalazal pole of the female gametophyte, have increased in intensity. Additionally, ZmPIN1a-YFP is visible in the integuments and strongly in the pedicel cells differentiating vascular tissue. Note that the pericarp was removed. (**D**) Fluorescence image of (C). (**E**) Stage FG5: ZmPIN1a-YFP signals are strongest in nucellus cells surrounding the chalazal pole of the female gametophyte. (**F**) Fluorescence image of (E). (**G**) Stage FG6: ZmPIN1a-YFP signals are strongest in nucellus cells surrounding and inside antipodal cells. (H) Fluorescence image of (G). (**I**) Mature stage FG7: Integuments were removed. ZmPIN1a-YFP signals inside antipodal cells seem to be mainly localized to the endosomal compartment. (**J**) Fluorescence image of (I). (A, C, E, G and I) merged bright field and fluorescence images. The female gametophyte is indicated by a black dashed line. Abbreviations: AP: antipodal cells, CC: central cell, EA: egg apparatus, II: inner integument, NU: nucellus, OI: outer integument, PD: pedicel. Scale bars: 50 μm.

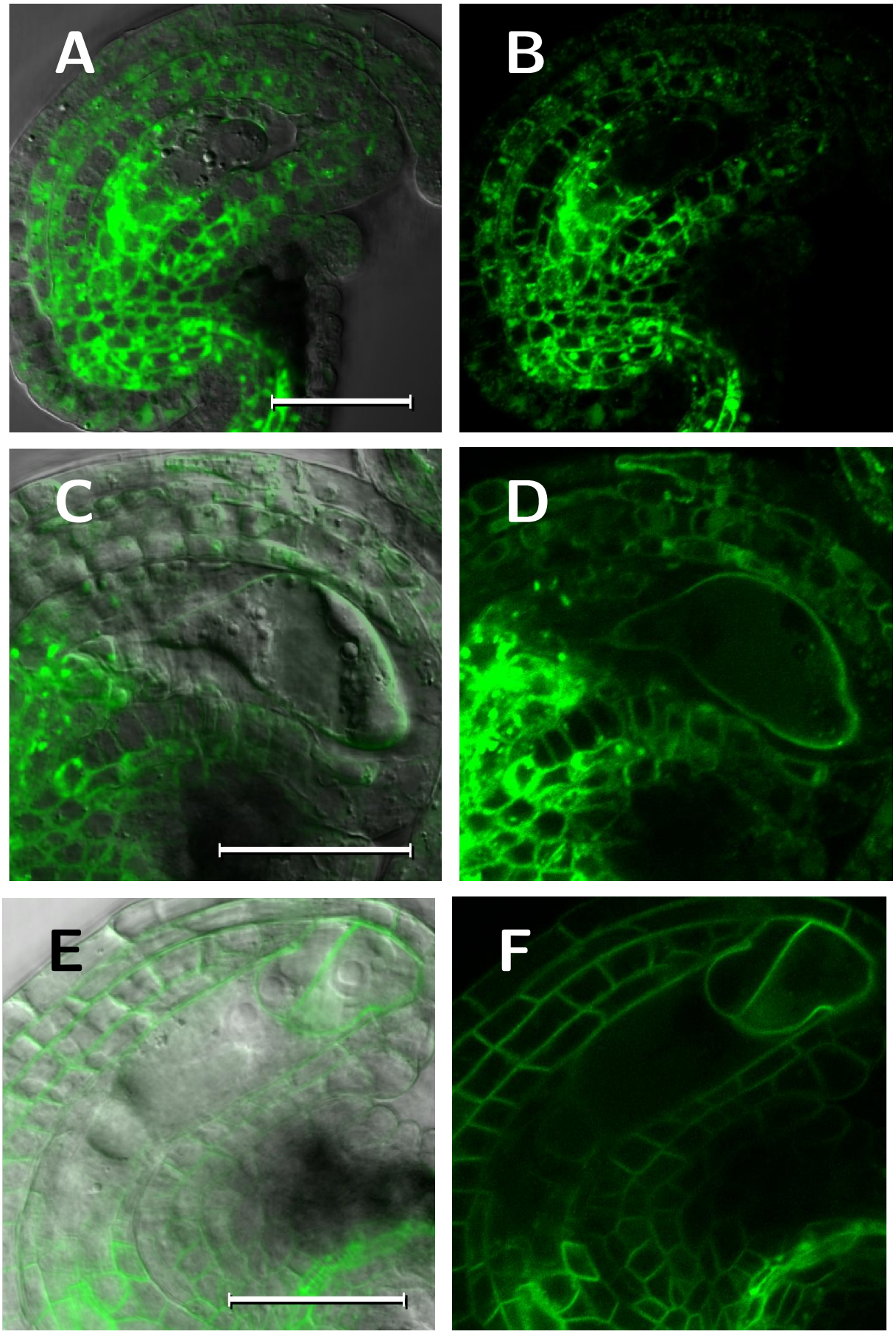
A
B
C
D
E
F

Fig. S3 *(preceding page)*. PGP1 is expressed and evenly distributed over the plasma membrane in the *Arabidopsis* female gametophyte. (**A, B**) FG3 stage: PGP1:GFP is highly expressed in the sporophytic tissue in the chalazal part of the nucellus, a moderate signal is also observed within the two-nucleate FG, (**C, D**) FG4 stage: the strong PGP1:GFP signal remains in the chalazal part of the nucellus; the almost uniform staining in the plasma membrane of the four-nucleate FG becomes more distinct; (**E, F**) FG6 stage: strong PGP1:GFP expression can now be observed within the synergid (the cell on the right in the top right corner) and the egg cell (the cell on the left). (A, C, and E) Overlay of the DIC and GFP channels; (B, D, and F) corresponding GFP channel alone. The samples A, B, and C, D were plasmolysed and cleared with the 1M glycin solution to better visualize the localization in the FG membrane. Scale bars: 30 μm.

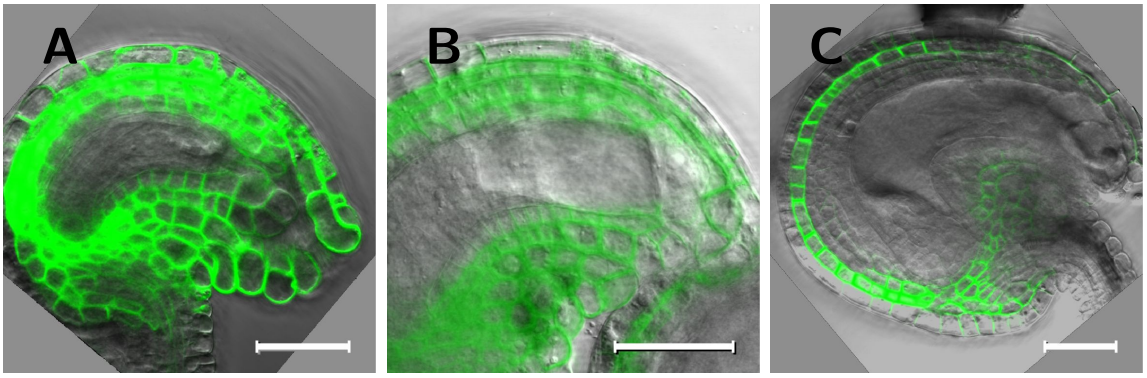

Fig. S4. PGP19 is expressed in the sporophytic tissues of the *Arabidopsis* ovules. (**A**) functional megaspore stage (FG1) and (**B**) FG6 stage: PGP19:GFP is expressed in the inner and outer integuments. (C) FG7 stage: PGP19:GFP is localized to the subepidermal cell layer only. Scale bars: 30 μm.

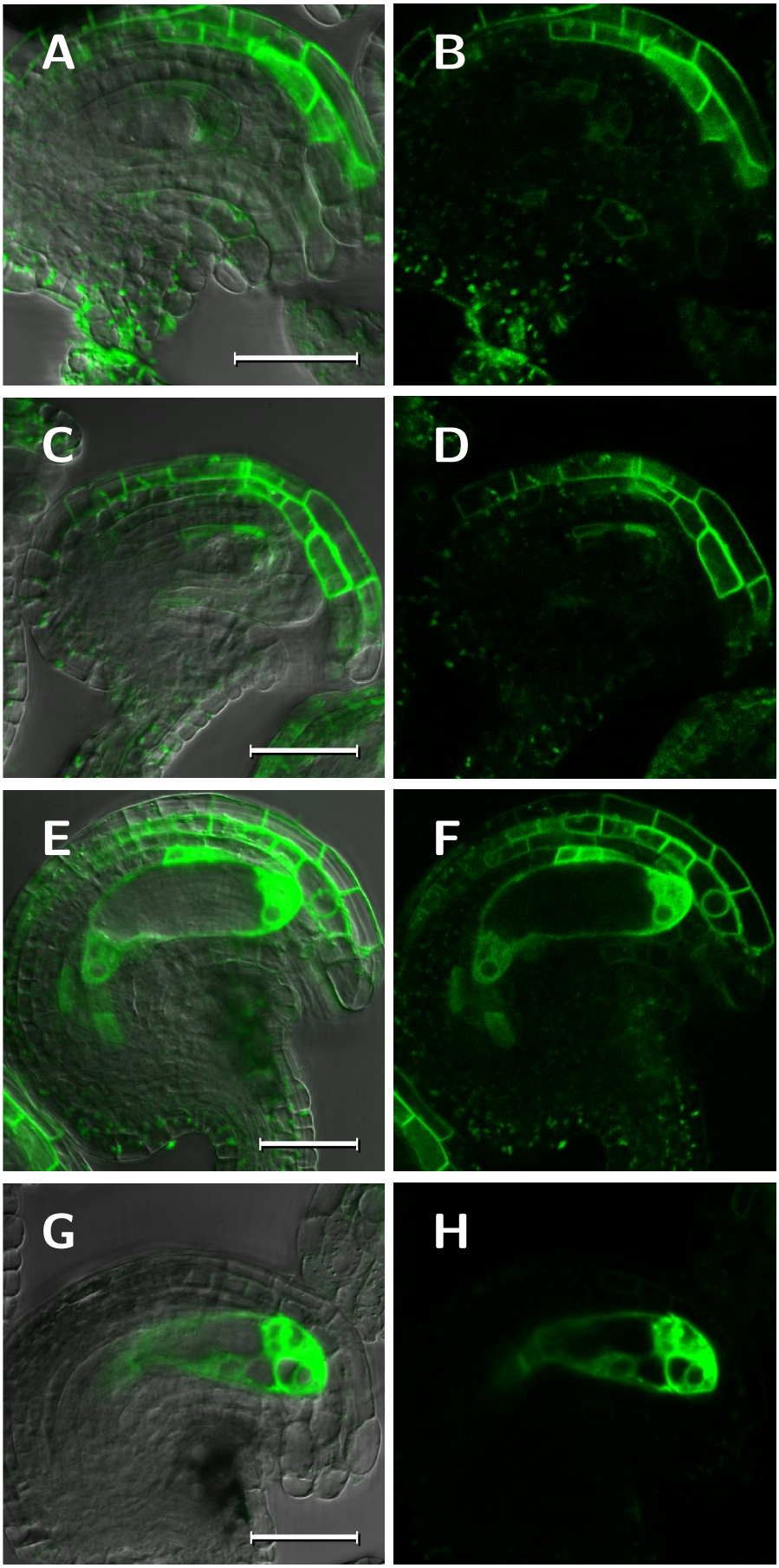
A
B
C
D
E
F
G
H

Fig. S5 *(preceding page).* AUX1 is expressed and polarly distributed in the plasma membrane in the *Arabidopsis* female gametophyte from the FG4 stage onward. (**A, B**) FG2 stage: AUX1:YFP is strongly expressed within the upper part of the outer integument and, at a lower extent, the sporophytic tissue of the nucellus. (**C, D**) FG3 stage: AUX1:YFP expression becomes stronger in the nucellus. (**E, F**) FG4 stage: AUX1:YFP expression appears within the FG first at the four-nulceate stage, with the YFP intensity in the micropylar compartment approximately 5 times higher than in the chalazal one; expression within the endothelium becomes stronger; some expression appears also in the chalazal part of the nucellus. (**G, H**) FG7 stage: AUX1:YFP expression becomes stongest in the cells of the FG, with signal in the surrounding tissues becoming undetectable. (A, C, E and G) Overlay of the DIC and GFP channels; (B, D, F and H) corresponding GFP channel alone. Scale bars: 30 μm.

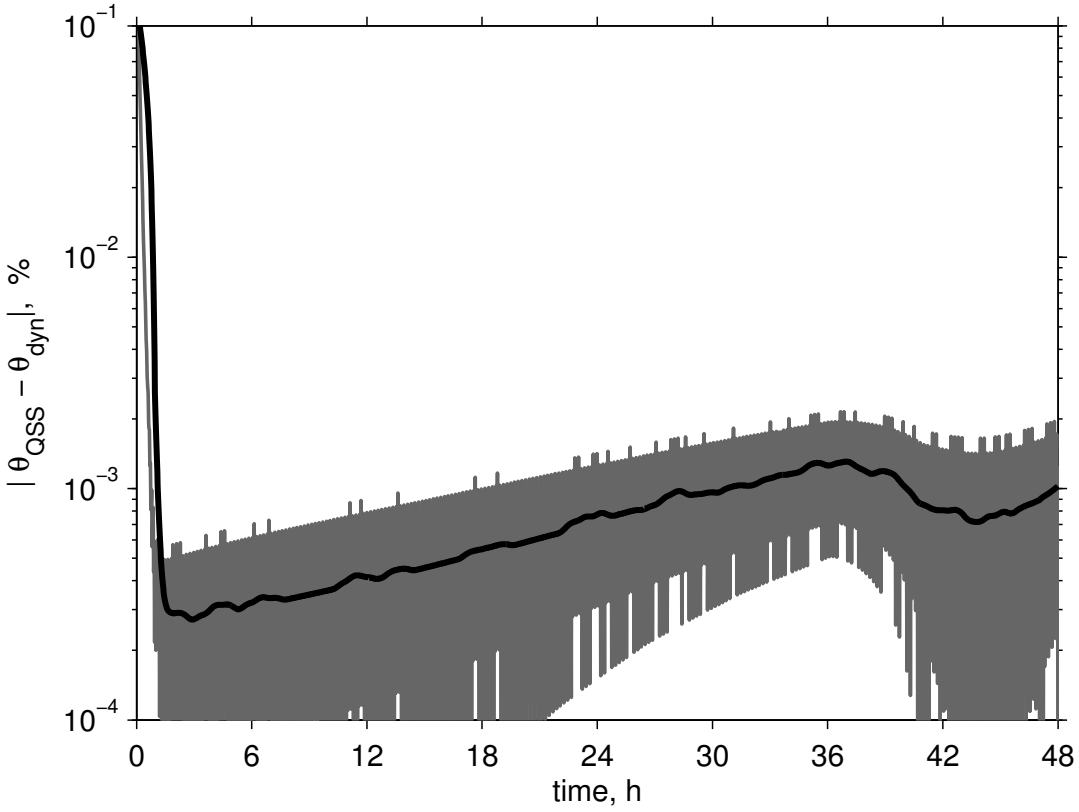

Fig. S6. Numerical studies suggest that a quasi-steady state assumption about growth leads to a negligibly small error in regime 1. The absolute value of difference between the gradient steepness found as quasi-steady state and dynamic solution $|\theta_{\mathrm{QSS}} - \theta_{\mathrm{dyn}}|$ expressed in percentage points. Note that the absolute value of the difference does not exceed 0.0022% after initial equilibration during the first 38 minutes. The original data (gray line) was smoothened with a moving average filter with window size of two hours (black line). The relative error tolerance of the ODE solver was set to 10^{-5}.

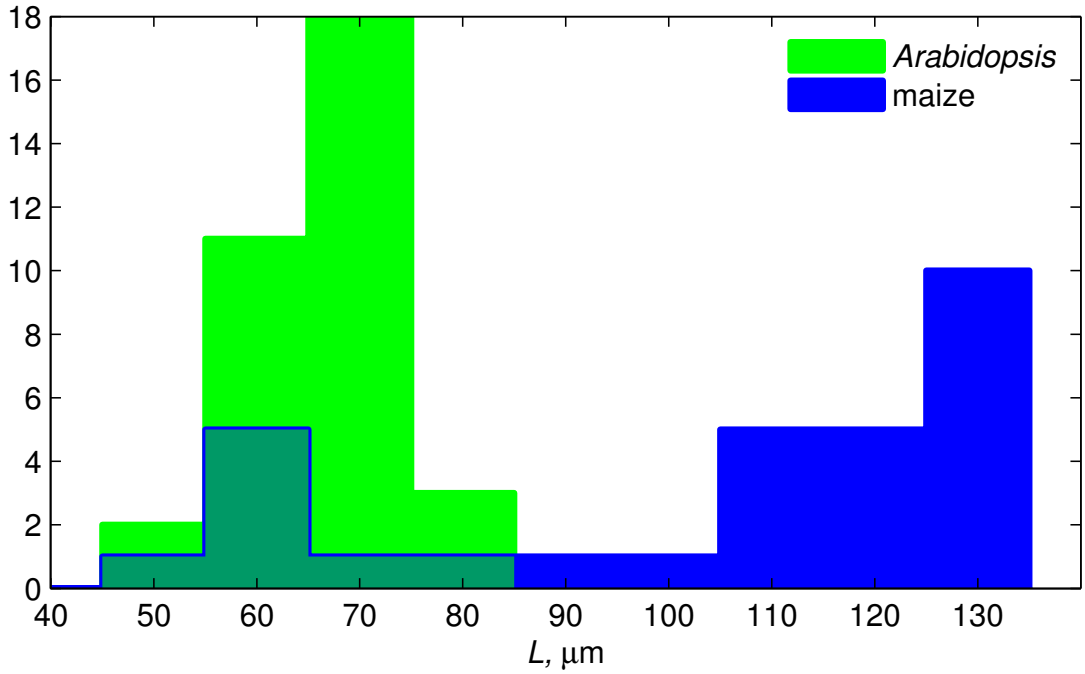

Fig. S7. Distribution of the female gametophyte lengths in Arabidopsis and maize at stage FG4/5. The graph shows the distribution of FG lengths (in µm) measured from micrographs. *Arabidopsis* is shown in green, maize in blue

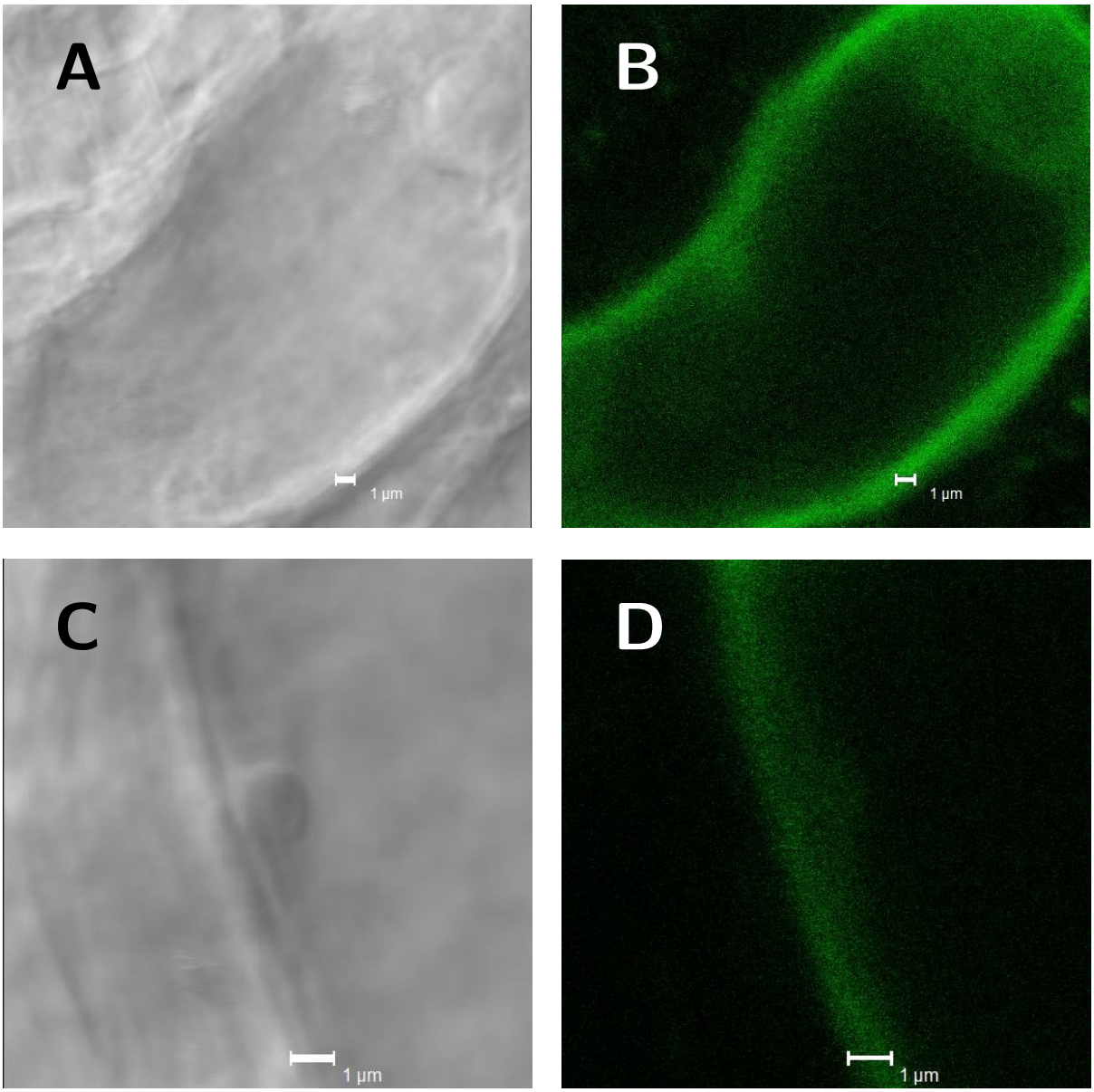

Fig. S8. The isthmus between central vacoule and female gametophyte membranes. (**A, C**) Differential interference contrast of *Arabidopsis* wild-type FG4 FGs. (**B, D**). Fluorescent micrographs of the same ovules expressing a membrane-localized GFP driven by an FG-specific promoter. The isthmus is around 1 µm in width.

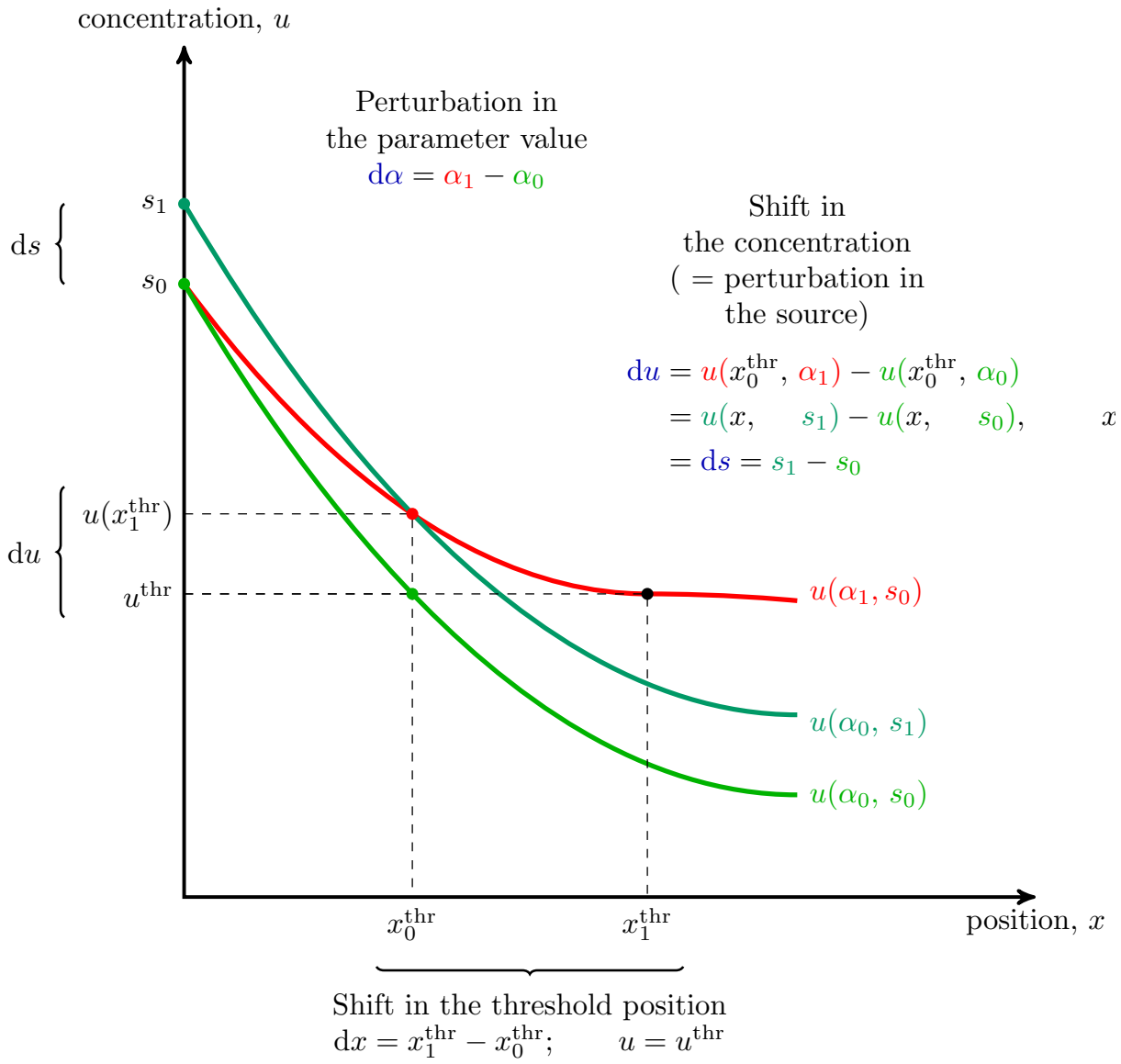

Fig. S9. The principle of the sensitivity analysis. The profile of the morphogen under physiological conditions is shown in green. We study the behavior of the threshold position (x_0^{thr}), defined by the threshold concentration (u^{thr}), upon perturbation in the parameter values. After perturbing parameter α by some small value $\mathrm{d}\alpha$, we obtain another, distorted profile (in red), where the threshold concentration (u^{thr}) is pointing to another x-position, x_1^{thr}. The concentration in the physiological threshold position is now shifted by $\mathrm{d}u$. Equivalently, the same value of concentration shift is achieved at all the x-positions if we perturb the source by $\mathrm{d}s = \mathrm{d}u$. The chain rule given in the supplementary text provides the connection between these shifts.

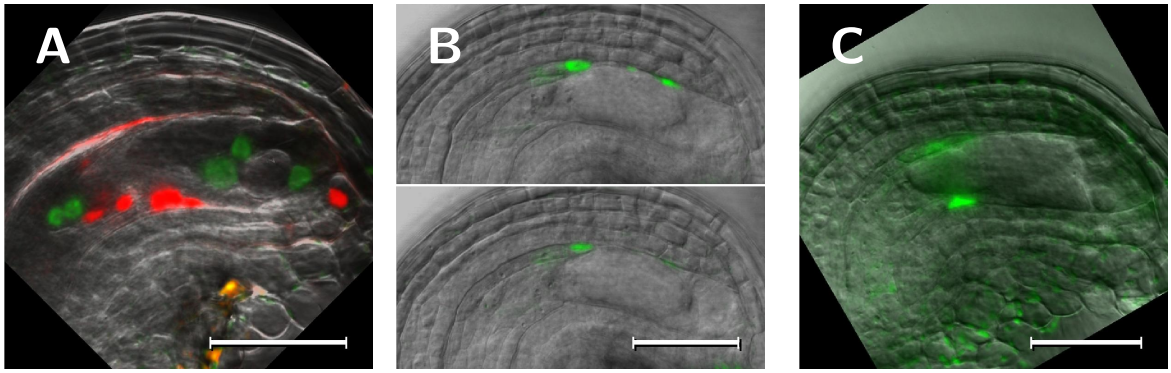

Fig. S10. *DR5* activity at the FG5 and FG6 stage in *Arabidopsis* ovules is observed only in the sporophytic tissue (**A**) At the FG5 stage, DR5::NLS:tdTomato expression in the ovule is localized to the nucellar cells on the lower (concave) side of the ovule along the whole length of the FG, with a stronger signal in the chalazal part; the gametic cell fate marker (green, AKV::H2B:YFP) shows no colocalization with the red DR5 signal. (**B**) Two z-sections of a FG at the FG5 stage are shown. DR5::SV40:3GFP is expressed in the endothelial cells adjacent to the chalazal pole of the FG. (**C**) DR5::GFP-ER expression in the FG5 stage: DR5 signal is observed in the endothelial cells surrounding the chalazal pole of the FG; the endothelial cells near the micropylar part have already degraded. Scale bars: 30 μm.

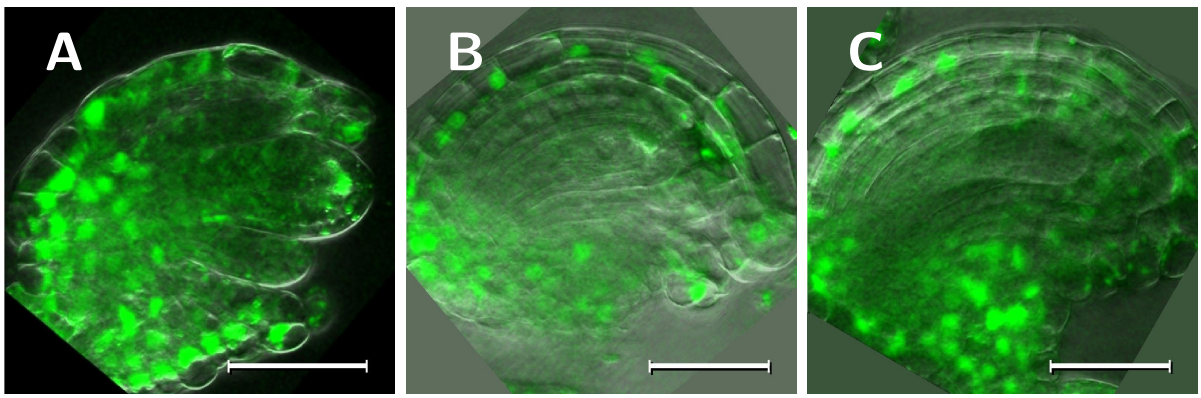

Fig. S11. The 35S::DII-Venus sensor is expressed in the outer integument and the chalazal pole but not in the female gametophyte of the *Arabidopsis* ovules. (**A**) Functional megaspore stage: the DII-Venus fluorescence is strong in the chalaza of the ovule and in a micropylar-most nucellar cells. (**B**) FG3 stage: the DII-Venus fluorescence appears in the outer integument. (**C**). FG4 stage. Note, at no stage can the DII-Venus fluorescence be seen within the FG. Scale bars: 30 μm.

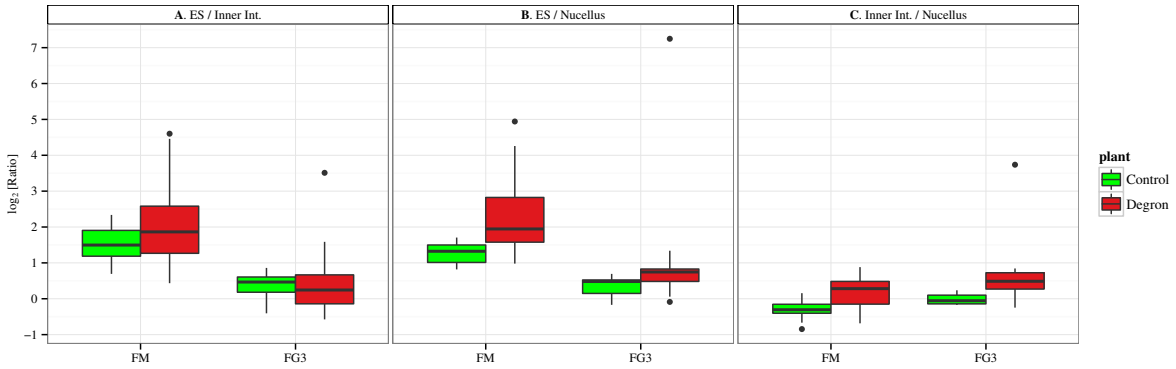

Fig. S12. Quantification of the fluorescence in the pUBQ10::degron:GFP and the pUBQ10::GFP plants indicates that the pattern of the auxin activity in the ovules is consistent with the *DR5* expression. Accounting for the non-uniform activity of the UBQ10 promoter driving the degron:GFP sensor construct, we performed intensity ratio measurements in the control pUBQ10::GFP and sensor pUBQ10::degron:GFP plants in order to infer the pattern of auxin distribution in the developing ovules. The GFP fluorescent images (grayscale, 12-bit) of the ovules from the degron (pUBQ10::degron:GFP) and the control (pUBQ10::GFP) transgenic lines were manually segmented and the median of the intensity was quantified using the ImageJ software. The intensity was measured for three regions (FG, endothelium surrounding the FG, and inner integument) from 2 degron lines and 6 control lines at stages the functional megaspore (FM) and late two-nucleate stage (FG3; all stages according to Christensen et al., 1997) ($n > 6$ per group). The $\log_2$-transformed ratios between the median intensity of the regions for each image were subjected to a one-sided Wilcoxon signed-rank test in R software (version 2.14.1). (**A**) The intensity ratio between the FG and the inner integument is insignificantly higher in the degron carrying plants at the FM stage and approximately the same at the FG3 stage, suggesting that the level of auxin is lower in the FG than in the inner integument at the FM stage and similar at the FG3 stage. (**B**) The intensity ratio between the FG and the nucellus is higher in the degron carrying plants at the functional megaspore (FM) stage (also referred to as FG1) and possibly lower at the FG3 stage, suggesting that the level of auxin is lower in the FG than in the nucellus at this stage and possibly lower at the FG3 stage. (**C**) In the degron plants, the fluorescence intensity ratio between the inner integument and the nucellus is significantly lower compared to the control at both FM and FG3 stage, which suggests that auxin activity in the inner integument is lower than in the nucellus. Significance levels: * –$p < 0.004$ (significant); † $p < 0.15$ (insignificant trend).

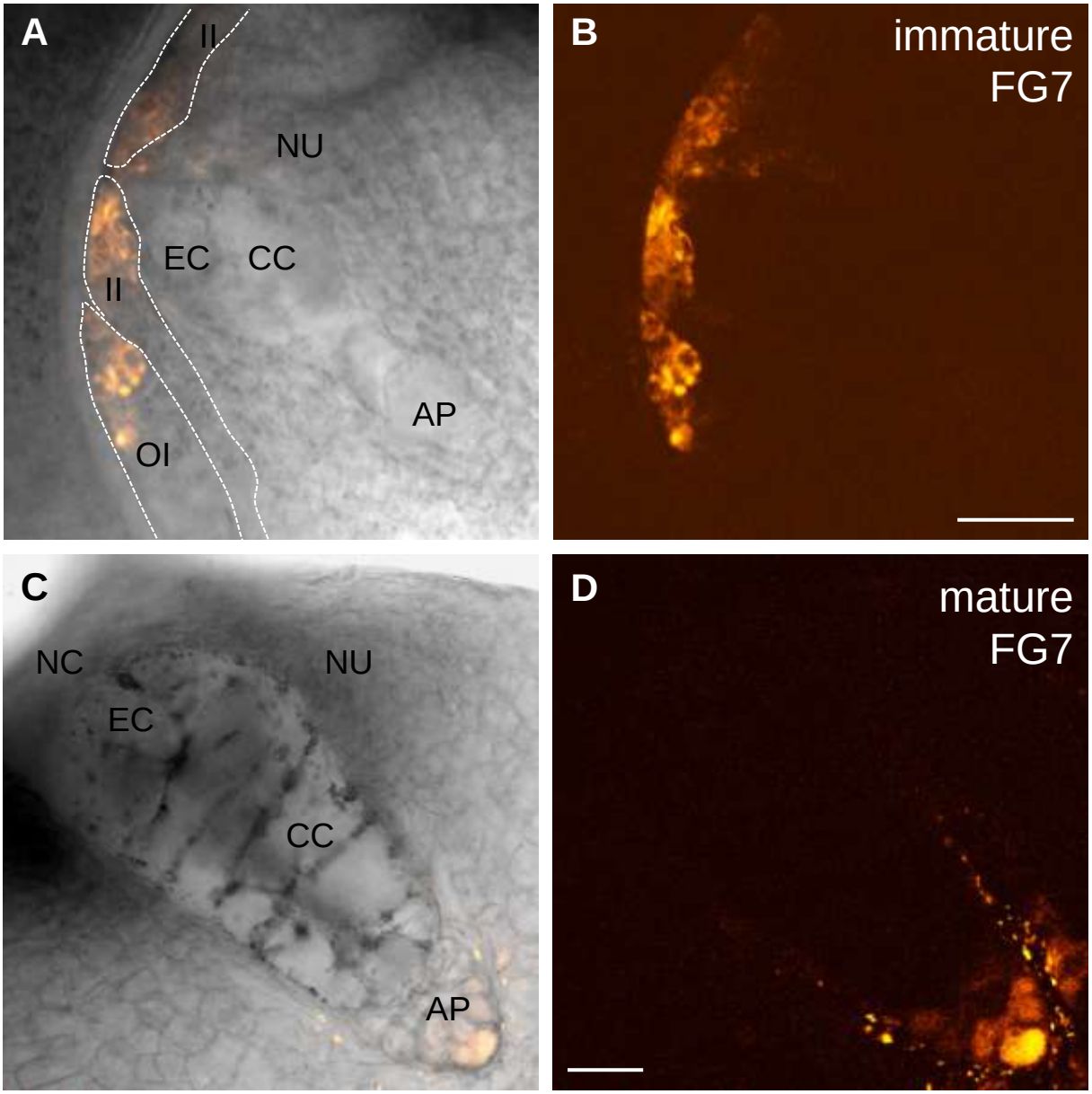

Fig. S13. Auxin response in the micropylar tips of integuments and at the chalazal pole inside the mature female gametophyte of maize. Auxin response is indirectly visualized by the activity of the synthetic *DR5* promoter driving ER localized mRFP marker protein expression. (**A**) Early FG at stage FG7. Antipodals start to proliferate. Strong mRFP signals signals are visible in the tips of the integuments (white dashed lines), but not in the micropylar nucellus cap. (**B**) Enhanced fluorescence image of (A) showing lack of mRFP signals inside the mature FG. (**C**) Mature FG. Integuments are removed. Strongest mRFP signal is visible in the antipodal cell most distant to the central cell. (**D**) Enhanced fluorescence image of (C) showing an mRFP gradient inside the antipodal cell cluster, with lowest signal in antipodal cells neighboring the central cell. (A and C) merged bright field and epifluorescent images. (B and D) Fluorescence images of (A) and (C), respectively. Abbreviations: AP: antipodal cells, CC: central cell, EC: egg cell, II: inner integument, NC: nucellar cap, NU: nucellus, OI: outer integument. Scale bars: 50 μm.

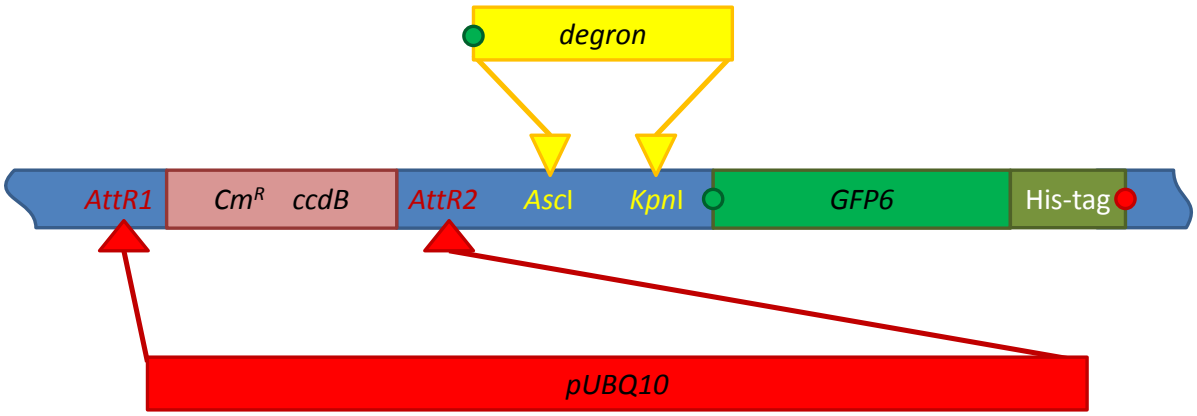

Fig. S14. Scheme of cloning of the pUBQ10::degron:GFP plasmid. The pUBQ10::degron:GFP plasmid was obtained in two steps. First, the pMDC111 (Curtis and Grossniklaus, 2003) destination vector was modified by inserting a sequence encoding the 6-amino acid long degron consensus core motif of domain II of AUX/IAA proteins, VGWPPV, between the AscI and KpnI restriction sites as a C-terminal in-frame fusion to GFP6-His-tag carried in the original vector. Subsequently, an entry clone carrying the 2.5 kb *Arabidopsis UBQ10* ubiquitin promoter was combined with the modified destination vector through a Gateway LR reaction.

Chapter 2. The role of auxin in the female gametophyte of *Arabidopsis thaliana* – a modelling approach

Dmytro S Lituiev, Ueli Grossniklaus, Barbara Hellriegel

Abstract

Background The dominating paradigm in plant growth and development regards the plant hormone auxin as a morphogen acting on the scale of tissues. During ovule development of *Arabidopsis thaliana*, however, auxin has been proposed to play a role in the patterning within the syncytial female gametophyte. This leaves unclear whether and how auxin metabolism and transport can be modified to scale auxin action down to the sub-cellular level.

Results We updated the existing morphogen reaction-diffusion model by explicitly accounting for boundary conditions and including transport processes. We found that under the conditions proposed earlier and with the rate of auxin diffusion, degradation and transport known from literature, one-dimensional models produce a very shallow gradient with concentration difference between the poles of about 1.4% of the highest one. Accounting for the large central vacuole in a two-dimensional model resulted in a steeper gradient to about 3.21%, which is still far shallower than of any other known morphogen of *Drosophila*. Sensitivity analysis shows that such shallow gradient cannot sustain any perturbation higher than 3.31%.

Conclusions Neither the existing conceptual model of auxin gradient formation, nor extended models accounting for spatial factors and transmembrane auxin fluxes can provide an adequately steep and robust auxin gradient necessary for immediate cell fate specification. This suggests that either the rates of auxin diffusion, metabolism, or transport within the female gametophyte differ dramatically from the known ones or the current conceptual model is incomplete.

Keywords: auxin, gradient, patterning, reaction-diffusion

2.1 Introduction

The female gametophyte, also called embryo sac, is a haploid female reproductive structure of higher plants enclosed into the diploid sporophytic tissue of the flower. It consists of a group of a few cells, usually seven, two synergids, one egg cell, one central cell formed by fusion of two polar nuclei, and three antipodals (Fig. 1). All these cells descend from a single cell, called functional megaspore, by means of three mitotic divisions followed by determination of the cell fate and formation of the cell membranes. Recently, the fate of the nuclei of the female gametophyte was suggested to be determined according to an intrinsic gradient of the plant hormone auxin, in a manner that is analogous to the way the cell fate is acquired in the syncytial *Drosophila* embryo. Moreover, the mechanisms suggested for auxin gradient formation are thought to be similar to those described for the *Drosophila* Bicoid (Bcd) morphogen. The Bcd gradient has been the subject of a number of modelling studies, which led to a deeper understanding of the processes maintaining it. They also led to interesting new questions, for example related to possible mechanisms allowing gradient scaling in different species and to the robustness of the patterning process and its result (reviewed in (Grimm et al., 2010)). Analogously, an array of models describing reaction-transport-diffusion processes of auxin at the tissues level has been developed (reviewed in (Krupinski and Jönsson, 2010)), which together with experimental data demonstrate the role of auxin as a morphogen acting on the scale of tissues. It remains, however, unclear which conditions can allow auxin to form a gradient at the narrow spatial scale of single cells.

Therefore, we developed a mathematical model that aims to explain the formation of the proposed gradient of auxin in the female gametophyte syncytium. To this end we had to refine the existing Bcd models to include the processes and conditions characteristic for the female gametophyte and for auxin. First, we had to re-specify the simplified boundary conditions of the Bcd reaction-diffusion models which assume that the morphogen diffuses in a semi-infinite domain. For Bcd this simplification is justified by specific parameter values leading to a fast drop of the Bcd concentration and thus to a short characteristic diffusion-decay length scale of the morphogen. For auxin we had to reject this simplification as the characteristic decay length is quite long relative to the size of the female gametophyte. As auxin diffusion takes place in a confined cell our model explicitly states conditions for its boundaries. Additionally, we allow for localized synthesis of auxin, rather than using the localized influx or its aproximation as 'point source' synthesis of analogous Bcd models (reviewed in (Grimm et al., 2010)), and we account for the efflux of auxin and the possibility of its localized degradation. In order to explore how observed patterns can be explained we first study five combinations of these factors in a one dimensional model and then simulate the two most realistic scenarios in two dimensions. The latter allows

us to account for important geometrical features of the female gametophyte such as the large vacuole.

Under the above assumptions and using parameter values collected from the literature our one-dimensional models produced only very shallow auxin gradients. The extension to two dimensions, e.g. accounting for the vacuole, generated gradients of slightly increased steepness. However, even these slightly higher gradients are too sentitive to perturbations to guarantee the necessary robustness of cell specification and can, therefore, not be sufficient alone for cell fate determination in the female gametophyte.

2.2 Model formulation

Experimental evidence (Pagnussat et al., 2009) suggests that there are at least two regimes of auxin metabolism in the female gametophyte involving influx and efflux carrier proteins. First, during the functional megaspore stage (FG1) auxin is delivered from the sporophytic epidermal tissue at the anterior (micropylar) pole of the ovule primordium due to PIN-FORMED 1 (PIN1) auxin efflux carrier activity there. Later, when the PIN1 protein cannot be detected in the adjacent sporophytic tissues anymore, the YUCCA1 (YUC1) auxin biosynthesis enzyme was detected in the micropylar part of the female gametophyte at the transcriptional level. This suggests that localized auxin production may be involved in the gradient formation. As we showed earlier (Lituiev et al., 2013), an auxin efflux carrier, the ABC transporter 1 (ABCB1), alternatively known as P-glycoprotein 1 (PGP1), and the AUXIN RESISTANT 1 (AUX1) influx carrier are expressed within the female gametophyte. Therefore, we studied several sub-models (afterwards called 'regimes', see table 1) in order to address the influence of the combination of these factors on the formation of the proposed auxin gradient.

2.2.1 General assumptions

As degradation is known to be important to achieve a stable gradient (steady-state) profile with reasonable steepness, we combine the auxin synthesis and influx described by Pagnussat et al.(Pagnussat et al., 2009) with an auxin degradation process (conceptually equivalent to irreversible conjugation). More specifically, we assume that auxin degradation can be described as exponential decay, i.e. that it follows first order kinetics as it has been observed experimentally within a physiological range of concentrations (Ljung et al., 2001) and up to 400 μM (Sequeira and Mineo, 1966).

As the model is linear in the concentration of auxin, it is also linear in the term describing auxin supply. Thus, the specific rate of auxin synthesis will only change the concentration of auxin as a multiplier and will not affect the shape of the gradient. Therefore, the model

does not require the consideration of any specific auxin synthesis rate.

This leads us to a partial differential equation for the relative concentration of auxin $u = u(x,t)$ in the point x at time t (both position and time are expressed in non-dimensional units, with x varying from 0 to 1; see supplement, section A2.1). The corresponding physical concentration can be calculated as the product of the average concentration of auxin in the female gametophyte and unitless concentration $u(x,t)$. The rate of concentration change can then be described as

$$\underbrace{\frac{\partial u}{\partial t}}_{\text{rate of auxin change}} = \underbrace{\nabla^2 u}_{\text{diffusion}} \underbrace{- a \cdot h(x) \cdot u}_{\text{degradation}} + \underbrace{a \cdot f(x,t)}_{\text{synthesis}} \tag{2.1}$$

with different boundary conditions describing transmembrane fluxes and different functions describing spatial inhomogeneity of degradation (h) and synthesis (f) depending on the regime. Here $\nabla^2 u$ represents the contribution of diffusion to the rate of concentration change, and a is the re-scaled auxin degradation rate:

$$a = \hat{a} \cdot \frac{L^2}{D} \tag{2.2}$$

where D is the diffusion constant, $\hat{a}$ is the degradation rate, L is the embryo sac length. The boundary conditions are specified for the gradient ($\nabla u|_{\text{boundary}}$) in one-dimensional models (Table 1); in two dimensional models the fluxes through the membranes are specified, and for the boundary of the system whether zero-flux ($\nabla u = 0$) or a constant concentration is set (see Fig 1).

2.2.2 Regime 1: External auxin source (influx)

Regime 1 includes the processes described by Pagnussat et al. (Pagnussat et al., 2009) for an early stage (FG1) of female gametophyte development, when auxin is delivered into the female gametophyte by polarized transport. The non-dimensional form of the equation presented in Table 1 depends on only one parameter grouping, the rescaled degradation rate a or, expressed alternatively, the unitless characteristic scale $\ell = \lambda/L = a^{-1/2}$.

2.2.3 Regime 2: Localized synthesis of auxin

Regime 2 is based on empirical data for later stages of female gametophyte development (beginning at FG3), when auxin is synthetized within the female gametophyte. In the synthesis term presented in Table 1, we define the relative distribution of auxin synthesis $f = f(x,t)$ so that $\int_0^1 f(x,t)\,dx = 1$.

We define the synthesis function $f(x)$ (see Table 1), assuming that local synthesis occurs

with a constant rate between the membrane and some point x_0 in the micropylar part and does not occur in the rest of the female gametophyte. Accounting for mass conservation, we define the synthesis function as $f(x) = {x_0}^{-1} \cdot \mathrm{H}(x_0 - x)$, where $\mathrm{H}(x)$ is the Heaviside step function.

2.2.4 Regime 3: Localized degradation of auxin

Regime 3 is based on the conjecture about the localized expression of auxin degrading enzymes at the posterior (chalazal) pole (Pagnussat et al., 2009) [p.1688]. Specifically, we assume that localized degradation is mediated by an enzyme which is absent in the micropylar part, but is uniformly distributed in the chalazal part beginning at some position x_0. The rate of localized degradation is estimated based on the assumption that the total concentration of the enzyme in case of localized degradation would be the same as with uniform degradation, i.e. we vary only the localization but not the total amount of the enzyme. This leads to a degradation function $h(x) = (1 - x_0)^{-1} \cdot \mathrm{H}(x - x_0)$.

2.2.5 Regime 4: Efflux of auxin

Regime 4 combines processes of regime 1 with a background efflux of auxin. Here, the efflux is expressed as the boundary condition. We assume first order kinetics. In the boundary condition given in table 1, the unitless efflux rate is obtained as $q = \hat{q} \cdot L/D$, where $\hat{q}$ is the efflux rate in physical units, e.g. m/s.

2.2.6 Regime 5: Auxin re-distribution by transmembrane fluxes

As in one dimension, influx serves purely as a source of the morphogen and the model is uniformly linearly dependent on it, one can arbitrarily chose its value. However, in two dimensions (2D) when the female gametophyte is considered in its extracellular context (apoplast), the influx controls the re-distribution of auxin within the system. Therefore in 2D we explicitly account for transmembrane fluxes between the apoplast, cytoplasm, and vacuole. The intracellular fluxes are assumed to be transporter-independent, as no intracellular transporter has been found in the female gametophyte. As before, we assume first order kinetics here. For the fluxes through the plasma membrane, we account for the auxin transporter contribution as described below.

2.2.7 Approximation of female gametophyte geometry in two dimensions

One way to make the model more realistic is to account for the large central vacuole which appears at the late two-nuclear stage and to study its possible influence on the

auxin distribution. In principal this would require a three-dimensional model. As we are, however, interested in the processes occurring during the FG5–6 stages, we can exploit the cylindrical symmetry of the female gametophyte and project its ellipsoidal shape into two dimensions as presented in Figure 1.

The main geometrical feature of the two-dimensional model, the central vacuole, splits the cytoplasmic content into two parts, micropylar and chalazal, leaving only a narrow region of cytoplasm near the plasma membrane connecting them. We parametrized the geometry using the width of the cytoplasmic isthmus (Δy_{vac}), which has a thickness of the order of 1 µm (Lituiev et al., 2013). Further we assumed the thickness of the ellipsoid (B) to be 2/5 of its length, and the vacuole length (r_{vac}) to comprise 2/3 of the length of the female gametophyte. The resulting list of parameters needed for the two-dimensional model is given in Table 4.

2.2.8 Measure of the gradient steepness

Classically, the characteristic length scale $\lambda = \sqrt{D/\hat{a}}$ is used to describe the steepness of the gradient (Lander et al., 2009). In the simplest morphogen diffusion models, where it is much smaller than the length of the domain of interest, $\lambda \ll L$, λ represents the distance from the point source in which the concentration drops to 37% of its initial value. In the case considered here, however, due to the long λ values and due to the effect of the boundary conditions, the values of λ do not have the same meaning and are, therefore, not comparable (see Fig. 2). This asks for an alternative metric for profile steepness. One possible metric is the logarithmic gradient, which has a constant value for the classical exponential model. It still changes, however, in the case considered here (see fig. 2). Therefore, we define the relative concentration change θ (further referred to as 'gradient steepness') as a quotient where the concentration change over the domain is divided by the maximal concentration:

$$\theta = \frac{u_{max} - u_{min}}{u_{max}} \equiv 1 - \frac{u_{min}}{u_{max}}$$

2.3 Analytical and numerical results

2.3.1 Parameter values

In order to simulate our models we compiled parameter values from the literature. A summary of the parameter values is given in Tables 2 and 3. Further we discuss the derivation of parameter values and experimental conditions used in the underlying literature.

2.3.1.1 Characteristic length scale of diffusion-decay, diffusion and degradations rates

In order to study the steepness of the concentration profile in a setting that is as realistic as possible, we collected values of input parameters from the literature.

During its development, the *Arabidopsis* syncytial female gametophyte increases in length from 20 µm to approximately 70 µm (Schneitz et al., 1995). Cell fate determination occurs before cellularization, when the female gametophyte length is typically under 70 µm. The diffusion rate of auxin is estimated as $7 \cdot 10^{-10}$ (Gutknecht and Walter, 1980), $6 \cdot 10^{-10}$ (Mitchison, 1980), and $3 \cdot 10^{-10}$ m^2/s (Laskowski et al., 2008). Inhomogeneity of cytoplasm can reduce the diffusion rate, while the cytoplasmic streaming can increase its effective value. In our model we used the value of $6 \cdot 10^{-10}$ m^2/s. Auxin degradation rates show a dramatic discrepancy between different studies spanning six orders of magnitude (see Table **5**). Such a divergence could be explained by a dependence of the degradation rate on environmental factors (Rapparini et al., 2002), or by idiosyncrasies of the objects studied. It is worth noting that the highest experimentally obtained value for the degradation rate that we found in the literature was close to the detection limit (Rapparini et al., 2002); thus, the highest possible degradation rate may not yet have been reported.

In Table **5** we present the values of degradation rates and half-lives measured or suggested in the literature, with corresponding values of a, λ, and θ calculated for $L = 70$ µm and the diffusion constant of $D = 6 \cdot 10^{-10}$ m^2/s. Therefore, from here forth we assume a characteristic length scale of diffusion-decay $\lambda = 562$ µm with $\ell = \lambda/L = 7.98$ corresponding to the fastest experimentally defined degradation rate of $1.93 \cdot 10^{-3}$ (Rapparini et al., 2002).

2.3.1.2 Transmembrane flux rates

Auxin flux between the cell and the extracellular environment can occur both freely through the membrane and mediated by auxin carrier proteins. In the *Arabidopsis* female gametophyte, the influx carrier AUX1 and the efflux carrier ABCB1 (PGP1) have been shown to be expressed (Lituiev et al., 2013). According to the chemiosmotic hypothesis (Rubery and Sheldrake, 1974), free cross-membrane diffusion of auxin enables mainly its influx into the cell, while the efflux strongly depends on efflux carriers. A detailed description of the extended model of carrier-independent transport used to estimate parameter values from literature is given in the supplementary material, sections A2.2 and A2.4.

Three experimental data sets are available, allowing us to estimate the background and carrier-mediated flux rates. The rates taken or estimated from literature are presented in Table **6**. One can see that two studies on protoplasts agree in the value of the net efflux rate of $1.4 \cdot 10^{-8}$ (estimated from (Geisler et al., 2005)) to $1.7 \cdot 10^{-8}$ (Hošek et al., 2012)

m/s. As the female gametophyte shows only ABCB1 but not ABCB19 expression, we use the value of efflux rate estimated from experiments with *pgp19* protoplasts (Geisler et al., 2005). However, as due to the experimental setup in (Geisler et al., 2005) the estimate of the influx rate can be less accurate, we use value of $2.35{\cdot}10^{-4}$ m/s from (Hošek et al., 2012).

Based on the chemiosmotic hypothesis and assuming impermeability of the membrane to ionized auxin (IAA^-) and very fast dissociation rate(Chavarría-Krauser and Ptashnyk, 2010), the rate of background efflux can be connected to the permeability to protonized (IAAH) auxin (q_{IAAH}) as $q_{\mathrm{background}} = q_{\mathrm{IAAH}} \cdot 10^{pK_a - pH}$. In this manner, we estimate the flux rates between the cytoplasm and vacuole in the two-dimensional model.

Active auxin influx is considered to be of less importance for plant morphogenesis than auxin efflux, because background influx of the protonated form of auxin is quite high. However, it plays a significant role in responses to environmental stimuli (Swarup and Péret, 2012). We found AUX1 to be expressed in the *Arabidopsis* female gametophyte starting at the four-nucleate stage (FG4), with a higher protein level in the anterior (micropylar) part (Lituiev et al., 2013). Active auxin influx has been estimated to contribute up to 75% (Delbarre et al., 1996) of total auxin influx, with AUX1 contributing about 50% (Marchant et al., 1999), the value was considered in our models.

2.3.2 Analytical solution in one dimension

Based on previous data indicating that the largest variation in auxin concentration is observed along the micropylar-chalazal axis (Pagnussat et al., 2009), we first studied the most simple, one-dimensional model featuring spatial inhomogeneity of the processes along this axis.

As the steady-state is reached during the first hour (see Fig. **10** in the supplementary material) whereas the development of the female gametophyte lasts nearly two days, we focused on the steady state profiles of the auxin concentration. By this means the partial differential equations are reduced to ordinary differential equations with the independent variable being the spatial coordinate x. The analytical solution of the problem can be found using Fourier analysis and the method of Green's functions. Analytical steady-state solutions for equation (2.1) with conditions specified in Table **1** are presented in the Table **7**.

When parameterizing the analytical solutions with the parameter values from the literature, very shallow concentration profiles are obtained (see Fig. **4**). Under regime 1, a steepness θ of only 0.783% is reached, i.e. the concentration drops down maximally by 0.783% of the value at the micropylar pole.

Assuming that localized synthesis occurs in the first quarter of the female gametophyte,

the gradient steepness reaches values of 0.588%. As can be expected intuitively, the solution of the model under regime 2 indicates that the steady state concentration profile is steeper when the source is localized more polarly (see Fig. **3**A). Moreover, regime 1 corresponds to the limiting case of regime 2, and thus point-localized synthesis is equivalent to the influx.

Analogously, assuming that the localized degradation occurs in the last quarter of the female gametophyte, a higher gradient steepness of 1.361% can be reached. In contrast to localized synthesis, the effect of localized degradation on the gradient steepness depends on the value of the degradation rate itself. For slow degradation rates $a < 2$ (which encompasses the physiological range of the parameter, see section 2.3.1), the more polar the degradation subdomain is localized, the steeper is the gradient (Fig. **3**). For faster rates, the polar localization of the degradation subdomain decreases the gradient steepness.

Using regime 4 in one dimension under the assumption that the auxin concentration outside of the cell is zero (i.e. with very fast auxin removal), we obtain a gradient steepness of 0.911%. Generally in regime 4, with a large λ as it is characterstic for our system (see below), the influence of diffusion and degradation is much smaller than that of auxin flux. Therefore, it is useful to consider the behaviour of the solution and the gradient steepness for $\lambda \to \infty$:

$$u_{\ell\to\infty}(x,q) = 1 + \frac{q}{q+2}\,(1-2\,x) + \mathcal{O}\left(\ell^{-2}\right); \qquad \theta_{\ell\to\infty} = \frac{q}{q+1} + \mathcal{O}\left(\ell^{-2}\right) \tag{2.3}$$

Dependance of the gradient steepness with the estimated (see section 2.3.1) and infinitely large λ on the efflux rate in is shown in Fig. **3**B.

2.3.3 Numerical simulation of two-dimensional model

As we have shown above, using values from the literature to parametrize the solution of the one-dimensional transport-reaction-diffusion equation results in gradients of rather shallow steepness. Geometrical features of the diffusion domain not described by this one-dimensional model could, however, significantly influence mass transfer and thus also gradient formation. Especially, a large vacuole separating the nuclei at each pole from the two-nuclear stage (FG2) onwards, by restricting the volume where diffusion occurs, could impede the transfer of auxin.

In order to assess the impact of the geometric features of the female gametophyte on diffusion, we approximated its shape by a volume contained between two concentric ellipsoids, the outer representing the cell membrane and the inner representing the central vacuole. Accounting for cylindrical symmetry, we study diffusion in a two-dimensional section of this domain (see Fig. **1**). The values of geometrical parameters shown in Fig. **1**

are given in Table 4 in the supplementary material.

The two-dimensional model was solved numerically using the finite elements method in COMSOL Multiphysics 4.3a software (COMSOL Group, Stockholm, Sweden) and the obtained data were post-processed in MATLAB 2011b (MathWorks, Natick, USA).

As expected, the spatial confinement caused by the central vacuole impedes diffusive transport of auxin and results in a steeper gradient (see fig. 3B,C). For regime 1 with an isthmus width of 1 µm (Lituiev et al., 2013), θ reaches 2.49% (compared to 1.56% in the one-dimensional model).

However, the most dramatic deviation from the one-dimensional model is observed when auxin fluxes between the apoplast, cytoplasm and the vacuole are included (regime 5). The solution in two dimensions reaches a steepness of $\theta = 3.21\%$ (compared to $\theta = 0.91\%$ in one dimension). This could intuitively be explained by a pronounced boundary effect, the contribution of which is intensified within the long and narrow path between the vacuole and plasma membranes.

2.3.4 Error contributed by the quasi steady-state assumption

In order to simplify calculations, we have taken into account that the velocity of female gametophyte growth, approximately $3{\cdot}10^{-10}$ m/s, is slower than all other rates, namely the diffusion velocity ($\hat{q}_D = D/L = 8.6{\cdot}10^{-6}$ m/s) and the transport velocity, which are of the order of 10^{-8} m/s. Therefore, we assume that a calculation of the concentration in each moment can neglect the fact that these processes take place in a growing organism. Here we estimate the error this will cause in our analyses.

The full dynamical model can be described in the following way. Given linear growth of the female gametophyte, i.e. with $L(t) = L_0\,(1 + w\,t)$ for an initial length of $L_0 = 20\,\mu\text{m}$ and a final length of $L_{\max} = 70$ µm, one can estimate the rescaled growth rate as:

$$w = \frac{\tau_0}{\hat{t}_{\max}} \cdot \frac{L(\hat{t}_{\max}) - L_0}{L_0} \tag{2.4}$$

with $\tau_0 = L_0^2/D$. For given D, L_0, and the growth time $\hat{t}_{\max}$ of 48 hours, this results in the unitless growth rate of $w = 1.157{\cdot}10^{-5}$. Further, equation (2.1) for regime 1 can be reformulated:

$$\frac{1}{\lambda_0^2}\frac{\partial u}{\partial t} = \frac{1}{\lambda^2(t)}\nabla^2 u - u \tag{2.5}$$

Additionally, we estimated the error resulting from this assumption by comparing the quasi steady-state (QSS) solution to the truly dynamic solution (equation 2.5). As one can see in figure 5, the mean root-square error for the QSS solution in regime 1 in one dimension does not exceed 0.01% of the maximal concentration. For regime 4 in two

dimensions the error is higher and reaches up to approximately 0.8% of the maximal concentration.

2.3.5 Sensitivity analysis

Environmental factors as well as intrinsic stochasticity of the biochemical processes contribute to the noise corrupting the positional information provided by the morphogen gradients. Therefore, robustness is regarded as a crucial property of the patterning mechanisms in developmental biology. In order to assess the robustness of the proposed auxin-dependent patterning mechanism, we apply a sensitivity analysis.

In the context of patterning, sensitivity can be thought of as a shift of positions of a morphogenic boundary in response to perturbations in parameter values. Namely the shift of the boundary caused by a change in the local concentration, which in turn depends on a relative shift in a parameter value. For a small perturbation, an analytical expression based on the Taylor expansion can be applied (Lachapelle and Bergmann, 2010):

$$\begin{aligned} \frac{\Delta u}{u_0} &\approx \frac{\partial \ln u}{\partial x} \cdot \Delta x + \frac{\partial \ln u}{\partial \ln \alpha} \cdot \frac{\Delta \alpha}{\alpha_0} \\ &= \epsilon_{u \to x}^{-1} \cdot \Delta x + \epsilon_{\alpha \to u} \cdot \frac{\Delta \alpha}{\alpha_0} \end{aligned} \tag{2.6}$$

where u_0 is the local concentration, Δu is a change in the concentration, Δx is a shift in position, α_0 is the initial value of a model parameter and $\Delta\alpha$ is a perturbation in it.

For the ease of interpretation, it is convenient to split the sensitivity of the threshold position into two multiplicative parts: (1) the sensitivity $\epsilon_{\alpha \to u}$ of the local morphogen concentration to the change in a parameter value (for a given position, $\Delta x := 0$) and (2) the sensitivity $\epsilon_{u \to x}$ of the morphogenic boundary position to the change in the local morphogen concentration (assuming the boundary shifts to the position where the concentration becomes the same as it was in the initial position before perturbation, $\Delta u := 0$). Then the shift in the morphogenic boundary Δx in response to a relative perturbation in the parameter value $\Delta\alpha/\alpha_0$ can be estimated as:

$$\Delta x = \epsilon_{u \to x} \cdot \epsilon_{\alpha \to u} \cdot \frac{\Delta \alpha}{\alpha_0} \tag{2.7}$$

As the governing partial differential equation is linear, any change in the source intensity will result in the proportional change in the local concentration with $\epsilon_{\text{source} \to u} = 1$. This provides a comprehensive interpretation of the first component ($\epsilon_{u \to x}$) as a shift of a morphogenic boundary in response to a perturbation in a source term. In particular, for a small perturbation in the source term, the local $\epsilon_{u \to x}(x_0)$ is inversely proportional to the

local gradient of the concentration (Lachapelle and Bergmann, 2010):

$$\epsilon_{u\to x} \approx u_0 \cdot \left(\left. \frac{\partial u}{\partial x} \right|_{x_0} \right)^{-1} \tag{2.8}$$

where $\epsilon_{u\to x}$ is the sensitivity of the threshold position to the perturbation in the local concentration value u_0 defining the developmental position x_0.

As in the female gametophyte, in contrast to *Drosophila*, the number of nuclei is small, the precise location of the thresholds is hard to establish experimentally. Therefore, we study the sensitivity by applying a series of perturbations to a densely spaced set of points on the whole domain (Fig. **6**). In Fig. **6** one can see that an up-regulation of the source by only 3.31% is sufficient to displace any morphogenic threshold out of the micropylar boundary (Fig. **6**). Analytically the mentioned highest permissible perturbation can be found in the following way. Assume such a perturbation δ^+ in the source term that brings the initial concentration at the micropylar pole u_0 to $u_0 \cdot (1+\delta^+)$ and the concentration in the chalazal pole from u_1 to $u_1 \cdot (1+\delta^+)$. Now notice that if the new concentration at the chalazal pole exceeds the initial concentration at the micropylar pole, all hypothetical threshold concentrations in the initial range $(u_0; u_1)$ cannot be attained within the domain. One can see that this is the case if $u_1 \cdot (1+\delta^+) \geq u_0$, which gives the expression for the perturbation corrupting patterning in any point within the domain:

$$\delta^+ \geq \frac{u_0 - u_1}{u_1} = \frac{\theta}{1-\theta} \tag{2.9}$$

In an analogous manner, for a down-regulation in the source term, the maximal permissible perturbation δ^- reducing the u_0 to $u_0 \cdot (1-\delta^-)$ can be shown to be less than θ. This means, the range of permissible perturbations lies in the interval $\left(-\theta, \frac{\theta}{1-\theta}\right)$.

The sensitivity of the local concentrations to the shift in the parameter values has been further analysed for all model parameters with a perturbation of 1% of the value (Fig. **7**). Apart from the source term mentioned above, the local auxin concentration appears to be most sensitive to the changes in the female gametophyte length ($\max|\epsilon_{L\to u}| = 3.99 \cdot 10^{-2}$), cytoplasmic pH ($\max|\epsilon_{pH\mathrm{cyt}\to u}| = 3.11 \cdot 10^{-2}$) the length of the vacuole ($\max|\epsilon_{r\mathrm{vac}\to u}| = 2.97 \cdot 10^{-2}$), and diffusion rate ($\max|\epsilon_{D\to u}| = 2.98 \cdot 10^{-2}$).

In summary, the auxin gradient obtained with known, realistic parameters is very sensitive to variation in the auxin source and, thus, would make cell specification highly unreliable. This may suggest either that the parameters known from literature dramatically differ from those realized in the female gametophyte (i.e. the diffusion is slower, degradation or transport rates are higher), that some yet unknown processes might increase the gradient steepness, or that the auxin gradient alone cannot supply sufficiently robust positional information for patterning within female gametophyte.

2.4 Discussion

Here, we described a model for the formation of a morphogen gradient in the plant female gametophyte. Even though the system is analogous to the *Drosophila* egg, which also develops as a multi-nuclear cell (syncitium), the plant female gametophyte has different physiological features. First, in contrast to the *Drosophila* egg, the plant female gametophyte is included in the context of maternal sporophytic tissue and is functionally connected to it, i.e. the flow of a potentially morphogenic substance (auxin) can occur between them. Second, the proposed morphogenic substance displayed a characteristic length scale of diffusion-decay. As a consequence, we showed that, under currently known physiological parameters, in both the one- and the two-dimensional model the boundary conditions significantly influence the behaviour of the system and thus need to be accounted for. Our preliminary tests with the known parameters (Fig. **2**) showed that these two facts make the consideration of the boundary conditions essential. Consequently, we included these factors explicitly into our model. Third, in contrast to the *Drosophila* egg, the *Arabidopsis* female gametophyte grows during its development. Therefore we additionally studied the influence of growth on the gradient formation. We found that as long as the degradation-diffusion and transport velocities are much faster than the growth rate, the latter can be neglected. Additionally, we included localized synthesis and degradation, which earlier have been proposed to occur in the female gametophyte.

As the model in one dimension produced solutions with a very shallow gradient only, we implemented our model in 2D geometry. With the parameters used here, found that the large vacuole in the female gametophyte can impede the diffusive auxin transport and increase the gradient steepness θ up to about 3.4-fold.

Simulations show that even under the most beneficial parameters and assumptions, the concentration of auxin drops from one end of the female gametophyte to the other only by 3.21% in *Arabidopsis*. Studying the sensitivity of the obtained gradient, we found that the robustness of cell specification is compromised, especially due to the fluctuations of intensity of the auxin source. Namely, a change in auxin supply rate of only 3.31% will make impossible cell differentiation in whole FG. In contrast in *Drosophila*, the correspondent variations of about 10% are considered for Bcd gradient (Gregor et al., 2005). Therefore, we conclude that the factors studied do not allow the production of a sufficiently steep auxin gradient that would provide enough positional information for cell specification in the female gametophyte.

The gradient steepness obtained in this study is much lower than, the steepness of the Bcd gradient in *Drosophila*, which is more than 90% (Gregor et al., 2005; He et al., 2010). Whereas the degradation rates for *Drosophila* Bcd and auxin are similar, the developmental domain is about 10 times longer in *Drosophila* and the diffusion rate is about 120 times

slower (Lachapelle and Bergmann, 2010). This translates into a characteristic length scale to domain length ratio $\ell = \lambda/L$ of 0.17 for Bcd in *Drosophila* compared to 7.89 for auxin in *Arabidopsis*. Even though the cross-membrane transport process in *Arabidopsis* could make the gradient steeper, it is still not comparable to the gradient in the *Drosophila* egg.

Therefore, even the addition of spatial factors and transport processes to the conceptual model proposed in (Pagnussat et al., 2009) does not allow formation of an auxin gradient sufficiently reliable to serve as a morphogen. Thus the patterning mechanisms in the female gametophyte remain to be clarified. One clue arising from this study is that it is more probably a macro-molecular compound having a lower diffusivity. Alternatively a mechanism irreversibly amplifying the tiny asymmetry in auxin concentration such as the wave-pinning mechanism (Mori et al., 2008) can be hypothesized.

Competing interests

The authors declare that they have no competing interests.

Author's contributions

UG designed the project and critically revised the manuscript, DSL developed and analysed the model and wrote the manuscript, BH provided expertise in modelling and critically revised the manuscript.

Acknowledgements

We thank Pierre Barbier de Reuille (University of Berne), Quy Ai Ngo (University of Zürich) , Enrico Martinoia (University of Zürich) and Markus Geisler (Université de Fribourg) for useful discussion. This work was supported by the Universities of Zürich and Regensburg, an iPhD Project of SystemsX.ch, the Swiss Initiative in Systems Biology.

Figures

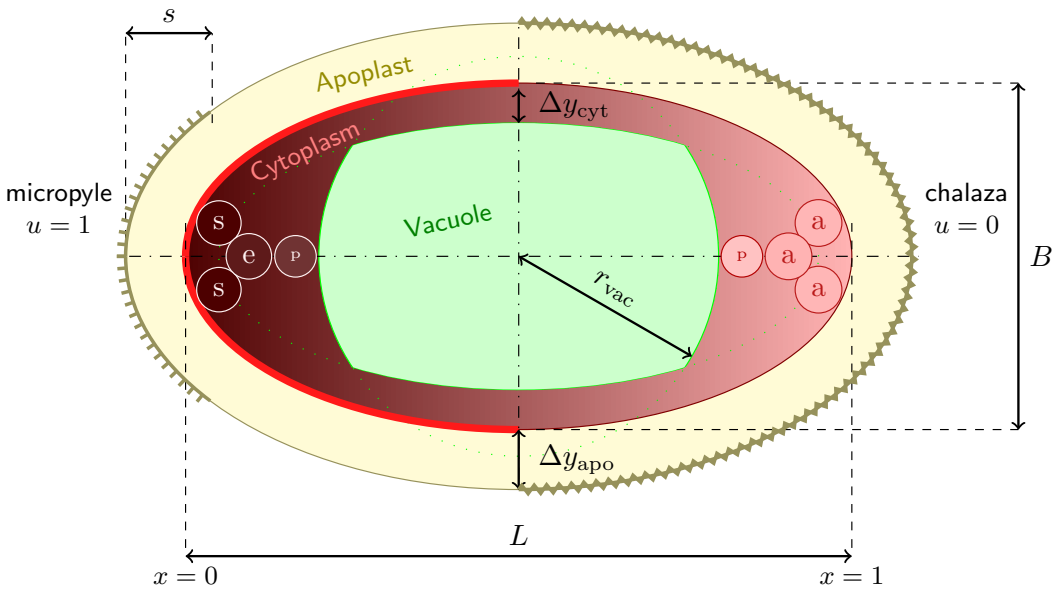

Figure 1: **A scheme of the female gametophyte showing features and geometrical parameters used in the simulations.** An auxin gradient which has been proposed to determine the fate of gametophytic nuclei to specify the synergid nuclei (s), egg nucleus (e), polar nuclei (p), and antipodal nuclei (a) with decreasing concentrations along the micropylar-chalazal axis is indicated. The long axis of the female gametophyte from the micropylar ($x = 0$) to the chalazal pole ($x = 1$) is aligned along the x-axis in all models. The zone of the auxin influx is shown in the dark yellow pin-lining. The zone where the concentration was set to zero is shown in dark yellow zigzag-lining. The zone of the membrane where AUX1 was assumed to be expressed five times higher than in the rest is shown in thick dark red line. Not all proportions are preserved. The description and values of geometric parameters are given in text and in Table 4

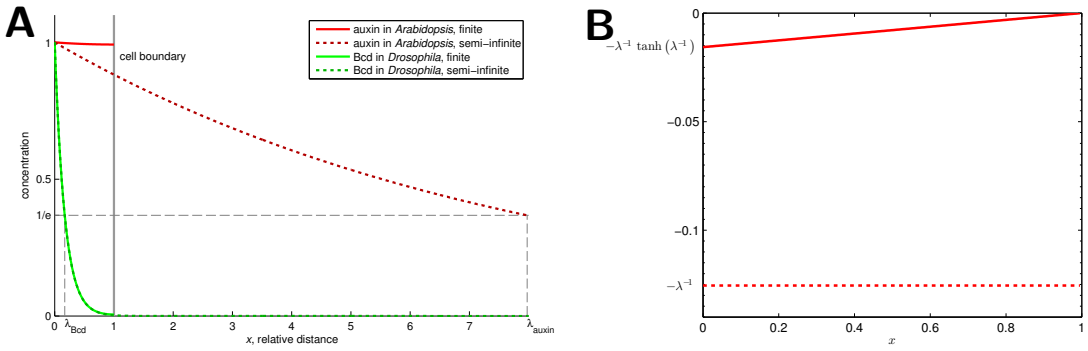

Figure **2**: **The concentration profile of the morphogen gradient strongly depends on the boundary condition at the distal (chalazal) pole under long characteristic scale of diffusion-decay λ. A** Profile of the morphogen concentration for the classical model for morphogen diffusion in the semi-confined domain (dashed lines) and the model with a confined domain proposed here (regime 1, continuous lines) with $\ell = \lambda/L = 7.98$ (red lines) and $\ell = 0.17$ as in *Drosophila* Bcd gradient (green lines). The length is shown in rescaled units, such that the domain length is equal one. The λ in this case represents the distance on which the the concentration falls to e^{-1}, which is around 37%. **B** In the classical model the logarithmic gradient of the concentration is constant, $\frac{d \ln u}{dx} = -\frac{1}{\ell}$. In contrast in the regime 1, the absolute value of the logarithmic gradient is lower, $\frac{d \ln u}{dx} = -\frac{1}{\ell} \cdot \tanh \frac{1-x}{\ell}$, and falls towards the posterior pole.

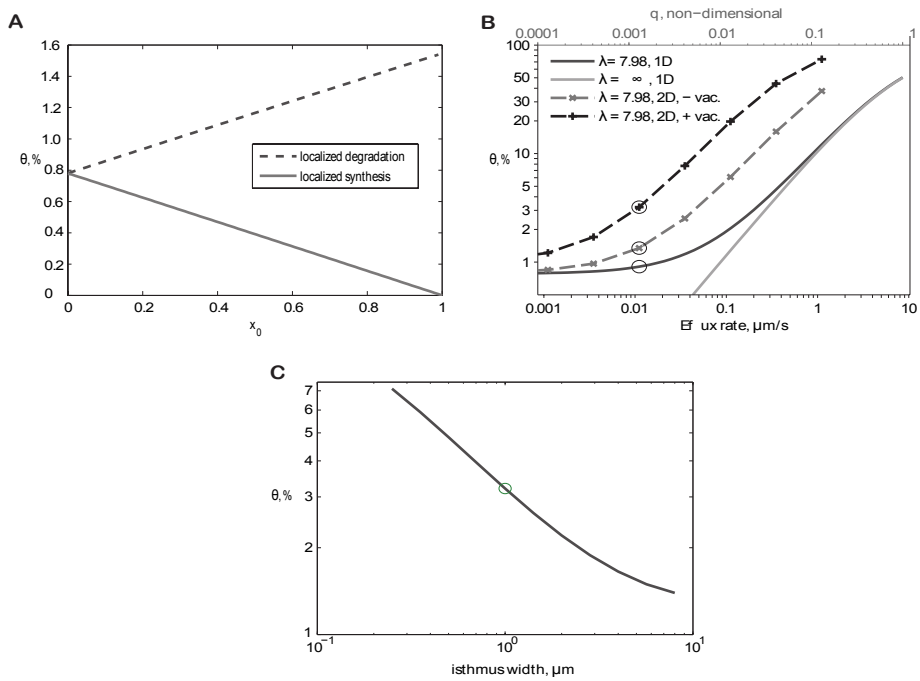

Figure **3**: **Dependence of gradient steepness θ on the model parameters.** **A** Dependence of θ on the localization of the auxin synthesizing enzymes (x_0) in regime 2 and on the localization of degradation enzymes (x_0) in regime 3 with $\ell = 7.98$, assuming the corresponding enzymes are localized in a step-wise manner (see text for details) **B** Dependence of the gradient steepness θ on background efflux rate q. The actual rates are indicated by circles. **C** Dependence of θ on the width of the cytoplasmic isthmus.

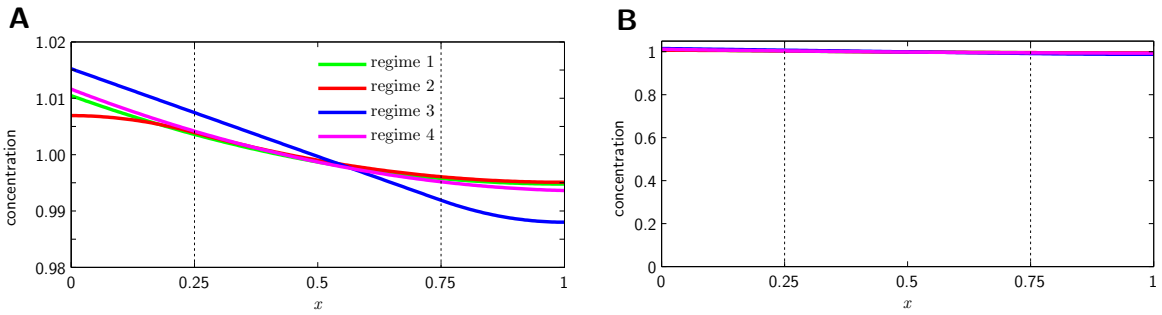

Figure **4**: **Concentration profiles for different regimes in one dimension.** The dotted lines indicate the boundaries of the domains of localized synthesis (left quarter) and degradation (right quarter)). In A, the concentration axis is scaled to emphesize the concentration differences. In B, the concentration axis begins with zero.

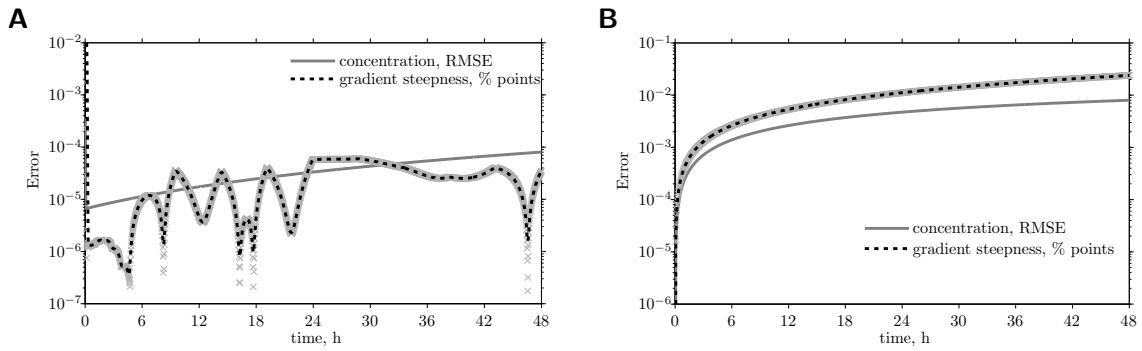

Figure 5: **The quasi-steady state assumption about growth leads to a negligibly small error.** A: Errors in the one-dimensional model. B: Errors in the two-dimensional model. The absolute value of difference between the gradient steepness found as quasi-steady state and dynamic solution expressed in percentage points (gray crosses, with black dotted line representing the smoothed data with a moving average filter with a window size of two hours) and the root mean-square error (RMSE) of the concentration values. The relative error tolerance of the ODE solver was set to 10^{-6}.

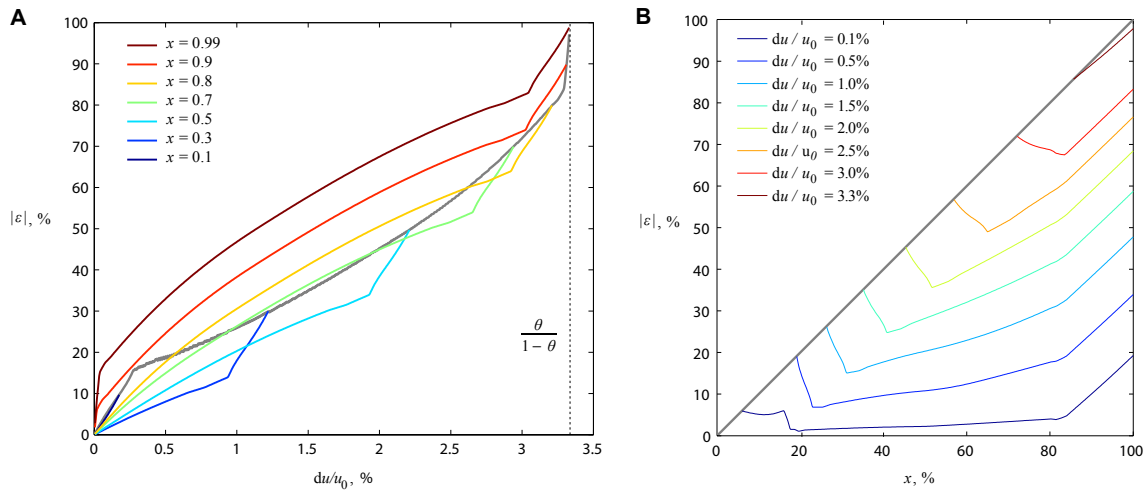

Figure 6: **The theoretically achievable auxin gradient is highly sensitive to the noise in auxin concentration.** The value of the sensitivity coefficient is shown, which corresponds to positional variability of the threshold position in response to a perturbation in the auxin concentration (equivalent to a perturbation in source intensity) in % of the female gametophyte length. A: Dependence of the sensitivity coefficient on the position of the threshold studied for a selected set of perturbation strength. The solid gray line corresponds to the line where the sensitivity coefficient ϵ (describing the shift of the threshold) equals to the location of the threshold; to the left of this line any perturbation leads to a shift of the position out of the studied domain, therefore no ϵ is defined there. B: Dependence of the sensitivity coefficient on the perturbation strength is shown for a selected set of x-positions. The solid gray line corresponds to the gray line in the graph above. Note that the maximal permissible perturbation in the concentration, which leaves the threshold position within the domain, corresponds to a ratio of $\theta/(1-\theta)$.

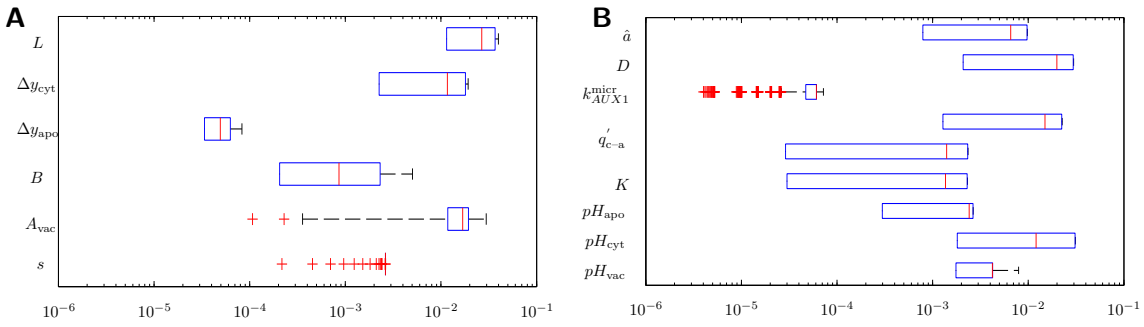

Figure **7**: **The range of the concentration sensitivity to the changes in the parameter values.** The sensitivity coefficient shows the change in the local concentrations caused by perturbation of 1% in the parameter values. A: Sensitivity to geometrical parameters. B: Sensitivity to rate and thermodynamic parameters.

Tables

Table **1**: Formulation of the sub-models

	Regime 1	Regime 2	Regime 3	Regime 4
Processes	Diffusion No synthesis Uniform degradation Influx at anterior pole No efflux	Diffusion *Localized synthesis* Uniform degradation *No influx* No efflux	Diffusion No synthesis *Localized degradation* Influx at anterior pole No efflux	Diffusion No synthesis Uniform degradation Influx at anterior pole *Efflux at posterior pole*
Degradation term	$-a \cdot u$	$-a \cdot u$	$-a \cdot h(x) \cdot u$	$-a \cdot u$
Synthesis term	0	$+a \cdot f(x,t)$	0	0
Left BC	$\nabla u\|_{x=0} = -a$	$\nabla u\|_{x=0} = 0$	$\nabla u\|_{x=0} = -a$	$\nabla u\|_{x=0} = -p$
Right BC	$\nabla u\|_{x=1} = 0$	$\nabla u\|_{x=1} = 0$	$\nabla u\|_{x=1} = 0$	$\nabla u\|_{x=1} = -q \cdot u$

Table **2**: Rate parameters

Abbreviation	Parameter	Value	Notes
L	length of the female gametophyte	$7.0 \cdot 10^{-5}$ m	
$\hat{a}$	degradation rate	$1.9 \cdot 10^{-3}$ s^{-1}	(Rapparini et al., 2002)
D	diffusion rate	$6.0 \cdot 10^{-10}$ m^2/s	(Mitchison, 1980)
λ	characteristic degradation-diffusion length scale	$5.6 \cdot 10^{-4}$ m	$\lambda = \sqrt{D/\hat{a}}$
$\hat{q}_D$	characteristic diffusion rate	$8.6 \cdot 10^{-6}$ m^2/s	$\hat{q}_D = D/L$
$\hat{q}$	net PGP1-dependent efflux rate	$1.1 \cdot 10^{-8}$ m/s	(Geisler et al., 2005)
$\hat{q}_{\text{apo–cyt}}$	net influx rate	$1.4 \cdot 10^{-6}$ m/s	(Hošek et al., 2012)
pH_{apo}	apoplastic pH	5.00	
pH_{cyt}	cytoplasmatic pH	7.60	(Chavarría-Krauser and Ptashnyk, 2010)
pH_{vac}	vacuolar pH	5.00	(Chavarría-Krauser and Ptashnyk, 2010)
pK_{d}	pH of IAA half-dissociation	4.75	(Chavarría-Krauser and Ptashnyk, 2010)
$\hat{q}_{\text{HA}}$	permeability to protonized auxin	$4.8{\cdot}10^{-6}$ m/s	(Geisler et al., 2005)

Table **3**: Key rescaled rate parameters

Abbreviation	Parameter	Value	Notes
a	rescaled degradation rate	0.0315	
ℓ	rescaled characteristic length scale	7.98	$\ell = \lambda/L = a^{-1/2}$
q	net PGP1-dependent efflux rate	$1.30{\cdot}10^{-3}$	$q = \hat{q}/\hat{q}_D$
$q_{\text{apo–cyt}}$	net influx rate	0.163	$q_{\text{apo–cyt}} = \hat{q}_{\text{apo–cyt}}/\hat{q}_D$

Table **4**: Geometric parameters

Abbreviation	Value	Parameter
L	$7 \cdot 10^{-5}$ m	*A. thaliana* embryo sac length at FG5 stage
$\Delta\hat{x}$	$5{\cdot}10^{-9}$ m	membrane width
$\Delta\hat{y}_{\text{cyt}}$	$1{\cdot}10^{-6}$ m	width of cytoplasmic path around the vacuole
$\Delta\hat{y}_{\text{apo}}$	$5 \cdot 10^{-8}$ m	apoplast width
Δx	$\Delta\hat{x}/L$	rescaled membrane width
Δy_{cyt}	$\Delta\hat{y}_{\text{cyt}}/L$	rescaled width of cytoplasmic path around the vacuole
Δy_{apo}	$\Delta\hat{y}_{\text{apo}}/L$	rescaled apoplast width
B	$2/5L$	embryo sac width-to-length ratio
r_{vac}	$2/3L$	vacuole length
s	$1/10\ L$	source localization parameter

Table **5**: Values of degradation rate and corresponding gradient steepness at regime 1

Ref.	Object	Degradation rate, $\hat{a}$, s^{-1}	Half-life	a	λ/L	θ
(Sequeira and Mineo, 1966)	Tobacco leaf protoplasts	$5 \cdot 10^{-4}$	23 min	$4.08 \cdot 10^{-3}$	15.6	0.204%
(Ljung et al., 2001)	Scots pine seedlings	$2.67 \cdot 10^{-5}$	7.2 h	$2.18 \cdot 10^{-4}$	67.7	0.0109%
(Rapparini et al., 2002)	*Lemna gibba* (aquatic monocot)	$1.93 \cdot 10^{-3}$	6 min	$1.58 \cdot 10^{-2}$	7.97	0.783%
(Grieneisen et al., 2012)	*Arabidopsis* root	$5 \cdot 10^{-6}$	3.85 h	$4.08 \cdot 10^{-5}$	156	0.00204%
(Liu et al., 2010)	Model fitting	2	0.35 s	16.3	0.247	96.5%

Table **6**: Values of auxin flux rates in m/s. The estimated values are indicated with an asterisk.

Ref.	Auxin type	Object	Permeability to the protonated auxin	Background efflux rate	Net efflux rate	Active influx rate	Net efflux rate without PGP19
(Gutknecht and Walter, 1980)	IAA	egg lecitin bilayer	$3.3{\cdot}10^{-5}$	$^{*}\,1.9{\cdot}10^{-7}$			
(Hošek et al., 2012)	2,4-D	tobacco protoplasts	$2.4{\cdot}10^{-4}$	$^{*}\,1.3{\cdot}10^{-8}$	$1.7{\cdot}10^{-8}$	$1.4{\cdot}10^{-6}$	
(Geisler et al., 2005)	IAA	*Arabidopsis* protoplasts	$^{*}\,4.8{\cdot}10^{-6}$	$^{*}\,9.7{\cdot}10^{-9}$	$^{*}\,1.4{\cdot}10^{-8}$	$^{*}\,4.3{\cdot}10^{-8}$	$^{*}\,1.1{\cdot}10^{-8}$
(Grieneisen et al., 2007)	IAA	phenomenological model			$1.0{\cdot}10^{-6}$	$2.0{\cdot}10^{-5}$	

Table **7**: Solution of the sub-model equations (indicated in the first column) in steady state and corresponding gradient steepness θ. The solutions are parametrized by unitless characteristic length scale $\ell = \lambda/L = 1/\sqrt{a}$, unitless efflux rate q and by the right boundary of synthesis domain and right boundary of degradation domain x_0.

	Solution	Gradient steepness θ
1	$u^* = \frac{1}{\ell} \cdot \operatorname{csch}\left(\frac{1}{\ell}\right) \cdot \cosh\left(\frac{1-x}{\ell}\right)$ $= \dfrac{\exp\left(-\frac{x}{\ell}\right) + \exp\left(\frac{x-2}{\ell}\right)}{\ell \cdot \left(1 - \exp(-\frac{2}{\ell})\right)}$	$1 - \dfrac{1}{\cosh\left(\frac{1}{\ell}\right)}$
2	$u^* = \int_0^1 f(\xi) \cdot g^*(x,\xi)\, d\xi$ $g^* = \frac{1}{2\ell} \cdot \sum_{n=-\infty}^{\infty} \left[\exp\left(-\frac{\lvert x-\xi+2\,n\rvert}{\ell}\right) + \exp\left(-\frac{\lvert x+\xi+2\,n\rvert}{\ell}\right)\right]$ $= 1 + 2 \cdot \sum_{k=1}^{\infty} \dfrac{\cos(\pi\, k\, x)\cos(\pi\, k\, \xi)}{(\pi\, k\, \ell)^2 + 1}$ $= 1 + \sum_{k=1}^{\infty} \dfrac{\cos(\pi\, k\, [x+\xi]) + \cos(\pi\, k\, [x-\xi])}{(\pi\, k\, \ell)^2 + 1}$ $f = {x_0}^{-1} \cdot \mathrm{H}(x_0 - x)$	$\dfrac{\sum_{k=1}^{\infty} \left(1 - (-1)^k\right) \cdot s(k)}{\frac{1}{2} + \sum_{k=1}^{\infty} s(k)}$ $s(k) = \dfrac{\operatorname{sinc}(\pi\, k\, x_0)}{(\pi\, k\, \ell)^2 + 1}$
3	$u^* = \begin{cases} B \cdot \left[\frac{x_0 - x}{\nu} \cdot \sinh(z) + \cosh(z)\right] & \text{if } 0 < x < x_0 \\ B \cdot \cos\left(\frac{1-x}{\nu}\right) & \text{if } x_0 \le x < 1 \end{cases}$ $\nu = \ell \cdot \sqrt{1 - x_0} \qquad z = \dfrac{1 - x_0}{\nu}$ $B = \left[x_0\, \cosh(z) + \dfrac{x_0^2 + 2\,\nu^2}{2\,\nu}\, \sinh(z)\right]^{-1}$	$1 - \dfrac{1}{\cosh(z) + \frac{x_0}{\nu} \cdot \sinh(z)}$
4	$u = \dfrac{1}{\ell} \cdot \dfrac{\cosh\left(\frac{x-1}{\ell}\right) - \ell\, q\, \sinh\left(\frac{x-1}{\ell}\right)}{\sinh\left(\frac{1}{\ell}\right) + \ell\, q\, \cosh\left(\frac{1}{\ell}\right) - \ell\, q}$	$1 - \dfrac{1}{\cosh\left(\frac{1}{\ell}\right) + \ell\, q\, \sinh\left(\frac{1}{\ell}\right)}$

Table **8**: Gradient steepness under different regimes

regime	steepness θ
1	0.783
2	0.588
3	1.361
4	0.911
5, no vacuole	1.328
5, with vacuole	3.213
5, no vacuole, polarized AUX1 expression	1.347
5, with vacuole, polarized AUX1 expression	3.207

Additional Files

Additional file 1 — Supplementary Text

See Appendix 2

Conclusion and Outlook

.1 Conclusion

In this study we analysed the role of auxin in the determination of nuclear fate in the syncytial female gametophyte of flowering plants using both modelling and experimental approach. Based on this work, following can be concluded:

The vacuole impedes diffusive transport within the female gametophyte. In addition to the factors suggested earlier, such as local production or influx of a morhpogen and its degradation, we identified the inhibition of diffusion by a vacuole as a mechanism able to increase the steepness of a morphogen gradient in the female gametophyte. Though this effect does not provide a condition for robust patterning through auxin gradient under known parameters, it can be crucial for distribution of other morphogenic substances. Therefore, the diffusion-decelerating effect of the vacuole must taken into consideration in further conceptual and mathematical models of the female gametophyte patterning.

PGP1 and AUX1 auxin carriers are expressed in the female gametophyte. Using earlier described promoter-fusion constructs we found PGP1 and AUX1 auxin carriers to be expressed within the female gametophyte. Moreover, AUX1 is concentrated to the micropylar half of the plasma membrane. On the other hand, no expression of auxin transporters PIN8 and PGP19 has been detected in the female gametophyte.

Auxin gradient theoretically achievable within the female gametophyte under known parameter values cannot provide a sufficiently robust positional information. The maximal steepness of the auxin gradient achieved under known parameters is 3.2% in *Arabidopsis*. With this steepness, all perturbations in the source of auxin higher than 3.4% will render all nuclei within the female gametophyte the same fate. This is unlikely to be biologically relevant morphogen gradient, since the required robustness to perturbations is expected to be around 10% (Gregor et al., 2007).

A novel auxin sensor based on auxin-dependent protein degradation can provide an immidiate read-out of auxin activity. In this study, I developed a novel auxin sensor named degron which shows auxin-sensitive response. As the principle of sensing is different from the commonly used *DR5* transcriptional reporter and relies on an earlier step in auxin perception cascade, the degron sensor is expected to have a different dynamic range and thus can bring additional information about auxin activity in plant tissues.

Auxin maximum migrates from the micropylar to the chalazal pole of the tissues adjacent to the female gametophyte in *Arabidopsis* during the megasporogenesis. While the micropylar-most cells of nucellus showing high auxin activity degenerate during FG2–4 stages, the auxin maximum shifts to the nucellus cells abutting the female gametophyte from the sides. Later, upon degeneration of the latter cells, the maximum shifts to the cells abutting the female gametophyte from its chalazal pole.

Auxin activity cannot be detected within the female gametophyte of flowering plants neither by traditional *DR5* transcriptional reporter nor by the original degron constructs.

Effects of auxin on the cell fate determination can be explained by other mechanisms than auxin-based positional information. One possible explanation of the effect of auxin on the female gametophyte development is that the polarized auxin activity in the sporophyte is necessary for polarized expression of a non-cell-autonomous signalling molecule in the same tissue. This putative molecule would determine patterning of the female gametophyte. Another hypothesis suggests that a shallow auxin gradient within the female gametophyte under detection limit can induce symmetry breaking in the distribution of another molecule within the female gametophyte, for example by so-called wave-pinning mechanism (Mori et al., 2008).

.2 Outlook

In order to address the questions that arose in the course of this study, I suggest following steps:

Study of the role of a putative non-cell-autonomous signal in FG patterning. Our model suggests that a non-cell-autonomous factor can explain the effects of auxin overproduction in the female gametophyte (Pagnussat et al., 2009). This is corroborated by the fact that in Solanaceæ, an auxin-inducible secreted peptide ScRALF3 is important for proper nuclei positioning and female gametophyte polarity (Chevalier et al., 2013). The closest orthologue of ScRALF3 in *Arabidopsis*, RALFL34 (encoded by *AT5G67070.1*), shares 74% of coding sequence similarity with it. Therefore, the phenotype and expression pattern of the RALFL34 and other related members of the protein family has to be investigated.

Study of the role of Rho-GTPases in FG patterning. Another alternative explanation of the role of auxin in the female gametophyte development is it being a trigger of spatial symmetry breaking of the distribution of another molecule via the wave-pinning mechanism. We suggest the proteins of Rho-GTPase family as candidates, as it is known that the Rho-GTPases ROP2 and ROP6 participate in patterning of leaf epidermis cells (Xu et al., 2010). Therefore, the localization of Rho-GTPases expressed in the female gametophyte as well as phenotype of plants with T-DNA insertions in these genes should be investigated in future.

Improvement of the degron sensor of auxin. Here I developed a novel fluorescent auxin sensor termed degron-GFP (Lituiev et al., 2013). In parallel, an analogous sensor named DII-Venus has been constructed (Brunoud et al., 2012). Still these sensors need improvement, as none of sensors combines all desirable properties, namely:

1. The sensor should have nuclear localization signal to facilitate observation and automatic segmentation of images.
2. The promoter of the sensor should provide a uniform expression of the protein. Alternatively, the sensor T-DNA cassete must carry an internal standard of promoter activity (another fluorescent protein expressed under the same promoter without degron sequence).
3. The sensor needs to be quantitatively calibrated. Additionally, the homogeneity of the response within cell populations should be studied. Technically it can be addressed by using flow cytometry of protoplasts from plants carrying the sensor.

Study of the effect of enhanced auxin degradation in the female gametophyte. An additional experiment which can clarify the role of auxin within the female gametophyte is xenogenic expression of *Pseudomonas savastanoi* iaaL auxin-conjugating enzyme. Presence of any fertility phenotype in plants carrying the construct driving iaaL expression in the female gametophyte will strengthen the conclusion about the role of auxin in the female gametophyte development. Otherwise, it will present additional contradiction to previous results by Pagnussat et al. (2009).

References

von Sachs, J. (1882). *Die Vorlesungen über Pflanzenphysiologie*. Leipzig: Wilhelm Engelmann.

Huang, B. Q. and W. F. Sheridan (1994). "Female Gametophyte Development in Maize: Microtubular Organization and Embryo Sac Polarity." *Plant Cell* **6**.6, pp. 845–861.

Schneitz, K., M. Hülskamp, and R. E. Pruitt (1995). "Wild-type ovule development in *Arabidopsis thaliana*: a light microscope study of cleared whole-mount tissue". *The Plant Journal* **7**.5, pp. 731–749.

Christensen, C. A., E. J. King, J. R. Jordan, and G. N. Drews (1997). "Megagametogenesis in *Arabidopsis* wild type and the *Gf* mutant". *Sexual Plant Reproduction* **10**.1, pp. 49–64.

Friedman, W. E. and K. C. Ryerson (2009). "Reconstructing the ancestral female gametophyte of angiosperms: Insights from Amborella and other ancient lineages of flowering plants". *American Journal of Botany* **96**.1, pp. 129–143.

Cass, D. D. and I. Karas (1974). "Ultrastractural organization of the egg of *Plumbago zeylanica*". *Protoplasma* **81**.1, pp. 49–62.

Rotman, N., A. Durbarry, A. Wardle, W. C. Yang, A. Chaboud, J. E. Faure, F. Berger, and D. Twell (2005). "A novel class of MYB factors controls sperm-cell formation in plants". *Curr. Biol.* **15**, pp. 244–248.

Escobar-Restrepo, J.-M., N. Huck, S. Kessler, V. Gagliardini, J. Gheyselinck, W.-C. Yang, and U. Grossniklaus (2007). "The FERONIA receptor-like kinase mediates male-female interactions during pollen tube reception." *Science* **317**.5838, pp. 656–660.

Lawit, S. J., M. A. Chamberlin, A. Agee, E. S. Caswell, and M. C. Albertsen (2013). "Transgenic manipulation of plant embryo sacs tracked through cell-type-specific fluorescent markers: cell labeling, cell ablation, and adventitious embryos". *Plant Reproduction* **26**.2, pp. 125–137.

Turing, A. M. (1952). "The chemical basis of morphogenesis". *Philosophical Transactions of the Royal Society B: Biological Sciences* **237**.641, pp. 37–72.

Wolpert, L. (1969). "Positional information and the spatial pattern of cellular differentiation". *Journal of Theoretical Biology* **25**.1, pp. 1–47.

Kay, R. R. and C. R. L. Thompson (2009). "Forming patterns in development without morphogen gradients: scattered differentiation and sorting out." *Cold Spring Harb Perspect Biol* **1**.6, a001503.

Xiong, F., A. R. Tentner, P. Huang, et al. (2013). "Specified neural progenitors sort to form sharp domains after noisy Shh signaling." *Cell* **153**.3, pp. 550–561.

Iber, D., J. Clarkson, M. D. Yudkin, and I. D. Campbell (2006). "The mechanism of cell differentiation in Bacillus subtilis." *Nature* **441**.7091, pp. 371–374.

Mori, Y., A. Jilkine, and L. Edelstein-Keshet (2008). "Wave-pinning and cell polarity from a bistable reaction-diffusion system." *Biophys J* **94**.9, pp. 3684–3697.

Bajon, C., C. Horlow, J. C. Motamayor, A. Sauvanet, and D. Robert (1999). "Megasporogenesis in *Arabidopsis thaliana* L.: an ultrastructural study". *Sexual Plant Reproduction* **12**.2, pp. 99–109.

Ebel, C., L. Mariconti, and W. Gruissem (2004). "Plant retinoblastoma homologues control nuclear proliferation in the female gametophyte." *Nature* **429**.6993, pp. 776–780.

Johnston, A. J., E. Matveeva, O. Kirioukhova, U. Grossniklaus, and W. Gruissem (2008). "A dynamic reciprocal RBR-PRC2 regulatory circuit controls Arabidopsis gametophyte development." *Curr Biol* **18**.21, pp. 1680–1686.

Evans, M. M. S. (2007). "The *indeterminate gametophyte1* gene of maize encodes a LOB domain protein required for embryo Sac and leaf development." *Plant Cell* **19**.1, pp. 46–62.

Lin, B.-Y. (1978). "Structural modifications of the female gametophyte associated with the indeterminate gametophyte (*ig*) mutant in maize". *Genome* **20**.2, pp. 249–257.

Sprunck, S. and R. Gross-Hardt (2011). "Nuclear behavior, cell polarity, and cell specification in the female gametophyte." *Sex Plant Reprod* **24**.2, pp. 123–136.

Pagnussat, G. C., M. Alandete-Saez, J. L. Bowman, and V. Sundaresan (2009). "Auxin-Dependent Patterning and Gamete Specification in the Arabidopsis Female Gametophyte". *Science* **324**.5935, pp. 1684–1689.

Ceccato, L., S. Masiero, D. Sinha Roy, et al. (2013). "Maternal Control of PIN1 Is Required for Female Gametophyte Development in Arabidopsis". *PLoS ONE* **8**.6, e66148.

Lituiev, D., N. G. Krohn, B. Müller, D. Jackson, B. Hellriegel, T. Dresselhaus, and U. Grossniklaus (2013). "Theoretical and experimental evidence indicates that there is no auxin gradient patterning the angiosperm female gametophyte". *Development* **140**.

Tucker, M. R., T. Okada, S. D. Johnson, F. Takaiwa, and A. M. G. Koltunow (2012). "Sporophytic ovule tissues modulate the initiation and progression of apomixis in Hieracium." *J. Exp. Bot.*

Chevalier, E., A. Loubert-Hudon, and D. P. Matton (2013). "ScRALF3, a secreted RALF-like peptide involved in cell-cell communication between the sporophyte and the female gametophyte in a solanaceous species". *The Plant Journal* **73**.6, pp. 1019–1033.

Kondo, S. and T. Miura (2010). "Reaction-diffusion model as a framework for understanding biological pattern formation". *Science* **329**.5999, pp. 1616–1620.

Maini, P. K., K. J. Painter, and H. Nguyen Phong Chau (1997). "Spatial pattern formation in chemical and biological systems". *Journal of the Chemical Society, Faraday Transactions* **93**.20, pp. 3601–3610.

Badugu, A., C. Kraemer, P. Germann, D. Menshykau, and D. Iber (2012). "Digit patterning during limb development as a result of the BMP-receptor interaction". *Scientific Reports* **2**.

Zeng, W., G. L. Thomas, and J. A. Glazier (2004). "Non-Turing stripes and spots: a novel mechanism for biological cell clustering". *Physica A: Statistical Mechanics and its Applications* **341**, pp. 482–494.

Sander, K. (1976). *Specification of the Basic Body Pattern in Insect Embryogenesis*. Elsevier, pp. 125–238.

Green, J. (2002). "Morphogen gradients, positional information, andXenopus: Interplay of theory and experiment". *Developmental Dynamics* **225**.4, pp. 392–408.

Dessaud, E., A. P. McMahon, and J. Briscoe (2008). "Pattern formation in the vertebrate neural tube: a sonic hedgehog morphogen-regulated transcriptional network." *Development* **135**.15, pp. 2489–2503.

Nüsslein-Volhard, C. and E. Wieschaus (1980). "Mutations affecting segment number and polarity in Drosophila." *Nature* **287**.5785, pp. 795–801.

Jaeger, J. and J. Reinitz (2006). "On the dynamic nature of positional information." *Bioessays* **28**.11, pp. 1102–1111.

Wuest, S. E., K. Vijverberg, A. Schmidt, et al. (2010). "Arabidopsis female gametophyte gene expression map reveals similarities between plant and animal gametes." *Curr Biol* **20**.6, pp. 506–512.

Hosseinpour, B., V. HajiHoseini, R. Kashfi, E. Ebrahimie, and F. Hemmatzadeh (2012). "Protein Interaction Network of Arabidopsis thaliana Female Gametophyte Development Identifies Novel Proteins and Relations". *PLoS ONE* **7**.12, e49931.

Yu, H.-J., P. Hogan, and V. Sundaresan (2005). "Analysis of the female gametophyte transcriptome of Arabidopsis by comparative expression profiling." *Plant Physiol* **139**.4, pp. 1853–1869.

Steffen, J. G., I.-H. Kang, J. Macfarlane, and G. N. Drews (2007). "Identification of genes expressed in the Arabidopsis female gametophyte." *Plant J* **51**.2, pp. 281–292.

Wang, D., C. Zhang, D. J. Hearn, et al. (2010). "Identification of transcription-factor genes expressed in the Arabidopsis female gametophyte." *BMC Plant Biol* **10**, p. 110.

Drews, G. N., D. Wang, J. G. Steffen, K. S. Schumaker, and R. Yadegari (2011). "Identification of genes expressed in the angiosperm female gametophyte." *J Exp Bot* **62**.5, pp. 1593–1599.

Groß-Hardt, R., C. Kägi, N. Baumann, J. M. Moore, R. Baskar, W. B. Gagliano, G. Jürgens, and U. Grossniklaus (2007). "*LACHESIS* Restricts Gametic Cell Fate in the Female Gametophyte of *Arabidopsis*". *PLoS Biol* **5**.3, e47.

Moll, C., L. von Lyncker, S. Zimmermann, C. Kägi, N. Baumann, D. Twell, U. Grossniklaus, and R. Gross-Hardt (2008). "CLO/GFA1 and ATO are novel regulators of gametic cell fate in plants." *Plant J* **56**.6, pp. 913–921.

Kägi, C., N. Baumann, N. Nielsen, Y. Stierhof, and R. Gross-Hardt (2010). "The gametic central cell of *Arabidopsis* determines the lifespan of adjacent accessory cells." *Proc Natl Acad Sci U S A* **107**.51, pp. 22350–5.

Krohn Nadia Gracieleand Lausser, A., M. Juranić, and T. Dresselhaus (2012). "Egg Cell Signaling by the Secreted Peptide ZmEAL1 Controls Antipodal Cell Fate". *Developmental Cell* **23**.1, pp. 219–225.

Köszegi, D., A. J. Johnston, T. Rutten, et al. (2011). "Members of the RKD transcription factor family induce an egg cell-like gene expression program". *The Plant Journal* **67**.2, pp. 280–291.

Lander, A. D., W.-C. C. Lo, Q. Nie, and F. Y. Wan (2009). "The measure of success: constraints, objectives, and tradeoffs in morphogen-mediated patterning." *Cold Spring Harb. Perspect. Biol.* **1**.1.

Pagnussat, G. C., H.-J. Yu, and V. Sundaresan (2007). "Cell-fate switch of synergid to egg cell in *Arabidopsis eostre* mutant embryo sacs arises from misexpression of the BEL1-like homeodomain gene *BLH1*." *Plant Cell* **19**.11, pp. 3578–3592.

Maruyama, D., Y. Hamamura, H. Takeuchi, D. Susaki, M. Nishimaki, D. Kurihara, R. D. Kasahara, and T. Higashiyama (2013). "Independent control by each female gamete prevents the attraction of multiple pollen tubes." *Dev Cell* **25**.3, pp. 317–323.

Völz, R., J. Heydlauff, D. Ripper, L. von Lyncker, and R. Groß-Hardt (2013). "Ethylene signaling is required for synergid degeneration and the establishment of a pollen tube block." *Dev Cell* **25**.3, pp. 310–316.

Kirioukhova, O., A. J. Johnston, D. Kleen, et al. (2011). "Female gametophytic cell specification and seed development require the function of the putative Arabidopsis INCENP ortholog WYRD". *Development* **138**.16, pp. 3409–3420.

Pastuglia, M., J. Azimzadeh, M. Goussot, et al. (2006). "Gamma-tubulin is essential for microtubule organization and development in Arabidopsis." *Plant Cell* **18**.6, pp. 1412–1425.

Tanaka, H., M. Ishikawa, S. Kitamura, Y. Takahashi, T. Soyano, C. Machida, and Y. Machida (2004). "The AtNACK1/HINKEL and STUD/TETRASPORE/AtNACK2 genes, which encode functionally redundant kinesins, are essential for cytokinesis in Arabidopsis". *Genes to Cells* **9**.12, pp. 1199–1211.

Srilunchang, K.-o., N. G. Krohn, and T. Dresselhaus (2010). "DiSUMO-like DSUL is required for nuclei positioning, cell specification and viability during female gametophyte maturation in maize." *Development* **137**.2, pp. 333–345.

Park, S. K., D. Rahman, S. A. Oh, and D. Twell (2004). "*gemini pollen 2*, a male and female gametophytic cytokinesis defective mutation". *Sexual Plant Reproduction* **17**.2.

Oh, S. A., A. Johnson, A. Smertenko, D. Rahman, S. K. Park, P. J. Hussey, and D. Twell (2005). "A Divergent Cellular Role for the FUSED Kinase Family in the Plant-Specific Cytokinetic Phragmoplast". *Current Biology* **15**.23, pp. 2107–2111.

Darwin, C. (1880). *The power of movement in plants.* London: John Murray.

Michniewicz, M., P. B. Brewer, and J. Friml (2007). "Polar Auxin Transport and Asymmetric Auxin Distribution". *The Arabidopsis Book* **57**.1, p. 1.

Cholodny, N. (1927). "Wuchshormone und Tropismen bei den Pflanzen." *Biologisches Zentralblatt* **475**.1, pp. 604–629.

Went, F. W. (1926). "On growth-accelerating substances in the coleoptile of *Avena sativa*." *Proceedings of the Koninklijke Nederlandse Akademie van Wetenschappen* **305**.1, pp. 10–19.

Kögl, F. and A. Haagen-Smith (1931). "Über die Chemie des Wuchsstoffs". *Proceedings of the Koninklijke Nederlandse Akademie van Wetenschappen Amsterdam. Section Science* **34**, pp. 1411–1416.

Kurosawa, E. (1926). "Experimental studies on the nature of the substance secreted by the 'bakanae' fungus". *Transactions of the Natural History Society of Formosa* **16**, pp. 213–227.

Yabuta, T. (1938). "On the crystal of gibberellin, a substance to promote plant growth." *J. Agric. Chem. Soc. Japan.* **14**, p. 1526.

Skoog, F. K., F. M. Strong, and C. O. Miller (1965). "Cytokinins". *Science* **148**.3669, pp. 532–533.

Vanstraelen, M. and E. Benková (2012). "Hormonal Interactions in the Regulation of Plant Development". *Annual Review of Cell and Developmental Biology* **28**.1, pp. 463–487.

Wang, Y. H. and H. R. Irving (2011). "Developing a model of plant hormone interactions". *Plant Signaling & Behavior* **6**.4, pp. 494–500.

Reinbothe, S., B. Mollenhauer, and C. Reinbothe (1994). "JIPs and RIPs: the regulation of plant gene expression by jasmonates in response to environmental cues and pathogens." *Plant Cell* **6**.9, pp. 1197–1209.

Ruyter-Spira, C., S. Al-Babili, S. van der Krol, and H. Bouwmeester (2013). "The biology of strigolactones". *Trends in Plant Science* **18**.2, pp. 72–83.

García-Mata, C. and L. Lamattina (2013). "Gasotransmitters are emerging as new guard cell signaling molecules and regulators of leaf gas exchange". *Plant Science* **201-202**, pp. 66–73.

Lander, A. D., Q. Nie, and F. Y. Wan (2002). "Do morphogen gradients arise by diffusion?" *Developmental cell* **2**.6, pp. 785–796.

Ljung, K. (2013). "Auxin metabolism and homeostasis during plant development". *Development* **140**.5, pp. 943–950.

Rubery, P. H. and A. R. Sheldrake (1974). "Carrier-mediated auxin transport". *Planta* **118**.2, pp. 101–121.

Raven, J. A. (1975). "Transport of indoleacetic acid in plant cells in relation to ph and electrical potential gradients, and its significance for polar IAA transport". *New Phytologist* **74**.2, pp. 163–172.

Okada, K., J. Ueda, M. K. K. Komaki, C. J. J. Bell, and Y. Shimura (1991). "Requirement of the Auxin Polar Transport System in Early Stages of Arabidopsis Floral Bud Formation." *The Plant Cell* **3**.7, pp. 677–684.

Mravec, J., P. Skůpa, A. Bailly, et al. (2009). "Subcellular homeostasis of phytohormone auxin is mediated by the ER-localized PIN5 transporter". *Nature* **459**.7250, pp. 1136–1140.

Sawchuk, M. G., A. Edgar, and E. Scarpella (2013). "Patterning of Leaf Vein Networks by Convergent Auxin Transport Pathways". *PLoS Genetics* **9**.2. Ed. by L.-J. Qu, e1003294.

Dal Bosco, C., A. Dovzhenko, X. Liu, et al. (2012). "The endoplasmic reticulum localized PIN8 is a pollen specific auxin carrier involved in intracellular auxin homeostasis." *Plant J.*

Geisler, M., J. J. Blakeslee, R. Bouchard, et al. (2005). "Cellular efflux of auxin catalyzed by the *Arabidopsis* MDR/PGP transporter AtPGP1." *Plant J* **44**.2, pp. 179–194.

Petrášek, J., J. Mravec, R. Bouchard, et al. (2006). "PIN proteins perform a rate-limiting function in cellular auxin efflux." *Science* **312**.5775, pp. 914–918.

Kramer, E. M. and M. J. Bennett (2006). "Auxin transport: a field in flux." *Trends Plant Sci* **11**.8, pp. 382–386.

Barbez, E., M. Kubeš, J. Rolčék, et al. (2012). "A novel putative auxin carrier family regulates intracellular auxin homeostasis in plants". *Nature* **485**.7396, pp. 119–122.

Maher, E. P. and S. J. B. Martindale (1980). "Mutants of Arabidopsis thaliana with altered responses to auxins and gravity". *Biochemical Genetics* **18**.11-12, pp. 1041–1053.

Bennett, M. J., A. Marchant, H. G. Green, et al. (1996). "Arabidopsis AUX1 Gene: A Permease-Like Regulator of Root Gravitropism". *Science* **273**.5277, pp. 948–950.

Swarup, R. and B. Péret (2012). "AUX/LAX family of auxin influx carriers – an overview". *Frontiers in Plant Science* **3**.225.

Delbarre, A., P. Muller, V. Imhoff, and J. Guern (1996). "Comparison of mechanisms controlling uptake and accumulation of 2,4-dichlorophenoxy acetic acid, naphthalene-1-acetic acid, and indole-3-acetic acid in suspension-cultured tobacco cells". *Planta* **198** (4), pp. 532–541.

Yang, Y., U. Z. Hammes, C. G. Taylor, D. P. Schachtman, and E. Nielsen (2006). "High-affinity auxin transport by the AUX1 influx carrier protein." *Curr Biol* **16**.11, pp. 1123–1127.

Swarup, K., E. Benková, R. Swarup, et al. (2008). "The auxin influx carrier LAX3 promotes lateral root emergence." *Nat Cell Biol* **10**.8, pp. 946–954.

Diekmann, W., M. A. Venis, and D. G. Robinson (1995). "Auxins induce clustering of the auxin-binding protein at the surface of maize coleoptile protoplasts." *Proceedings of the National Academy of Sciences* **92**.8, pp. 3425–3429.

Löbler, M and D Klämbt (1985). "Auxin-binding protein from coleoptile membranes of corn (*Zea mays* L.). I. Purification by immunological methods and characterization." *Journal of Biological Chemistry* **260**.17, pp. 9848–53. eprint: http://www.jbc.org/content/260/17/9848.full.pdf+html.

Xu, T., M. Wen, S. Nagawa, et al. (2010). "Cell Surface- and Rho GTPase-Based Auxin Signaling Controls Cellular Interdigitation in *Arabidopsis*". *Cell* **143**.1, pp. 99–110.

Robert, S., J. Kleine-Vehn, E. Barbez, et al. (2010). "ABP1 mediates auxin inhibition of clathrin-dependent endocytosis in Arabidopsis." *Cell* **143**.1, pp. 111–121.

Sauer, M. and J. Kleine-Vehn (2011). "AUXIN BINDING PROTEIN1: The Outsider". *The Plant Cell* **23**.6, pp. 2033–2043.

Ulmasov, T., G. Hagen, and T. J. Guilfoyle (1999). "Dimerization and DNA binding of auxin response factors". *The Plant Journal* **19**.3, pp. 309–319.

Guilfoyle, T. J., T. Ulmasov, and G. Hagen (1998). "The ARF family of transcription factors and their role in plant hormone-responsive transcription." *Cell Mol Life Sci* **54**.7, pp. 619–627.

Tan, X., L. I. A. Calderon-Villalobos, M. Sharon, C. Zheng, C. V. Robinson, M. Estelle, and N. Zheng (2007). "Mechanism of auxin perception by the TIR1 ubiquitin ligase". *Nature* **446**.7136, pp. 640–645.

Dharmasiri, N., S. Dharmasiri, and M. Estelle (2005). "The F-box protein TIR1 is an auxin receptor." *Nature* **435**.7041, pp. 441–445.

Woodward, A. W. and B. Bartel (2005). "Auxin: regulation, action, and interaction." *Ann Bot* **95**.5, pp. 707–735.

Guilfoyle, T. J. and G. Hagen (2007). "Auxin response factors." *Curr. Opin. Plant Biol.* **10**.5, pp. 453–460.

Grieneisen, V. A., B. Scheres, P. Hogeweg, and A. F. M Marée (2012). "Morphogengineering roots: comparing mechanisms of morphogen gradient formation". *BMC Systems Biology* **6**.1, p. 37.

Band, L. R., D. M. Wells, A. Larrieu, et al. (2012). "Root gravitropism is regulated by a transient lateral auxin gradient controlled by a tipping-point mechanism". *Proceedings of the National Academy of Sciences* **109**.12, pp. 4668–4673.

Middleton, A. M., J. R. King, M. J. Bennett, and M. R. Owen (2010). "Mathematical modelling of the Aux/IAA negative feedback loop." *Bul.l Math. Biol.* **72**.6, pp. 1383–1407.

Liu, J., S. Mehdi, J. Topping, P. Tarkowski, and K. Lindsey (2010). "Modelling and experimental analysis of hormonal crosstalk in Arabidopsis." *Mol. Syst. Biol.* **6**.

Sankar, M., K. S. Osmont, J. Rolcik, B. Gujas, D. Tarkowska, M. Strnad, I. Xenarios, and C. S. Hardtke (2011). "A qualitative continuous model of cellular auxin and brassinosteroid signaling and their crosstalk." *Bioinformatics* **27**.10, pp. 1404–1412.

Jönsson, H., M. G. Heisler, B. E. Shapiro, E. M. Meyerowitz, and E. Mjolsness (2006). "An auxin-driven polarized transport model for phyllotaxis". *Proceedings of the National Academy of Sciences* **103**.5, pp. 1633–1638.

Smith, R. S., S. Guyomarc'h, T. Mandel, D. Reinhardt, C. Kuhlemeier, and P. Prusinkiewicz (2006). "A plausible model of phyllotaxis". *Proceedings of the National Academy of Sciences of the United States of America* **103**.5, pp. 1301–1306. eprint: `http://www.pnas.org/content/103/5/1301.full.pdf+html`.

Stoma, S., M. Lucas, J. Chopard, M. Schaedel, J. Traas, and C. Godin (2008). "Flux-based transport enhancement as a plausible unifying mechanism for auxin transport in meristem development." *PLoS Comput. Biol.* **4**.10, e1000207.

Heisler, M. G. and H. Jönsson (2007). "Modelling meristem development in plants". *Current Opinion in Plant Biology* **10**.1, pp. 92–97.

Lucas, M., Y. Guédon, C. Jay-Allemand, C. Godin, and L. Laplaze (2008). "An auxin transport-based model of root branching in *Arabidopsis thaliana*". *PLoS ONE* **3**.11. Ed. by N. Monk, e3673.

Grimm, O., M. Coppey, and E. Wieschaus (2010). "Modelling the Bicoid gradient". *Development* **137**.14, pp. 2253–2264.

Krupinski, P. and H. Jönsson (2010). "Modeling auxin-regulated development." *Cold Spring Harb Perspect Biol* **2**.2, a001560.

Ljung, K., A. Ostin, L. Lioussanne, and G. Sandberg (2001). "Developmental regulation of indole-3-acetic acid turnover in Scots pine seedlings." *Plant Physiol.* **125**.1, pp. 464–475.

Sequeira, L. and L. Mineo (1966). "Partial purification and kinetics of indoleacetic acid oxidase from tobacco roots." *Plant physiology* **41**.7, pp. 1200–1208.

Gutknecht, J. and A. Walter (1980). "Transport of auxin (indoleacetic acid) through lipid bilayer membranes". *J. Membr. Biol.* **56**.1, pp. 65–72.

Mitchison, G. J. (1980). "The Dynamics of Auxin Transport". *Proceedings of the Royal Society B: Biological Sciences* **209**.1177, pp. 489–511.

Laskowski, M., V. A. Grieneisen, H. Hofhuis, C. T. A. Hove, P. Hogeweg, A. F. Marée, and B. Scheres (2008). "Root system architecture from coupling cell shape to auxin transport." *PLoS Biol.* **6**.12, e307+.

Rapparini, F., Y. Y. Y. Tam, J. D. Cohen, and J. P. Slovin (2002). "Indole-3-acetic acid metabolism in Lemna gibba undergoes dynamic changes in response to growth temperature." *Plant Physiology* **128**.4, pp. 1410–1416.

Hošek, P., M. Kubeš, M. Lankova, et al. (2012). "Auxin transport at cellular level: new insights supported by mathematical modelling". *Journal of Experimental Botany* **63**.10, pp. 3815–3827.

Chavarría-Krauser, A. and M. Ptashnyk (2010). "Homogenization of long-range auxin transport in plant tissues". *Nonlinear Anal. Real World Appl.* **11**.6, pp. 4524–4532.

Marchant, A., J. Kargul, S. T. May, P. Muller, A. Delbarre, C. Perrot-Rechenmann, and M. J. Bennett (1999). "AUX1 regulates root gravitropism in Arabidopsis by facilitating auxin uptake within root apical tissues." *EMBO J* **18**.8, pp. 2066–2073.

Lachapelle, A. M. de and S. Bergmann (2010). "Precision and scaling in morphogen gradient read-out." *Molecular systems biology* **6**.

Gregor, T., W. Bialek, R. R. de Ruyter van Steveninck, D. W. Tank, and E. F. Wieschaus (2005). "Diffusion and scaling during early embryonic pattern formation". *Proceedings of the National Academy of Sciences* **102**.51, pp. 18403–18407.

He, F., T. E. Saunders, Y. Wen, D. Cheung, R. Jiao, P. Rein ten Wolde, M. Howard, and J. Ma (2010). "Shaping a Morphogen Gradient for Positional Precision". *Biophysical Journal* **99**.3, pp. 697–707.

Grieneisen, V. A., J. Xu, A. F. M. Maree, P. Hogeweg, and B. Scheres (2007). "Auxin transport is sufficient to generate a maximum and gradient guiding root growth". *Nature* **449**.7165, pp. 1008–1013.

Gregor, T., D. W. Tank, E. F. Wieschaus, and W. Bialek (2007). "Probing the Limits to Positional Information". *Cell* **130**.1, pp. 153–164.

Brunoud, G., D. M. Wells, M. Oliva, et al. (2012). "A novel sensor to map auxin response and distribution at high spatio-temporal resolution." *Nature* **482**.7383, pp. 103–106.

Meng, T. C., S. Somani, and P. Dhar (2004). "Modeling and simulation of biological systems with stochasticity." *In Silico Biol* **4**.3, pp. 293–309.

Burrage, K., P. M. Burrage, A. Leier, T. Marquez-Lago, and D. V. Nicolau (2011). *Stochastic Simulation for Spatial Modelling of Dynamic Processes in a Living Cell*. Springer-Verlag, pp. 43–62.

Sbalzarini, I. F., A. Mezzacasa, A. Helenius, and P. Koumoutsakos (2005). "Effects of organelle shape on fluorescence recovery after photobleaching." *Biophys J* **89**.3, pp. 1482–1492.

Einstein, A. (1905). "Über die von der molekularkinetischen Theorie der Wärme geforderte Bewegung von in ruhenden Flüssigkeiten suspendierten Teilchen". *Ann. Phys.* **322**.8, pp. 549–560.

Chow, T. (2000). *Mathematical Methods for Physicists: A Concise Introduction*. Cambridge University Press.

Arfken, G. B., H. J. Weber, and F. E. Harris (2012). *Mathematical Methods for Physicists, Seventh Edition: A Comprehensive Guide*. Academic Press.

Schultz, S. G (1980). *Basic Principles of Membrane Transport*. IUPAB Biophysics Series. Cambridge University Press.

Austin, R. S., D. Vidaurre, G. Stamatiou, et al. (2011). "Next-generation mapping of Arabidopsis genes." *Plant J* **67**.4, pp. 715–725.

Schneeberger, K., S. Ossowski, C. Lanz, et al. (2009). "SHOREmap: simultaneous mapping and mutation identification by deep sequencing." *Nat Methods* **6**.8, pp. 550–551.

Lindner, H., M. T. Raissig, C. Sailer, H. Shimosato-Asano, R. Bruggmann, and U. Grossniklaus (2012). "SNP-Ratio Mapping (SRM): Identifying Lethal Alleles and Mutations in Complex Genetic Backgrounds by Next-Generation Sequencing." *Genetics* **191**.4, pp. 1381–1386.

Singer, T., Y. Fan, H.-S. Chang, T. Zhu, S. P. Hazen, and S. P. Briggs (2006). "A High-Resolution Map of *Arabidopsis* Recombinant Inbred Lines by Whole-Genome Exon Array Hybridization". *PLoS Genet* **2**.9, e144.

Ehrenfest, P. u. T. (1907). "Über zwei bekannte Einwände gegen das Boltzmannsche H-Theorem". *Physikalishce Zeitschrift* **8**, pp. 311–314.

Feingold, E. (1993). "Markov Processes for Modeling and Analyzing a New Genetic Mapping Method". *Journal of Applied Probability* **30**.4, pp. 766–779.

Töpfer, A., O. Zagordi, S. Prabhakaran, V. Roth, E. Halperin, and N. Beerenwinkel (2013). "Probabilistic Inference of Viral Quasispecies Subject to Recombination". *Journal of Computational Biology* **20**.2, pp. 113–123.

Anders, S. and W. Huber (2010). "Differential expression analysis for sequence count data". *Genome Biology* **11**.10, R106.

Gillespie, D. T. (1976). "A general method for numerically simulating the stochastic time evolution of coupled chemical reactions". *Journal of Computational Physics* **22**.4, pp. 403–434.

Lander, E. S. and M. S. Waterman (1988). "Genomic mapping by fingerprinting random clones: a mathematical analysis." *Genomics* **2**.3, pp. 231–239.

Wöll, D., C. Kölbl, B. Stempfle, and A. Karrenbauer (2013). "A novel method for automatic single molecule tracking of blinking molecules at low intensities." *Phys Chem Chem Phys* **15**.17, pp. 6196–6205.

Yu, H. Y., S.-H. Hong, M. M. Lee, and J.-G. Choi (2004). "A new user-assisted segmentation and tracking technique for an object-based video editing system". In: *SPIE Proceedings. Microelectronics: Design, Technology, and Packaging*. Ed. by D. Abbott, K. Eshraghian, C. A. Musca, D. Pavlidis, and N. Weste. Vol. 5274. SPIE - International Society for Optical Engineering, pp. 470–481.

Esche, M., M. Karaman, and T. Sikora (2010). "Semi-automatic object tracking in video sequences by extension of the MRSST algorithm". In: *Image Analysis for Multimedia Interactive Services (WIAMIS), 2010 11th International Workshop on*, pp. 1–4.

Thévenaz, P., U. Ruttimann, and M. Unser (1998). "A Pyramid Approach to Subpixel Registration Based on Intensity". *IEEE Transactions on Image Processing* **7**.1, pp. 27–41.

Appendix 1. Diffusion, Transport, and Reactions: Physical Basis, Analytical and Numerical Techniques

> " ... every particle of Space is always, and every indivisible moment of Duration is every where..."
>
> Isaac Newton. "General Scholium". English translation by Andrew Motte (1729)

In this work I address spatial and, to a less extent, temporal inhomogeneity of auxin in female gametophyte. To this end, here I summarize general background connected to matter transport and metamorphosis.

The notion of matter is usually defined as anything having mass and occupying some space. The physical laws describing transport of matter are rooted in the law of mass conservation formulated by Antoine Lavoisier. Freely it can be restated as that in a closed space, i.e. whose boundaries are not passed by mass transfer, the amount of mass is conserved. Mathematically it is reflected in the divergence theorem, also known as Gauss's theorem or Ostrogradsky's theorem. Also some mass of a particular chemical substance can be converted to the same mass of another substance staying in a closed volume. In this thesis, I consider three processes occuring with the matter: diffusive transport, transmembrane transport, and chemical reactions, whose quantitative description is summarized furter.

A1.1 Simulation of diffusion, transport, and reactions in developmental biology

A1.1.1 Methods of spatio-temporal simulation for physico-chemical biology

The problem of simulation of reaction-diffusion and transport can be conceptually split into two components: simulation of dynamical processes (in our case simulation of the chemical reactions) that do not depend on spatial component (so called zero-dimensional models relying on assumption of well-stirred solutions), and simulation of the wide sense transport processes such as diffusion, convection and inter-compartmental transport.

Simulation of chemical reactions. The first and conceptually easier zero-dimensional dynamical models exist of two types: deterministic (systems governed by so called reaction rate equation) and stochastic (ones governed by chemical master equations). Computational realization of chemical master equations relies on the stochastic simulation techniques such as Gillespie's or Stochsim schemes (reviewed in Meng et al., 2004; Burrage et al., 2011), while one of the deterministic systems relies on the integration schemes for ordinary differential equations.

Simulation of transport processes. The spatio-temporal computational models built upon the zero-dimensional models with addition of specific techniques handling (wide sense) transport processes. The transport can as well can be handled as stochastic or deterministic. The stochastic description of diffusion is random walk (RW), while one particular instance of the stochastic inter-compartmental transport models can be the Ehrenfests' model. Much broader is the choice of deterministic simulation schemes for diffusion, including lattice-based finite difference method (FDM), tessellation-based finite elements method (FEM), and particle strength exchange (PSE)(Sbalzarini et al., 2005).

Stochastic vs. deterministic. The choice between the stochastic and deterministic simulation schemes based on the assumptions about the studied system. As stochastic simulations are computationally more expensive and need to be run repetitively to obtain ensemble statistics, and as in larger systems stochastic effects are getting negligible, the application of stochastic schemes is justified for small-scale systems i.e. those with the small number of molecules.

A1.2 Physical Basis of Diffusion and Transmembrane Transport

Diffusion is a process of mass transport, when no bulk macroscopic movement of matter is involved. For example in everyday life, the process of diffusion can be observed when a tea bag is placed in still hot water. With time the black colourant spreads from the tea bag to the whole cup.

The basis of diffusion of substances is thermal movement of molecules (recurring to everyday experience, that tea infuses quicker in hot water). The first random motion of pollen grains reminiscent of random motion of molecules was observed by Robert Brown in 1827. Later in 19^{th} century, Fick described mathematically the macroscopic effect of diffusional spreading of matter. He formulated two laws, the first relating a steady-state flux to a gradient of diffusing substance, and the second relating the the dynamics

of diffusing substance. Later, Einstein (1905) provided a physical model explaining the microscopic random motion and linked it to the second Fick's law.

The macroscopic description of diffusion (second Fick's law) involves a partial differential equation (PDE). An introduction to PDE can be found elsewhere (Chow, 2000; Arfken et al., 2012). Further I briefly review the principles of modelling and two methods of solution of differential equations.

A1.3 Analytical solution of partial differential equations

A1.3.1 Method of Green's functions

Formulation of the problem. One of the question of this study is to find the spatial distribution of auxin given some spatially localized auxin synthesis. This problem can be expressed as a linear PDE in non-dimensional form:

$$\frac{\partial}{\partial t}u = \frac{\partial^2}{\partial x^2}u - \lambda^{-2}\cdot u + f(x,t) \qquad \frac{\partial}{\partial x}u\Big|_{\substack{x=0\\x=1}} = 0 \tag{A1.10}$$

where u is concentration of auxin, a is a rescaled degradation rate, and f is the function describing distribution of auxin synthesis in time and space. Suppose the boundary conditions are known.

Further we think of this PDE as a linear operator, which by acting on one function (auxin concentration) produces another function (distribution of auxin synthesis), $L : u \to f$

$$L[u(x,t)] = \frac{\partial}{\partial t}u - \frac{\partial^2}{\partial x^2}u + \lambda^{-2}\cdot u = f(x,t) \tag{A1.11}$$

A general idea of Green's function. This linear PDEs can be solved with a Green's function, which is an impulse-response function of a differential operator with given boundary conditions. Applied to the problem of auxin diffusion, suppose an impulse (Dirac's δ[1]) of auxin is applied at point x_0 at time t_0:

$$f(x,t) = \delta(x - x_0, t - t_0) \tag{A1.12}$$

[1]Dirac's $\delta(x)$ is an idealized generalized function ("distribution") having following properties: in the point $x = 0$ the function assumes infinitely large value $\delta(x) = \infty$, otherwise it is zero, $\delta(x) = 0$. Its total "weight" is unity: $\int_{-\infty}^{-\infty}\delta(x)\,\mathrm{d}x = 1$

The Green's function $g(x,t)$ is a function that describes the dynamics of auxin in this case:

$$L\,G(x,x_0,t,t_0) = \delta(x-x_0,t-t_0) \tag{A1.13}$$

Knowing the impulse response (Green's) function of the differential operator L, one can find the solution for an arbitrary function $f(x,t)$ as:

$$u(x,t) = \int_{-\infty}^{-\infty} f(x_0,t_0)\cdot G(x,x_0,t,t_0)\,\partial x\,\partial t \tag{A1.14}$$

The Green's function can be constructed from eigenfunctions and eigenvalues of the linear differential operator[2]. Let us denote the n^{th} eigenfunction of the operator L as ψ_n and corresponding eigenvalue as α_n:

$$L\,\psi_n = \alpha_n\,\psi_n \tag{A1.15}$$

Knowing the eigenfunctions, we can decompose the functions of interest, $u(\mathbf{x})$ and $f(\mathbf{x})$, with $\mathbf{x} := (x,t)$, into some linear combination of former functions:

$$u = \sum_n c_n\,\psi_n; \qquad f = \sum_n d_n\,\psi_n \tag{A1.16}$$

The coefficients c_n and d_n are found as an inner product (projection length) of corresponding function onto an eigenfunction:

$$c_n = \langle u,\psi_n\rangle; \qquad d_n = \langle f,\psi_n\rangle = \int_{-\infty}^{+\infty} f\cdot\psi_n^* \tag{A1.17}$$

Taking into account linear independence of eigenfunctions and decomposition A1.16 we can re-express the equation A1.11 as:

$$\begin{aligned} L\,u &= \sum_n \alpha_n\,c_n\,\psi_n \\ \sum_n \alpha_n\,c_n\,\psi_n &= \sum_n d_n\,\psi_n \\ \alpha_n\,c_n &= d_n \end{aligned} \tag{A1.18}$$

[2]Eigenfunctions are functions, which upon the action of the operator are not distorted anyhow, but scaled up or down by some value. This value specific to each of these functions is called eigenvalue. The eigenfunctions are linearly independent, i.e. none of these function can be expressed as a scaled sum of other eigenfunctions.

Therefore,

$$\begin{aligned} u(\mathbf{x}) &= \sum_n c_n \cdot \psi_n(\mathbf{x}) = \\ &= \sum_n \frac{\langle f, \psi_n \rangle}{\alpha_n} \cdot \psi_n = \\ &= \sum_n \psi_n(\mathbf{x}) \cdot \frac{1}{\alpha_n} \int_{-\infty}^{+\infty} f(\mathbf{x}') \cdot \psi_n^*(\mathbf{x}') \, \mathrm{d}\mathbf{x}' = \\ &= \int_{-\infty}^{+\infty} f(\mathbf{x}') \cdot \sum_n \frac{\psi_n(\mathbf{x}) \cdot \psi_n^*(\mathbf{x}')}{\alpha_n} \, \mathrm{d}\mathbf{x}' \end{aligned} \tag{A1.19}$$

where

$$G(\mathbf{x}) = \sum_n \frac{\psi_n(\mathbf{x}) \cdot \psi_n^*(\mathbf{x}')}{\alpha_n} \, \mathrm{d}\mathbf{x}' \tag{A1.20}$$

Finding the Green's function for the problem in steady state. For an operator

$$L[u] = u'' - \lambda^{-2} \, u \equiv u'' - a \, u$$

with simpler boundary conditions, $u(x = 0) = 1$ and $u(x = \infty) = 0$ defined on $x \in (0, \infty)$, one can note that it is the function

$$\psi := \exp(x/\lambda) \equiv \exp(\sqrt{a} \cdot x)$$

for which

$$\psi'' = \lambda^{-2} \, \exp(x/\lambda) = \lambda^{-2} \, \psi \equiv a \, \psi$$

and thus $L[\psi] = \psi'' - \lambda^{-2} \, \psi = 0$. Also any arbitrary function $\psi_b := \exp(\sqrt{b} \, x)$ will be an eigenfunction of the operator, cf. equation (A1.15):

$$L[\psi_b] = \psi_b'' - a \, \psi_b = (b - a) \cdot \psi_b$$

As the equation of interest (A1.10) contains Neumann boundary conditions, i.e. zero-flux at boundaries: $u'_{\text{boundary}} = 0$, we need to ensure that the first derivative of the candidate Green's function produces zero at the boundary points $x = 0$ and $x = 1$. One possible solution is to draw upon Fourier series and select appropriate cosine functions, as discussed in the next section. Another method is to construct the Green function by the method of mirror images, by adding together mirrored exponential, whose first derivatives

will annihilate at the boundary points:

$$u = \int_0^1 f(\xi) \cdot g(x,\xi)\, d\xi$$
$$g(x,\xi) = \frac{1}{2\,\lambda} \cdot \sum_{n=-\infty}^{\infty} \left(\exp\left(-\frac{|x-\xi+2\,n|}{\lambda} \right) + \exp\left(-\frac{|x+\xi+2\,n|}{\lambda} \right) \right) \tag{A1.21}$$

A1.3.2 Method of Fourier series

Jean-Baptiste Joseph Fourier (1768–1830) introduced harmonic series decomposition as a method to solve the heat equation, which belongs to the same type as the diffusion equation. The method represents any function of space or time $f(x)$ as a series ($\tilde{f}$) of harmonic (trigonometric) functions of a new variable, frequency (ω): $\tilde{f}(\omega)$. Further it was shown that such series converges almost everywhere for the square-integrable (L_2 class) functions by Lennart Carleson in 1966.

In the light of the method of Green's function, with the Fourier method, we look for a set of harmonic eigenfunctions. The set of harmonic functions $\{\exp(i \cdot \omega_n \cdot x)\}$ is known to be orthogonal.

The theory of the Fourier analysis allows to re-express differential operators in space/time domain into operation of multiplication in frequency domain:

$$\begin{aligned} f(x) &\to \tilde{f}(\omega) \\ \frac{\partial f(x)}{\partial x} &\to i \cdot \omega \cdot \tilde{f}(\omega) \end{aligned} \tag{A1.22}$$

Taking Fourier transform of the equation A1.10 in respect to space (not time), one obtains:

$$\frac{\partial}{\partial t}\tilde{u}(\omega,t) = -(\omega^2 + \lambda^{-2}) \cdot \tilde{u}(\omega,t) + \tilde{f}(\omega,t) \tag{A1.23}$$

This way, an ordinary differential equation is yielded. It can be solved as:

$$\tilde{u}(\omega,t) = \exp(-(\omega^2 + \lambda^{-2}) \cdot t) \cdot \left(\tilde{u}(\omega, t=0) + \int^t \exp((\omega^2 + \lambda^{-2}) \cdot \tau) \cdot f(\omega,\tau)\, \mathrm{d}\tau \right) \tag{A1.24}$$

Inverse Fourier transform will provide a solution for $u(x,t)$. However, for simplicity, let us consider a stationary case of this problem with Neumann boundary condition (i.e. impenetrable/'reflecting' boundary):

$$-(\omega^2 + a) \cdot \tilde{u}(\omega, t) + \tilde{f}(\omega, t) = 0 \tag{A1.25}$$
$$\frac{\partial}{\partial x} u \Big|_{x \in \text{boundary}} = 0$$

The boundary condition states that the functions satisfying the equation (or in other words a set of functions which the differential operator accepts as input) have zero derivative at the boundary. Therefore, all eigenfunctions should also conform to this condition. In the case of harmonic functions, it is the cosines which have zero-derivative at points $\omega\,\pi$ for integer $\omega = 0, 1, 2, \ldots \infty$. Thus we look for eigenfunctions of type $\cos(\,\pi\,\omega\,x)$ with integer ω and apply discrete cosine Fourier transform. The forward transform in generic case of equation A1.25 stays the same, while the inverse transform yields:

$$u^* = \int_0^1 f(\xi) \cdot g^*(x, \xi)\, d\xi \tag{A1.26}$$
$$g^*(x, \xi) = 1 + 2 \cdot \sum_{\omega=1}^{\infty} \frac{\cos(\pi\,\omega\,x)\cos(\pi\,\omega\,\xi)}{(\pi\,\omega\,\lambda)^2 + 1}$$
$$= 1 + \sum_{\omega=1}^{\infty} \frac{\cos(\pi\,\omega\ [x + \xi]) + \cos(\pi\,\omega\ [x - \xi])}{(\pi\,\omega\,\lambda)^2 + 1}$$

Appendix 2: Supplementary material to the chapter 2 (modelling paper)

A2.1 Formulation of the model in natural dimensions and rescaling

A2.1.1 Equations for variables in natural units

Regime 1 Rate of concentration change in point $\hat{\mathbf{r}}$ at time $\hat{t}$ for regime 1 is expressed as:

$$\underbrace{\frac{\partial \hat{u}(\hat{\mathbf{r}},\hat{t})}{\partial \hat{t}}}_{\text{Rate of concentration change}} = \underbrace{D \cdot \hat{\nabla}^2 \hat{u}(\hat{\mathbf{r}},\hat{t})}_{\text{Diffusion}} - \underbrace{\hat{a} \cdot \hat{u}(\hat{\mathbf{r}},\hat{t})}_{\text{Degradation}} \tag{A2.27}$$

where $\hat{u}(\hat{\mathbf{r}},\hat{t})$ is the concentration, D is diffusion constant, $\hat{a}$ is degradation rate. The 'hat' accent over variables indicates that they are expressed in natural dimensions (as opposed to re-scaled variables introduced in the main text and later here). The 'hat' over 'nabla' operator ($\hat{\nabla}$) indicates that the differentiation is done by the spatial coordinate $\hat{\mathbf{r}}$ expressed in natural dimensions (m). The boundary conditions are following:
a) boundary with influx (micropilar pole):

$$D \cdot \mathbf{n} \cdot \hat{\nabla} \hat{u}(\hat{\mathbf{r}},\hat{t})|_{\hat{\mathbf{r}} \in S_{\text{influx}}} = \hat{p}$$

b) impenetrable boundary (other parts of the membrane):

$$D \cdot \mathbf{n} \cdot \hat{\nabla} \hat{u}(\hat{\mathbf{r}},\hat{t})|_{\hat{\mathbf{r}} \in S \setminus S_{\text{influx}}} = 0$$

where $\mathbf{n}$ is outward pointing unit vector, S is the boundary (plasma membrane), and S_{influx} – part of boundary where influx occurs.

Regime 2 Rate of concentration change in point $\hat{\mathbf{r}}$ at time $\hat{t}$ for regime 2 is expressed as:

$$\underbrace{\frac{\partial \hat{u}(\hat{\mathbf{r}},\hat{t})}{\partial \hat{t}}}_{\text{Rate of concentration change}} = \underbrace{D \cdot \nabla^2 \hat{u}(\hat{\mathbf{r}},\hat{t})}_{\text{Diffusion}} - \underbrace{\hat{a} \cdot \hat{u}(\hat{\mathbf{r}},\hat{t})}_{\text{Degradation}} + \underbrace{\hat{b}(\hat{\mathbf{r}},\hat{t})}_{\text{Synthesis}} \tag{A2.28}$$

where $\hat{u}(\hat{\mathbf{r}},\hat{t})$ is the concentration, D is diffusion constant, $\hat{a}$ is degradation rate. Zero-flux boundary conditions:

$$\mathbf{n} \cdot \hat{\nabla} \hat{u}(\hat{\mathbf{r}}, \hat{t})|_{\hat{\mathbf{r}} \in S} = 0$$

A2.1.2 Regime 4

For the regime for, we use the equation (A2.27) with modified boundary conditions. In natural dimensional units the right (efflux, in one dimension at $x = 1$) boundary condition reads as:

$$D\, \hat{\nabla} \hat{u} = -\hat{q}\, \hat{u} \tag{A2.29}$$

where v is influx velocity (m/s) D is diffusion constant (m^2/s);

A2.1.3 Rescaling scheme

In order to simplify the equations A2.27 and A2.28, we rescale the variables as following:

$$\hat{\mathbf{r}} = \mathbf{r} \cdot L \qquad \hat{t} = t \cdot \tau$$

$$\tau = L^2/D \qquad \hat{u} = u \cdot \hat{u}_T^*$$

$$\hat{b}(\hat{\mathbf{r}}, \hat{t}) = \hat{b}_0 \cdot \hat{f}(\hat{\mathbf{r}}, \hat{t}) \qquad \int_V \hat{f}(\hat{\mathbf{r}}, \hat{t})\, d\hat{\mathbf{r}} = 1$$

$$\hat{b}_0 = \frac{\hat{u}_T^*}{\tau} \cdot b \qquad \hat{p} = \frac{D \cdot \hat{u}_T^*}{L} \cdot p$$

$$a = \hat{a} \cdot \tau = \hat{a} \cdot \frac{L^2}{D} \qquad \ell = \frac{\lambda}{L} = \frac{1}{a} = \frac{1}{L} \cdot \sqrt{\frac{D}{a}}$$

Where V is the volume of the domain (FG). The final non-dimensional form is given in Table **1** in the main text.

A2.1.4 Parameter interdependence

Experimental estimation of the synthesis rate is more challenging than one of degradation rate, because it requires study of precursor conversion kinetics. However, taking the steady-state concentration and degradation rate of auxin, the rate of synthesis can be estimated based on mass conservation. We define average concentration of auxin in the FG as:

$$\hat{u}_T(t) = \frac{1}{V} \cdot \int_V \hat{u}(\hat{\mathbf{r}}, \hat{t})\, d\hat{\mathbf{r}} \tag{A2.30}$$

Assuming that the concentration along the boundaries is approximately the same (which is true, as we further find), the conservation conditions read as:

	regime 1 & 4	regime 2
Dynamic	$\frac{\partial}{\partial t}\hat{u}_T = -\hat{a}\cdot\hat{u}_T + \hat{p}(t)\cdot\frac{S_{\text{influx}}}{V}$ $+\hat{q}\cdot(\hat{u}_T - \hat{u}_{\text{out}})\cdot\frac{S_{\text{influx}}}{V}$	$\frac{\partial}{\partial t}\hat{u}_T = -\hat{a}\cdot\hat{u}_T + \hat{b}_0(t)$
Steady state	$\hat{p}^* = \hat{a}\cdot\hat{u}_T^*\cdot\frac{V}{S_{\text{influx}}}$	$\hat{b}_0^* = \hat{a}\cdot\hat{u}_T^*$

where $\hat{u}_T^*$ is the average steady state concentration of auxin within the FG and $\hat{u}_{\text{out}}$ is the auxin concentration outside.

In the rescaled form in the steady state, the source terms can be expressed in terms of degradation rate as:

$$p = a\cdot\frac{V}{L\cdot S_{\text{influx}}} + q\cdot(1-\hat{u}_{\text{out}}/\hat{u}_T); \qquad \text{for regimes 1 \& 4}$$

$$b = a \qquad \text{for regimes 2}$$

A2.2 A model for carrier-independent transmembrane fluxes due to auxin dissociation

General formulation of the carrier-independent flux model. Auxin undergoes dissociation according to reaction:

$$\underbrace{\mathrm{HA}}_{u_1} \underset{k_a}{\overset{k_d}{\rightleftharpoons}} \mathrm{H^+} + \underbrace{\mathrm{A^-}}_{u_2} \tag{A2.31}$$

where $\mathrm{A^-}$ is its dissociated (anionic) form and HA is the protonated form. Dissociation constant represents ratio of product of dissociation product concentrations to the protonated form in equilibrium:

$$K = \frac{k_d}{k_a} = \frac{[\mathrm{H^+}]^{**} \cdot [\mathrm{A^-}]^{**}}{[\mathrm{HA}]^{**}} \tag{A2.32}$$

Let us denote:

$$\mathbf{u} = \begin{bmatrix} [\mathrm{HA}] \\ [\mathrm{A^-}] \end{bmatrix}$$

Then dissociation-reassociation dynamics can be described in non-dimensional units as:

$$\frac{\partial}{\partial t}\mathbf{u} = \tau \begin{bmatrix} -k_d & k_a \cdot [\mathrm{H^+}] \\ k_d & -k_a \cdot [\mathrm{H^+}] \end{bmatrix} \mathbf{u} = \beta \begin{bmatrix} -1 & \gamma \\ 1 & -\gamma \end{bmatrix} \mathbf{u}$$

with $\beta = \tau \cdot k_d$ and $\gamma = [\mathrm{H^+}]/K = 10^{(pK-pH)}$. For the homogeneous system (eq. A2.31) at the steady state, γ represents the concentration ratio of anionic to the protonated form:

$$\gamma = \frac{u_1^{**}}{u_2^{**}} = \frac{[\mathrm{HA}]^{**}}{[\mathrm{A^-}]^{**}}$$

Reaction-diffusion process can be expressed as a PDE:

$$\frac{\partial}{\partial t}\mathbf{u} = \nabla^2\mathbf{u} - a\,\mathbf{u} + \beta \begin{bmatrix} -1 & \gamma \\ 1 & -\gamma \end{bmatrix} \mathbf{u} \tag{A2.33}$$

Let us put:

$$\mathbf{B} = \begin{bmatrix} -(a+\beta) & \beta\,\gamma \\ \beta & -(a+\beta\,\gamma) \end{bmatrix}; \qquad \mathbf{p} = p \begin{bmatrix} 1 \\ 0 \end{bmatrix}; \qquad \mathbf{Q} = \begin{bmatrix} q_1 & 0 \\ 0 & q_2 \end{bmatrix}$$

Then we can rewrite:

$$\frac{\partial}{\partial t}\mathbf{u} = \nabla^2\mathbf{u} + \mathbf{B}\,\mathbf{u} \tag{A2.34}$$

with boundary conditions: $\nabla\mathbf{u}|_{\Gamma_m} = -\mathbf{p}$ and $\nabla\mathbf{u}|_{\Gamma_c} = -\mathbf{Q}\,(\mathbf{u}|_{\Gamma_c} - \mathbf{u}_{out})$, where p is influx rate and q is permeability.

In dimensional form they can be re-writen as

$$D \cdot \hat{\nabla}\hat{\mathbf{u}}|_{\Gamma_m} = -\hat{\mathbf{p}} \quad \text{and} \quad D \cdot \hat{\nabla}\hat{\mathbf{u}}|_{\Gamma_c} = -\hat{\mathbf{Q}}\,(\hat{\mathbf{u}}|_{\Gamma_c} - \hat{\mathbf{u}}_{out})$$

Simplification of the model for carrier-independent fluxes. Taking into account the fact that auxin dissociation is quite fast, $\beta \approx 10^5 \gg 1$, in other words $k_d \gg D \cdot L^{-2}$, the equation A2.33 can be re-written as:

$$\begin{bmatrix} -1 & \gamma \\ 1 & -\gamma \end{bmatrix} \mathbf{u}^{**} = \frac{1}{\beta}\left(\frac{\partial}{\partial t}\mathbf{u}^{**} - \nabla^2\mathbf{u}^{**} + a\,\mathbf{u}^{**}\right) \approx 0 \quad \Rightarrow \quad u_1^{**} \approx \gamma \cdot u_2^{**}$$

Assume $\mathbf{u}_{out} = 0$. Then the efflux rate for aggregate concentration, $u_{\text{aggr}} = u_1 + u_2$, satisfying

$$\nabla u_{\text{aggr}}|_{x=1} = q_{\text{aggr}} \cdot\, u_{\text{aggr}}|_{x=1}$$

can be estimated as:

$$q_{\text{aggr}} \approx \frac{\mathbf{u}^{**} \cdot \mathbf{q}}{\mathbf{u}^{**} \cdot \mathbf{e}} = \frac{\mathbf{r} \cdot \mathbf{q}}{\mathbf{r} \cdot \mathbf{e}} = \frac{\gamma\, q_1 + q_2}{\gamma + 1} \tag{A2.35}$$

Where $\mathbf{r} = \begin{bmatrix}\gamma & 1\end{bmatrix}^T$, $\mathbf{e} = \begin{bmatrix}1 & 1\end{bmatrix}^T$.

$$p \approx \frac{2 \cdot q_{\text{aggr}}}{q_{\text{aggr}} + 2}$$

Thermodynamic aspect of the carrier-independent flux model and formulation in terms of anisotropic diffusion. Here we re-formulate the trans-membrane flow in terms of continuously defined function to facilitate its simulation. We include the apoplast and membrane as subdomains alongside with the cytosole. Generally, the flux can be described as (Schultz, 1980):

$$j(x) = -\hat{u} \cdot v$$

where $v = \zeta \cdot f$ is the velocity of the particles with mobility ζ driven by the force f. The force in our case is the difference in Gibbs potentials, $\Delta\mu$, where potential in each compartment can be found as:

$$\mu = \mu^0 + RT \ln u + z_i \cdot \psi \cdot F$$

We assume no influence of electric potential, ψ. The mobility is given by the Einstein's relation:

$$\zeta = \frac{D}{RT}$$

Thus the flux

$$\hat{j}(\hat{x}) = -\hat{u} \cdot \zeta \cdot \left[RT \frac{\partial \ln(\hat{u})}{\partial \hat{x}} + \frac{\partial \mu_0(\hat{x})}{\partial \hat{x}} \right] = -D \cdot \exp\left(-\frac{\mu_0}{RT}\right) \cdot \frac{\partial}{\partial \hat{x}} \left[\hat{u} \cdot \exp\left(\frac{\mu_0(\hat{x})}{RT}\right) \right]$$

Assuming quasi-steady state, namely the constant flux of the matter throughout the membrane:

$$j_{\mathrm{m}} \not\sim j_{\mathrm{m}}(\hat{x}) \qquad \left.\frac{\partial \hat{u}}{\partial \hat{x}}\right|_{\mathrm{m}} = \frac{\Delta_{\mathrm{m}} \hat{u}}{\Delta_{\mathrm{m}} \hat{x}}$$

The flux can be expressed in terms of permeability as:

$$j_{\mathrm{m}} = -P \cdot \Delta_{\mathrm{m}} \hat{u} = -D_{\mathrm{m}} \cdot K_{\mathrm{p}} \cdot \frac{\Delta_{\mathrm{m}} \hat{u}}{\Delta_{\mathrm{m}} \hat{x}}$$

where P is the membrane permeability, D_{m} is the coefficient of the species diffusion within the lipid (membrane); K_{p} is the partition coefficient of the chemical species between lipid (membrane) and water (cytosol) phase:

$$K_{\mathrm{p}} = \frac{u_{\mathrm{m}}}{u_{\mathrm{cyt}}} = \exp\left(\frac{\mu_0^{\mathrm{cyt}} - \mu_0^{\mathrm{m}}}{RT}\right)$$

Thus one can estimate diffusion coefficient as

$$D_{\mathrm{m}} = P \cdot \Delta_{\mathrm{m}} \hat{x} \cdot K_{\mathrm{p}}^{-1}$$

It is worth to note that the error in the values of $\Delta_{\mathrm{m}} \hat{x}$, K_{p}, and as a result in D_{m} will affect not the accuracy of the transmembrane flux rate (j_{m}) values, but only the accuracy of the intramembrane concentration values.

A2.3 A general inter-compartmental flux model for estimation of flux parameters

Assume the efflux of auxin from the protoplasts is un-saturated (as only 500 nM were applied; cf. $K_M^{\mathrm{AUX1}} = 843$ nM, Yang et al., 2006) and follows the equation:

$$\begin{aligned} \frac{\partial}{\partial \hat{t}} \hat{u} &= \underline{\hat{\nabla}} \cdot \underline{J(\hat{u})} = \widehat{\mathrm{div}} \left(\underline{J(\hat{u})} \right) \\ J(\hat{u})|_V &= D \, \hat{\nabla} \, \hat{u} \\ J(\hat{u})|_S \cdot \mathbf{n} &= -q \cdot \hat{u} + p \cdot \hat{v} \end{aligned} \tag{A2.36}$$

where $\hat{u}$ is the auxin concentration (within the cell), $\hat{v}$ – outside the cell. Here we assumed linear dependence of the efflux rate on the concentration (no saturation as Michaelis-Menten or Hill), with the efflux rate in wild type protoplasts comprised of the efflux due to PGP1 and other transport mechanisms: $q = q_{\mathrm{PGP1}} + q_{pgp1}$. The transport rate due to the PGP1 depends on a transport rate constant and the concentration of the PGP1 (molecules per unit area): $q_{\mathrm{PGP1}} = k \cdot \hat{c}_{\mathrm{PGP1}}$.

Applying Gauss theorem to the equation (A2.37):

$$\begin{aligned} \frac{\partial}{\partial \hat{t}} \int_V \hat{u} &= -\int_V \hat{\nabla} J(\hat{u}) = -\oint_S J(\hat{u}) \\ \frac{\partial}{\partial \hat{t}} \int_V \hat{u} &= -\oint_S (q_{pgp19} + k \cdot \hat{c}_{\mathrm{PGP1}}) \cdot \hat{u} + \oint_S p \cdot \hat{v} \end{aligned} \tag{A2.37}$$

Assume the concentration of both auxin and transporters is constant:

$$\begin{aligned} \frac{\partial}{\partial \hat{t}} \hat{u} &= -\frac{S}{V} \cdot (q_{pgp19} + q_{\mathrm{PGP1}}) \cdot \hat{u} \\ q_{\mathrm{PGP1}} = k \times \hat{c}_{\mathrm{PGP1}} &= \left[\left(s \cdot \frac{mol}{m^3} \right)^{-1} \times \frac{mol}{m^2} \right] = [m/s] \end{aligned} \tag{A2.38}$$

Where the ratio of the surface area to the volume of the spheric protoplasts is $S/V = 3/R$.

Rescaling of the linear inter-compartmental flux model of protoplasts in suspension
By applying following re-scaling

$$\begin{aligned} t &:= \hat{t}/\tau && \text{where } \tau := R/q && \text{is characteristic efflux time} \\ x &:= \hat{x}/R && \text{where } r := D/R && \text{is characteristic diffusion velocity} \\ u &:= \hat{u}/\hat{u}_T && \text{where } \hat{u}_T := \int_V \hat{u}(t=0) && \text{is the total auxin amount in the cells} \end{aligned} \tag{A2.39}$$

to the equation (A2.37) one obtains:

$$\begin{aligned} J(u)|_V &= \frac{r}{q} \nabla u \\ \frac{\partial}{\partial t} u &= \nabla J(u) = \frac{r}{q} \cdot \nabla^2 u \\ J(u)|_S \cdot \mathbf{n} &= -u + \frac{p}{q} \cdot v \end{aligned} \tag{A2.40}$$

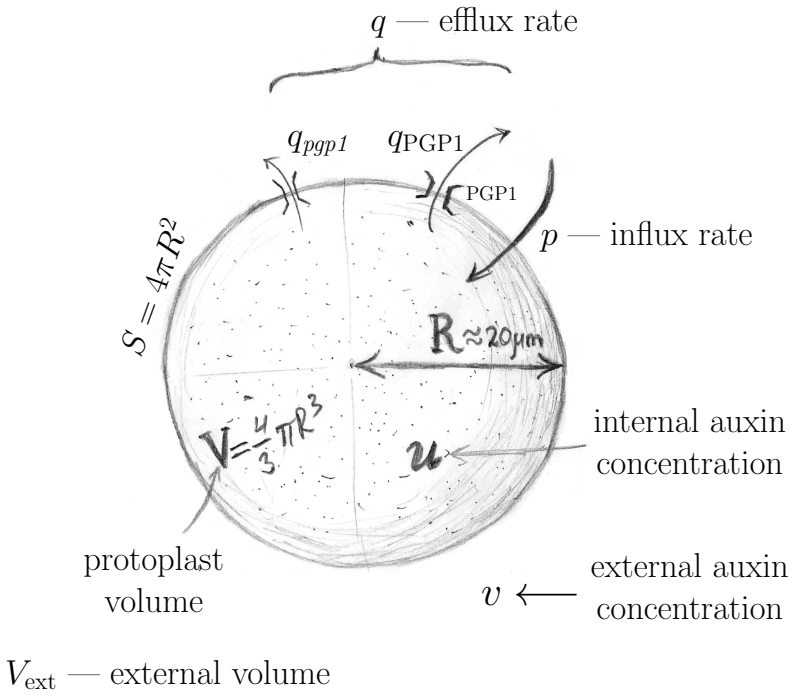

Figure **8**: Schematic representation of the parameters and processes of the transmembrane flux model

Now, assume that at the given length scale L, diffusion is much faster than efflux, $r(L) \gg q$:

$$\frac{q}{r} \cdot J(u)\Big|_V = \nabla u|_V \approx 0 \quad \Rightarrow \quad u \neq u(x) \tag{A2.41}$$
$$J(u)|_S = \left[-u + \frac{p}{q} \cdot v\right]_S$$

This allows us to connect the total amount (in mole,) and the average concentrations (from now on denoted simply u and v) as $\hat{u}_T = u \cdot V$ and $\hat{v}_T = v \cdot V_{\text{ext}}$. To find the total amount, we integrate over the volume for the auxin within protoplast:

$$\frac{\partial}{\partial t}\int_V u = -\oint_S J(u) = -\oint_S u + \frac{p}{q} \cdot \oint_S v \tag{A2.42}$$

and analogously for auxin in the external medium. Now we rewrite it by replacing the

total concentrations by the averages:

$$\begin{aligned} \frac{V}{S} \cdot \frac{\partial}{\partial t} u &= -u + \frac{p}{q} \cdot v \\ \frac{V_{\text{ext}}}{S} \cdot \frac{\partial}{\partial t} v &= \quad u - \frac{p}{q} \cdot v \end{aligned} \tag{A2.43}$$

Further we define auxillary parameter groups:

$$\begin{aligned} \omega &:= \frac{V}{V_{\text{ext}}} && \text{volume ratio} \\ \kappa &:= \frac{p}{q} && \text{ratio of the in- and efflux rates} \\ \beta &:= \omega\, \kappa \\ \alpha &:= 3 \cdot (1 + \beta) \end{aligned} \tag{A2.44}$$

and re-write the equation (A2.42) as:

$$\begin{aligned} \dot{u} &= 3\,(-u + \kappa \cdot v) \\ \dot{v} &= -\omega \cdot \dot{u} \end{aligned} \tag{A2.45}$$

The steady-state solution can then be fount as:

$$\begin{aligned} u^*/v^* &= \kappa \\ v &= \omega\,(u_0 - u) \end{aligned} \tag{A2.46}$$

Hence, the stationary ratio of the auxin concentration within the protoplast to the concentration in the medium is equal to the ratio of the influx rate to the efflux rate. The constant u_0 is given by the initial condition $u(t = 0) = u_0$ and $v(t = 0) = 0$ of the equation (A2.42), i.e. it is the amount of auxin loaded into the cells before the beginning of the experiment. The dynamic solution can then be found as:

$$\begin{aligned} u &= C_1\,\kappa - C_2\,\frac{1}{\omega}\exp(-\alpha\, t) \\ v &= C_1 + C_2 \exp(-\alpha\, t) \end{aligned} \tag{A2.47}$$

Setting the initial conditions:

$$\begin{aligned} v(t=0) := 0 = C_1 + C_2 \quad &\Rightarrow \quad C_2 = -C_1 \\ u(t=0) := u_0 = C_1 \left(\kappa + \frac{1}{\omega}\right) & \\ C_1 = \left(\kappa + \frac{1}{\omega}\right)^{-1} \cdot u_0 &= \frac{\omega}{\beta+1}\, u_0 \end{aligned} \tag{A2.48}$$

We arrive to

$$\begin{aligned} u(t) &= u_0\, \frac{\beta + \exp(-\alpha\, t)}{\beta+1} \\ v(t) &= \omega\, u_0\, \frac{1 - \exp(-\alpha\, t)}{\beta+1} \end{aligned} \tag{A2.49}$$

Assuming further that the volume of the external medium is large and the influx rate is small compared to the efflux rate so that $\beta \approx 0$. Then:

$$u = u_0 \cdot \exp(-3\, t) = u_0 \cdot \exp\Big(-\frac{3\, q}{R} \cdot \hat{t}\Big) \tag{A2.50}$$

Define measured efflux rate as:

$$\hat{q} := \frac{3}{\tau} = q\, \frac{\hat{S}}{\hat{V}} = q\, \frac{3}{R} = \left[s^{-1}\right] = \left[\frac{\mathrm{m/s}}{\mathrm{m}}\right] \tag{A2.51}$$

then

$$u = u_0 \exp\Big(-\hat{q}\, \hat{t}\Big) \tag{A2.52}$$

Analogously for the case of a large β, define measured aggregate flux rate:

$$\hat{\alpha} := \alpha/\tau = \alpha\, \frac{q}{R} = \frac{3}{R}\, (1+\beta)\, q = (1+\beta)\, \hat{q} = \frac{3}{R}\, (q + p\, \omega) \tag{A2.53}$$

Log-linear equations become:

$$\begin{aligned} \ln\Big(\frac{u}{u_0}\, (1+\beta) - \beta\Big) &= -\alpha\, t = -(1+\beta)\, \hat{q}\, \hat{t} \\ \ln\Big(1 - \frac{v}{\omega\, u_0}\, (1+\beta)\Big) &= -\alpha\, t = -(1+\beta)\, \hat{q}\, \hat{t} \end{aligned} \tag{A2.54}$$

Alternatively, assume that the membrane is non-selectively permeable, $p = q$ hence $\beta = \omega$, then the equilibrium concentration with $t \to \infty$ in both compartments will be $u_0\, \frac{V}{V+V_{\mathrm{ext}}}$.

PGP1 efflux rate estimated with the linear model. Given the estimate of the efflux rate for the wild type (wt) and mutant (*pgp1*, *pgp19*, and {*pgp1, pgp19*}) protoplasts, we can estimate the contribution of the transporters assuming additivity of rates:

$$q_{\text{wt}} = q_{pgp1} + q_{\text{PGP1}} \tag{A2.55}$$

$$= q_{pgp19} + q_{\text{PGP19}} \tag{A2.56}$$

$$= q_{pgp1,\ pgp19} + q_{\text{PGP1}} + q_{\text{PGP19}} \tag{A2.57}$$

These parameters can be estimated from the data of the study of ^{3}H-IAA efflux presented in (Geisler et al., 2005). Additionally we assume that the diameter of the *A.thaliana* protoplasts is around 30 – 50 µm. Taking the average radius $r = 20\mu\text{m}$, one can estimate the specific PGP1-dependent transport activity as:

$$q = \hat{q} \times \frac{R}{3} \tag{A2.58}$$

$$q = 1.1 \cdot 10^{-3} s^{-1} \times \frac{20\,\mu\text{m}}{3} = 7.3 \cdot 10^{-3}\,\mu\text{m / s} = 7.3 \cdot 10^{-9}\,\text{m / s}$$

Three alternative assumptions can be made as to the product of the influx rate and the cytoplasm-to-medium ratio: (1) it is independent in all the samples; (2) it is common for all the samples; (3) there is no influx. The results obtained based on these assumptions are presented in the fig. **9** and tables **??**, **??**, and **??**.

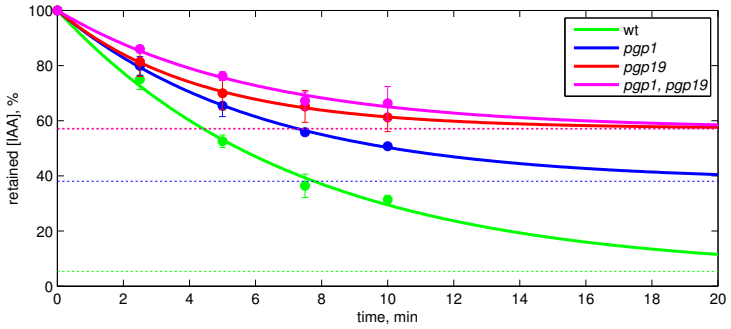

(a)

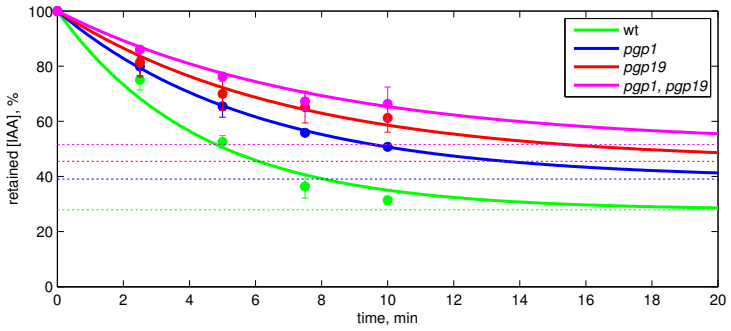

(b)

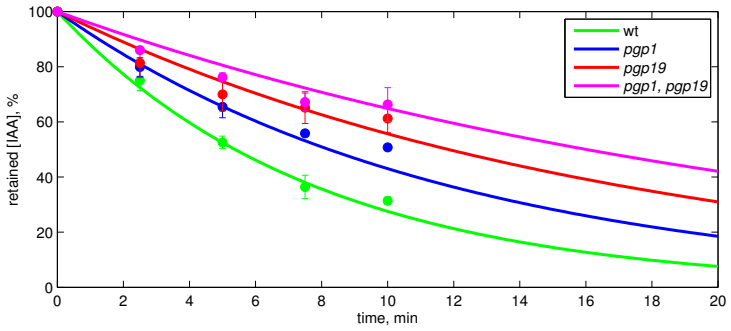

(c)

Figure **9**: Non-linear least squares fit,
Simple, $\hat{q}_{PGP1} = 0.48 \cdot 10^{-3}\text{s}^{-1}$; $R^2 = 2.64 \cdot 10^{-3}$
a Assuming the common influx rate p and volume ratio ω for all experiments,
$\hat{q}_{PGP1} = 1.10 \cdot 10^{-3}\text{s}^{-1}$; $\omega \times \hat{p} = 1.08 \cdot 10^{-3}\text{s}^{-1}$; $R^2 = 4.43 \cdot 10^{-3}$
b Assuming no influx, $\beta = 0$,
$\hat{q}_{PGP1} = 7.44 \cdot 10^{-4}\text{s}^{-1}$; $R^2 = 7.89 \cdot 10^{-3}$

Table **9**: Fitted efflux rate values, non-fixed $\omega \times p$, $R^2 = 2.64 \cdot 10^{-3}$

	q [m/s]	$\hat{q}$ [s^{-1}]	τ_q [min]
PGP1	$3.44 \cdot 10^{-9}$	$5.17 \cdot 10^{-4}$	32.3
PGP19	$3.20 \cdot 10^{-9}$	$4.79 \cdot 10^{-4}$	34.8
PGP1 + PGP19	$4.61 \cdot 10^{-9}$	$6.92 \cdot 10^{-4}$	24.1
wt	$14.3 \cdot 10^{-9}$	$21.5 \cdot 10^{-4}$	7.8
pgp1	$10.9 \cdot 10^{-9}$	$16.3 \cdot 10^{-4}$	10.2
pgp19	$11.1 \cdot 10^{-9}$	$16.7 \cdot 10^{-4}$	10
pgp1 pgp19	$9.71 \cdot 10^{-9}$	$14.6 \cdot 10^{-4}$	11.4

Table **10**: Fitted efflux rate values with the common influx rate and volume ratio, $\omega \times \hat{p} = \text{const} = 1.08 \cdot 10^{-3} s^{-1}$, $R^2 = 4.43 \cdot 10^{-3}$

	q [m/s]	$\hat{q}$ [s^{-1}]	τ_q [min]
PGP1	$7.34 \cdot 10^{-9}$	$1.10 \cdot 10^{-3}$	15.1
PGP19	$9.94 \cdot 10^{-9}$	$1.49 \cdot 10^{-3}$	11.2
PGP1 + PGP19	$11.8 \cdot 10^{-9}$	$1.77 \cdot 10^{-3}$	9.4
wt	$18.6 \cdot 10^{-9}$	$2.78 \cdot 10^{-3}$	6.0
pgp1	$11.2 \cdot 10^{-9}$	$1.68 \cdot 10^{-3}$	9.9
pgp19	$8.62 \cdot 10^{-9}$	$1.29 \cdot 10^{-3}$	12.9
pgp1 pgp19	$6.75 \cdot 10^{-9}$	$1.01 \cdot 10^{-3}$	16.4

Table **11**: Fitted efflux rate values assuming no influx, $\beta = 0$, $R^2 = 7.89 \cdot 10^{-3}$

	q [m/s]	$\hat{q}$ [s^{-1}]	τ_q [min]
PGP1	$4.96 \cdot 10^{-9}$	$0.744 \cdot 10^{-3}$	22.4
PGP19	$7.80 \cdot 10^{-9}$	$1.17 \cdot 10^{-3}$	14.2
PGP1 + PGP19	$9.52 \cdot 10^{-9}$	$1.43 \cdot 10^{-3}$	11.7
wt	$14.3 \cdot 10^{-9}$	$2.15 \cdot 10^{-3}$	7.8
pgp1	$9.37 \cdot 10^{-9}$	$1.41 \cdot 10^{-3}$	11.9
pgp19	$6.51 \cdot 10^{-9}$	$97.6 \cdot 10^{-3}$	17.1
pgp1 pgp19	$4.81 \cdot 10^{-9}$	$72.2 \cdot 10^{-3}$	23.1

A2.4 Estimation of auxin degradation rate

Here we estimate degradation rate based on data presented in (Sequeira and Mineo, 1966). For the auxin mass-to-molarity conversion we use following constants:

$$\text{molecular weight of IAA} = 175.19\text{g/mol} \tag{A2.59}$$
$$1\ \mu\text{g/ml} \equiv 5.7\ \mu\text{M}$$

The substrate inhibition of of crude IAA oxidase enzymatic activity observed at concentrations higher than 400 µM, should not be relevant, as physiological concentrations are under 50 µM. Michaelis-Menten constant as determined by the authors: $K_M = 0.42 \ldots 0.45$ mM ≈ 435 µM. For the linear region the crude oxidase activity can be estimated as following:

$$\dot{\hat{c}} = \frac{dc}{dt} = -\hat{a} \cdot \hat{c} \tag{A2.60}$$
$$\hat{a} = \frac{v_{0,\max}}{K_M} = \frac{k \cdot [\text{Enzyme}]}{K_M}$$
$$\hat{a}_{in\ vitro} = \frac{\dot{\hat{c}}}{\hat{c}} = 0.019\ \text{min}^{-1} = 3.17 \cdot 10^{-4}\ \text{min}^{-1}$$

where we will denote the dimensional values with 'hat' accent.

As the reaction rate depends on concentration of the enzyme, we need to account for the dilution factor. The 'crude IAA oxidase' is obtained from root tissue ground in phosphate solution in proportion of 10g:50ml (dilution factor 1/6); after dialysis and precipitation the pellet was dissolved in 1/4 of the initial volume. Aggregate dilution factor: $4/6 = 2/3$=0.67. Thus, the value of $\hat{a}$ for in vitro experiment should be multiplied by 3/2=1.5. Finally, the oxidation rate *in vivo* is estimated as:

$$\hat{a}_{in\ vivo} = 1.5 \times \hat{a}_{in\ vitro}; \tag{A2.61}$$
$$\hat{a}_{in\ vivo} = 1.5 \times 3.17 \cdot 10^{-4}\ \text{s}^{-1} =$$
$$= 4.85 \cdot 10^{-4}\ \text{s}^{-1} \approx 5 \cdot 10^{-4}\ \text{s}^{-1};$$

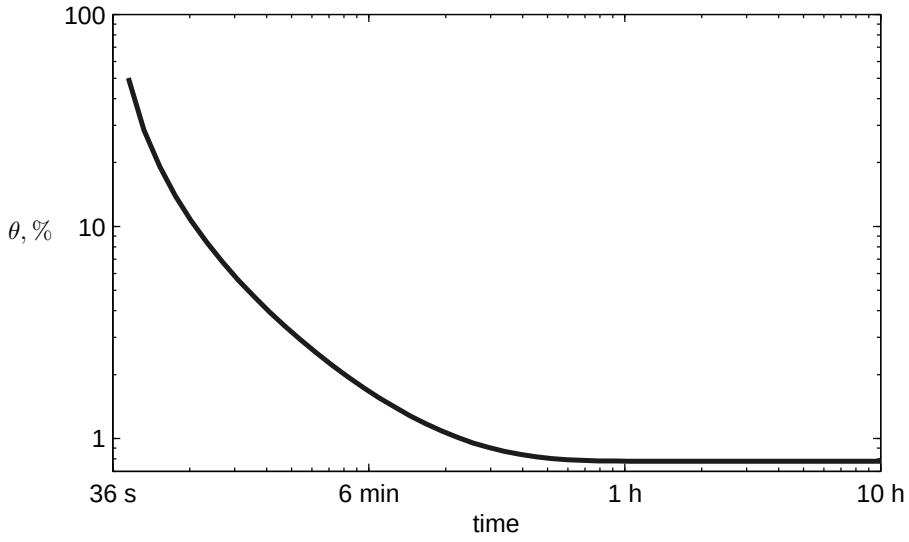

(a)

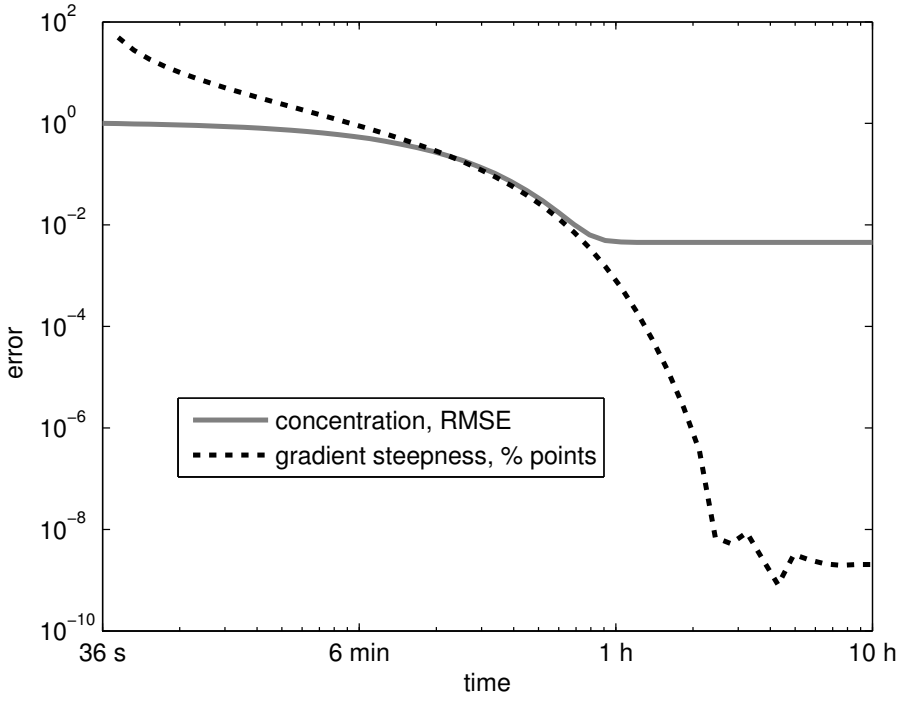

(b)

Figure **10**: The steady state is reached within the first 2 hours with accuracy of a root mean-square error (RMSE) = 0.0046, and error in θ of $\approx 5 \cdot 10^{-4}$ percentage points in the one dimensional model, regime 1. **10**a Dynamics of the gradient steepness. **10**b Dynamics of the root mean-square error of the concentration and the absolute value of the error of the gradient steepness θ. Relative error tolerance of the PDE solver was set to 10^{-6}.

Appendix 3. Inference Algorithm for Mutation Mapping with High-Throughput Sequencing

Dmytro Lituiev, Ueli Grossniklaus,
Institute of Plant Biology, University of Zürich

A3.1 Introduction

A3.1.1 Background

The mapping of mutations and their molecular cloning is a key step in genetic studies and important for many aspects of breeding. Using high-throughput DNA sequencing, the time required for mapping and cloning can be drastically reduced by substituting the screening of individual markers with multiple analytical reactions by a single sequencing run.

However, the inherent stochasticity of mutagenesis and sequencing technologies leads to noisiness in the sequencing data. This leads to high sequencing costs for high sequence coverage. Several algorithms have been proposed for handling the noise, based on kernel filtering (Austin et al., 2011; Schneeberger et al., 2009) or goodness-of-fit tests for linkage (Lindner et al., 2012). However, a further increase in the effectiveness of these approaches will require more reliable statistical prediction procedures which also incorporates available prior knowledge.

A3.1.2 Aim

The aim of this study is to develop an inference procedure for sequencing-assisted genetic mapping and find optimal experimental setup, namely the number of plants taken for analysis and sequencing coverage. For this, we implement a continuous space hidden Markov chain model describing the inheritance of the mutations under and without selection for inference of the position of the former ones. The model is designed to provide for possibility to incorporate the knowledge on genetic linkage and effect of the mutations on the protein sequence.

A3.1.3 Experimental Procedure: Crosses and Selection

After the chemical mutagenesis, the individual with desired phenotype is picked out and subjected to analytical crosses. The **first cross** for any kind of genetic mapping aims at the introduction of allelic inhomogeneity via:

- back-cross (employs 'background' mutations)
- out-cross (employs polymorphisms from another ecotype or cultivar)

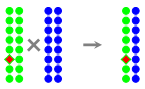

The **second cross** aims at obtaining recombinant progeny to study linkage and segregation by means of:

- back-cross

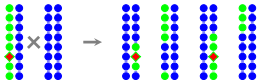

- selfing

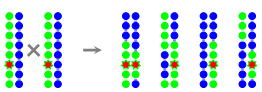

As an example we considered data by Lindner et al. (2012). The mutagenised plant with desired trait was backcrossed twice and

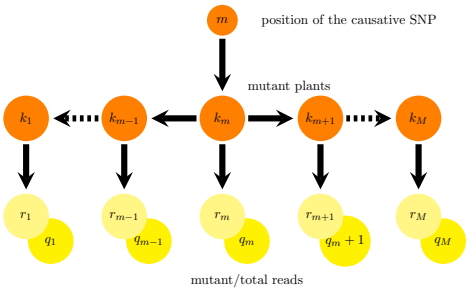

Fig. 1: Graph model of the mutation mapping process. See text for description

DNA from a pool of second generation individuals with the phenotype of interest was analyzed. Sequencing yielded a set of short reads which indirectly characterize the genotype of the studied individuals.

A3.2 Results

A3.2.1 Graph Model

The model describes the joint probability distribution for the mutant plants and read frequencies in F_2 population (and its DNA pool) along the chromosomes. The number of SNP-carrying plants are hidden nodes (shown in orange), while the read frequencies are observed ones (yellow).

A3.2.2 Probability Assignment

The probabilities are assigned based on the following three considerations:

1. The joint probabilities of SNP inheritance are defined by **genetic linkage**. The correspondence between the physical position and the sequence is interpolated from published data (Singer et al., 2006). The probability of frequencies of SNP-carriers adjacent to the locus under selection (the causative SNP) is defined by the continuous space Markov chain (Ehrenfest-like (Ehrenfest, 1907)) model (Feingold, 1993; Töpfer et al., 2013):

$$\frac{\mathrm{d}}{\mathrm{d}t}\mathbf{p} = \mathbf{p}\,\mathbf{Q}; \qquad \mathbf{T}(\tau) = e^{-\mathbf{Q}^{(1)}\cdot\tau}$$
$$\mathbf{p}(t_0+\tau) = \mathbf{p}(t_0)\;\mathbf{T}(\tau)$$

where $\mathbf{p}$ is the N-entry vector, N – number of plants, τ – genetic distance.

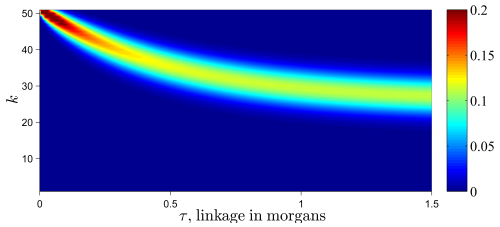

Fig. 2: Conditional probability for k individuals to carry the mutation in F_2 dependent on the linkage distance

2. The conditional probability of **mutant read** frequencies (r_m mutant out of q_m total) on the **mutant allele carrier** frequencies (k_m out of N plants) is assumed to be determined by a binomial process:

$$P[r|q,k,N] =$$
$$= \binom{r}{q} \cdot \left(\frac{k}{2\,N}\right)^{r} \cdot \left(1-\frac{k}{2\,N}\right)^{q-r}$$

As a more realistic estimate of sampling accounting for over-dispersion (i.e. variance higher than expected with binomial distribution), the negative binomial distribution can be used

(Anders and Huber, 2010).

3. The prior knowledge about **the effect of mutations** is incorporated with the following ranking:
   stop>nsSNP>sSNP >intronic

Additionally, if mutation is known to affect development or physiology of some particular organ or at some particular stage/phase, the expression level of the genes, relative to their expression levels in other organs or during other stages/phases, can be used to extract prior information.

A3.2.3 Simulator

A simulator has been set up to produce data from the described distribution for some population size N.

Recombination. To simulate the recombination process, N vectors of alternating binary states (original/recombined) is generated together with N corresponding vectors of recombination spots taken from an exponential distribution as in (Gillespie, 1976, p.419). Further the recombination pattern is assembled by summing the binary state vectors to obtain the number of recombined and un-recombined plants per point of chromosome.

Sampling. The sampling process is realized in two steps: (1) mutagenisis (SNP emergence) and (2) sequencing. The SNPs are assumed to arise uniformely. Likewise, the sequencing is assumed to cover the chromosomes uniformely, with the number of sequencing reads given by genome coverage of the sequencing run or by actual total number of reads. In former case, the classical Lander-Waterman equation (Lander and Waterman, 1988) can be used for conversion:

$$C = \frac{L \cdot N_r}{G} \tag{A3.62}$$

where C is coverage, G is the haploid genome length, L_r is the read length, and N_r is the number of reads.

After assignment of sequenicing start x_s for each read, we test whether any mutation physically located in point x_m is detectable within the read, i.e. if $x_s \leq x_m \leq x_s + L_r$.

A3.2.4 Data and Preliminary Results

Three data sets are available now, including the previously published one (Lindner et al., 2012).

Application of the forward-backward algorithm finds the causative mutation in the data set from (Lindner et al., 2012) only if a weakened linkage strength (by factor of 100) is supplied. This can point to either (1) the roughness of the initial genetic map, or (2) the fact that erroneous read mapping introduces wrong linkage interactions, or (3) that the assumptions behind the Haldane mapping function implemented here are violated, e.g. due to the effect of cross-over interference. As accounting for cross-over interference can be prohibitively computationally expensive, and read mapping might still not be absolutely correct, the relaxation of linkage by a certain factor can be a solution. Optimization linkage relaxation factor

needs to be further implemented via Baum-Welch algorithm.

Of the list of top hits from the data by A. Boisson-Dernier, the SNP with sixth highest posterior probability and likelihood is the causative one according to indirect experimental evidence available (A. Boisson-Dernier, personal comminication). The list was compiled with an *ad hoc* filter of coverage more than 40 reads and read ratio more than 0.4 to account for over-dispersion. In further implementations, a possible step to exclude *ad hoc* filters is by considering sampling step of negative binomial distribution.

A3.3 Open Questions and Outlook

- Estimate optimal sequencing coverage and number of the F_2 plants to be pooled.
- Include information on the quality of the reads in the likelihood calculation.
- Add possibility to integrate relevant gene-ontology or stage-specific transcriptomics data in the calculation of prior.
- Apply an optimization procedure for tweaking the parameters (i.e. linkage strength and ones used for read filtering; Baum-Welch algorithm)

A3.4 Acknowledgements

We would like to thank Heike Lindner, Michael Raissig and Aurélien Boisson-Dernier (IPB University of Zürich) for providing their data to test the algorithm and useful discussions; Prof. Niko Beerenwinkel, Armin Töpfer (BSSE ETHZ, Basel, Switzerland), Aleksey Mikaberidze and George Shirreff (Theoretical Biology ETHZ), Oleksandr Ivanov (Rijksuniversiteit Groningen, the Netherlands), Quy Ai Ngo, Christian Heichinger, Nuno Pires and Stefan Wyder (IPB University of Zürich) for useful discussions and help.

A3.5 References for Appendix 3

Austin, R. S., D. Vidaurre, G. Stamatiou, et al. (2011). "Next-generation mapping of Arabidopsis genes." *Plant J* **67**.4, pp. 715–725.

Schneeberger, K., S. Ossowski, C. Lanz, et al. (2009). "SHOREmap: simultaneous mapping and mutation identification by deep sequencing." *Nat Methods* **6**.8, pp. 550–551.

Lindner, H., M. T. Raissig, C. Sailer, H. Shimosato-Asano, R. Bruggmann, and U. Grossniklaus (2012). "SNP-Ratio Mapping (SRM): Identifying Lethal Alleles and Mutations in Complex Genetic Backgrounds by Next-Generation Sequencing." *Genetics* **191**.4, pp. 1381–1386.

Singer, T., Y. Fan, H.-S. Chang, T. Zhu, S. P. Hazen, and S. P. Briggs (2006). "A High-Resolution Map of *Arabidopsis* Recombinant Inbred Lines by Whole-Genome Exon Array Hybridization". *PLoS Genet* **2**.9, e144.

Ehrenfest, P. u. T. (1907). "Über zwei bekannte Einwände gegen das Boltzmannsche H-Theorem". *Physikalishce Zeitschrift* **8**, pp. 311–314.

Feingold, E. (1993). "Markov Processes for Modeling and Analyzing a New Genetic Mapping Method". *Journal of Applied Probability* **30**.4, pp. 766–779.

Töpfer, A., O. Zagordi, S. Prabhakaran, V. Roth, E. Halperin, and N. Beerenwinkel (2013). "Probabilistic Inference of Viral Quasispecies Subject to Recombination". *Journal of Computational Biology* **20**.2, pp. 113–123.

Anders, S. and W. Huber (2010). "Differential expression analysis for sequence count data". *Genome Biology* **11**.10, R106.

Gillespie, D. T. (1976). "A general method for numerically simulating the stochastic time evolution of coupled chemical reactions". *Journal of Computational Physics* **22**.4, pp. 403–434.

Lander, E. S. and M. S. Waterman (1988). "Genomic mapping by fingerprinting random clones: a mathematical analysis." *Genomics* **2**.3, pp. 231–239.

Appendix 4. A tool for user-assisted tracking of the pollen tube tip

A4.1 Background

Several tip-growing and oblong moving objects are encountered in biological research such as pollen tubes, fungal hyphae and worms. Novel microscopic techniques allowing to monitor biochemical activities within living cells brought demand on tracking procedures for such class of objects. Very often it is not, or not mainly the outline, which is of interest for the researchers, but the location of the growing tip.

Object tracking is a widely used application of computer vision. Though several tools exist allowing fully automatic tracking of particle-like objects (e.g. Sbalzarini et al., 2005; Wöll et al., 2013), tracking of other non-compact or non-convex objects is a more challenging task. Therefore, a number of user-assisted segmentation tools have been developed (e.g. Yu et al., 2004; Esche et al., 2010) focusing on contour tracking.

As the specific method of image acquisition technique for which this method is intended is intensiometric calcium measurements, where object intensity is inherently highly variable, we developed semi-automatic tool allowing for experts' input. Moreover, the specific task of is not contour (one-dimensional manifold) tracking, but tracking of the growing tip of the object (point, i.e. zero-dimensional manifold), which simplified our task. Of suitable tools, to date only a purely manual object tracking tool is available as an ImageJ plugin by Fabrice P. Cordelières[3], which requires specification of the object/point position in each frame of the film. This requires extensive manual work and the obtained path is hard to modify or visualize after initial input by the expert.

In our approach we preserve the strength of interactivity with the human, while speeding up the input and improving the ease of post-processing and modification of the object path. To this end, we exploit the method of kymogram representation, allowing to render a curve in three dimensions by means of two two-dimensional images.

A4.2 Algorithm

Here I give a brief description of the algorithm and describe some details on its parameters. The overview of the algorithm and its implementation is given in Figure A2.7.

Before proceeding to the details of the algorithm, let us specify the expert input. The expert draws a x, y-path on a time series showing the set of points where the tip of the

[3] http://rsbweb.nih.gov/ij/plugins/track/Manual%20Tracking%20plugin.pdf

pollen tube has been travelling. The first rough approximation is obtained by drawing the mid-line of the pollen tube on the time-frame preceding the pollen tube burst. It is further refined by scrolling back to previous frames, where position of the tip may be different from the mid-line of the pollen tube in the final position. The path is drawn as control points of a cubic spline curve. This step is realized in the ImageJ software and is done after completion of the step 2 of the algorithm. An example movie frame and a pollen tube x, y-path are shown in Figure A2.4.

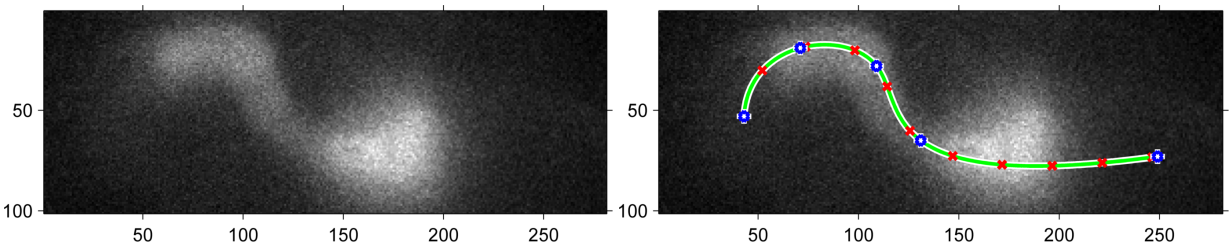

Figure A2.3: A frame of a Ca^{2+}-intensiometric film portraying the onset of the pollen tube burst (from Quy Ai Ngo). The control points are shown as blue stars, the spline curve ROI is shown in green. The red crosses represent points equally spread (each 25 pixels) providing a landmark of the curvilinear coordinate r.

Figure A2.4

The obtained 2D path contains $\{x, y\}$-projection of the 3D path of the pollen tube.

1. **Alignment (registration).** Availability of channels monitoring static objects in the same experiment can be helpful to correct for the effect of drift during the experiment. To this end, image registration is performed using the most static channel as a reference. Additionally, before frame alignment (registration), filtering in time and space is carried out on the reference channel in order to reduce spurious mismatches between neighbouring images, while preserving the long-term drift effects further used by the alignment (registration) algorithm. For registration, we use the pyramid approach described by (Thévenaz et al., 1998) restricted to rigid body motions. A detailed scheme of this step is given in figure A2.8. This step is necessary for the next step of background subtraction.

2. **Subtraction of static background.** The static background is subtracted from the film. The static background of a film $A = \{A(x, y, t) | t \in 1 \dots T\}$ is defined as a 2D image $B(x, y) = \text{quantile}_\alpha[A(x, y, t)]$, i.e. some lower quantile $\alpha \ll 0.5$ of the pixel intensities for all time-points corresponding to each frame point.

3. **Kymogram generation.** A kymogram is obtained based on the $\{x, y\}$-curve provided by the user as control points of a cubic spline curve. This step is realized in

the ImageJ software.

4. **Edge detection** in the kymogram for construction of the r, t-path. The kymogram is padded and filtered with a Canny edge detecting filter (including Gaussian pre-filtering) to obtain a binary edge-kymogram.

5. **Output of the kymogram edges**. The obtained edges are saved to allow editing by user.

6. **Path assembly.** The object path is extracted from the kymogram edges by taking positions of inter-connected bright pixels starting from top-left corner, $(t = 0; r = 0)$, or any closest bright pixel. A constrain that the object cannot retract backwards, i.e. that the path is a non-decreasing function is imposed. If no connected pixel can be found at some point, the path is extended in t-direction (horizontally), until any bright pixel is hit.

7. **Reconstruction of the x, y, t-path.**

8. **Generation of the 3D ROI** based on the x, y, t-path.

9. **Retrieval of the pixel intensities within the 3D ROI.**

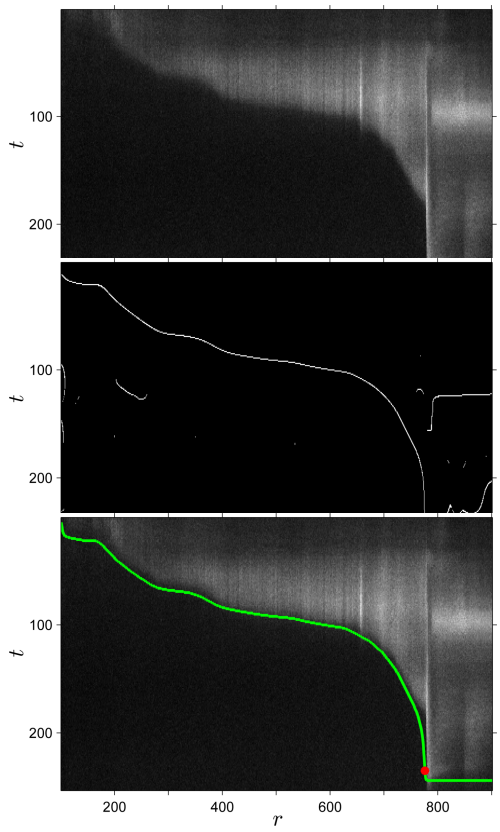

Figure A2.5: Steps of the kymogram processing: upper row: a raw grayscale kymogram; middle row: segmented binary kymogram image with edges in white; lower row: the raw grayscale kymogram with the detected r, t-path (in green) and the burst point (red).

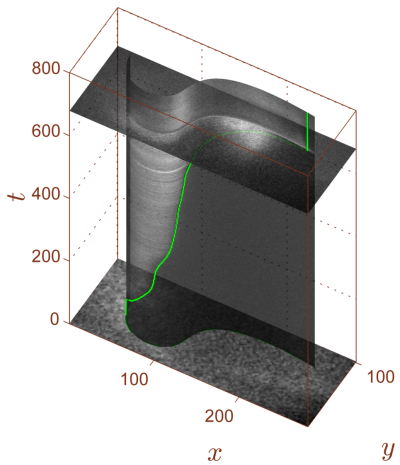

Figure A2.6: The kymogram (a vertical curved surface) and movie frames (horizontal x, y-surfaces) in x, y, t-space.

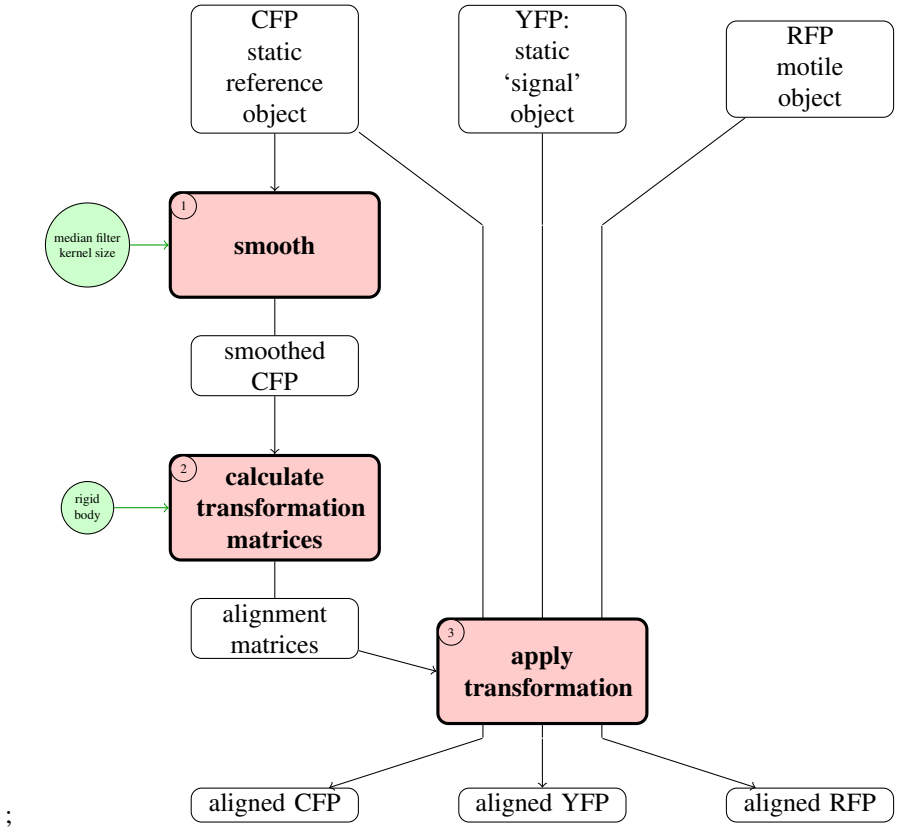

;

Figure A2.7: A block diagram of alignment (registration) for three parallel film channels with content of different motility and different variability of the intensity. The *a priori* least motile and least variable channel is taken as a reference for generation of transformation matrices. The matrices are further applied to individual channels. The parameters controlling automatized steps are shown in green circles. Implemented in ImageJ macros language and Java.

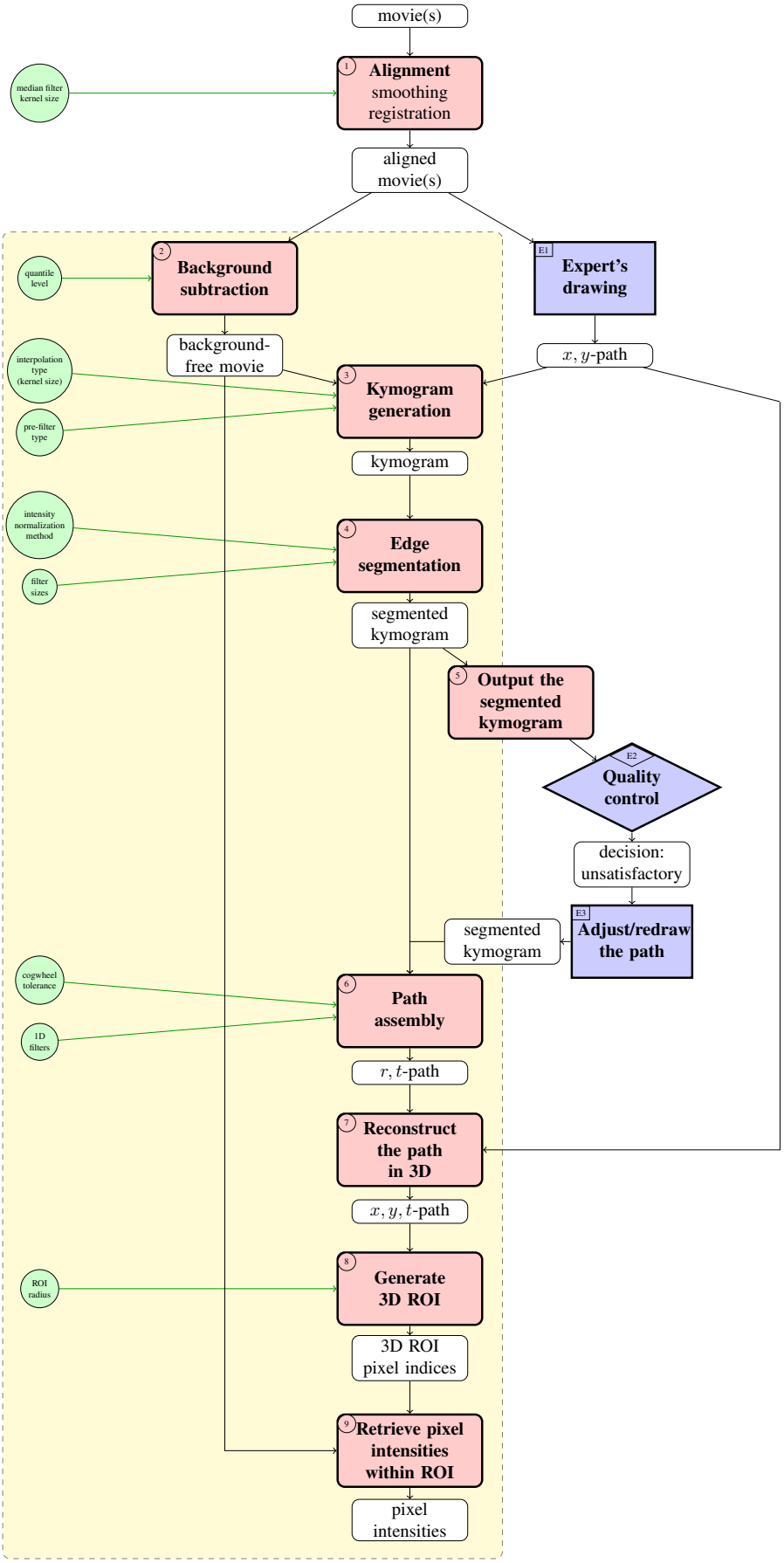

Figure A2.8: A block diagram of expert-assisted pollen tube tip tracking algorithm. The automatized part is depicted in pink, the expert's input in blue. The part of algorithm which is currently implemented as a MATLAB script is enclosed in a yellow cartouche (the rest is implemented in ImageJ). The parameters controlling automatized steps are shown in green circles.

A4.3 Outlook

As the next step, the performance of the algorithm needs to be assessed when the data becomes available.

The output of the r, t-path for quality control and input by user can be implemented as a (cubic) spline to simplify the input.

Further, the constrain that the pollen tube cannot retract can be implemented as a cost function, as some retraction in the observed signal can still occur due to the temporal variation of intenisty caused by Ca^{2+} oscillations.

A4.4 References for Appendix 4

Sbalzarini, I. F., A. Mezzacasa, A. Helenius, and P. Koumoutsakos (2005). "Effects of organelle shape on fluorescence recovery after photobleaching." *Biophys J* **89**.3, pp. 1482–1492.

Wöll, D., C. Kölbl, B. Stempfle, and A. Karrenbauer (2013). "A novel method for automatic single molecule tracking of blinking molecules at low intensities." *Phys Chem Chem Phys* **15**.17, pp. 6196–6205.

Yu, H. Y., S.-H. Hong, M. M. Lee, and J.-G. Choi (2004). "A new user-assisted segmentation and tracking technique for an object-based video editing system". In: *SPIE Proceedings. Microelectronics: Design, Technology, and Packaging*. Ed. by D. Abbott, K. Eshraghian, C. A. Musca, D. Pavlidis, and N. Weste. Vol. 5274. SPIE - International Society for Optical Engineering, pp. 470–481.

Esche, M., M. Karaman, and T. Sikora (2010). "Semi-automatic object tracking in video sequences by extension of the MRSST algorithm". In: *Image Analysis for Multimedia Interactive Services (WIAMIS), 2010 11th International Workshop on*, pp. 1–4.

Thévenaz, P., U. Ruttimann, and M. Unser (1998). "A Pyramid Approach to Subpixel Registration Based on Intensity". *IEEE Transactions on Image Processing* **7**.1, pp. 27–41.

Appendix 5: ANXUR Receptor-Like Kinases Coordinate Cell Wall Integrity with Growth at the Pollen Tube Tip via NADPH Oxidases

OPEN ACCESS Freely available online

PLOS | BIOLOGY

ANXUR Receptor-Like Kinases Coordinate Cell Wall Integrity with Growth at the Pollen Tube Tip Via NADPH Oxidases

Aurélien Boisson-Dernier[1,2]*, Dmytro S. Lituiev[1,2], Anna Nestorova[1,2], Christina Maria Franck[1,2], Sharme Thirugnanarajah[1,2], Ueli Grossniklaus[1,2]*

1 Institute of Plant Biology, University of Zürich, Zürich, Switzerland, **2** Zürich-Basel Plant Science Center, ETH Zürich, Zürich, Switzerland

Abstract

It has become increasingly apparent that the extracellular matrix (ECM), which in plants corresponds to the cell wall, can influence intracellular activities in ways that go far beyond their supposedly passive mechanical support. In plants, growing cells use mechanisms sensing cell wall integrity to coordinate cell wall performance with the internal growth machinery to avoid growth cessation or loss of integrity. How this coordination precisely works is unknown. Previously, we reported that in the tip-growing pollen tube the ANXUR receptor-like kinases (RLKs) of the CrRLK1L subfamily are essential to sustain growth without loss of cell wall integrity in *Arabidopsis*. Here, we show that over-expression of the ANXUR RLKs inhibits growth by over-activating exocytosis and the over-accumulation of secreted cell wall material. Moreover, the characterization of mutations in two partially redundant pollen-expressed NADPH oxidases coupled with genetic interaction studies demonstrate that the ANXUR RLKs function upstream of these NADPH oxidases. Using the H_2O_2-sensitive HyPer and the Ca^{2+}-sensitive YC3.60 sensors in NADPH oxidase-deficient mutants, we reveal that NADPH oxidases generate tip-localized, pulsating H_2O_2 production that functions, possibly through Ca^{2+} channel activation, to maintain a steady tip-focused Ca^{2+} gradient during growth. Our findings support a model where ECM-sensing receptors regulate reactive oxygen species production, Ca^{2+} homeostasis, and exocytosis to coordinate ECM-performance with the internal growth machinery.

Citation: Boisson-Dernier A, Lituiev DS, Nestorova A, Franck CM, Thirugnanarajah S, et al. (2013) ANXUR Receptor-Like Kinases Coordinate Cell Wall Integrity with Growth at the Pollen Tube Tip Via NADPH Oxidases. PLoS Biol 11(11): e1001719. doi:10.1371/journal.pbio.1001719

Academic Editor: June B. Nasrallah, Cornell University, United States of America

Received May 17, 2013; **Accepted** October 16, 2013; **Published** November 26, 2013

Funding: This work was supported by the University of Zürich, the Forschungskredit der Universität Zürich and the European Union through a Marie Curie International Reintegration grant to ABD, and grants of the Swiss National Science Foundation (31003AB-126006 and 31003A_141245) and SystemsX.ch (iPhD and an RTD project "Plant Growth") to UG. The funders had no role in study design, data collection and analysis, decision to publish, or preparation of the manuscript.

Competing Interests: The authors have declared that no competing interests exist.

Abbreviations: BFA, Brefeldin A; CW, cell wall; ECM, extracellular matrix; FDA, fluorescein diacetate; FRAP, fluorescence recovery after photobleaching; GFP, green fluorescent protein; NADPH, nicotinamide adenine dinucleotide phosphate; PM, plasma membrane; PT, pollen tube; Rboh, respiratory burst oxidase homologue; RLK, receptor-like kinase; ROP, Rho GTPase, of plants; ROS, reactive oxygen species; TE_M, male transmission efficiency; TE_F, female transmission efficiency; WT, wild type; YFP, yellow fluorescent protein.

* E-mail: aboisson@access.uzh.ch (ABD); grossnik@botinst.uzh.ch (UG)

Introduction

It is well established that growing animal cells control the biogenesis, deposition, and remodeling of their extracellular matrix (ECM). *In vivo* the ECM contributes to the bulk, shape, and strength of many tissues and, therefore, plays a central role in development [1]. However, it is often underappreciated that the ECM also controls intracellular activities far beyond providing mechanical stability. For example, the ECM is under continuous cellular surveillance in order to monitor the loss of adhesion to the surrounding matrix, which leads to apoptosis. Consequently, disruption of signaling between the ECM and the cell is associated with tumorigenicity [2]. Similarly, growing plant cells direct the deposition of the primary cell wall (CW): the plants rigid, carbohydrate-rich ECM that resists turgor pressure, yet is flexible enough to allow cell expansion. Growing plant cells tightly coordinate the loosening and pressure-driven deformation of the CW with the addition of new membrane and CW materials through exocytosis. Thus, the cell must be kept informed about any environmental changes modifying the CW properties in order to avoid growth arrest or rupture. To circumvent these catastrophic scenarios, it has become increasingly evident that plant cells have developed mechanisms to sense CW integrity, which relay information about CW performance to the internal growth machinery. The molecular nature of this relay mechanism, however, remains largely unknown [3].

Since the first reports on THESEUS1 (THE1 [4]) and FERONIA (FER [5]), these *Arabidopsis* receptor-like kinases (RLKs) of the *Catharanthus roseus* RLK1-like subfamily (CrRLK1L) have received increasing attention as putative sensors that coordinate cellular growth and CW integrity (reviewed in [6–8]). How this coordination precisely works and which molecular players of the growth machinery are involved remained elusive, although Rho GTPases of plants (ROPs) and the production of NADPH oxidase-dependent reactive oxygen species (ROS) have emerged as putative downstream components. The role of NADPH oxidases, the ROS-producing enzymes that, based on their homology to the catalytic glycoprotein subunit of the mammalian phagocyte oxidase ($gp91^{phox}$), are also called "respiratory burst oxidase homologues (Rboh)", has been firmly

Author Summary

Tip-growing cells, such as plant root hairs and pollen tubes or fungal hyphae, are characterized by a tip-focused Ca^{2+} gradient. These tip-growing cells tightly coordinate the loosening and pressure-driven deformation of their extracellular matrix (ECM)—the cell wall in plant cells—by locally adding new membrane and cell wall materials. In pollen tubes, which grow at amazing speeds to effect fertilization in plants, a class of kinases called the ANXUR receptor-like kinases (RLKs) sense perturbations in cell wall integrity, and their loss leads to pollen tube rupture. Here, we gain new insights into the mechanism of cell wall surveillance by these RLKs in the model plant *Arabidopsis*. We show that over-expressing ANXUR RLKs over-activates exocytosis, causing an over-accumulation of secreted cell wall material that eventually leads to growth arrest. Moreover, we find that the ANXUR RLKs function upstream of NADPH oxidases, which are membrane-anchored enzymes that produce reactive oxygen species (ROS). Using H_2O_2- and Ca^{2+}-sensitive reporters, we show that NADPH oxidases generate tip-localized H_2O_2 production, which is required to maintain a steady, tip-focused Ca^{2+} gradient that is essential for pollen tube growth. We postulate that ECM-sensing receptors, such as the ANXUR RLKs, regulate ROS production, Ca^{2+} homeostasis, and exocytosis to coordinate the status of the ECM with the cell's internal growth machinery.

established in various fundamental processes. These include localized lignin deposition [9], stomatal closure [10], pathogen responses [11], and root hair growth [12]. NADPH oxidases are plasma membrane (PM)-bound enzymes with six trans-membrane domains, an N-terminal region that contains EF-hands, and a C-terminal oxidase domain responsible for oxidizing O_2 to produce superoxide radicals in the apoplast (reviewed in [13,14]). The latter can quickly be dismutated, enzymatically or otherwise, into H_2O_2 that can freely diffuse back from the apoplast into the cytosol.

Connections between members of the CrRLK1L and NADPH oxidase families have been proposed or established for THE1 and FER, respectively. For example, *THE1* has been reported to be a positive regulator of CW damage-induced ROS production in seedlings, possibly through RbohD [15], while *FER* is both a negative regulator of H_2O_2 production in unchallenged leaves [16] and of ROS in guard cells [17]. Furthermore, in root hairs that elongate by tip-growth, FER is a positive regulator of ROS production through the ROP2-RbohC pathway [18]. Similar to the *rbohC* loss-of-function mutant (also called *root hair defective2* [*rhd2*]), disruption of *FER* leads to an impairment of ROS production and defective root hairs that burst [12,18]. Disruption of the redundant CrRLK1Ls *ANXUR1* (*ANX1*) and *ANX2*, the two closest homologues of *FER*, triggers the rupture of pollen tubes (PTs), the tip-growing male gametophytes of flowering plants, resulting in male sterility [19,20]. Similar to *fer* root hairs, *anx1 anx2* double mutant pollen form bulges and burst, failing to maintain their integrity during growth. This indicates that the FER and ANX RLKs could be cell-surface receptors that control CW integrity in tip-growing cells. In PTs, genetic evidence for the involvement of NADPH oxidases is lacking, but several studies have revealed a role for ROS during PT growth that remains to be precisely characterized. For example, it has been shown that either the use of ROS scavengers or the NADPH oxidase inhibitor diphenylene iodonium (DPI), or the down-regulation of a NADPH oxidase, reduces PT growth in tobacco [21]. In addition, the application of DPI at higher concentrations has also been reported to induce PT rupture in lily [22].

Because of the difficulty to image the dynamics of ROS production with good spatial and temporal resolution, and because of its multi-faceted impacts on CW properties and the activation of intracellular signaling, it is unknown how NADPH oxidase-dependent ROS control polar growth [23,24]. It was first reported that RbohC/RHD2 is required for calcium influx via the stimulation of Ca^{2+} channels and for the generation of a tip-focused gradient of cytosolic free calcium $[Ca^{2+}]_{cyt}$, which is essential for polar growth [12,25]. Later, Monshausen and colleagues reported that, under certain conditions, *rbohC* root hairs still display a tip-focused Ca^{2+} gradient, showing that *RbohC* was not essential for its establishment [26]. Moreover, they showed that artificially increasing or decreasing apoplastic ROS leads to growth cessation and root hair bursting, respectively, consistent with a role for ROS in regulating CW properties [27]. Finally, oscillations in apoplastic ROS levels just behind the tip were reported during root hair growth and correlated with growth rate, leading the authors to propose a model in which ROS rigidify the CW behind the tip, such that growth would be restricted to the tip [26]. However, due to the irreversible nature of the ROS-sensitive oxidation of the dye they used, the observed oscillations are unlikely to reflect the true nature of ROS dynamics [28]. Nonetheless, both models—namely the growth-promoting effect at the tip related to intracellular Ca^{2+} signaling and the growth-inhibiting effect behind the tip by rigidifying the CW—are not mutually exclusive as they could recruit different forms of ROS at different times and in different locations.

In this study we show that over-expression of the ANX RLKs inhibits PT growth by the over-activation of exocytosis and the over-accumulation of secreted membrane and CW materials. Genetic interaction studies coupled with a phenotypic characterization of loss-of-function mutants of two partially redundant, pollen-expressed NADPH oxidases, *RbohH* and *RbohJ*, demonstrate that the ANX RLKs function upstream of these NADPH oxidases. Furthermore, analyses of the genetically encoded H_2O_2-sensitive HyPer and Ca^{2+}-sensitive YC3.60 sensors in NADPH oxidase-deficient pollen revealed that NADPH oxidases generate tip-localized, pulsating ROS that are responsible—possibly through activation of Ca^{2+} channels—for maintaining a steady, tip-focused Ca^{2+} gradient.

Results

The Functional ANX1-YFP and ANX2-YFP Fusions Inhibit Pollen Tube Growth

We have previously shown that ANX1-yellow fluorescent protein (YFP) and ANX2-YFP protein fusions are polarly localized in the PM at the tip of growing PTs in independent T1 transgenic *Arabidopsis* lines [19]. Although in T1 lines, which contain a mixture of untransformed and transformed pollen grains, no obvious fertilization-related phenotypes could be detected, *in vitro* pollen germination and growth assays of homozygous lines that carry a single insertion of the constructs in the T3 generation revealed that ANX1-YFP and, to a lesser extent, ANX2-YFP inhibit pollen germination and PT growth compared to the wild type (WT) (Figures 1A, 1B, and S1). To investigate whether these phenotypes are due to over-expression or non-functionality of the fusion proteins, we transformed *anx1-2/anx1-2 anx2-2/ANX2* and *anx1-1/anx1-1 anx2-1/ANX2* plants with ANX1-YFP and ANX2-YFP fusions, respectively. In all T1 *anx1-2/anx1-2 anx2-2/ANX2* lines expressing ANX1-YFP and *anx1-1/anx1-1 anx2-1/ANX2*

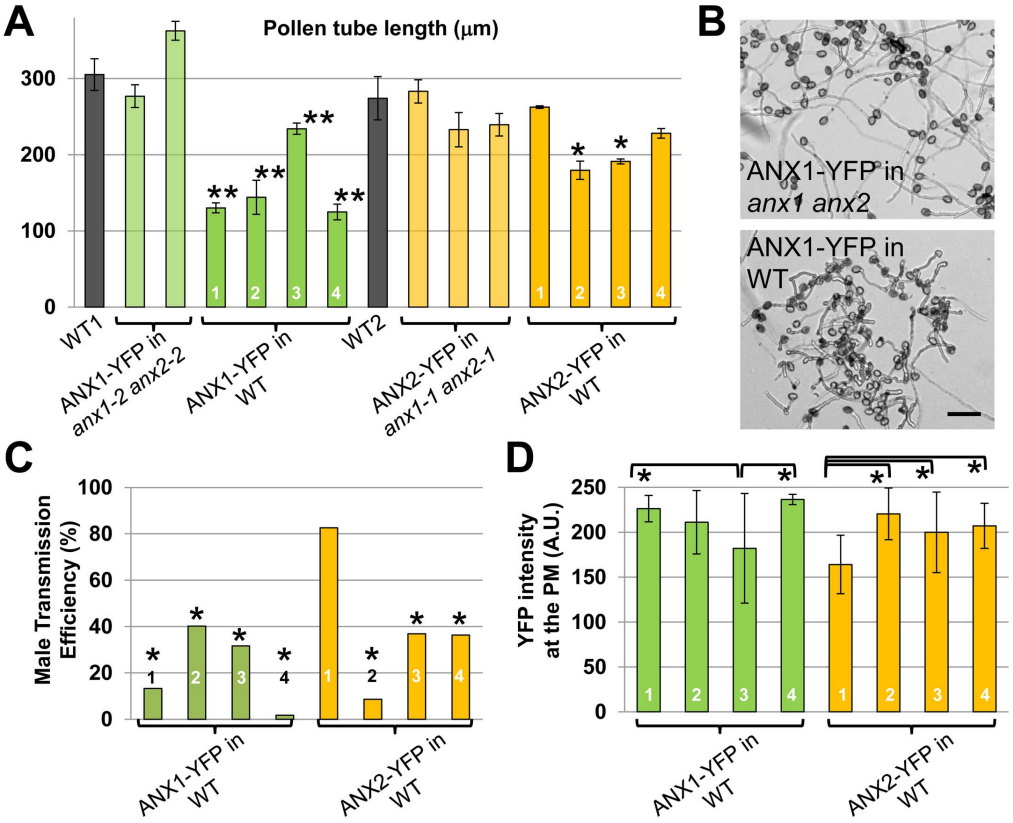

Figure 1. Over-expression of ANX RLKs inhibits pollen germination, pollen tube growth, and decreases male transmission efficiency. (A) Quantification of PT length after 5 h of *in vitro* growth for WT, two ANX1-YFP and three ANX2-YFP independent T3 complemented lines, and four independent T3 ANX1-YFP and ANX2-YFP over-expression lines. Data represent mean values ± standard error of the mean (SEM) of three independent experiments with more than 40 PTs per genotype and experiment. Single and double asterisks indicate significant differences from the WT according to a Student's *t* test with $p<0.05$ and $p<0.01$, respectively. See also Figure S1A. (B) Overview images of pollen of ANX1-YFP complemented and over-expression lines grown *in vitro* for 5 h. Scale bar = 100 μm. (C) TE_M of ANX1-YFP and ANX2-YFP for four independent over-expression lines. For each independent over-expression line, heterozygous T2 plants were crossed as pollen donor to the WT. More than 250 seeds resulting from each cross were grown on MS plates containing hygromycin and resistance was scored. TE_M was calculated as 100*(resistant/sensitive) in percent. Asterisks denote significant difference from the expected 1:1 ratio for normal transmission with $p<0.0001$ (two-tailed exact Fisher's test). (D) Quantification of YFP fluorescence at the apical PM of growing PTs for each ANX1-YFP and ANX2-YFP over-expression line. Data represent mean values ± standard deviation (SD) ($n>19$ tubes for each line). Asterisks indicate significant difference among each ANX1-YFP or each ANX2-YFP over-expressing line (one-way ANOVA test, $p<0.01$).
doi:10.1371/journal.pbio.1001719.g001

expressing ANX2-YFP PT rupture was reduced compared to the corresponding untransformed genotype (Figure S2). Moreover, in all T3 homozygous lines with good ANX1/2-YFP expression in the *anx1 anx2* double mutant background, pollen germination, PT rupture, and PT length was indistinguishable from the WT (Figures 1A, 1B, S1, and S2). Thus, both ANX1-YFP and ANX2-YFP fusion proteins are functional, and the phenotypes observed in WT pollen expressing these fusion proteins are due to over-expression. Hereafter, independent homozygous lines expressing the ANX-YFP fusion proteins in the *anx1 anx2* background will be called either complemented lines or ANX-YFP in *anx1 anx2*, while homozygous lines expressing the same fusion proteins in a WT background will be referred to as ANX-OX or ANX-YFP in WT.

Pollen of ANX-OX lines germinated poorly and produced shorter and wider PTs than pollen of either WT or complemented lines (Figure 1A, 1B, and S1). To check whether these *in vitro* phenotypes impact the fitness of PTs *in vivo*, the male transmission efficiency (TE_M) was assayed for each of the ANX-OX lines. Male transmission of ANX-YFP fusions was significantly decreased for all but one ANX2-OX line, showing that PTs over-expressing ANX-YFP fusion proteins are not as competitive as untransformed WT PTs (Figure 1C). Interestingly, the difference in the severity of these phenotypes between ANX1-OX lines or between ANX2-OX lines nicely correlated with the difference in the level of YFP fluorescence imaged at the PM of growing ANX-OX PTs (Figure 1D). The two strongest ANX1-OX lines (#1 and #4) and one ANX1-YFP complemented line were selected for further investigations.

Over-expression of ANX1-YFP Triggers Cell Wall Accumulation and Plasma Membrane Invagination Via Increased Exocytosis

Time-lapse imaging of YFP fluorescence in growing PTs 6 hours after incubation showed that all PTs of the complemented line display the previously reported asymmetric distribution of YFP in the PM at the PT tip [19] and were growing normally ($n>100$, Figure 2A, left panels). In contrast, only 43% to 47% of ANX1 over-expressing PTs grew and exhibited the same YFP distribution ($n>100$ PTs, ANX1-OX #4 and #1, respectively). The remaining ANX1-OX PTs (53% to 57% of all PTs) had

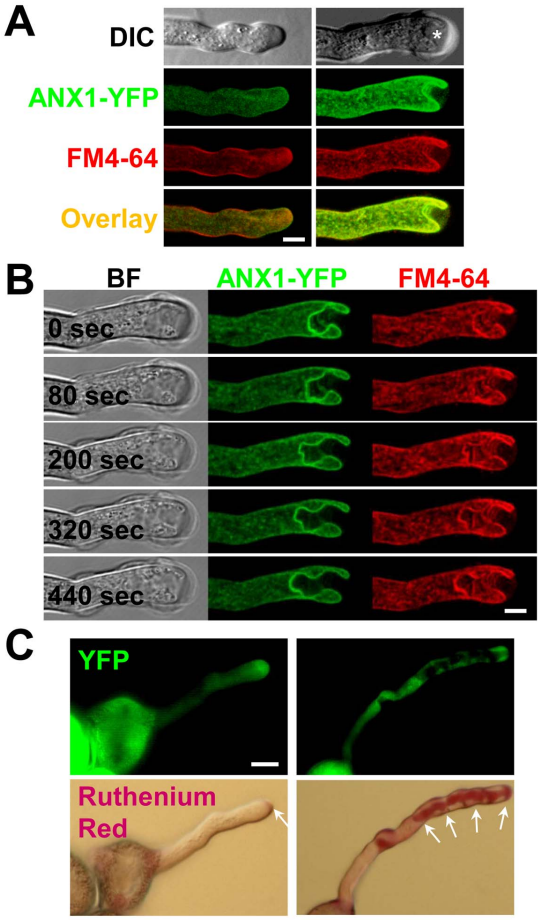

Figure 2. Over-expression of ANX RLKs triggers cell wall accumulation that leads to a cessation of pollen tube elongation and plasma membrane invagination. (A) Representative single median plane images of a normally growing PT of an ANX1-YFP complemented line (left) and an arrested PT of ANX1-YFP over-expressing line with apical membrane invagination (right). The different filters are indicated on the left. Before imaging, PTs were treated for 5 min with germination liquid medium containing FM4-64 (2 μM). Scale bar = 5 μm. (B) Time-course imaging of the apical PM invagination of an ANX1-YFP over-expressing PT that ceased to elongate. PTs were treated as in (A). See also corresponding Video S1. Filters are indicated at the top. Scale bar = 5 μm. (C) Representative bright-field and YFP fluorescence images of ANX1-YFP complemented (left) and over-expressing (right) PTs treated with 0.01% Ruthenium red, which stains acidic pectins. Note that staining is restricted to the tip of growing complemented PT (left, arrow), while it accumulates inwards following the invaginated apical membrane in the over-expressing PT (right, arrows). Scale bar = 10 μm.
doi:10.1371/journal.pbio.1001719.g002

ceased to elongate and displayed PM invaginations at the PT tip as observed with both YFP and the lipophilic dye FM4-64 (Figure 2A, right panels). Intriguingly, in the ANX1 over-expressing PTs that had ceased to elongate, the PM at the tip kept growing inwards, creating tunnel-like structures, instead of outwards as normally observed for tip-growing cells (Figures 2B and S3A; Video S1). Invaginations can start early as they were observed even in pollen grains that did not yet produce a tube (Figure S3B). The PM invagination phenotype was also observed in ANX2 over-expressing lines, while we never saw it in any of the ANX1-YFP or ANX2-YFP complemented lines ($n>100$ PTs, two independent lines for each fusion protein). PM invaginations were accompanied by thick extracellular deposits of CW material (Figure 2A, asterisk), which were pectinaceous as revealed by Ruthenium red staining (Figure 2C). This finding indicates that secretion of CW material still occurred at the site of PM invagination. In addition, detailed observations of ANX-OX PTs showed that apical CW thickening occurred before the invagination of the apical membrane.

Since the surface of both the PM and the secreted CW material increase at the tip, we hypothesize that the balance between endocytosis and exocytosis rates might be tilted towards exocytosis at the tip of ANX-OX PTs. This could be achieved by a decrease or increase in the rate of endocytosis or exocytosis, respectively, or by a combination of both. For example, CW accumulation and PM invaginations have also been reported for tobacco PTs that over-express the phosphatidylinositol-4-phosphate 5-kinases PIP5K4, PIP5K5, and PIP5K6 [29–31]. The PIP5K-OX phenotypes originate from an over-initiation of aborted endocytosis in PIP5K-OX PTs, which show a dramatic inhibition of FM4-64 uptake [30,31]. To investigate this phenotype further, we conducted two types of experiments on growing PTs of complemented and ANX1-OX lines before they start to show PM invaginations and apical CW accumulation. First, we labeled PTs for 5 min with FM4-64, a styryl dye that quickly labels the PM and is internalized via endocytosis. In growing PTs of complemented lines (as in WT), FM4-64 is observed at the PM and in the apical cytoplasm as an inverted cone that presumably contains both endocytotic and secretory vesicles (Figure 3A and Video S2, upper panels). In growing ANX1-OX PTs, the same distribution was observed (Figure 3A and Video S2, lower panels), indicating that, in contrast to PIP5K-OX PTs, FM4-64 uptake and thus endocytosis was not impaired [30,31]. However, FM4-64 fluorescence intensity at the PM *versus* the apical cytoplasm was significantly lower than in complemented PTs, suggesting that there were globally more endocytotic and secretory vesicles in ANX1 over-expressing PTs (Figure 3A and 3B; $n>25$ each, $p<0.01$).

As evidenced by Brefeldin A (BFA) treatment, a well-known inhibitor of exocytosis, ANX1-YFP is inserted at the apical PM via exocytosis (Figure S4A). Thus, we performed fluorescence recovery after photobleaching (FRAP) experiments for ANX1-OX and complemented PTs to analyze exocytosis dynamics in growing PTs as described previously [31,32]. Photobleaching was applied to the tip of growing PTs and measurements of the recovery of YFP fluorescence in the apical PM of the PT tips were carried out every 4 seconds. For ANX1 complemented PTs, the relative fluorescence recovery in the PM 10 seconds after photobleaching (I_{10sec}) reached on average 47%±9% of the maximum relative fluorescence with a PT growth rate of 4.02±1.41 μm min^{-1} ($n=18$; Figure 3C and 3D, left panels; Table S1; Video S3). No correlation was observed between I_{10sec} and the fluorescence intensity pre-bleaching ($R^2=0.0092$; Figure S4B), suggesting that the secretion rate of new ANX1-YFP fusion protein in the PM is independent of the amount of fusion protein originally present in the PM. Furthermore, no correlation was observed between I_{10sec} and PT growth rate ($R^2=0.0001$; Figure S4C), indicating that exocytosis and PT growth rate do not share a direct linear relationship.

Interestingly, for PTs of both ANX1 over-expressing lines, I_{10sec} was significantly higher than in the complemented line (57%±10%, $p<0.01$ for line #1; 57%±13%, $p<0.05$ for line #4), while their PT growth rate was significantly decreased to 1.34±0.68 μm min^{-1} and 1.78±0.53 μm min^{-1}, respectively ($n=17$ and $n=20$ for ANX1-OX lines #1 and #4, respectively, $p<0.01$; Figure 3C and 3D right panels; Table S1; Video S3). The faster fluorescence recovery is unlikely to be due to a secondary effect of slow PT growth, because all the mutant PTs tested so far

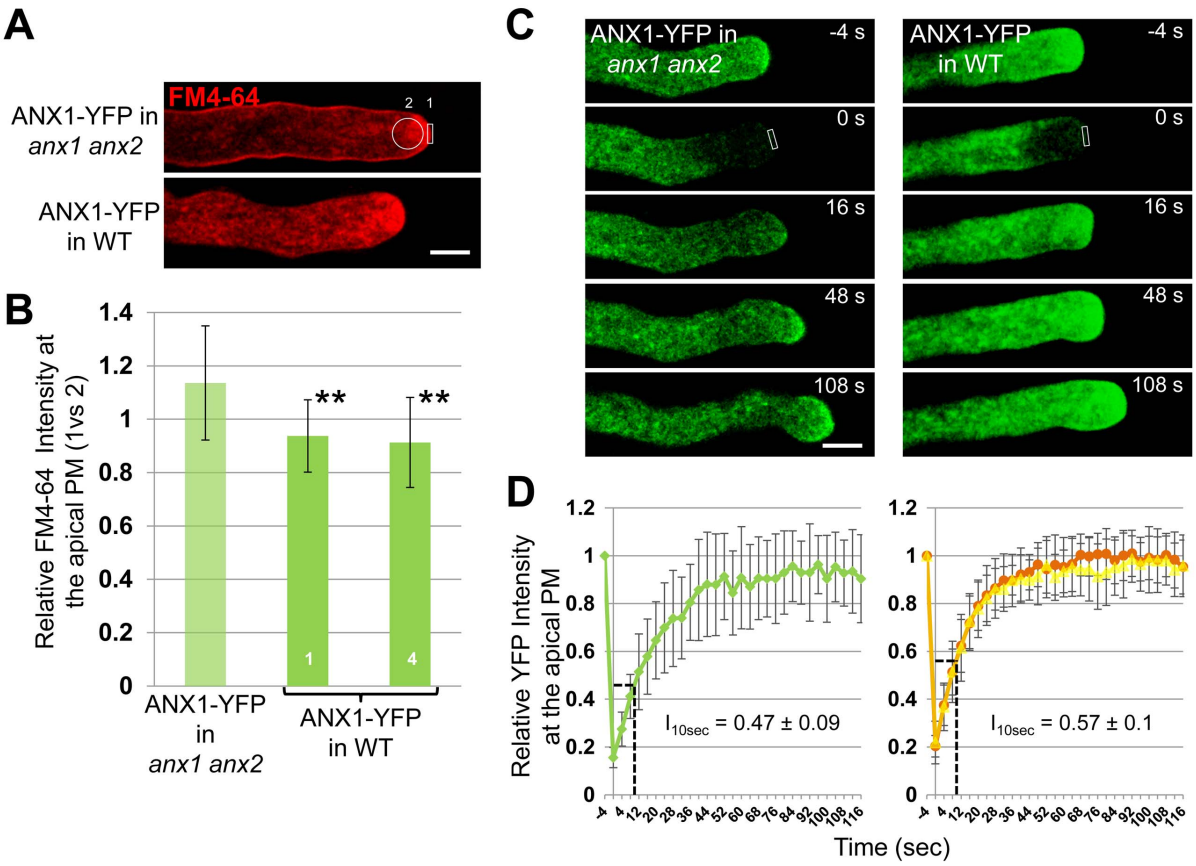

Figure 3. ANX RLK over-expressing pollen tubes do not exhibit endocytosis defects but display an increased rate of exocytosis. (A) Representative single median plane images of a normally growing PT of the ANX1-YFP complemented line (top) and a slow growing PT of the ANX1-YFP over-expressing line (bottom) treated for 5 min with FM4-64 (2 μM). FM4-64 derived fluorescence was quantified in the apical PM (region 1) and the apical cytoplasm (region 2) for $n>25$ PTs of each line. Note that there are more endocytotic and secretory vesicles in the apical cytoplasm of over-expressing PTs. See also corresponding Video S2 and (B). Scale bar = 5 μm. (B) Quantitative analysis of relative FM4-64 fluorescence in the apical PM *versus* the apical cytoplasm in growing PTs of one ANX1-YFP complemented and two over-expressing lines. Data are presented as mean values ± standard deviation (SD) ($n>25$ each). Double asterisks indicate significant differences from the complemented line according to a Student's *t* test with $p<0.01$. (C) Representative time-course imaging of FRAP for a complemented (left) and an over-expressing growing PT (right). Refer to Video S3 for more examples. Scale bar = 5 μm. (D) Quantitative analysis of FRAP time-courses of growing PTs of the complemented line (left, $n=18$) and two over-expressing lines (right, $n>17$ for each). Relative intensity of apical PM-localized ANX1-YFP compared with fluorescence prior to photobleaching was used to quantify the rate of fluorescence recovery. FRAP signals are shown as mean values ± SD. The relative intensity after recovery for 10 s after photobleaching (I_{10sec}) is indicated. See also corresponding Table S1.
doi:10.1371/journal.pbio.1001719.g003

in FRAP experiments, namely DN-ROP1-OX (dominant negative ROP1), CA-ROP1-OX (constitutively active ROP1), RIC3-OX, RIC4-OX, and PIP5K6-OX grow slower than controls and show an inhibition of fluorescence recovery [31,32]. Thus, increased rates of fluorescence recovery at the apical PM indicate that the rate of exocytosis is increased at the apical PM of growing ANX1-OX PTs as compared to controls.

Altogether, our results support the hypothesis that ANX over-expression tilts the balance of exo- to endocytosis towards more exocytosis, which progressively leads to CW accumulation. PT growth slows down as the apical CW thickness increases. When the latter reaches a certain threshold where the CW is not deformable anymore, expansion ceases and apical PM grows inwards due to continuing exocytosis.

Disruption of the Pollen-Expressed NADPH Oxidases RbohH and RbohJ Triggers Anxur-Like Phenotypes

A better understanding of how the ANX RLKs regulate exocytosis requires the identification of downstream components of the ANX-dependent pathway. Recently, FER, which is the closest homologue of the ANX RLKs in *Arabidopsis*, has been shown to function as an upstream regulator of the ROP2/NADPH oxidase RbohC signaling pathway that controls ROS-dependent root hair growth [18]. Moreover, down-regulation of a pollen-expressed NADPH oxidase and application of ROS scavengers inhibit PT growth in tobacco [21]. Thus, we hypothesized that pollen-expressed NADPH oxidases could be downstream components of the ANX RLK pathway that coordinates CW integrity and PT growth. In *Arabidopsis*, NADPH oxidases belong to a family with ten members, two of which, RbohH (At5g60010) and RbohJ (At3g45810), sharing 81% amino acid identity, define a subgroup that is preferentially expressed in pollen (Figure S5C) [13,14]. We isolated two independent single T-DNA insertional mutants for each of these NADPH oxidases, namely *rbohH-1* (GABI_028G04), *rbohH-3* (SALK_136917), *rbohJ-2* (SAIL_31_D07), and *rbohJ-3* (SALK_050665), which show little or no expression of the corresponding gene (Figure S5B). Pollen germination assays showed that PTs of single *rbohJ-2* and *rbohJ-3*

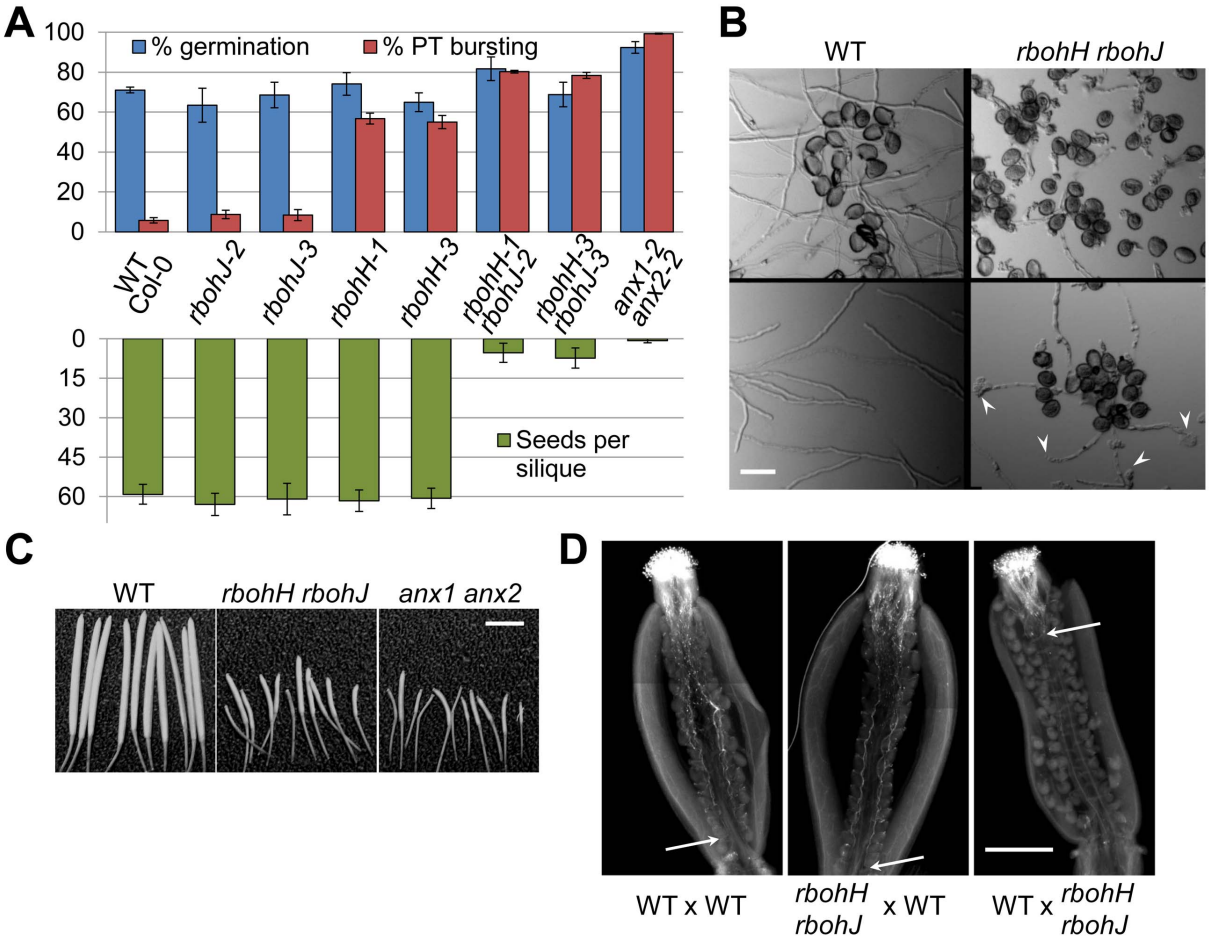

Figure 4. *rbohH rbohJ* mutant pollen display *anxur*-like phenotypes. (A) Quantification of pollen germination and PT rupture percentages (top histogram) and seed per siliques (bottom histogram) for WT, single, and double *rboh* as well as *anx1 anx2* mutant plants. Data are mean ± standard error of the mean (SEM) of three independent experiments with more than 150 pollen grains or ten siliques per genotype and experiment. (B) Representative overview images of WT and *rbohH rbohJ* pollen grown *in vitro* for 5 h. Up to 80% of germinated pollen from *rbohH rbohJ* ruptured with clear traces of cytoplasmic content that was released into the medium (top right), while the remaining germinated grains produce PTs that will burst later on (bottom right, arrowheads) as opposed to WT PTs that grow normally (bottom left). Scale bar = 50 μm. (C) Photographs of siliques from WT, *rbohH rbohJ*, and *anx1 anx2* plants. Scale bar = 500 μm. (D) Representative images of aniline blue staining of a WT pistil pollinated with WT pollen (left), a *rbohH rbohJ* pistil with WT pollen (middle), and a WT pistil with *rbohH rbohJ* pollen (right). Eighteen hours after manual pollination, WT PTs (left and middle panels) had grown through the entire pistil to reach the female gametophytes. In contrast, most of the *rbohH rbohJ* mutant PTs (right) were arrested in the transmitting tract. White arrows indicate the tip of the longest PT. Scale bar = 5 mm.
doi:10.1371/journal.pbio.1001719.g004

mutant plants behaved like WT (~8.5% bursting), while around 57% of PTs of single *rbohH-1* and *rbohH-3* mutant plants ruptured *in vitro* (Figure 4A). However, this mild PT rupture phenotype did not significantly reduce seed set or TE_M *in vivo* (Figure 4A; Table S2). To investigate whether *RbohH* and *RbohJ* are redundant, single mutants were crossed to generate independent double mutant *rbohH-1 rbohJ-2* and *rbohH-3 rbohJ-3* plants. First, double homozygous mutant plants were only rarely found in the progeny of *rbohH-1/RbohH rbohJ-2/rbohJ-2* and *rbohH-3/RbohH rbohJ-3/rbohJ-3* (Table S3). Secondly, PTs of both independent *rbohH-1 rbohJ-2* and *rbohH-3 rbohJ-3* double mutants ruptured up to 80% *in vitro* (Figure 4A and 4B). The remaining germinating grains produced longer PTs, but they eventually also burst (Figure 4B). As a consequence, double homozygotes for *rbohH-1 rbohJ-2* and *rbohH-3 rbohJ-3* were partially sterile, producing only five to seven seeds per silique as compared to ~60 seeds in WT or single mutant plants (Figure 4A and 4C). As evidenced by aniline blue staining after reciprocal crosses of *rbohH rbohJ* with WT, this sterility was due to the double mutant pollen being unable to grow sufficiently *in vivo* to reach and fertilize the female gametophytes (Figure 4D). This was further supported by analyses of male and female transmission efficiencies (TEs) of the *rbohH-1 rbohJ-2* and *rbohH-3 rbohJ-3* mutations, which showed a greatly reduced TE_M while TE_F was not significantly affected (Table S2).

Taken together, these results provide compelling evidence that disruption of both *RbohH* and *RbohJ* leads to spontaneous PT rupture, preventing PTs to reach and fertilize the female gametophytes *in vivo*. Interestingly, all the above mentioned phenotypes are reminiscent of the *anx1 anx2* double mutant phenotype [19,20]. Moreover, our results show partial functional redundancy between pollen-expressed NADPH oxidases, with *RbohH* being able to perfectly substitute for the loss of *RbohJ*, while the latter can only partially substitute for the loss of *RbohH*.

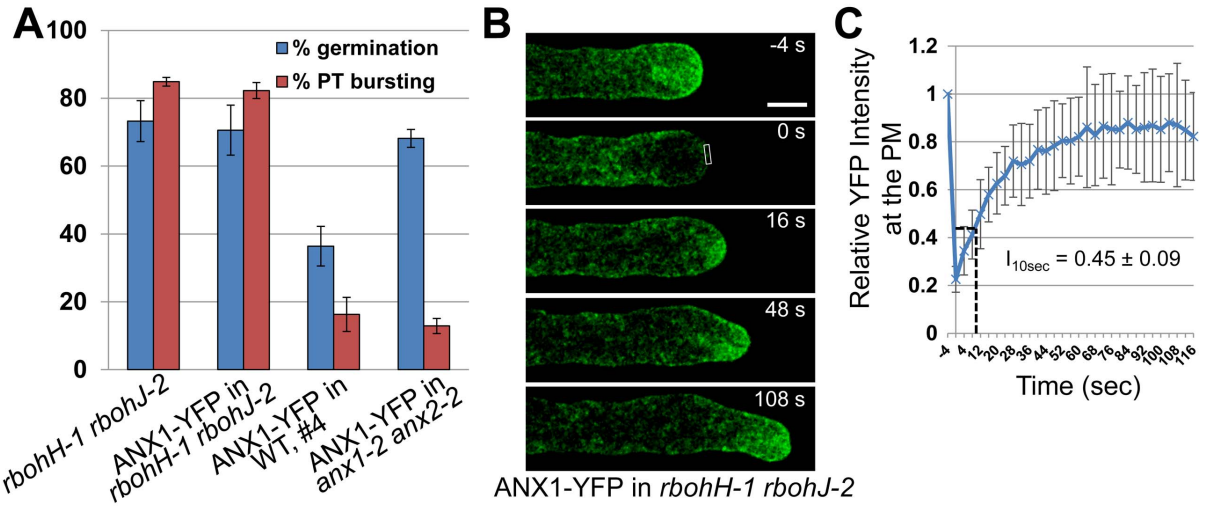

Figure 5. ANX1-YFP over-expression phenotypes are dependent on functional *RbohH* and *RbohJ*. (A) Quantification of pollen germination and PT rupture for *rbohH-1 rbohJ-2*, ANX1-YFP in WT (line #4), ANX1-YFP in *anx1-2 anx2-2* (complemented line), and ANX1-YFP in *rbohH-1 rbohJ-2* plants. Data are mean ± standard error of the mean (SEM) of three independent experiments with more than 150 pollen grains per genotype and experiment. (B) Representative time-course imaging of FRAP for a *rbohH-1 rbohJ-2* PT expressing ANX1-YFP. Scale bar = 5 µm. (C) Quantitative analysis of FRAP time-courses for growing PTs of ANX1-YFP in *rbohH-1 rbohJ-2* ($n = 24$). Relative intensity of apical PM-localized ANX1-YFP compared with fluorescence prior to photobleaching was used to quantify the rate of fluorescence recovery. FRAP signals are shown as mean values ± standard deviation (SD). The relative intensity after recovery for 10 s after photobleaching (I_{10sec}) is indicated. See also corresponding Table S1.

ANX1 Over-expression Phenotypes Depend on Functional RbohH and RbohJ NADPH Oxidases

To test whether *RbohH* and *RbohJ* are indeed downstream effectors of the ANX RLK-dependent pathway, the strong ANX1-OX line (#4) was crossed to *rbohH-1 rbohJ-2* double mutant plants. Partially male sterile plants homozygous for *rbohH-1 rbohJ-2* and homozygous for ANX1-YFP were retrieved in the F2 generation. Intriguingly, *rbohH-1 rbohJ-2* pollen strongly expressing ANX1-YFP behaved exactly like *rbohH-1 rbohJ-2* pollen with germination and PT rupture rates of ~70% and 82%, respectively (Figure 5A). Furthermore, none of the growing PTs ($n>100$) of *rbohH-1 rbohJ-2* plants homozygous for ANX1-YFP displayed CW accumulation or PM invagination, phenotypes observed in ANX1-OX PTs. To independently confirm these results, we directly transformed *rbohH-1 rbohJ-2* mutant with ANX1-YFP fusion. Four independent, partially male sterile *rbohH-1 rbohJ-2* transgenic lines homozygous for ANX1-YFP were recovered in the T2 generation. Again, neither CW accumulation nor PM invagination was observed in growing PTs ($n>100$ PTs for each), which eventually ruptured similar to the *rbohH-1 rbohJ-2* PTs without the ANX1-OX construct. Furthermore, FRAP analyses also showed that the fast recovery rate at the apical PM observed in ANX1-OX PTs was suppressed in the *rbohH rbohJ* background as I_{10sec} for *rbohH rbohJ* PTs over-expressing ANX1-YFP was similar to the complemented line (45% ± 9%, $n = 23$; Figure 5B and 5C; Table S1). Interestingly, a few *rbohH rbohJ* PTs over-expressing ANX1-YFP did not recover 80% of the initial fluorescence, a phenomenon that was never observed in controls or ANX1-YFP over-expressing PTs (Figure S6), indicating that exocytosis may become defective in these *rbohH rbohJ* ANX1-OX PTs.

In summary, these results demonstrate that ANX1-OX phenotypes are dependent on functional *RbohH* and *RbohJ* and, consequently, that these pollen-expressed NADPH oxidases are positive downstream effectors of the ANX RLK-dependent pathway.

NADPH Oxidases RbohH and RbohJ Are Responsible for H_2O_2 Production at the Tip of Growing Pollen Tubes

To check whether disruption of *RbohH* and *RbohJ* impairs the production of ROS, we made use of the fluorescent ROS-sensitive dye 5-(and 6-)chloromethyl-2′,7′-dichlorodihydrofluorescein diacetate (CM-H_2DCFDA) to stain PTs of WT and *rbohH rbohJ* double mutants. Fluorescence quantification of the apical cytoplasm in growing PTs treated for 5 minutes with 2 µM CM-H_2DCFDA showed that PTs of the *rbohH-1 rbohJ-2* and *rbohH-3 rbohJ-3* double mutants displayed only 25% of the CM-H_2DCFDA-derived fluorescence signal observed in WT PTs ($p<0.01$; Figure S7A and S7C). These low levels of CM-H_2DCFDA-derived fluorescence were not due to a defect in dye uptake, as mutant and WT PTs exhibited the same level of fluorescence derived from the ROS-insensitive dye fluorescein diacetate (FDA) (Figure S7B and S7D). These results show that ROS production is indeed impaired in *rbohH rbohJ* PTs as expected for NADPH oxidase mutants [12]. However, because CM-H_2DCFDA oxidation is sensitive to different reactive oxygen and nitrogen species, sensitive to light, and irreversible, this dye cannot be used to monitor ROS production over time in growing PTs. Thus, we generated stably transformed *Arabidopsis* lines with PT expression of the genetically encoded YFP-based ratiometric sensor HyPer, which has been shown to faithfully report H_2O_2 production in bacteria, animal, and plant cells [33,34]. Curiously, in growing WT PTs expressing cytosolic HyPer ($n = 27$), the HyPer activity measured as the ratio of F_{488}/F_{405} was stronger in the shank of PTs than at the tip (Figure 6A and 6B). We hypothesized that this strong shank activity could either be due to the presence of H_2O_2-producing organelles, such as mitochondria and/or peroxisomes in this region, an artifact of HyPer due to its pH sensitivity, or a combination of both. Indeed, it was shown that HyPer's activity artificially increases when the pH increases [33] and that PTs display a pH gradient with an acidic tip and a alkaline shank [35]. Interestingly, at the tip of growing PTs, HyPer activity displayed

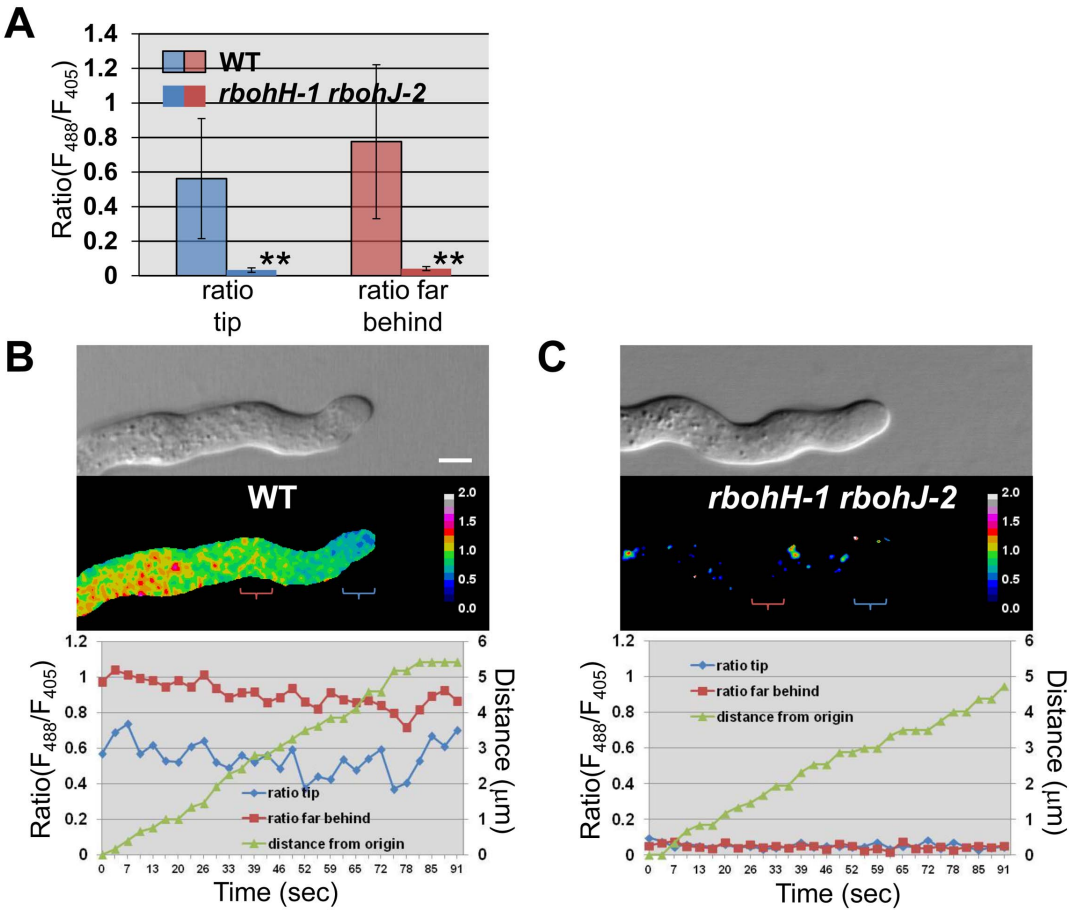

Figure 6. H_2O_2-sensitive HyPer sensor ratiometric imaging shows that RbohH and RbohJ are responsible for H_2O_2 production at the tip of growing pollen tubes. (A) Quantification of HyPer ratio (F_{488}/F_{405}) at the tip and further back in the shank of growing WT ($n = 27$) and *rbohH-1 rbohJ-2* ($n = 22$) PTs. Data are shown as the mean of ratios over 90 seconds ± standard deviation (SD). Double asterisks indicate significant differences from the WT according to a Student's *t* test with $p < 0.01$. (B) Representative images of a growing WT PT expressing cytosolic HyPer and the corresponding histogram displaying the ratios (F_{488}/F_{405}) at the tip (blue line) and behind the tip (red line) over 90 s, as well as the travelled distance of the PT tip (green line). The blue and red parentheses indicate where the circles of 4 µm diameter were positioned for measurements at the tip and behind the tip, respectively. See corresponding Video S4. Scale bar = 5 µm. (C) Representative images of growing *rbohH-1 rbohJ-2* PT expressing cytosolic HyPer. See (B) for details.
doi:10.1371/journal.pbio.1001719.g006

irregular oscillations originating from the tip periphery (Figures 6B and S8A; Video S4). However, oscillations of HyPer activity did not seem to correlate with growth rates (Figure S8B). In growing *rbohH-1 rbohJ-2* PTs, HyPer activity was 16 and 18 times lower at the tip and in the shank, respectively, as compared to the WT ($n = 22$, $p < 0.001$; Figure 6A and 6C). This indicates that membrane-bound RbohH and RbohJ are responsible for most of the H_2O_2 production revealed by the HyPer sensor. Moreover, since HyPer activity in the shank was also strongly reduced in *rbohH-1 rbohJ-2* double mutant PTs (Figure 6A and 6C), the strong activity in the shank of WT PTs is likely due to propagation of the tip-derived H_2O_2 in the alkaline shanks, which artificially increases HyPer activity.

To investigate if Rboh localization is consistent with the Rboh-dependent H_2O_2 production observed at the tip-periphery, we transformed partially sterile *rbohH-3 rbohJ-3* plants with a green fluorescent protein (GFP)-RbohH fusion. Forty-four independent T1 transgenic lines out of 50 displayed rescue of sterility with WT-like elongated siliques (e.g., for three independent T1 lines with good GFP expression, the average of seeds per silique was 40.8±3.8, 40.9±11.1, and 43.4±6.9 as opposed to 6.2±3.5 in untransformed *rbohH-3 rbohJ-3*, $n = 12$ siliques per plant). *In vitro* pollen growth assays confirmed that the *rbohH rbohJ* bursting phenotypes were rescued by GFP-RbohH (Figure S8C) and that GFP-RbohH localized polarly to the plasma membrane at the tip of growing PTs (Figure S8D, left panels). These results show that GFP-RbohH protein fusion is functional and that its localization is consistent with both ANX1-YFP localization (Figure 2A, left panels) and Rboh-dependent H_2O_2 production at the tip periphery (Figure S8A). Furthermore, unlike the *rbohH rbohJ* complemented plants, in WT plants expressing the GFP-RbohH fusion, PM invagination and over-accumulation of CW material were also observed (Figure S8D, right panels), although these phenotypes appeared milder and less frequent than in ANX1-OX PTs.

Calcium Homeostasis Is Impaired in Growing *rbohH rbohJ* Double Mutant Pollen Tubes

ROS and H_2O_2 have been shown to regulate calcium-permeable channels, e.g., in protoplast of root hairs [12] and pear pollen [36], and a tip-focused Ca^{2+} gradient is essential for polar growth [37]. Therefore, we crossed WT plants expressing the genetically encoded FRET-based Ca^{2+}-cameleon YC3.60 in

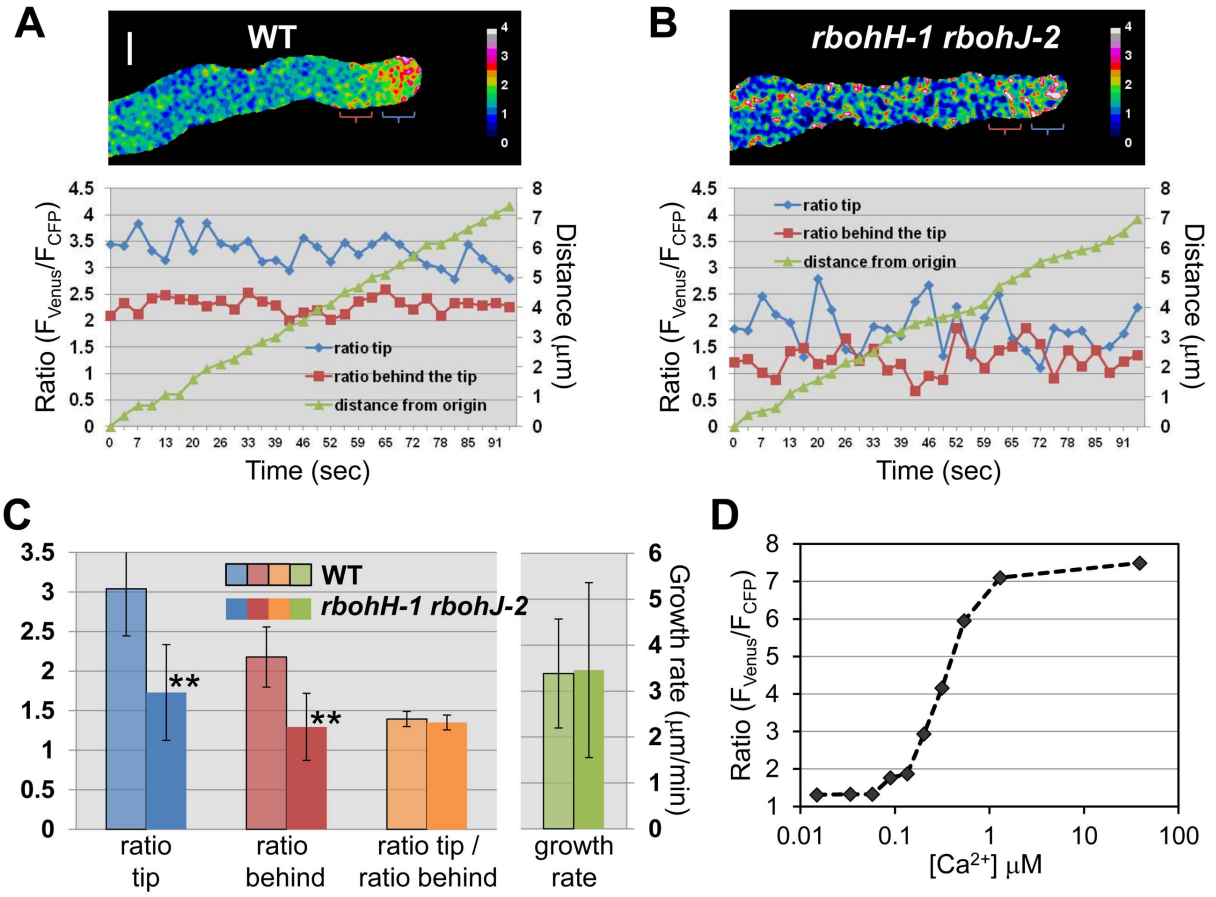

Figure 7. Ca^{2+}-sensitive cameleon YC3.60 ratiometric imaging shows that $[Ca^{2+}]_{cyt}$ levels are decreased and less steady in growing *rbohH-1 rbohJ-2* pollen tubes. (A) Representative images of growing WT PTs expressing cytosolic YC3.60 and the corresponding histogram displaying the ratios (F_{CFP}/F_{Venus}) at the PT tip (blue line) and behind the tip (red line) over 90 seconds, as well as the travelled distance of the PT tip (green line). On the ratiometric image, the blue and red parentheses indicate where the circles of 4 µm diameter were positioned for measurements at the PT tip and behind the tip, respectively. See also corresponding Video S6. Scale bar = 5 µm. (B) Representative images of growing *rbohH-1 rbohJ-2* PTs expressing cytosolic YC3.60. For details, see (A). (C) Quantification of YC3.60 ratio (F_{CFP}/F_{Venus}) at the PT tip (blue bars) and just behind the tip (red bars), as well as the tip-focused Ca^{2+}gradient (ratio at the tip/ratio behind the tip; orange bars) and growth rates (green bars) of growing WT ($n = 46$) and *rbohH-1 rbohJ-2* ($n = 30$) PTs. Data are shown as the mean of ratios or growth rates over 90 seconds ±standard deviation (SD). Double asterisks indicate significant differences from the WT according to a Student's *t* test with $p<0.01$. (D) Titration curve for YC3.60.
doi:10.1371/journal.pbio.1001719.g007

PTs [38] with the *anx1-2 anx2-2* and *rbohH-1 rbohJ-2* double mutants, and partially male sterile *anx1-2 anx2-2* and *rbohH-1 rbohJ-2* plants homozygous for YC3.60 were recovered in subsequent generations. Cytosolic Ca^{2+} concentrations ($[Ca^{2+}]_{cyt}$, measured as F_{CFP}/F_{Venus}) were monitored over time at the PT tip and behind the tip when possible, and compared to YC3.60-expressing WT PTs grown and imaged under the same conditions. First, we attempted to study Ca^{2+} dynamics in *anx1 anx2* bulges before bursting, young growing WT PTs, and arrested WT bulges. Bulges of *anx1 anx2* never produced a growing tube, and only two out 17 burst during imaging. Interestingly, for both *anx1 anx2* bulges that eventually burst, a sudden increase of $[Ca^{2+}]_{cyt}$ was observed (Figure S9A, white arrow) before the first visible sign of rupture (Figure S9A, black arrow; Video S5). However, before bursting, $[Ca^{2+}]_{cyt}$ in non-growing *anx1 anx2* bulges was on average lower than at the tip of growing WT PTs but similar to the arrested WT bulges (Figure S9B). Because one cannot conclude if the decreased levels of $[Ca^{2+}]_{cyt}$ in *anx1 anx2* are due to the lack of ANX RLKs or rather to an indirect effect of arrested growth, we focused on studying Ca^{2+} dynamics in growing WT PTs and *rbohH rbohJ* pollen grains, which produce a few growing PTs that eventually burst.

In steadily growing WT PTs, the tip-focused Ca^{2+} gradient (i.e., higher $[Ca^{2+}]_{cyt}$ at the PT tip compared to behind the tip) was always observed and quite stable ($n = 46$; Figures 7A, 7C, S10A, and S10D; Video S6). Furthermore, as reported previously for *in vitro* grown *Arabidopsis* PTs [38,39], but unlike lily PTs [40], we did not observe regular oscillations for either the PT growth rate or $[Ca^{2+}]_{cyt}$ (Figure 7A). In growing *rbohH rbohJ* PTs ($n = 30$), $[Ca^{2+}]_{cyt}$ was significantly lower than in the WT ($p<0.001$ for both tip and behind the tip regions; Figure 7B and 7C; Video S6). However, the tip-focused Ca^{2+} gradient and the PT growth rate were on average similar to that of WT PTs (Figure 7B and 7C; $p = 0.054$ for gradient, $p = 0.84$ for growth rate). But both the tip-focused Ca^{2+} gradient and the PT growth rate were significantly less steady over time in the *rbohH rbohJ* double mutant than in the WT, as evidenced by a significantly higher variance ($p = 4.1280 \cdot 10^{-13}$ and $p = 0.008737$ for $[Ca^{2+}]_{tip}/[Ca^{2+}]_{behind}$ and growth rate, respectively; Figure S10A–S10F). The steady and jerky growth rate of WT and *rbohH rbohJ* PTs, respectively,

were quite obvious during live-imaging of growing FM4-64 stained PTs (Video S7).

These results indicate that disruption of the pollen-expressed NADPH oxidases *RbohH* and *RbohJ* does not abolish the tip-focused Ca^{2+} gradient but results in PTs that display (i) overall lower $[Ca^{2+}]_{cyt}$ levels, and (ii) unstable tip-focused Ca^{2+} gradients and growth rates. Finally, increasing the external $[Ca^{2+}]$ in the germination medium from 5 mM to 15 mM or 30 mM, significantly decreased the rupture of *rbohH rbohJ* PTs, while lowering the external $[Ca^{2+}]$ had the opposite effect ($p<0.05$; Figure S11). These findings indicate that supplementing Ca^{2+} externally can partially stabilize the growth of *rbohH rbohJ* PTs. Conversely, decreasing external $[Ca^{2+}]$ strongly, increases the frequency of PTs that rupture in the WT (Figure S11), consistent with a pioneering report from the 1980s [41].

Discussion

The Pollen-Expressed NADPH Oxidases RbohH and RbohJ Are Downstream Components of the ANX RLK-Dependent Cell Wall Integrity Pathway

In tip-growing root hairs, *FER* and *RbohC/RHD2* have been proposed to function in the same pathway based on the facts that: (i) *fer* and *rbohC/rhd2* display similar phenotypes with stunted, collapsed, and bursting root hairs, and (ii) that roots and root hairs of *fer* and one FER-OX line accumulate less and more ROS than WT, respectively [12,18]. Similarly, we show here that two independent *rbohH rbohJ* double mutants display *anx*-like phenotypes, i.e., PTs that burst, preventing them from growing to fertilize the female gametophytes (Figure 4). Consequently, both *anx1 anx2* and *rbohH rbohJ* mutant plants are nearly male sterile. In addition, over-expression of both ANX1-YFP and GFP-RbohH triggers over-accumulation of membrane and CW materials (Figures 2 and S8D, right panels). Furthermore, we provide strong genetic evidence for the NADPH oxidases to function downstream of the ANX RLKs, by showing that the phenotypes observed in ANX-OX lines are abolished in the *rbohH rbohJ* mutant background (Figure 5). Therefore, the CrRLK1L-NADPH oxidase signaling module appears to be conserved in tip-growing cells. However, it is unlikely that the CW integrity pathway in pollen is a carbon copy of the root hair pathway, as the biological functions, growth habits and patterns, CW compositions, and growth environments are quite different between these tip-growing cells [42]. For example, in root hairs *FER* has been shown to positively regulate RbohC-dependent ROS production through ROP2-signaling [18]. In PTs, however, it remains unclear whether ANX RLKs also activate the NADPH oxidases RbohH and RbohJ through ROP-signaling, because over-activation of ROP-signaling leads to growth depolarization but does not trigger CW accumulation, PM invagination, or increased apical exocytosis [32,43,44], as we observed it in ANX1-OX lines (Figures 2 and 3).

NADPH Oxidases RbohH and RbohJ Are Responsible for ROS and Pulsating H_2O_2 Production at the Tip of Growing Pollen Tubes

Our understanding of the role of NADPH oxidase-derived ROS signaling in plant development and in responses to abiotic and biotic stresses has improved tremendously over the past few years [13,14,27]. Production of different ROS species has been imaged in different plant tissue and cell types, but because of the irreversible oxidation of the different dyes used (e.g., diaminobenzidine tetrahydrochloride, nitro blue tetrazolium [NBT], H_2DCFDA and derivatives) meaningful information about the dynamics of ROS production is still scarce [45]. GFP-based, genetically encoded sensors such as roGFPs and HyPer, which display reversible changes in fluorescence to alterations in redox/ROS levels, have been successfully developed and tested in plant cells [45]. However, none of them have been assayed in a mutant background affecting ROS-producing enzymes. Here, we used the cytoplasmic H_2O_2-selective HyPer sensor expressed in PTs in a *rbohH rbohJ* NADPH oxidase-deficient mutant background to gain more insights into H_2O_2 production in tip-growing cells. HyPer activity displayed irregular oscillations at the tip of growing WT PTs (Figures 6B and S8). HyPer oscillations are unlikely due to pH oscillations reported for the tip of growing PTs, because (i) pH at the tip varies [35] in a range where HyPer is not really pH-sensitive [33], and (ii) HyPer activity is completely abolished in growing *rbohH rbohJ* mutant PTs (Figure 6A and 6C). Moreover, HyPer activity originated from the periphery of the growing tip (Figure S8A), which is consistent with (i) the tip-preferential PM RbohH localization (Figure S8D, left panels) and the reported PM localization of other NADPH oxidases [9,46], (ii) the NADPH oxidase activity reported at the PM [47,48], and (iii) the extracellular, tip-localized $O_2^{\cdot -}$ distribution revealed by NBT staining of PTs [21,48].

NADPH Oxidases Fine Tune Calcium Homeostasis

The exact mechanism by which NADPH oxidase-dependent ROS regulate polar growth is still not fully understood. One reason for this is that quantitative information with good temporal and spatial resolution is difficult to obtain from growing CrRLK1L and/or NADPH-oxidase mutant cells (root hairs or PTs), owing to their rapid loss of cellular integrity. On one hand, the NADPH oxidase RbohC has been proposed to generate ROS that activate Ca^{2+}-permeable channels at the PM to establish the tip-focused Ca^{2+} gradient and to promote expansion at the tip of root hairs [12,25]. On the other hand, a tip-focused Ca^{2+} gradient was observed in *rbohC* root hairs under certain conditions, indicating that *RbohC* was not essential to generate the Ca^{2+} gradient, but rather plays a role in restricting growth to the tip by rigidifying the CW behind the tip [26]. On the basis of our results we propose a third alternative. Unlike *anx1 anx2*, a small but appreciable number (~20%) of germinating *rbohH rbohJ* pollen grains are able to produce longer tubes *in vitro* that, however, will eventually burst, too. We took advantage of this opportunity to study $[Ca^{2+}]_{cyt}$ dynamics with a good spatial and temporal resolution on growing NADPH oxidase-deficient PTs. First, the tip-focused Ca^{2+} gradient, visualized by the ratio between $[Ca^{2+}]_{tip}/[Ca^{2+}]_{behind}$, was clearly visible in growing *rbohH rbohJ* PTs, confirming that NADPH oxidases are not required to generate the Ca^{2+} gradient. However, unlike steadily growing WT PTs, which maintain a constant Ca^{2+} gradient over time (Figure S10A, S10D, and S10E), *rbohH rbohJ* PTs displayed a very unstable gradient, which could sometimes be steep but was abolished a few seconds later (Figure S10B, S10D, and S10E). This was correlated with more variable growth rates in *rbohH rbohJ* mutant compared to steadily growing WT PTs. Moreover, the global cytosolic Ca^{2+} levels were significantly lower in the growing *rbohH rbohJ* mutant PTs compared to WT PTs (Figure 7C). An increase in external $[Ca^{2+}]$ partially rescued the rupture of *rbohH rbohJ* PTs, while lowering the external $[Ca^{2+}]$ increased PT rupture in both the mutant and WT (Figure S11). This is in agreement with previous studies, which showed that lowering external $[Ca^{2+}]$ or limiting/blocking Ca^{2+} influx causes PTs and root hairs to burst [41,49]. The data reported here are consistent with NADPH oxidase-dependent ROS activating Ca^{2+}-permeable channels for Ca^{2+} influx [12,36]. However, we propose that these yet unidentified

channels do not generate the tip-focused Ca^{2+} gradient on their own; rather, they fine tune the Ca^{2+} gradient by stabilizing it to sustain steady growth of *Arabidopsis* PTs. It is noteworthy that different types of PM-localized Ca^{2+} channels have been characterized recently in tip-growing cells [37,50]. Among these, the Cyclic-Nucleotide-Gated Channel (CNGC) family is of particular interest, because single *cngc18* or double *cngc7 cngc8* mutant PTs spontaneously rupture after germination or produce kinky PTs that often burst as well [51,52]. Thus, CNGCs constitute good candidates for Ca^{2+} channels that are regulated by the CrRLK1L-NADPH oxidase signaling module at the PM. Annexins are also possible candidates as ANN1 has recently been shown to function as a ROS-activating Ca^{2+} transporter in root cells [53].

ANX RLKs Regulate Exocytosis at the Apical Plasma Membrane of Pollen Tubes

One of the many roles proposed for the tip-focused Ca^{2+} gradient is to facilitate and stimulate exocytosis at the site of growth [54,55], where the exocyst complex has been shown to function [56]. Increasing external [Ca^{2+}] leads to root hair and PT growth inhibition and CW thickening [41,49]. However, in this case it is not clear whether the accumulation of secreted CW material is due to an increase of the exocytosis rate or to uncoupling of exocytosis (that otherwise remains the same) from growth. Interestingly, we found that ANX over-expressing PTs grow slower than controls and also display CW accumulation (Figure 2). By performing FRAP analyses in the apical membrane of growing PTs of WT, *anx1 anx2*, and *rbohH rbohJ* plants expressing the ANX1-YFP fusion protein, we show that the rate of exocytosis is significantly increased in ANX1-OX PTs compared to controls. In contrast, for some of the *rbohH rbohJ* mutant PTs that have low calcium levels and an unsteady Ca^{2+} gradient, the recovery was impaired during our analysis. In agreement, the Ca^{2+}channel blocker $LaCl_3$, which has been shown to trigger the rupture of root hairs [49], appears to inhibit FRAP at the PT tip [32].

A Model for the CrRLK1L-NADPH Oxidase Signaling Pathway

Altogether our data are consistent with the following sequence of events: ANX RLKs positively regulate the NADPH oxidases RbohH and RbohJ, possibly through ROP signaling, to periodically produce ROS. Subsequently, ROS activate Ca^{2+}-permeable channels for calcium influx to fine tune the tip-focused Ca^{2+} gradient, which in turn sustains secretion at the apical tip enabling PTs to elongate steadily without a loss of CW integrity. Perturbations of the pathway by over-expressing ANX RLKs would lead to a NADPH oxidase-dependent over-production of ROS and Ca^{2+} influx at the PT tip, which in turn would increase the secretion rate of membrane and CW materials, progressively leading to growth cessation and membrane invagination. Conversely, disrupting the ANX RLKs or NADPH oxidase would abolish NADPH oxidases-dependent ROS production and impair the opening of ROS-activated Ca^{2+}-permeable channels, thus limiting the cell's ability to buffer $[Ca^{2+}]_{cyt}$ variation that is required to maintain a steady tip-focused Ca^{2+} gradient. Consequently, the Ca^{2+} gradient and exocytosis at the PT tip would become erratic and, if not stabilized by compensatory mechanisms, the CW thickness would decrease until turgor pressure would lead to PT rupture. Finally, our model does not exclude that, in parallel to the signaling events described above, NADPH oxidase-dependent ROS and/or Ca^{2+} could directly alter CW properties, thereby affecting PT tip-growth. To investigate this possibility, direct measurements of the impact of ROS on CW properties during tip-growth would need to be established. We are confident that combining the continuously improving polar growth models and techniques to measure mechanical properties of growing cells [57,58] with genetic approaches, will soon uncover some of the remaining mysteries of the fascinating coordination between CW integrity and polar growth.

Materials and Methods

Ruthenium Red, FM4-64, CM-H_2DCFDA, and FDA Imaging

After 3 h to 5 h of *in vitro* incubation on solid germination medium, 100 µl of liquid germination medium containing 0.01% Ruthenium red (Sigma, R-2751) or 2 µM of either FM4-64 (Molecular Probes, Invitrogen, T3166), CM-H_2DCFDA (Molecular Probes, Invitrogen, C6827), or FDA (Sigma, F7378) were applied for 5 min to PTs, then washed away with fresh dye-free medium before imaging. PTs stained with Ruthenium red were imaged with a Leica DM6000 (Leica Microsystems). PTs stained with either FM4-64, CM-H_2DCFDA, or FDA were imaged with a Leica SP2 or SP5 confocal microscope. For FM4-64 stained PTs, the apical PM region was defined as the first 2.5 µm along PM at the apex. A circle (2.5 µm in diameter) 3 µm away from tip was chosen for measurement of apical cytosol intensity. Relative localization of the FM4-64 dye on the PM *versus* the apical cytosol was calculated to illustrate the degree of FM4-64 internalization. For CM-H_2DCFDA and FDA stained PTs, a circle (4 µm in diameter) 3 µm away from tip was chosen to measure apical cytosol intensity. All dye-derived fluorescence intensities were measured using the ImageJ 1.47d software after background subtraction. PTs of different genotypes were all imaged and quantified under the same conditions.

FRAP Imaging and Analyses

Growing PTs expressing ANX1-YFP in an *anx1-2 anx2-2* (complemented line), WT (ANX-OX, lines #1 and #4), and *rbohH-1 rbohJ-2* backgrounds were used for FRAP analyses with the same imaging and quantification parameters. The apical region of PTs was photobleached using 100% power of a 514-nm laser (Leica SP5), and the recovery of fluorescence was monitored every 4 s in the following 2 min. The apical PM region was defined on the bright-field pictures at every time frame as the first 2.5 µm along PM at the apex, and fluorescence intensities were measured with ImageJ 1.47d software after background subtraction. Relative intensity of PM-localized ANX1-YFP compared with fluorescence before photobleaching was used to quantify the speed of fluorescence recovery. See Table S1 for curve fitting.

Ratiometric Imaging of HyPer and YC3.60 and Relative Analyses

Fluorescence in growing PTs of WT and *rbohH-1 rbohJ-2* expressing either HyPer or YC3.60 were acquired (Leica SP2 confocal microscope) and quantified (ImageJ 1.47d) in the exact same conditions. For HyPer, fluorescence was acquired with the sequential mode and excitation at 488 nm and emission between 500–540 nm for F_{488} and excitation at 405 nm and emission between 500–540 nm for F_{405}. Two circular regions of interest (ROIs; 4 µm in diameter), one 0.5 µm, the other 20 µm away from the apex were drawn for measurement of apical cytosol and far behind the tip intensities, respectively, for each single time point of each PT. For YC3.60, excitation was 458 nm then emission 469–501 nm for F_{CFP} and 522–554 nm for F_{Venus}. Two

circular ROIs (4 μm in diameter), one 0.5 μm, the other 10 μm away from the apex, were drawn for measurement of apical cytosol and behind the tip intensities, respectively, for each single time point of each PT. All ratiometric measurements, i.e., F_{488}/F_{405} and F_{CFP}/F_{Venus}, were determined with ImageJ 1.47d and its Ratio ROI Manager plugin after background subtraction. Ratiometric pictures were generated with the plugin Ratio Stack after median filtering. The YC3.60 titration curve (Figures 7D) was obtained as described before [38].

All primers used in this study are listed in Table S4. Additional protocols are described in Text S1.

Supporting Information

Figure S1 Over-expression of ANX RLKs inhibits pollen germination and increases pollen tube width. (A) Quantification of pollen germination rate after 5 h of *in vitro* growth for WT, two and three independent ANX1-YFP and ANX2-YFP T3 complemented lines, respectively, as well as four independent T3 ANX1-YFP and ANX2-YFP over-expression lines. Data are representative of three experiments with more than 150 pollen for each genotype. The corresponding PT length measurements are displayed in Figure 1A. (B) Quantification of PT width after 5 h of *in vitro* growth for WT, one ANX1-YFP, and one ANX2-YFP T3 complemented lines, as well as three independent T3 ANX1-YFP and ANX2-YFP over-expression lines. Data represent mean values ± standard error of the mean (SEM) of three independent experiments with more than 40 PTs per genotype and experiment. Double asterisks indicate statistically significant differences from the WT according to a Student's *t* test with $p<0.01$.
(TIF)

Figure S2 ANX1-YFP and ANX2-YFP fusion proteins complement the *anx1 anx2* pollen tube rupture phenotype. Quantification of pollen germination rate and PT rupture after 5 h of *in vitro* growth for WT, *anx1-2 anx2-2*, *anx1-2/anx1-2 anx2-2/ANX2*, 6, and 5 independent T1 lines of ANX1-YFP in *anx1-2/anx1-2 anx2-2/ANX2* and ANX2-YFP in *anx1-1/anx1-1 anx2-1/ANX2*, respectively, as well as two and three independent T3 homozygous ANX1-YFP in *anx1-2 anx2-2* and ANX2-YFP in *anx1-1 anx2-1* complemented lines, respectively. More than 150 pollen were analyzed per genotype.
(TIF)

Figure S3 ANX RLK over-expression triggers plasma membrane invagination. (A) Median plane confocal image of an ANX1-YFP over-expressing PT, in which the apical membrane grows inwards. Filters are indicated on the left. Scale bar = 5 μm. (B) Single plane confocal image of plasma membrane invagination in an ANX1-YFP over-expressing pollen grain.
(TIF)

Figure S4 BFA treatment disrupts the enrichment of ANX1-YFP at the apical plasma membrane. (A) Representative median plane sections of *anx1 anx2* complemented PTs expressing ANX1-YFP with (right) or without (left) BFA treatment. Note that the YFP-derived fluorescence is much weaker in the apical membrane-derived region of interest of the BFA-treated PTs compared to that of non-treated PTs (left). The same regions of interest (ROIs) were used for FRAP experiments. No correlation between relative fluorescence recovery 10 s after photobleaching and original amount of fluorescent protein in the apical plasma membrane (B) nor with PT growth rate (C).
(TIF)

Figure S5 Structure and expression of *Rboh* genes in *Arabidopsis*. (A) The genomic organization of the pollen-expressed NADPH oxidase genes *RbohH* and *RbohJ* and positions of the *rbohH-1*, *rbohH-3*, *rbohJ-2*, and *rbohJ-3* T-DNA insertions. The orientation of the left border sequence of the respective T-DNAs is represented by black arrows. The positions of the primers used to genotype the mutants are indicated. (B) RT-PCR analyses of cDNAs from open-flowers show no *RbohH* transcripts in the T-DNA insertion lines *rbohH-1 and rbohH-3*. There are much less or no *RbohJ* transcripts in the T-DNA insertion lines *rbohJ-2* and *rbohJ-3*, respectively. *UBC21* (*At5g25760*) was used as a control. Amplification was performed for 30 cycles for *UBC21* and for 35 cycles for *RbohH* and *RbohJ*. (C) Multiple alignments of *Arabidopsis* Rboh proteins were performed with ClustalW 1.83 and the phylogenetic tree was reconstructed with MEGA4 using the protein sequence parsimony method (bootstrap test, 1,000 replicates). Black and grey circles at nodes indicate bootstrap values of more than 900 and between 800 and 900, respectively. The HsNOX5 was used as outgroup. The tree was then combined with the relative gene expression of *Arabidopsis Rboh* family members in various plant tissues according to the Genevestigator microarray database using the Meta-Profile Analysis tool, Anatomy Profile [59].
(TIF)

Figure S6 Distribution of pollen tubes of ANX1-YFP in *anx1 anx2*, in wild-type (over-expressor line #1 and #4), and *rbohH rbohJ* backgrounds relative to the time required to recover 80% of the initial fluorescence. Unlike PTs from complemented and over-expressor lines, some *rbohH rbohJ* PTs expressing ANX1-YFP were not able to recover 80% of the initial fluorescence at the apical plasma membrane.
(TIF)

Figure S7 *rbohH rbohJ* pollen tubes display decreased levels of ROS-sensitive CM-H_2DCFDA-derived fluorescence compared to the wild type. (A) Single median plane images of growing WT and *rbohH rbohJ* PTs stained with the ROS-sensitive CM-H_2DCFDA dye and imaged with the same settings. Scale bar = 5 μm. (B) Single median plane images of growing WT and *rbohH rbohJ* PTs stained with the ROS-insensitive FDA dye and imaged with the same settings. The scale is the same as in (A). (C) Quantification of ROS-sensitive CM-H_2DCFDA-derived fluorescence in a circle with 4 μm diameter at the tip of growing WT and *rbohH rbohJ* PTs. Data are mean ± standard error of the mean (SEM) of three independent experiments with more than eight PTs per genotype and experiment. Double asterisks indicate significant differences from the WT according to a Student's *t* test with $p<0.01$. (D) Quantification of ROS-insensitive FDA-derived fluorescence in a circle with 4 μm diameter at the tip of growing WT and *rbohH rbohJ* PTs. Data are mean ± SEM of three independent experiments with more than eight PTs per genotype and experiment.
(TIF)

Figure S8 Pulsating H_2O_2-sensitive HyPer activity at the tip of growing wild-type pollen tubes correlates with GFP-RbohH localization. (A) Time-course ratiometric imaging of the tip of growing WT PT expressing cytosolic HyPer and the corresponding histogram (B) displaying the ratio (F_{488}/F_{405}) at the tip (blue line) over 90 s, as well as the PT growth rates (green line). Scale bar = 5 μm. (C) *In vitro* PT growth assay showing that the GFP-RbohH protein fusion complements the *rbohH rbohJ* PT bursting phenotype in T1 *rbohH-3 rbohJ-3* heterozygous for GFP-RbohH. Left, *rbohH-3 rbohJ-3* pollen. Right, pollen of a representative T1 *rbohH-3 rbohJ-3* line expressing GFP-RbohH. (D) Representative single median plane images of a normally growing PT of a GFP-RbohH complemented line (left) and an arrested PT of an GFP-RbohH over-expressing line with apical

membrane invagination (right) and over-accumulation of CW material (asterisk). The different filters are indicated. Before imaging, PTs were treated for 5 min with germination liquid medium containing FM4-64 (2 μM). Scale bar = 5 μm.
(TIF)

Figure S9 Ca^{2+}− sensitive cameleon YC3.60 ratiometric imaging shows that $[Ca^{2+}]_{cyt}$ levels are decreased in *anx1 anx2* bulges compared to young, growing wild-type pollen tubes but are similar to arrested wild-type bulges. (A) Representative ratiometric images of young growing WT PT, arrested WT bulge, and bursting *anx1 anx2* bulge expressing cytosolic YC3.60. On the ratiometric images, the black circles represent the region of interests of 4 μm diameter used for measurements at the PT tip. At time = 76 s, a white arrow indicates a sudden increase of $[Ca^{2+}]_{tip}$ in *anx1 anx2* before the bulge actually bursts (black arrow at time = 84 s). Note how external Ca^{2+} enters the *anx1 anx2* bulge once it has ruptured. See also corresponding Video S5. The calibration bar is the same as in Figure 7A. Scale bar = 5 μm. (B) Quantification of YC3.60 ratio (F_{CFP}/F_{Venus}) at the tip of young, growing WT PTs, arrested WT bulges, and *anx1 anx2* bulges before rupture ($n>15$ for each category). Data are shown as the mean of ratios over 90 s±standard deviation (SD). Double asterisks indicate significant differences from the growing WT PTs according to a Student's *t* test with $p<0.01$.
(TIF)

Figure S10 Tip-focused Ca^{2+} gradient and pollen tube growth rates are less stable in *rbohH-1 rbohJ-2* than in the wild type. Representative images of growing WT (A) and *rbohH-1 rbohJ-2* (B) PTs expressing cytosolic YC3.60 and the corresponding histograms displaying the ratio of $[Ca^{2+}]_{tip}/[Ca^{2+}]_{behind}$ (i.e., tip-focused Ca^{2+} gradient, orange line) over 90 s, and the travelled distance of the PT tip (green line). Note how both the tip-focused Ca^{2+} gradient and the PT growth rate are more stable in WT compared to the mutant. Scale bar = 5 μm. (C) Histogram of the variance of $[Ca^{2+}]_{tip}$ in M^2 of WT (green) and *rbohH-1 rbohJ-2* (red). The variance of the $[Ca^{2+}]_{tip}$ is significantly elevated in mutant PTs compared to the WT ($p = 2.8 \cdot 10^{-10}$; Wilcoxon sum rank test). (D) Histogram in arbitrary units of the ratio of the YC3.60 of $[Ca^{2+}]_{tip}/[Ca^{2+}]_{behind}$ in growing PTs of WT (green) and *rbohH-1 rbohJ-2* (red). (E) Histogram of the variance (arbitrary units) of the ratio of $[Ca^{2+}]_{tip}/[Ca^{2+}]_{behind}$ in growing PTs of WT (green) and *rbohH-1 rbohJ-2* (red). The variance of the ratio of $[Ca^{2+}]_{tip}/[Ca^{2+}]_{behind}$ is significantly increased in mutant pollen tubes ($p = 4.1280 \cdot 10^{-13}$; Wilcoxon sum rank test), indicating that the tip-focused Ca^{2+} gradient is less stable in the mutants than in the WT. (F) Histogram of the variance of the growth rates in $(mm/s)^2$ for WT (green) and *rbohH-1 rbohJ-2* (red) PTs. Note that the variance of the growth rates is significantly higher in mutant PTs compared to the WT ($p = 0.008737$, Wilcoxon one-sided rank-sum test), indicating that *rbohH-1 rbohJ-2* PT growth is unstable compared to PT growth of the WT.
(TIF)

Figure S11 External Ca^{2+} partially suppresses pollen tube rupture of *rbohH rbohJ* mutants. (A) Quantification of the germination rate of pollen from WT, *rbohH-1 rbohJ-2*, and *rbohH-3 rbohJ-3* plants on different Ca^{2+}-containing media. Data are mean ± standard error of the mean (SEM) of three independent experiments with more than 150 pollen grains per genotype and experiment. Single asterisks indicate statistically significant differences from the corresponding control at 5 mM $[Ca^{2+}]$ (indicated by #) according to a Student's *t* test with $p<0.05$. (B) Quantification of PT rupture from WT, *rbohH-1 rbohJ-2*, and *rbohH-3 rbohJ-3* plants on different Ca^{2+}-containing media. Data are mean ± SEM of three independent experiments with more than 150 pollen grains per genotype and experiment. Single asterisks indicate statistically significant differences from the corresponding control at 5 mM $[Ca^{2+}]$ (indicated by #) according to a Student's *t* test with $p<0.05$. (C) Representative images of WT (top) and *rbohH rbohJ* (bottom) pollen grains grown *in vitro* for 5 h on 0 (left) and 15 mM $[Ca^{2+}]$ (right). Scale bar = 5 μm.
(TIF)

Table S1 Parameters of fluorescence recovery after photobleaching (FRAP) at the apical plasma membrane of growing pollen tubes for ANX1-YFP in different backgrounds.
(DOCX)

Table S2 Segregation analysis of *rboh* mutations by PCR-based genotyping or scoring herbicide resistance of the progeny resulting from reciprocal crosses with the wild type (Col-0).
(DOCX)

Table S3 Segregation analysis of *rboh* mutations by PCR-based genotyping in the progeny after self-fertilization.
(DOCX)

Table S4 Oligonucleotides used in this study.
(DOCX)

Text S1 Supporting protocols.
(DOCX)

Video S1 Time-course imaging of plasma membrane invagination in an ANX1-YFP over-expressing pollen tube that ceased to elongate. Top, bright-field; middle, YFP-derived fluorescence; bottom, FM4-64-derived fluorescence. The focal plane was adjusted between the different frames to focus on the apical membrane growing inwards. Δt = 40 s. Scale bar = 5 μm.
(AVI)

Video S2 Representative time-course imaging of complemented (top) and ANX1-YFP over-expressing pollen tubes (bottom) treated for 5 min with FM4-64 (2 μM). Δt = 0.56 s. Scale bar = 5 μm.
(AVI)

Video S3 Time-course imaging of representative FRAP experiments on two complemented (top) and two ANX1-YFP over-expressing (bottom) pollen tubes. Bleaching time-stamp occurs at t = 0 s. Green arrow time-stamps appear when 80% of the initial fluorescence is recovered in the apical plasma membrane. Note that ANX1-YFP over-expressing PTs grow slower but recover their fluorescence faster that complemented lines. Δt = 4 s. Scale bar = 5 μm.
(AVI)

Video S4 Time-course imaging of growing wild-type pollen tube expressing the cytosolic H_2O_2-sensitive HyPer. Top and middle panels show the fluorescence collected between 500 and 540 nm after excitation at 488 nm and 405 nm, respectively. Bottom panel shows the corresponding ratiometric image (F_{488}/F_{405}). Note the oscillating HyPer activity at the tip of the growing PT. Δt = 3.26 s. Scale bar = 5 μm.
(AVI)

Video S5 Time-course ratiometric imaging of a young, growing wild-type pollen tube, an arrested wild-type

bulge, and a bursting *anx1 anx2* bulge. $\Delta t = 4$ s. The calibration bar is the same as in Figure 7A. Scale bar = 5 μm. At time = 76 s, a white arrow indicates a sudden increase of $[Ca^{2+}]_{tip}$ in *anx1 anx2* before the bulge actually bursts (black arrow at time = 84 s).
(AVI)

Video S6 Time-course ratiometric imaging of three growing wild-type (left) and three *rbohH rbohJ* pollen tubes expressing the cytosolic Ca^{2+}-sensitive YC3.60. $\Delta t = 3.26$ s. Scale bar = 5 μm.
(AVI)

Video S7 Time-course imaging of FM4-64 stained wild-type and *rbohH rbohJ* pollen tubes growing steadily and unsteadily, respectively. $\Delta t = 1$ s. Scale bar = 5 μm.
(AVI)

Acknowledgments

We thank all members of the Grossniklaus group for enriching discussions, V. Gagliardini, A. Bolaños, C. Eichenberger, D. Guthörl, and P. Kopf (University of Zürich) for general lab support, and M. Iwano (Nara Institute of Science and Technology) for providing us seeds of the pAct1-YC3.60 line and purified YC3.60 protein.

Author Contributions

The author(s) have made the following declarations about their contributions: Conceived and designed the experiments: ABD UG. Performed the experiments: ABD. Analyzed the data: ABD DSL. Contributed reagents/materials/analysis tools: AN CMF ST. Wrote the paper: ABD UG.

References

1. Brown NH (2011) Extracellular matrix in development: insights from mechanisms conserved between invertebrates and vertebrates. Cold Spring Harb Perspect Biol 3: pii.
2. Okayama H (2012) Cell cycle control by anchorage signaling. Cell Signal 24: 1599–1609.
3. Wolf S, Hématy K, Höfte H (2012) Growth control and cell wall signaling in plants. Annu Rev Plant Biol 63: 381–407.
4. Hématy K, Sado P-E, Van Tuinen A, Rochange S, Desnos T, et al. (2007) A receptor-like kinase mediates the response of *Arabidopsis* cells to the inhibition of cellulose synthesis. Curr Biol 17: 922–931.
5. Escobar-Restrepo J-M, Huck N, Kessler S, Gagliardini V, Gheyselinck J, et al. (2007) The FERONIA receptor-like kinase mediates male-female interactions during pollen tube reception. Science 317: 656–660.
6. Lindner H, Müller LM, Boisson-Dernier A, Grossniklaus U (2012) CrRLK1L receptor-like kinases: not just another brick in the wall. Curr Opin Plant Biol 15: 659–669.
7. Cheung AY, Wu H-M (2011) THESEUS1, FERONIA and relatives: a family of cell wall-sensing receptor kinases? Curr Opin Plant Biol 14: 632–641.
8. Boisson-Dernier A, Kessler SA, Grossniklaus U (2011) The walls have ears: the role of plant CrRLK1Ls in sensing and transducing extracellular signals. J Exp Bot 62: 1581–1591.
9. Lee Y, Rubio MC, Alassimone J, Geldner N (2013) A mechanism for localized lignin deposition in the endodermis. Cell 153: 402–412.
10. Kwak JM, Mori IC, Pei Z-M, Leonhardt N, Torres MA, et al. (2003) NADPH oxidase *AtrbohD* and *AtrbohF* genes function in ROS-dependent ABA signaling in *Arabidopsis*. EMBO J 22: 2623–2633.
11. Torres MA, Dangl JL, Jones JDG (2002) *Arabidopsis* gp91phox homologues AtrbohD and AtrbohF are required for accumulation of reactive oxygen intermediates in the plant defense response. Proc Natl Acad Sci U S A 99: 517–522.
12. Foreman J, Demidchik V, Bothwell JHF, Mylona P, Miedema H, et al. (2003) Reactive oxygen species produced by NADPH oxidase regulate plant cell growth. Nature 422: 442–446.
13. Marino D, Dunand C, Puppo A, Pauly N (2012) A burst of plant NADPH oxidases. Trends Plant Sci 17: 9–15.
14. Suzuki N, Miller G, Morales J, Shulaev V, Torres MA, et al. (2011) Respiratory burst oxidases: the engines of ROS signaling. Curr Opin Plant Biol 14: 691–699.
15. Denness L, McKenna JF, Segonzac C, Wormit A, Madhou P, et al. (2011) Cell wall damage-induced lignin biosynthesis is regulated by a reactive oxygen species- and jasmonic acid-dependent process in *Arabidopsis*. Plant Phys 156: 1364–1374.
16. Keinath NF, Kierszniowska S, Lorek J, Bourdais G, Kessler SA, et al. (2010) PAMP (pathogen-associated molecular pattern)-induced changes in plasma membrane compartmentalization reveal novel components of plant immunity. J Biol Chem 285: 39140–39149.
17. Yu F, Qian L, Nibau C, Duan Q, Kita D, et al. (2012) FERONIA receptor kinase pathway suppresses abscisic acid signaling in *Arabidopsis* by activating ABI2 phosphatase. Proc Natl Acad Sci U S A 109: 14693–14698.
18. Duan Q, Kita D, Li C, Cheung AY, Wu H-M (2010) FERONIA receptor-like kinase regulates RHO GTPase signaling of root hair development. Proc Natl Acad Sci U S A 107: 17821–17826.
19. Boisson-Dernier A, Roy S, Kritsas K, Grobei M a, Jaciubek M, et al. (2009) Disruption of the pollen-expressed *FERONIA* homologs *ANXUR1* and *ANXUR2* triggers pollen tube discharge. Development 136: 3279–3288.
20. Miyazaki S, Murata T, Sakurai-Ozato N, Kubo M, Demura T, et al. (2009) *ANXUR1* and *2*, sister genes to *FERONIA/SIRENE*, are male factors for coordinated fertilization. Curr Biol 19: 1327–1331.
21. Potocký M, Jones MA, Bezvoda R, Smirnoff N, Zárský V (2007) Reactive oxygen species produced by NADPH oxidase are involved in pollen tube growth. New Phytol 174: 742–751.
22. Cárdenas L, McKenna ST, Kunkel JG, Hepler PK (2006) NAD(P)H oscillates in pollen tubes and is correlated with tip growth. Plant Phys 142: 1460–1468.
23. Knight MR (2007) New ideas on root hair growth appear from the flanks. Proc Natl Acad Sci U S A 104: 20649–20650.
24. Lee YJ, Yang Z (2008) Tip growth: signaling in the apical dome. Curr Opin Plant Biol 11: 662–671.
25. Wymer CL, Bibikova TN, Gilroy S (1997) Cytoplasmic free calcium distributions during the development of root hairs of Arabidopsis *thaliana*. Plant J 12: 427–439.
26. Monshausen GB, Bibikova TN, Messerli MA, Shi C, Gilroy S (2007) Oscillations in extracellular pH and reactive oxygen species modulate tip growth of *Arabidopsis* root hairs. Proc Natl Acad Sci U S A 104: 20996–21001.
27. Swanson S, Gilroy S (2010) ROS in plant development. Physiol Planta 138: 384–392.
28. Monshausen GB, Bibikova TN, Weisenseel MH, Gilroy S (2009) Ca^{2+} regulates reactive oxygen species production and pH during mechanosensing in *Arabidopsis* roots. Plant Cell 21: 2341–2356.
29. Ischebeck T, Stenzel I, Heilmann I (2008) Type B phosphatidylinositol-4-phosphate 5-kinases mediate *Arabidopsis* and *Nicotiana tabacum* pollen tube growth by regulating apical pectin secretion. Plant Cell 20: 3312–3330.
30. Sousa E, Kost B, Malhó R (2008) *Arabidopsis* phosphatidylinositol-4-monophosphate 5-kinase 4 regulates pollen tube growth and polarity by modulating membrane recycling. Plant Cell 20: 3050–3064.
31. Zhao Y, Yan A, Feijó JA, Furutani M, Takenawa T, et al. (2010) Phosphoinositides regulate clathrin-dependent endocytosis at the tip of pollen tubes in *Arabidopsis* and tobacco. Plant Cell 22: 4031–4044.
32. Lee YJ, Szumlanski A, Nielsen E, Yang Z (2008) Rho-GTPase-dependent filamentous actin dynamics coordinate vesicle targeting and exocytosis during tip growth. J Cell Biol 181: 1155–1168.
33. Belousov V V, Fradkov AF, Lukyanov KA, Staroverov DB, Shakhbazov KS, et al. (2006) Genetically encoded fluorescent indicator for intracellular hydrogen peroxide. Nat Methods 3: 281–286.
34. Costa A, Drago I, Behera S, Zottini M, Pizzo P, et al. (2010) H_2O_2 in plant peroxisomes: an *in vivo* analysis uncovers a Ca(2+)-dependent scavenging system. Plant J 62: 760–772.
35. Michard E, Dias P, Feijó JA (2008) Tobacco pollen tubes as cellular models for ion dynamics: improved spatial and temporal resolution of extracellular flux and free cytosolic concentration of calcium and protons using pHluorin and YC3.1 CaMeleon - Springer. Sex Plant Rep 21: 169–181.
36. Wu J, Shang Z, Wu J, Jiang X, Moschou PN, et al. (2010) Spermidine oxidase-derived H_2O_2 regulates pollen plasma membrane hyperpolarization-activated Ca(2+) -permeable channels and pollen tube growth. Plant J 63: 1042–1053.
37. Konrad KR, Wudick MM, Feijó JA (2011) Calcium regulation of tip growth: new genes for old mechanisms. Curr Opin Plant Biol 14: 721–730.
38. Iwano M, Entani T, Shiba H, Kakita M, Nagai T, et al. (2009) Fine-tuning of the cytoplasmic Ca^{2+} concentration is essential for pollen tube growth. Plant Phys 150: 1322–1334.
39. Rounds CM, Lubeck E, Hepler PK, Winship LJ (2011) Propidium iodide competes with Ca(2+) to label pectin in pollen tubes and *Arabidopsis* root hairs. Plant Phys 157: 175–187.
40. Messerli M, Robinson KR (1997) Tip localized Ca^{2+} pulses are coincident with peak pulsatile growth rates in pollen tubes of *Lilium longiflorum*. J Cell Sci 110: 1269–1278.
41. Picton JM, Steer MW (1983) Evidence for the role of Ca^{2+} ions in tip extension in pollen tubes. Protoplasma 115: 11–17.
42. Rounds CM, Bezanilla M (2013) Growth mechanisms in tip-growing plant cells. Annu Rev Plant Biol 64: 243–265.
43. Kost B (1999) Rac homologues and compartmentalized phosphatidylinositol 4,5-bisphosphate act in a common pathway to regulate polar pollen tube growth. J Cell Biol 145: 317–330.

44. Li H (1999) Control of pollen tube tip growth by a Rop GTPase dependent pathway that leads to tip-localized calcium influx. Plant Cell 11: 1731–1742.
45. Choi W-G, Swanson SJ, Gilroy S (2012) High-resolution imaging of Ca^{2+}, redox status, ROS and pH using GFP biosensors. Plant J 70: 118–128.
46. Takeda S, Gapper C, Kaya H, Bell E, Kuchitsu K, et al. (2008) Local positive feedback regulation determines cell shape in root hair cells. Science 319: 1241–1244.
47. Potocký M, Pejchar P, Gutkowska M, Jiménez-Quesada MJ, Potocká A, et al. (2012) NADPH oxidase activity in pollen tubes is affected by calcium ions, signaling phospholipids and Rac/Rop GTPases. J Plant Phys 169: 1654–1663.
48. Liu P, Li R-L, Zhang L, Wang Q-L, Niehaus K, et al. (2009) Lipid microdomain polarization is required for NADPH oxidase-dependent ROS signaling in *Picea meyeri* pollen tube tip growth. Plant J 60: 303–313.
49. Monshausen GB, Messerli MA, Gilroy S (2008) Imaging of the yellow cameleon 3.6 indicator reveals that elevations in cytosolic Ca^{2+} follow oscillating increases in growth in root hairs of *Arabidopsis*. Plant Phys 147: 1690–1698.
50. Hepler PK, Kunkel JG, Rounds CM, Winship LJ (2012) Calcium entry into pollen tubes. Trends Plant Sci 17: 32–38.
51. Tunc-Ozdemir M, Rato C, Brown E, Rogers S, Mooneyham A, et al. (2013) Cyclic nucleotide gated channels 7 and 8 are essential for male reproductive fertility. PloS One 8: e55277. doi:10.1371/journal.pone.0055277
52. Frietsch S, Wang Y-F, Sladek C, Poulsen LR, Romanowsky SM, et al. (2007) A cyclic nucleotide-gated channel is essential for polarized tip growth of pollen. Proc Natl Acad Sci U S A 104: 14531–14536.
53. Laohavisit A, Shang Z, Rubio L, Cuin TA, Véry A-A, et al. (2012) *Arabidopsis annexin1* mediates the radical-activated plasma membrane Ca^{2+}- and K^{+}-permeable conductance in root cells. Plant Cell 24: 1522–1533.
54. Battey N, James N, Greenland A, Brownlee C (1999) Exocytosis and endocytosis. Plant Cell 11: 643–660.
55. Roy SJ, Holdaway-Clarke TL, Hackett GR, Kunkel JG, Lord EM, et al. (1999) Uncoupling secretion and tip growth in lily pollen tubes: evidence for the role of calcium in exocytosis. Plant J 19: 379–386.
56. Hála M, Cole R, Synek L, Drdová E, Pecenková T, et al. (2008) An exocyst complex functions in plant cell growth in *Arabidopsis* and tobacco. Plant Cell 20: 1330–1345.
57. Kroeger J, Geitmann A (2012) The pollen tube paradigm revisited. Curr Opin Plant Biol 15: 618–624.
58. Vogler H, Draeger C, Weber A, Felekis D, Eichenberger C, et al. (2013) The pollen tube: a soft shell with a hard core. Plant J 73: 617–627.
59. Hruz T, Laule O, Szabo G, Wessendorp F, Bleuler S, et al. (2008) Genevestigator v3: a reference expression database for the meta-analysis of transcriptomes. Adv Bioinformatics 2008: 420747.

Appendix 6: A Robust and Sensitive Synthetic Sensor to Monitor the Transcriptional Output of the Cytokinin Signaling Network in Planta

A Robust and Sensitive Synthetic Sensor to Monitor the Transcriptional Output of the Cytokinin Signaling Network in Planta[1][C][W][OA]

Evelyne Zürcher[2], Deborah Tavor-Deslex[2], Dmytro Lituiev, Katalin Enkerli, Paul T. Tarr, and Bruno Müller*

Institute of Plant Biology, Zurich-Basel Plant Science Center, University of Zurich, CH–8008 Zurich, Switzerland (E.Z., D.T.-D., D.L., K.E., B.M.); and Division of Biology, California Institute of Technology, Pasadena, California 91125 (P.T.T.)

Cytokinins are classic plant hormones that orchestrate plant growth, development, and physiology. They affect gene expression in target cells by activating a multistep phosphorelay network. Type-B response regulators, acting as transcriptional activators, mediate the final step in the signaling cascade. Previously, we have introduced a synthetic reporter, *Two Component signaling Sensor* (*TCS*)::*green fluorescent protein* (*GFP*), which reflects the transcriptional activity of type-B response regulators. *TCS*::*GFP* was instrumental in uncovering roles of cytokinin and deepening our understanding of existing functions. However, *TCS*-mediated expression of reporters is weak in some developmental contexts where cytokinin signaling has a documented role, such as in the shoot apical meristem or in the vasculature of Arabidopsis (*Arabidopsis thaliana*). We also observed that GFP expression becomes rapidly silenced in *TCS*::*GFP* transgenic plants. Here, we present an improved version of the reporter, *TCS new* (*TCSn*), which, compared with *TCS*, is more sensitive to phosphorelay signaling in Arabidopsis and maize (*Zea mays*) cellular assays while retaining its specificity. Transgenic Arabidopsis *TCSn*::*GFP* plants exhibit strong and dynamic GFP expression patterns consistent with known cytokinin functions. In addition, GFP expression has been stable over generations, allowing for crosses with different genetic backgrounds. Thus, *TCSn* represents a significant improvement to report the transcriptional output profile of phosphorelay signaling networks in Arabidopsis, maize, and likely other plants that display common response regulator DNA-binding specificities.

The plant hormone cytokinin comprises a class of small, adenine-derived organic molecules that influence plant development and physiology in diverse contexts throughout the plant life cycle. Cytokinins initiate a multistep phosphorelay (MSP) signaling cascade by binding to and activating the cognate receptors, hybrid kinases with a cyclases/His kinases-associated sensory extracellular ligand-binding domain (Anantharaman and Aravind, 2001; Mougel and Zhulin, 2001). In Arabidopsis (*Arabidopsis thaliana*), these are encoded by the *ARABIDOPSIS HIS KINASE2* (*AHK2*), *AHK3*, and *AHK4* genes. Ligand binding triggers autophosphorylation at a conserved His residue in the receiver domain and subsequent transfer of the phosphoryl group to a conserved Asp residue in the attached transmitter domain. Besides the cytokinin receptors, eight other hybrid kinases are encoded by the Arabidopsis genome, including *CYTOKININ INDEPENDENT1* (*CKI1*), which can potentially activate the MSP signaling network. From the Asp of the hybrid kinase, the phosphoryl group is passed on to one of five ARABIDOPSIS HIS PHOSPHOTRANSFER proteins and then to a nuclear ARABIDOPSIS RESPONSE REGULATOR (ARR), of which there are type-A, type-B, and type-C. Members of the type-B class bind to promoters of target genes via their Myb-like DNA-binding domain and activate transcription, while type-A and type-C ARRs inhibit signaling activity. At the same time, type-A ARRs are immediate-early target genes of activated type-B ARR proteins, which establishes a negative feedback loop to the signaling pathway (Werner and Schmülling, 2009; Argueso et al., 2010; Perilli et al., 2010; Bishopp et al., 2011a; Hwang et al., 2012).

Despite the apparent simplicity of the MSP signaling mechanism, the precise identification and functional characterization of the diverse signaling locales poses several challenges. First, the distribution of active cytokinin ligands in planta is difficult to determine. Cytokinins are produced by complex enzymatic biosynthetic pathways in different cellular compartments and are

[1] This work was supported a Syngenta Fellowship from the Zurich-Basel Plant Science Center, University of Zurich (to B.M.) and a grant from the Swiss National Science Foundation (to B.M.).

[2] These authors contributed equally to the article.

* Corresponding author; e-mail bruno.mueller@uzh.ch.

The author responsible for distribution of materials integral to the findings presented in this article in accordance with the policy described in the Instructions for Authors (www.plantphysiol.org) is Bruno Müller (bruno.mueller@uzh.ch).

[C] Some figures in this article are displayed in color online but in black and white in the print edition.

[W] The online version of this article contains Web-only data.

[OA] Open Access articles can be viewed online without a subscription.

www.plantphysiol.org/cgi/doi/10.1104/pp.112.211763

subject to long- and short-range transport and degradation (Werner et al., 2006; Hirose et al., 2008; Bishopp et al., 2011b). Although distribution patterns of cytokinins using monoclonal antibodies have been reported (Aloni et al., 2004, 2005), the available antibodies detect only a subset of active cytokinins, as well as inactive precursor forms (Eberle et al., 1986). Besides AHK2, AHK3, and AHK4, cytokinin-independent hybrid kinases, in particular CKI1 (Pischke et al., 2002; Hejátko et al., 2003, 2009; Deng et al., 2010), but potentially also the ethylene receptor ETR1 (Cho and Yoo, 2007; Hall et al., 2012) or AHK5 (Mira-Rodado et al., 2012; Pham et al., 2012), can activate the MSP network. The use of mutants is complicated because of redundantly acting signaling components, which require the generation of higher order mutants. For many gene families, these are difficult or impractical to generate due to the high number of genes involved, the lack of null mutants, or the close linkage of loci. Moreover, phenotypes caused by a loss of signaling are often pleiotropic or cause early lethality, which can mask functions of interest. In contrast to these difficulties, visualizing the transcriptional MSP output with a synthetic reporter reveals the sites of action during wild-type development. This information then allows focusing on the specific context for functional analyses, such as applying targeted genetic approaches or chemical and pharmacological treatments, and tracking the immediate consequences on the signaling output. The Myb-like DNA-binding domain of the 11 different type-B ARR family members is conserved, in particular, in the nine residues that were shown to make direct DNA contact (Hosoda et al., 2002). Accordingly, in vitro binding studies with the DNA-binding domains of different type-B ARRs identified very similar binding specificities, with the consensus sequence 5′-(A/G)GAT(C/T)-3′ (Sakai et al., 2000; Hosoda et al., 2002; Imamura et al., 2003). This apparent similarity in the DNA binding specificity of the different type-B ARR family members was exploited to design a specific synthetic sensor, *Two Component signaling Sensor* (*TCS*), which is based on concatemeric 5′-(A/G)GAT(C/T)-3′ binding sites (Fig. 1, A–D; Müller and Sheen, 2008). In transgenic *TCS*::*GFP* plants, the *GFP* signal reflecting the signaling output pattern has facilitated describing novel cytokinin functions (Müller and Sheen, 2008; Bencivenga et al., 2012; Marsch-Martínez et al., 2012), as well as refining and deepening the understanding of existing cytokinin functions (Leibfried et al., 2005; Gordon et al., 2009; Zhao et al., 2010; Bielach et al., 2012; Chickarmane et al., 2012; Murray et al., 2012). Despite the documented value of *TCS*-controlled reporters, some limitations emerged, which motivated us to construct an improved version. First, *TCS*-induced expression is weak in certain developmental contexts where cytokinin signaling has a documented role, such as in the embryo sac (Pischke et al., 2002; Hejátko et al., 2003; Deng et al., 2010; Bencivenga et al., 2012), in the shoot (Gordon et al., 2009; Zhao et al., 2010; Chickarmane et al., 2012), and in the vasculature (Mähönen et al., 2000, 2006a, 2006b; Dello Ioio et al., 2008). Second, we observed that GFP expression becomes progressively reduced with increasing generations, such as in the root meristem of the seedling (Fig. 1B), presumably due to silencing effects triggered by the monotony of the repetitive sequence in *TCS* (Chan et al., 2005). Here, we present a superior version, *TCS new* (*TCSn*)::*GFP*, which exhibits higher sensitivity to cytokinin and MSP components in transient transfection assays (Fig. 2) and a much brighter GFP signal in most tissues analyzed (Figs. 3 and 4). Thus, the *TCSn*::*GFP* expression pattern reveals aspects of the MSP output that were not reported by *TCS*::*GFP*. Furthermore, GFP expression has been stable during propagation, indicating that unlike *TCS*::*GFP*, it does not easily get silenced.

RESULTS

Defining Relevant Parameters to Improve TCS Activity

To reliably and consistently monitor low-to-intermediate output levels of the MSP network in planta and to avoid transgene silencing, we sought to improve the current synthetic sensor TCS (Müller and Sheen, 2008). Its design is based on the in vitro-defined DNA consensus sequence 5′-(A/G)GAT(C/T)-3′, as recognized by type-B ARRs (Sakai et al., 2000; Hosoda et al., 2002; Imamura et al., 2003). To identify parameters that affect the activity of TCS, derivatives were constructed with variations in the number of binding sites, phasing, and identity of flanking nucleotides. All of the resulting fragments were cloned upstream of the cauliflower mosaic virus minimal 35S promoter and transcriptionally fused to luciferase (LUC). The ability of these constructs to confer cytokinin-dependent transcriptional activation was experimentally tested in transient transfection assays of primary mesophyll protoplasts (Müller and Sheen, 2008). An oligonucleotide harboring four such bindings sites, separated by arbitrarily selected flanking nucleotides, represented the basic building block for *TCS* (Fig. 1C). Multimerization of this sequence fragment resulted in various derivatives with an increasing number of binding sites (Fig. 1A). The arrangement of binding sites was chosen to realize all possible orientations that two given motifs can have relative to each other: tandem, tail to tail, and head to head (Fig. 1, A and D). Minimal but robust activity was observed with eight binding sites, while 16 sites resulted in a sensitivity comparable to *ARR6*::*LUC*, a reporter based on the 5′ cis-regulatory region of *ARR6* (Hwang and Sheen, 2001), a type-A *ARR* with 11 clustered 5′-(A/G)GAT(C/T)-3′ motifs in its promoter (Fig. 1A; Supplemental Table S2). A dramatic increase in cytokinin responsiveness occurred when the number of sites increased from 16 to 24. Such a sigmoidal response curve is indicative of synergistic interactions among activator binding sites (Carey, 1998). The addition of more sites did not stimulate the activity further (Fig. 1A). Thus, 24 binding sites were chosen for the final design, which was named TCS (Müller and Sheen, 2008). A variant of *TCS*,

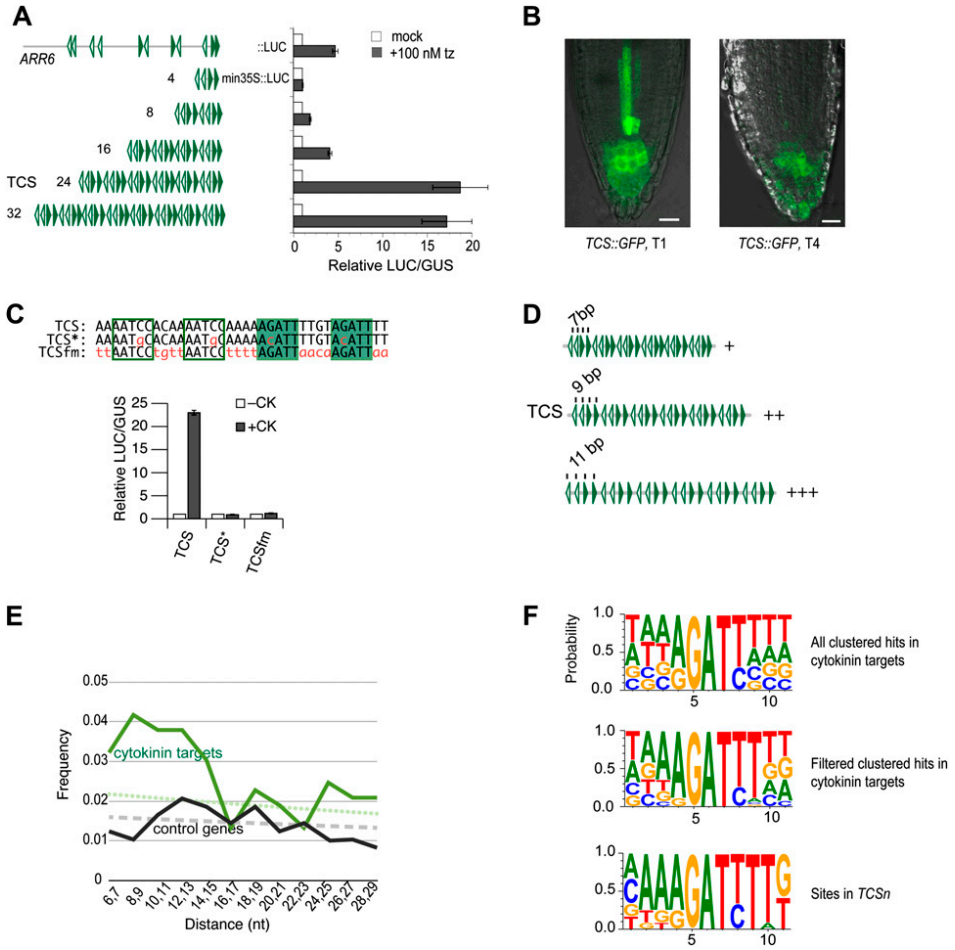

Figure 1. Optimization of *TCS*. A, A concatemer of 24 repeats of the 5′-(A/G)GAT(C/T)T-3′ binding motif caused the strongest cytokinin-dependent induction of a LUC reporter in transient transfection assays. B, Reduced GFP signal in the primary root meristem of a 5-d-old transgenic *TCS*::*GFP* seedling in the fourth generation (T4) compared with a primary transformant (T1). C, Similar to mutating nucleotides essential for in vitro binding of type-B ARRs (*TCS**::*LUC*, where the asterisk indicates point mutation G→C), the mutation of flanking nucleotides (*TCSfm*::*LUC*) abolished cytokinin-dependent response of *TCS*::*LUC*. D, Scheme representing the quantitative effects of different phasings of core 5′-(A/G)GAT(C/T)T-3′ motifs. Phasing of 11 bp results in strongest reporter gene expression. E, The frequency of 5′-(A/G)GAT(C/T)T-3′ motifs with a distance of 7 to 15 bp in cytokinin target genes (top curve) is higher than expected (dotted line), while the same motifs are not significantly higher than expected in control genes (lower curve and dashed line). F, Sequence logos (Crooks et al., 2004) generated from the alignment of clustered 5′-(A/G)GAT(C/T)T-3′ motifs in cytokinin target genes as listed in Supplemental Table S2 (top) after filtering with 5′-A(A/G)GAT (C/T)T-3′ and 5′-A (A/G)GAT(C/T)TT-3′ (middle), and the alignment based on the 12 motifs used to construct *TCSn* as listed in Supplemental Table S4 (bottom). Filled or empty arrowheads (A and D) or boxes (C) indicate 5′-A (A/G)GAT(C/T)TT-3′ motifs on the forward or reverse DNA strand, respectively. Bars = 20 μm. [See online article for color version of this figure.]

TCSfm (for *flanking nucleotides mutated*), harbors mutations in the nucleotides that flank the in vitro-defined core sequences and was expected to integrate cytokinin-dependent induction similar to *TCS*, recapitulating the results of in vitro binding studies. Notably, *TCSfm* is insensitive to cytokinin (Fig. 1C), indicating that the in vitro-defined core motif 5′-(A/G)GAT(C/T)-3′ is too short to support transcriptional activation in vivo. Other derivatives of *TCS* differ in the distance between binding sites (Fig. 1D). Compared to *TCS* with a 9-bp distance between the core motifs, 11 bp resulted in higher activity, while reducing the distance to 7 bp caused a substantial reduction in activity (Fig. 1D). Eleven base pairs correspond approximately to one helical turn of the DNA double helix in its common B configuration (Wang, 1979). In agreement with our findings, helical phasing has been shown to be an important parameter for the functionality of transcription factor binding motifs in individual genes (Bouallaga et al., 2000; Mack et al., 2000; D'Alonzo et al., 2002) and has also been observed at a global scale (Ioshikhes et al., 1999; Makeev et al., 2003). Based on these experiments, we reasoned that improving *TCS* could be achieved by using extended type-B ARR binding motifs and adjusting the phasing of motifs to 11 bp.

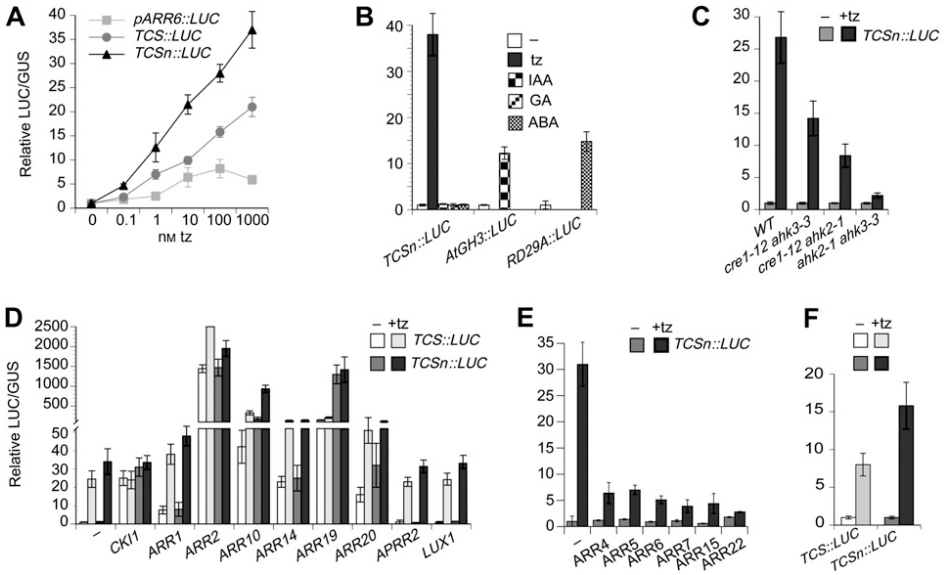

Figure 2. Sensitivity and specificity of *TCSn*::*LUC* in transient transfection assays. A, Induction of *ARR6*::*LUC*, *TCS*::*LUC*, and *TCSn*::*LUC* to increasing concentrations of transzeatin. B, *TCSn*::*LUC* is induced by transzeatin, but not by auxin, GA_3, or abscisic acid. *AtGH3*::*LUC* and *RD29A*::*LUC* serve as positive controls for auxin and abscisic acid hormone induction, respectively (Müller and Sheen, 2008). C, Cytokinin-dependent induction of *TCSn*::*LUC* is compromised in *ahk4 ahk3*, *ahk4 ahk2*, and *ahk2 ahk3* double mutant cells. *cre1-12* is a mutant allele of *AHK4* (Higuchi et al., 2004). D, Positive regulators of the MSP network induce *TCSn*::*LUC* expression. APRR2 and LUX have no effect. E, Type-A and type-C ARR attenuate cytokinin-dependent induction of *TCSn*::*LUC*. F, *TCS*::*LUC* and *TCSn*::*LUC* are induced in maize protoplasts by transzeatin. tz, Transzeatin; IAA, auxin; GA, GA_3; ABA, abscisic acid.

Bioinformatic Analyses to Identify Relevant Type-B ARR Consensus Binding Sites in Vivo

To analyze the type-B ARR binding motifs as they occur in vivo, we analyzed the sequence of the 10 type-A *ARR* genes (*ARR3*–*ARR9* and *AAR15*–*AAR17*). These genes represent the best-documented direct cytokinin target genes (D'Agostino et al., 2000; Taniguchi et al., 2007; Brenner et al., 2012). As a negative control, genes were randomly picked from a list of genes that showed stable expression irrespective of developmental stage, stress, and pharmacological or physiological treatments (Czechowski et al., 2005). Since the cis-regulatory sequence is typically found upstream, but can also be located the within transcribed sequence (Yant et al., 2010; Ritter et al., 2012), about 3 kb of the 5′-upstream sequence, as well as the transcribed sequence from each gene, was included in the analysis, totaling 45 kb of sequence for the 10 type-A *ARR* genes and 58 kb for the control genes (Supplemental Table S6). In each set, the number of hits to the 5′-(A/G)GAT(C/T)-3′ motif was counted. This motif has been shown to be indispensable for type-B *ARR* binding in vitro (Sakai et al., 2000; Hosoda et al., 2002; Imamura et al., 2003) and for function in vivo (Ross et al., 2004; Müller and Sheen, 2008; Zhao et al., 2010; Liang et al., 2012). However, it is short and degenerate and thus occurs frequently by chance: on average, once in 108 bp of random DNA sequence. In the control genes, the frequency of motifs falls within a 95% confidence interval of a Poisson distribution, consistent with random frequency. By contrast, a hit is found every 86 bp in the cytokinin target genes. Such, or even higher, densities are very unlikely to occur by chance assuming Poisson distribution ($P < 10^{-7}$), suggesting that a considerable fraction of the 5′-(A/G)GAT(C/T)-3′ motifs found in cytokinin target genes is functional in integrating cytokinin input (Supplemental Table S1). Next, distances and relative orientations of these motifs were analyzed. Specifically, we measured the distances between two given hits and sorted them into different size classes. The motif itself measures 5 bp; thus, the shortest distance between two hits is 6 bp. Because we were mainly interested in clustered hits, we did not resolve distances greater than an arbitrary 30 bp. The expected size distribution follows the function: $F(n) = (1 - P)^{n-1}P$, where P is the probability to find a hit (Basler, 2000). In the cytokinin target genes, distances from 6 to 30 bp are significantly overrepresented (X^2 [1, n = 527] = 21.1, $P < 0.00001$), suggesting that these motifs are functional to support cooperativity of transcription factor binding in natural promoters, similar to what was observed in synthetic sequences (Fig. 1A). The observed enrichment concentrates to distances of 7 to 14 bp (Fig. 1E; Supplemental Table S3). When the relative orientation of clustered motifs was analyzed, no apparent bias either toward tandem or inverse orientations was detected (Supplemental Table S3). The analysis suggests that clustered 5′-(A/G)GAT(C/T)-3′ hits are

significantly enriched in cytokinin target genes, and we used these hits to create an alignment. An additional three nucleotides flanking the core site were included, totaling 11 nucleotides, which was determined as the optimal phasing based on transient transfection experiments reported above (Fig. 1D). The resulting alignment, represented by a sequence logo (Crooks et al., 2004), revealed the tendency for conservation of nucleotides flanking the core (Fig. 1F). Specifically, sequences accompanied by a 5′ extension, 5′-A-3′ and/or a 3′ extension, 5′-T-3′ appear more frequently, similarly to previous findings (Rashotte et al., 2003; Taniguchi et al., 2007). We used this information to reduce the number of nonspecific motifs from the alignment and filtered the list of motifs using the sequences 5′-A(A/G)GAT(C/T)-3′ and 5′-(A/G)GAT(C/T)T-3′ (Supplemental Table S2). The resulting smaller set of binding motifs yielded a sequence logo with a AA(A/G)GAT(C/T)TT consensus (Fig. 1F). This consensus was also found enriched in the cytokinin target genes compared with the control genes (not shown), similar to previous studies (Brenner et al., 2012).

Based on the refined sequence logo, we created 12 sites, each slightly different from the other. Their alignment creates a sequence logo, which is similar to the natural sites (Fig. 1F; Supplemental Table S4). These synthetic sites were combined in random order to result in a synthetic sequence fragment that was repeated once to harbor 24 binding sites (Supplemental Table S5). Since clustered sites in cytokinin targets show no preference for a specific relative orientation, we preserved the relative site arrangement of *TCS*, which supports all possible orientations (Fig. 1A). This improved synthetic fragment was named *TCSn*. To summarize, the results obtained from transient transfection assays combined with bioinformatic analyses of bona fide cytokinin target genes allowed us to construct a new synthetic cytokinin promoter with an optimized number, spacing, and sequence of motifs, while also including variations to reflect the range of potential diversity among sites found in natural targets. At the same time, sequence variations avoid sequence monotony that could trigger the silencing of *TCSn*::*GFP* in transgenic plants.

TCSn Specifically Integrates MSP Activity

Using transient transfection experiments of mesophyll protoplasts, *TCSn*::*LUC* was subjected to various assays to determine its sensitivity and specificity to MSP signaling (Fig. 2). Its sensitivity to cytokinin was higher compared with *TCS*::*LUC* or *ARR6*::*LUC* (Fig. 2A). Similar to *TCS* (Müller and Sheen, 2008), *TCSn* did not cause transcription of *LUC* upon incubation with the auxin indole-3-acetic acid, GA_3, or abscisic acid (Fig. 2B). Compared with wild-type cells, cytokinin-dependent expression of *TCSn*::*LUC* is compromised in cells that are mutated in two out of the three cytokinin receptor genes *AHK2*, *AHK3*, and *AHK4* (Fig. 2C). Cotransfection with positively acting signaling components, including CKI1 and type-B ARRs, stimulated *TCSn*::*LUC* expression. Notably, overexpression of ARR10, ARR19, and ARR20 caused markedly stronger induction of *TCSn*::*LUC* than of *TCS*::*LUC*, while the remaining type-B ARRs showed similar induction of both reporters. By contrast, ARABIDOPSIS PSEUDO-RESPONSE REGULATOR2 (APRR2) and LUX ARRHYTHMO (LUX), both of which share a very similar DNA-binding domain with type-B ARRs (Hwang et al., 2002; Helfer et al., 2011), do not activate *TCS* nor *TCSn* transcription (Fig. 2D). As expected, cotransfection with type-A ARRs attenuated cytokinin-dependent induction (Fig. 2E). Next, we tested the reporters in maize (*Zea mays*) mesophyll protoplasts. As could be predicted from the similarity of the type-B response regulators between monocots and dicots (Chu et al., 2011), *TCS*::*LUC* and *TCSn*::*LUC*

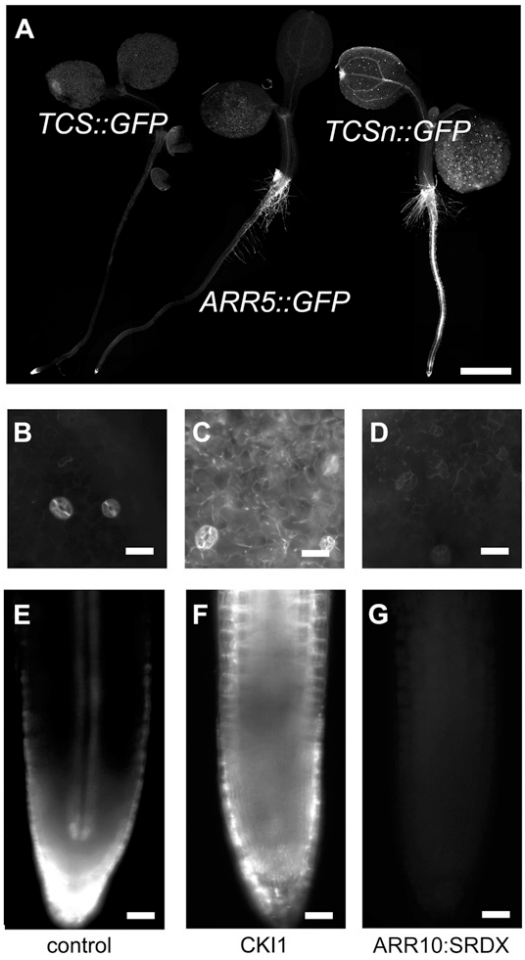

Figure 3. *TCSn*::*GFP* in the seedling. A, Compared with *TCS*::*GFP* and *ARR5*::*GFP*, *TCSn*::*GFP* exhibits strong GFP expression both in the root and shoot of the seedling. B to G, Induced overexpression of CKI1 (C and F) and ARR10:SRDX (D and G) causes ectopic activation or repression of *TCSn*::*GFP*, respectively, compared with controls (B and E) in the cotyledons (B–D) and the root meristem (E–G). Bars = 20 μm.

expression is activated by cytokinin in maize protoplasts (Fig. 2F). In summary, *TCSn* performs superior to *TCS* using protoplast transient assays, while retaining its specificity.

TCSn-Directed GFP Signals in the Seedling Are Brighter Than ARR5- or TCS-Controlled Reporters and Depend on MSP Signaling

Next, we analyzed the GFP expression pattern in plants that were transformed with a *TCSn*::*GFP* construct. Overall, *TCSn*::*GFP* expression levels are higher than *TCS*::*GFP* or *ARR5*::*GFP*, another frequently used cytokinin reporter (Fig. 3A). To address whether *TCSn*::*GFP* expression in planta is also controlled by MSP signaling, we transiently overexpressed proteins that either dominantly activate or repress MSP signaling. Compared with steady mutants, this approach avoids lethality issues and secondary effects. CKI1 induces MSP activity constitutively independent of cytokinins (Hwang and Sheen, 2001; Hejátko et al., 2009). Thus, *CKI1* expression was ubiquitously induced for 30 h in 3-d-old seedlings. Consequently, both in the main root tip and in epidermal cells of the cotyledons, ectopic and ubiquitous signaling activity is observed (Fig. 3, C and F), compared with the control (Fig. 3, B and E). By contrast, *TCSn*-dependent expression is affected by a dominant-negative version of the type-B ARR10. Specifically, ubiquitously expressed ARR10:SRDX caused a loss of the endogenous expression domains (Fig. 3, D and G). This result is in agreement with previous experiments where type-B ARRs harboring a chimeric repressor domain suppress phosphorelay signaling (Heyl et al., 2008; Müller and Sheen, 2008). Thus, ectopic activation of MSP signaling in planta induces *TCSn*::*GFP* expression, while dominant-negative interference with MSP output causes loss of the *TCSn*::*GFP* domains, indicating that *TCSn* specifically integrates MSP output.

TCSn::GFP Expression Patterns Correlate with Known Cytokinin Functions and Also Reveal New Functions

A detailed analysis of the *TCSn*::*GFP* expression patterns in different tissues revealed that the GFP activity is consistent with documented cytokinin functions. For example, during ovule primordia formation, *TCSn*-directed GFP expression, similar to *TCS*::*GFP* (Bencivenga et al., 2012), localizes to the basal part of the funiculus (Fig. 4I). However, while *TCS*::*GFP* expression levels are below the detection level at later stages, *TCSn*::*GFP* expression is visible till female gametophyte stage 7 of ovule development (Fig. 4K). A very weak signal is also detected in the nuclei of the female gametophyte nuclei at the micropylar pole of the embryo sac (Figure 4, J and K, arrows). During embryogenesis, *TCSn*::*GFP* expression is detected in the suspensor and later in the hypophysis. GFP expression is down-regulated in progenitors of the hypophysis defining the basal cell lineage, while a weak signal is detected in the lens-shaped cell, similar to *TCS*::*GFP* (Müller and Sheen, 2008). Notably, expression levels in suspensor and suspensor-derived cells is much weaker compared with *TCS*::*GFP*. By contrast,

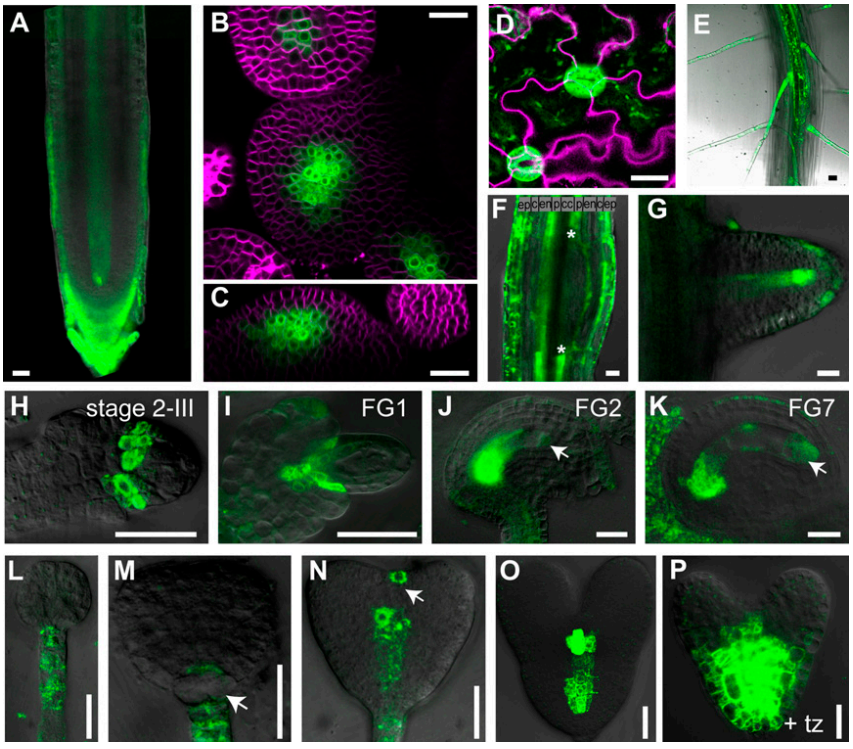

Figure 4. *TCSn*::*GFP* expression in different developmental contexts. A, Primary root meristem of 5-d-old seedling. B, Top view of shoot apical meristem. C, Side view of shoot apical meristem. D, Pavement cells and guard cells. E, Primary seedling root with root hairs. F, Lateral root primordium, early stage. Asterisks delineate lateral root primordium founder cells of pericycle that down-regulate MSP output. G, Emerging lateral root primordium. H, Ovule primordium after first mitotic division of megaspore mother cell stages, according to Schneitz et al. (1995). I to K, Embryo sac, stages according to Christensen et al. (1997). Arrows denote faint GFP signal in nuclei of embryo sac. L to P, Embryos. L, Globular stage. M, Transition stage, arrow denotes down-regulation of GFP in basal cell lineage. N, Heart stage, arrow denotes transient signal in the prospective shoot meristem. O, Late heart stage. P, Late heart stage, overnight incubation with 10 μM transzeatin. The signal from the membrane stain FM4-64 is shown in magenta. tz, Transzeatin; ep, epidermis; c, cortex; en, endodermis; p, pericycle cells; cc, central cylinder. Bars = 20 μm.

provascular cells and the prospective cells of the shoot meristem exhibit distinct and bright GFP signals (Fig. 4, N and O), which potentially allow for addressing novel cytokinin functions in these contexts. As expected, application of exogenous cytokinin leads to increased and expanded GFP expression (Fig. 4P). Expression in the columella cells of the root meristem in the seedling (Fig. 4A), in the vasculature of root (Figs. 3, A and E, and 4A), in the lateral root primordia (Fig. 4, F and G), in root hairs (Fig. 4E), in the shoot meristem (Fig. 4, B and C), in the shoot vasculature (Fig. 3A), and in pavement cells and guard cells (Fig. 4D) are qualitatively very similar to *TCS*::*GFP* (Müller and Sheen, 2008; Bielach et al., 2012; Chickarmane et al., 2012), but much stronger. Thus, in addition to revealing the peaks of cytokinin output, *TCSn*::*GFP* shows intermediate to low levels of signaling output as well. Furthermore, no reduction in GFP levels has been observed after three generations of selfing of transgenic plants (data not shown), indicating that unlike *TCS*::*GFP*, *TCSn*::*GFP* is not subject to transgene silencing.

DISCUSSION

Cytokinins activate a MSP network in target cells, which culminates in transfer of phosphoryl groups to type-B response regulators, nuclear proteins that specifically bind to DNA and activate transcription of selected target genes. Concatemeric binding motifs combined with a minimal promoter and transcriptionally fused with LUC or GFP resulted in a reporter that specifically mediates MSP output in vivo (Müller and Sheen, 2008). Ideally, activity mediated by a synthetic promoter reflects the pure and universal transcriptional output profile of the signaling activity, devoid of tissue-specific aspects or unrelated signaling input. Indeed, *TCS*-dependent expression patterns of GFP or GUS were useful in monitoring the specific sites of phosphorelay signaling output in different tissues, which guided the discovery of previously unknown cytokinin functions (Müller and Sheen, 2008; Bencivenga et al., 2012; Marsch-Martínez et al., 2012) and refined existing models of cytokinin function (Gordon et al., 2009; Zhao et al., 2010; Bielach et al., 2012; Chickarmane et al., 2012; Murray et al., 2012). However, *TCS*-mediated expression in planta is low in many contexts where MSP is known to be important, which motivated us to revise the design of *TCS* by optimizing and extending the binding motifs for the type-B ARRs. Furthermore, to counteract the silencing, we introduced sequence variations in nonessential nucleotides, which broke the monotony of the repetitive *TCS* sequence. These modifications resulted in *TCSn*, which, compared with *TCS*, demonstrates higher sensitivity to cytokinin (Fig. 2A) and a more balanced response to different type-B family members (Fig. 2D).

In transgenic plants, these improvements translate into increased GFP activity in all tissues analyzed (Figs. 3A and 4, A–K, N, and O), except for the suspensor and suspensor-derived cells of the embryo (Fig. 4, L–N). Qualitatively, the expression patterns of *TCS*::*GFP* and *TCSn*::*GFP* in planta are very similar during, for example, ovule primordia formation, embryogenesis, lateral root development, shoot meristem function, and vasculature formation (Figs. 3A and 4). The increased sensitivity of *TCSn*::*GFP* renders additional aspects of phosophorelay readout visible, which remained below the level of detection with *TCS*::*GFP*. Specifically, the expression domain in the shoot meristem is broader (Fig. 4, B and C; Gordon et al., 2009; Chickarmane et al., 2012), a GFP signal in pavement cells becomes visible (Fig. 4D), and a transient signal in the shoot meristem of the embryo at the heart stage is observed (Fig. 4N; Müller and Sheen, 2008). The apparent resistance against silencing will allow the crossing of the *TCSn*::*GFP* line in various genetic backgrounds with a reduced risk of decreased or variable GFP expression in the progeny. This will facilitate the analysis of phosphorelay signaling in many contexts, including the little-known roles in root hair development (Fig. 4E) or the emerging role in pavement (Fig. 4D; Li et al., 2012) and guard cells (Fig. 4D; Desikan et al., 2008; Mira-Rodado et al., 2012), among others.

Ideally, a synthetic reporter integrates the activities of all transcription factors involved in relaying the signal without bias toward specific family members. The 11 members of the type-B ARR family differ in their inherent activity levels, both in transient assays and in planta (Hwang and Sheen, 2001; Sakai et al., 2001; Imamura et al., 2003; Hass et al., 2004; Tajima et al., 2004; Heyl et al., 2008; Müller and Sheen, 2008; Kim et al., 2012; Liang et al., 2012). However, no reference exists for a given family member or relevant combinations thereof, and consequently, it is not clear how the ideal synthetic reporter would respond. Thus, while all type-B ARRs tested activate *TCS* and *TCSn* (Fig. 2D), we cannot exclude that the reporters may exhibit some bias toward specific type-B ARRs. For example, the low expression levels in the suspensor mediated by *TCSn*, compared with *TCS*, might reflect the better binding conditions for the set of type-B ARRs expressed in the suspensor, which facilitates integration of phosphorelay response; while in all other tissues, *TCSn* appears to provide better conditions.

Our experiments using an increasing number of binding elements in synthetic promoters suggest cooperative binding of the type-B ARRs (Fig. 1A). The statistical analysis of cytokinin target genes revealed an enrichment of clustered binding motifs, indicating that cooperative binding occurs in vivo as well. Further support for cooperative binding of type-B ARRs comes from the recent finding that ARR18 can homomerize in planta (Veerabagu et al., 2012). In prokaryotes, DNA-binding response regulators have been shown to dimerize and oligomerize (for review, see Galperin, 2006). Thus, in plants, an analogous model could be realized.

In summary, the improved sensor *TCSn* will allow a detailed study of MSP signaling in various

developmental contexts, shedding new light on plant development and physiology.

MATERIALS AND METHODS

Plant Growth and Treatments

Seedlings were germinated on vertical agar plates containing 1% (w/v) Suc, 0.8% (w/v) phytagar, and one-half-strength Murashige and Skoog medium with a 16-h/8-h photoperiod at 120 μmol m^{-2} s^{-1} and 21°C. After 3 d of growth on vertical plates, seedlings were transferred to liquid medium plates containing 1% (w/v) Suc, one-half-strength Murashige and Skoog medium, 2mM MES, pH 5.7, and 2% (v/v) ethanol for transgene induction in 12-well plates, sealed with parafilm, and incubated for 30 h before recording GFP fluorescence. Plants that needed to be grown to adulthood were kept in the greenhouse with a 16-h/8-h photoperiod at 150 μmol m^{-2} s^{-1} and 21°C during the light period and 18°C during the dark period. Plants used for protoplast transient transfection assays were grown with a 12-h/12-h photoperiod at 90 μmol m^{-2} s^{-1} and 21°C during the light period and 18°C during the dark period. Embryo in vitro cultivation and hormone treatments with transzeatin were performed as described (Müller and Sheen, 2008).

Plant Materials and Reporter and Effector Constructs

The *TCS*::*GFP* reporter line and the expression plasmids used in transient transfection assays were previously described (Hwang and Sheen, 2001; Yoo et al., 2007; Müller and Sheen, 2008). *LUX*, *APRR2*, and *ARR19* coding sequences were cloned into the expression vector as described (Hwang and Sheen, 2001). The *ARR5*::*GFP* reporter is composed of 2.3 kb of upstream regulatory sequence transcriptionally fused to GFP that localizes to the endoplasmatic reticulum (Ottenschläger et al., 2003) in the binary vector pCB302 conferring Basta resistance (Xiang et al., 1999). Plants carrying the inducible transgene *RIBOSOMAL PROTEIN S5A*::*AlcR*/*AlcA*::*ARR10*:SRDX are described in Müller and Sheen (2008). For the *35S*::*AlcR*/*AlcA*::*CKI1* transgene, the DM7 vector conferring kanamycin resistance (Müller and Sheen, 2008) was modified with a ligation-independent cloning adaptor annealed into linearized DM7 vector, digested with *Eco*RI and *Sal*I, to allow ligation of a *CKI1* PCR fragment, amplified from genomic ecotype Columbia DNA, which covers the *CKI1* locus from start to stop codons (see Supplemental Table S5 for sequences of the oligonucleotides). The *TCSn* plasmids *TCSn*::*GFP* and *TCSn*::*LUC* differ from the *TCS* variants (Müller and Sheen, 2008) by the synthetic promoter sequence. Plasmid and oligonucleotide sequences are provided in Supplemental Table S5. All plasmids have been sequenced to ensure no unwanted mutations have been introduced during cloning.

Phenotypic Analysis and Microscopy

GFP expression patterns (Fig. 3) were recorded using a Leica DM6000 microscope equipped with epifluorescence and a Leica DFC350FX camera, or with a Leica SP2 laser scanning confocal microscope (Fig. 4). Micrographs of whole seedlings in Figure 3A were assembled from individual pictures using Adobe Photoshop Creative Suite 4. The lipophilic dye FM4-64 (Molecular Probes) was used at a concentration of 10 μg mL^{-1} to demarcate cell membranes in Figure 4, B to D. Imaging for Figure 4, B and C was done using a Zeiss 510 Meta laser scanning confocal microscope with a 63× air-water dipping lens using the multitracking mode.

Transient Expression in Protoplasts

Protoplast isolation and transfection experiments were performed as reported (Sheen, 1990; Yoo et al., 2007). All protoplast experiments were performed in duplicates, and independent biological replicates yielded similar results.

Supplemental Data

The following materials are available in the online version of this article.

Supplemental Table S1. Summary of 5′-(A/G)GAT(T/C)-3′ hits in cytokinin target genes, control genes, and random sequence.

Supplemental Table S2. List of clustered 5′-NNN(A/G)GAT(T/C)NNN-3′ hits in cytokinin target genes and control genes.

Supplemental Table S3. Distance and orientation of clustered hits in cytokinin target genes and control genes.

Supplemental Table S4. Sites used for *TCSn*.

Supplemental Table S5. Plasmid and oligonucleotide sequences.

Supplemental Table S6. Gene sequences used for the bioinformatic analyses.

ACKNOWLEDGMENTS

We thank Ueli Grossniklaus (University of Zurich) for helpful discussions, financial support, and critical reading of the manuscript; Marco Celio (University of Fribourg), Jean-Pierre Métraux (University of Fribourg), and Jen Sheen (Harvard Medical School) for financial support; Tatsuo Kakimoto (Osaka University) for *ahk* mutant seeds; and Eva Benková (Institute of Science and Technology Austria), Ari Pekka Mähönen (University of Helsinki), and Jan Hejátko (Masaryk University) for testing *TCSn*::*GFP*.

Received November 27, 2012; accepted January 24, 2013; published January 25, 2013.

LITERATURE CITED

Aloni R, Langhans M, Aloni E, Dreieicher E, Ullrich CI (2005) Root-synthesized cytokinin in Arabidopsis is distributed in the shoot by the transpiration stream. J Exp Bot **56:** 1535–1544

Aloni R, Langhans M, Aloni E, Ullrich CI (2004) Role of cytokinin in the regulation of root gravitropism. Planta **220:** 177–182

Anantharaman V, Aravind L (2001) The CHASE domain: a predicted ligand-binding module in plant cytokinin receptors and other eukaryotic and bacterial receptors. Trends Biochem Sci **26:** 579–582

Argueso CT, Raines T, Kieber JJ (2010) Cytokinin signaling and transcriptional networks. Curr Opin Plant Biol **13:** 533–539

Basler K (2000) EMBO Gold Medal 1999. Waiting periods, instructive signals and positional information. EMBO J **19:** 1168–1175

Bencivenga S, Simonini S, Benková E, Colombo L (2012) The transcription factors BEL1 and SPL are required for cytokinin and auxin signaling during ovule development in *Arabidopsis*. Plant Cell **24:** 2886–2897

Bielach A, Podlesáková K, Marhavý P, Duclercq J, Cuesta C, Müller B, Grunewald W, Tarkowski P, Benková E (2012) Spatiotemporal regulation of lateral root organogenesis in *Arabidopsis* by cytokinin. Plant Cell **24:** 3967–3981

Bishopp A, Benková E, Helariutta Y (2011a) Sending mixed messages: auxin-cytokinin crosstalk in roots. Curr Opin Plant Biol **14:** 10–16

Bishopp A, Lehesranta S, Vatén A, Help H, El-Showk S, Scheres B, Helariutta K, Mähönen AP, Sakakibara H, Helariutta Y (2011b) Phloem-transported cytokinin regulates polar auxin transport and maintains vascular pattern in the root meristem. Curr Biol **21:** 927–932

Bouallaga I, Massicard S, Yaniv M, Thierry F (2000) An enhanceosome containing the Jun B/Fra-2 heterodimer and the HMG-I(Y) architectural protein controls HPV 18 transcription. EMBO Rep **1:** 422–427

Brenner WG, Ramireddy E, Heyl A, Schmülling T (2012) Gene regulation by cytokinin in Arabidopsis. Front Plant Sci **3:** 8

Carey M (1998) The enhanceosome and transcriptional synergy. Cell **92:** 5–8

Chan SW, Henderson IR, Jacobsen SE (2005) Gardening the genome: DNA methylation in *Arabidopsis thaliana*. Nat Rev Genet **6:** 351–360

Chickarmane VS, Gordon SP, Tarr PT, Heisler MG, Meyerowitz EM (2012) Cytokinin signaling as a positional cue for patterning the apical-basal axis of the growing Arabidopsis shoot meristem. Proc Natl Acad Sci USA **109:** 4002–4007

Cho YH, Yoo SD (2007) ETHYLENE RESPONSE 1 histidine kinase activity of Arabidopsis promotes plant growth. Plant Physiol **143:** 612–616

Chu ZX, Ma Q, Lin YX, Tang XL, Zhou YQ, Zhu SW, Fan J, Cheng BJ (2011) Genome-wide identification, classification, and analysis of two-component signal system genes in maize. Genet Mol Res **10:** 3316–3330

Christensen CA, King EJ, Jordan JR, Drews GN (1997) Megagametogenesis in Arabidopsis wild type and the *Gf* mutant. Sex Plant Reprod **10:** 49–64

Crooks GE, Hon G, Chandonia JM, Brenner SE (2004) WebLogo: a sequence logo generator. Genome Res **14:** 1188–1190

Czechowski T, Stitt M, Altmann T, Udvardi MK, Scheible WR (2005) Genome-wide identification and testing of superior reference genes for transcript normalization in Arabidopsis. Plant Physiol **139:** 5–17

D'Agostino IB, Deruère J, Kieber JJ (2000) Characterization of the response of the Arabidopsis response regulator gene family to cytokinin. Plant Physiol **124:** 1706–1717

D'Alonzo RC, Selvamurugan N, Karsenty G, Partridge NC (2002) Physical interaction of the activator protein-1 factors c-Fos and c-Jun with Cbfa1 for collagenase-3 promoter activation. J Biol Chem **277:** 816–822

Dello Ioio R, Nakamura K, Moubayidin L, Perilli S, Taniguchi M, Morita MT, Aoyama T, Costantino P, Sabatini S (2008) A genetic framework for the control of cell division and differentiation in the root meristem. Science **322:** 1380–1384

Deng Y, Dong H, Mu J, Ren B, Zheng B, Ji Z, Yang WC, Liang Y, Zuo J (2010) *Arabidopsis* histidine kinase CKI1 acts upstream of histidine phosphotransfer proteins to regulate female gametophyte development and vegetative growth. Plant Cell **22:** 1232–1248

Desikan R, Horák J, Chaban C, Mira-Rodado V, Witthöft J, Elgass K, Grefen C, Cheung MK, Meixner AJ, Hooley R, et al (2008) The histidine kinase AHK5 integrates endogenous and environmental signals in Arabidopsis guard cells. PLoS ONE **3:** e2491

Eberle J, Arnscheidt A, Klix D, Weiler EW (1986) Monoclonal antibodies to plant growth regulators. III. Zeatinriboside and dihydrozeatinriboside. Plant Physiol **81:** 516–521

Galperin MY (2006) Structural classification of bacterial response regulators: diversity of output domains and domain combinations. J Bacteriol **188:** 4169–4182

Gordon SP, Chickarmane VS, Ohno C, Meyerowitz EM (2009) Multiple feedback loops through cytokinin signaling control stem cell number within the Arabidopsis shoot meristem. Proc Natl Acad Sci USA **106:** 16529–16534

Hall BP, Shakeel SN, Amir M, Ul Haq N, Qu X, Schaller GE (2012) Histidine kinase activity of the ethylene receptor ETR1 facilitates the ethylene response in Arabidopsis. Plant Physiol **159:** 682–695

Hass C, Lohrmann J, Albrecht V, Sweere U, Hummel F, Yoo SD, Hwang I, Zhu T, Schäfer E, Kudla J, et al (2004) The response regulator 2 mediates ethylene signalling and hormone signal integration in Arabidopsis. EMBO J **23:** 3290–3302

Hejátko J, Pernisová M, Eneva T, Palme K, Brzobohatý B (2003) The putative sensor histidine kinase CKI1 is involved in female gametophyte development in Arabidopsis. Mol Genet Genomics **269:** 443–453

Hejátko J, Ryu H, Kim GT, Dobesová R, Choi S, Choi SM, Soucek P, Horák J, Pekárová B, Palme K, et al (2009) The histidine kinases CYTOKININ-INDEPENDENT1 and ARABIDOPSIS HISTIDINE KINASE2 and 3 regulate vascular tissue development in *Arabidopsis* shoots. Plant Cell **21:** 2008–2021

Helfer A, Nusinow DA, Chow BY, Gehrke AR, Bulyk ML, Kay SA (2011) LUX ARRHYTHMO encodes a nighttime repressor of circadian gene expression in the Arabidopsis core clock. Curr Biol **21:** 126–133

Heyl A, Ramireddy E, Brenner WG, Riefler M, Allemeersch J, Schmülling T (2008) The transcriptional repressor ARR1-SRDX suppresses pleiotropic cytokinin activities in Arabidopsis. Plant Physiol **147:** 1380–1395

Higuchi M, Pischke MS, Mähönen AP, Miyawaki K, Hashimoto Y, Seki M, Kobayashi M, Shinozaki K, Kato T, Tabata S, et al (2004) *In planta* functions of the Arabidopsis cytokinin receptor family. Proc Natl Acad Sci USA **101:** 8821–8826

Hirose N, Takei K, Kuroha T, Kamada-Nobusada T, Hayashi H, Sakakibara H (2008) Regulation of cytokinin biosynthesis, compartmentalization and translocation. J Exp Bot **59:** 75–83

Hosoda K, Imamura A, Katoh E, Hatta T, Tachiki M, Yamada H, Mizuno T, Yamazaki T (2002) Molecular structure of the GARP family of plant Myb-related DNA binding motifs of the *Arabidopsis* response regulators. Plant Cell **14:** 2015–2029

Hwang I, Chen HC, Sheen J (2002) Two-component signal transduction pathways in Arabidopsis. Plant Physiol **129:** 500–515

Hwang I, Sheen J (2001) Two-component circuitry in Arabidopsis cytokinin signal transduction. Nature **413:** 383–389

Hwang I, Sheen J, Müller B (2012) Cytokinin signaling networks. Annu Rev Plant Biol **63:** 353–380

Imamura A, Kiba T, Tajima Y, Yamashino T, Mizuno T (2003) *In vivo* and *in vitro* characterization of the ARR11 response regulator implicated in the His-to-Asp phosphorelay signal transduction in *Arabidopsis thaliana*. Plant Cell Physiol **44:** 122–131

Ioshikhes I, Trifonov EN, Zhang MQ (1999) Periodical distribution of transcription factor sites in promoter regions and connection with chromatin structure. Proc Natl Acad Sci USA **96:** 2891–2895

Kim K, Ryu H, Cho YH, Scacchi E, Sabatini S, Hwang I (2012) Cytokinin-facilitated proteolysis of ARABIDOPSIS RESPONSE REGULATOR2 attenuates signaling output in two-component circuitry. Plant J **69:** 934–945

Leibfried A, To JP, Busch W, Stehling S, Kehle A, Demar M, Kieber JJ, Lohmann JU (2005) WUSCHEL controls meristem function by direct regulation of cytokinin-inducible response regulators. Nature **438:** 1172–1175

Li H, Xu T, Lin D, Wen M, Xie M, Duclercq J, Bielach A, Kim J, Reddy GV, Zuo J, et al (2012) Cytokinin signaling regulates pavement cell morphogenesis in Arabidopsis. Cell Res **23:** 290–299

Liang Y, Wang X, Hong S, Li Y, Zuo J (2012) Deletion of the initial 45 residues of ARR18 induces cytokinin response in Arabidopsis. J Genet Genomics **39:** 37–46

Mack CP, Thompson MM, Lawrenz-Smith S, Owens GK (2000) Smooth muscle alpha-actin CArG elements coordinate formation of a smooth muscle cell-selective, serum response factor-containing activation complex. Circ Res **86:** 221–232

Mähönen AP, Bishopp A, Higuchi M, Nieminen KM, Kinoshita K, Törmäkangas K, Ikeda Y, Oka A, Kakimoto T, Helariutta Y (2006a) Cytokinin signaling and its inhibitor AHP6 regulate cell fate during vascular development. Science **311:** 94–98

Mähönen AP, Bonke M, Kauppinen L, Riikonen M, Benfey PN, Helariutta Y (2000) A novel two-component hybrid molecule regulates vascular morphogenesis of the Arabidopsis root. Genes Dev **14:** 2938–2943

Mähönen AP, Higuchi M, Törmäkangas K, Miyawaki K, Pischke MS, Sussman MR, Helariutta Y, Kakimoto T (2006b) Cytokinins regulate a bidirectional phosphorelay network in Arabidopsis. Curr Biol **16:** 1116–1122

Makeev VJ, Lifanov AP, Nazina AG, Papatsenko DA (2003) Distance preferences in the arrangement of binding motifs and hierarchical levels in organization of transcription regulatory information. Nucleic Acids Res **31:** 6016–6026

Marsch-Martínez N, Ramos-Cruz D, Irepan Reyes-Olalde J, Lozano-Sotomayor P, Zúñiga-Mayo VM, de Folter S (2012) The role of cytokinin during Arabidopsis gynoecia and fruit morphogenesis and patterning. Plant J **72:** 222–234

Mira-Rodado V, Veerabagu M, Witthöft J, Teply J, Harter K, Desikan R (2012) Identification of two-component system elements downstream of AHK5 in the stomatal closure response of *Arabidopsis thaliana*. Plant Signal Behav **7:** 1467–1476

Mougel C, Zhulin IB (2001) CHASE: an extracellular sensing domain common to transmembrane receptors from prokaryotes, lower eukaryotes and plants. Trends Biochem Sci **26:** 582–584

Müller B, Sheen J (2008) Cytokinin and auxin interaction in root stem-cell specification during early embryogenesis. Nature **453:** 1094–1097

Murray JA, Jones A, Godin C, Traas J (2012) Systems analysis of shoot apical meristem growth and development: integrating hormonal and mechanical signaling. Plant Cell **24:** 3907–3919

Ottenschläger I, Wolff P, Wolverton C, Bhalerao RP, Sandberg G, Ishikawa H, Evans M, Palme K (2003) Gravity-regulated differential auxin transport from columella to lateral root cap cells. Proc Natl Acad Sci USA **100:** 2987–2991

Perilli S, Moubayidin L, Sabatini S (2010) The molecular basis of cytokinin function. Curr Opin Plant Biol **13:** 21–26

Pham J, Liu J, Bennett MH, Mansfield JW, Desikan R (2012) Arabidopsis histidine kinase 5 regulates salt sensitivity and resistance against bacterial and fungal infection. New Phytol **194:** 168–180

Pischke MS, Jones LG, Otsuga D, Fernandez DE, Drews GN, Sussman MR (2002) An Arabidopsis histidine kinase is essential for megagametogenesis. Proc Natl Acad Sci USA **99:** 15800–15805

Rashotte AM, Carson SD, To JP, Kieber JJ (2003) Expression profiling of cytokinin action in Arabidopsis. Plant Physiol **132:** 1998–2011

Ritter DI, Dong Z, Guo S, Chuang JH (2012) Transcriptional enhancers in protein-coding exons of vertebrate developmental genes. PLoS ONE **7:** e35202

Ross EJ, Stone JM, Elowsky CG, Arredondo-Peter R, Klucas RV, Sarath G (2004) Activation of the *Oryza sativa* non-symbiotic haemoglobin-2

promoter by the cytokinin-regulated transcription factor, ARR1. J Exp Bot **55:** 1721–1731

Sakai H, Aoyama T, Oka A (2000) Arabidopsis ARR1 and ARR2 response regulators operate as transcriptional activators. Plant J **24:** 703–711

Sakai H, Honma T, Aoyama T, Sato S, Kato T, Tabata S, Oka A (2001) ARR1, a transcription factor for genes immediately responsive to cytokinins. Science **294:** 1519–1521

Schneitz K, Hülskamp M, Pruitt RE (1995) Wild-type ovule development in *Arabidopsis thaliana*; a light microscope study of cleared whole mount tissue. Plant J **7:** 731–749

Sheen J (1990) Metabolic repression of transcription in higher plants. Plant Cell **2:** 1027–1038

Tajima Y, Imamura A, Kiba T, Amano Y, Yamashino T, Mizuno T (2004) Comparative studies on the type-B response regulators revealing their distinctive properties in the His-to-Asp phosphorelay signal transduction of *Arabidopsis thaliana.* Plant Cell Physiol **45:** 28–39

Taniguchi M, Sasaki N, Tsuge T, Aoyama T, Oka A (2007) ARR1 directly activates cytokinin response genes that encode proteins with diverse regulatory functions. Plant Cell Physiol **48:** 263–277

Veerabagu M, Elgass K, Kirchler T, Huppenberger P, Harter K, Chaban C, Mira-Rodado V (2012) The Arabidopsis B-type response regulator 18 homomerizes and positively regulates cytokinin responses. Plant J **72:** 721–731

Wang JC (1979) Helical repeat of DNA in solution. Proc Natl Acad Sci USA **76:** 200–203

Werner T, Köllmer I, Bartrina I, Holst K, Schmülling T (2006) New insights into the biology of cytokinin degradation. Plant Biol (Stuttg) **8:** 371–381

Werner T, Schmülling T (2009) Cytokinin action in plant development. Curr Opin Plant Biol **12:** 527–538

Xiang C, Han P, Lutziger I, Wang K, Oliver DJ (1999) A mini binary vector series for plant transformation. Plant Mol Biol **40:** 711–717

Yant L, Mathieu J, Dinh TT, Ott F, Lanz C, Wollmann H, Chen X, Schmid M (2010) Orchestration of the floral transition and floral development in *Arabidopsis* by the bifunctional transcription factor APETALA2. Plant Cell **22:** 2156–2170

Yoo SD, Cho YH, Sheen J (2007) Arabidopsis mesophyll protoplasts: a versatile cell system for transient gene expression analysis. Nat Protoc **2:** 1565–1572

Zhao Z, Andersen SU, Ljung K, Dolezal K, Miotk A, Schultheiss SJ, Lohmann JU (2010) Hormonal control of the shoot stem-cell niche. Nature **465:** 1089–1092